Scalar and vector tracking algorithms with fault detection and exclusion for GNSS receivers : design and performance evaluation

Elie Amani

UNIVERSITÉ PARIS-EST

Tshwane University of Technology
We empower people

THESE

EN VUE DE L'OBTENTION DU

DOCTORAT DE L'UNIVERSITE PARIS-EST

EN COTUTELLE AVEC

TSHWANE UNIVERSITY OF TECHNOLOGY

Présentée et soutenue le 11 Décembre 2017 par
ELIE AMANI

Scalar and Vector Tracking Algorithms with Fault Detection and Exclusion for GNSS Receivers: Design and Performance Evaluation

---

JURY

M. Serge Reboul	Professeur	Rapporteur
M. Olivier Julien	Professeur	Rapporteur
M. François Rocaries	Professeur	Examinateur
Mme Geneviève Baudouin	Professeur	Examinateur
M. Ben Van Wyk	Professeur	Examinateur
M. Karim Djouani	Professeur	Directeur de thèse
M. Anish Kurien	Professeur	Co-Directeur de thèse
M. Marc Pollina	Ingénieur	Examinateur

Ecole Doctorale : Mathématiques et Sciences et Technologies de l'Information et de la Communication (MSTIC)
Spécialité : Signal, Image et Automatique
Laboratoire d'Accueil : Laboratoire Images, Signaux et Systèmes Intelligents (LISSI)
Directeurs de Thèse : Karim Djouani et Anish Kurien

For Jean-Baptiste Kikongo and Christine Kaburo, my parents

Mon fils, garde les préceptes de ton père, et ne rejette pas l'enseignement de ta mère. Lie-les constamment sur ton cœur, attache-les à ton cou. Ils te dirigeront dans ta marche, ils te garderont sur ta couche, ils te parleront à ton réveil. Car le précepte est une lampe, et l'enseignement une lumière, et les avertissements de la correction sont le chemin de la vie.

— Proverbes 6, 20-23

SUMMARY

Navigation with Global Navigation Satellite Systems (GNSS) is a real challenge in harsh environments (suburban, urban, heavy foliage) due to multipath and signal blockage. This thesis proposes a number of GNSS receiver architectural and algorithmic solutions to deal with this challenge. These solutions aim at exploiting the strengths of scalar and vector tracking while minimizing their weaknesses and at utilizing the efficiency of some nonlinear Bayesian filtering techniques in addressing the nonlinearities and non-Gaussianities associated with the navigation and vector tracking problem. Attention is given to some Bayesian estimators that approximate the posterior distribution without linearizing the filtering model, namely the unscented Kalman and particle filtering methods, as well as to the extended Kalman filter, whose posterior estimation is grounded on linearization of the filtering model.

First, a brief literature review that presents the fundamentals of GNSS and GNSS receivers together with the applied navigation and tracking algorithms is provided. Then an investigation of the GNSS receiver operation in multipath environments is performed. The thesis proposes models for characterizing multipath induced tracking errors in a vector tracking loop. These models make it possible to express the tracking errors with respect to multipath delay, multipath phase and multipath fading frequency. By exploiting the fact that multipath presence is mirrored on the Early-minus-Late correlator output, novel multipath detectors are devised. A correlator-based non-line-of-sight detector is designed as well.

Attention is then directed towards the design of robust tracking and positioning GNSS receiver architectures that incorporate the proposed detectors among other signal quality indicators. A vector tracking scheme capable of detecting and excluding unhealthy measurements from position-velocity-time calculation in the navigator using correlator-based signal quality indicators is suggested. Two other novel tracking schemes, the adaptive scalar-vector tracking loop and the conjoint scalar-vector tracking loop, with the same fault detection and exclusion capability, are formulated. They benefit from vector tracking robustness in harsh environments and scalar tracking positioning accuracy in open sky environments. Experimental results show that the proposed solutions have better tracking and positioning performance than the usual scalar and vector tracking loops.

Finally, the thesis presents a number of nonlinear Bayesian filtering approaches to solve the navigation and vector tracking problem. Iterative and adaptive strategies as applied to the unscented Kalman filter are studied. A novel unscented particle filter approach, the iterated adaptive unscented particle filter (IAUPF), is proposed. This approach exploits the convergence properties of iterative methods, the divergence suppression benefits of adaptive filters and the synergy of unscented Kalman and particle filtering approaches. Monte-Carlo simulations conducted with a posterior Cramér-Rao lower bound used as benchmarking reference as well as experimental results demonstrate that the IAUPF outperforms the other Bayesian estimators that are presented.

RESUME

La navigation avec les systèmes de navigation par satellites (GNSS) est un réel défi dans des environnements contraints (semi-urbain, urbain, feuillage dense) à cause des multitrajets et du masquage du signal. Cette thèse propose un nombre de solutions architecturales et algorithmiques pour le récepteur GNSS afin de pallier ces problèmes. Ces solutions se veulent capables d'exploiter les atouts des poursuites scalaire et vectorielle tout en minimisant leurs défauts et de profiter de l'efficacité de certaines techniques de filtrage Bayésien non linéaire quant à aborder la non-Gaussianité et les non-linéarités associées au problème de navigation et de poursuite vectorielle. Une attention particulière est accordée à certains estimateurs Bayésiens qui essaient d'approximer la loi a posteriori sans linéariser le modèle de filtrage, notamment le filtre de Kalman *unscented* et les méthodes de filtrage particulaire, mais aussi au filtre de Kalman étendu, dont l'estimation de la loi a posteriori est basée sur la linéarisation du modèle de filtrage.

En premier lieu, une brève étude bibliographique présentant les fondamentaux des systèmes et des récepteurs GNSS ainsi que les algorithmes de navigation et de poursuite y associés est faite. Ensuite le fonctionnement d'un récepteur GNSS en milieux contraints est investigué. La thèse propose des modèles pour caractériser les erreurs de poursuite induites par les multitrajets dans une boucle de poursuite vectorielle. Ces modèles permettent d'exprimer les erreurs de poursuite en fonction du délai, de la phase et de la fréquence d'évanouissement des multitrajets. En exploitant le fait que la présence des multitrajets se reflète sur la sortie *Early*-moins-*Late* des corrélateurs, de nouveaux détecteurs de multitrajets sont formulés. Un détecteur de masquage du signal direct est aussi proposé.

L'attention se tourne ensuite vers la conception d'architectures robustes de poursuite et positionnement pour un récepteur GNSS, incorporant les détecteurs proposés et d'autres indicateurs de qualité. Une boucle de poursuite vectorielle capable de détecter et d'exclure des mesures qui ne sont pas saines du calcul de la solution de navigation en utilisant les indicateurs de qualité est proposée. Deux autres boucles de poursuite, la boucle de poursuite adaptative scalaire-vectorielle et la boucle de poursuite conjointe scalaire-vectorielle, avec la même capacité de détection et exclusion de fautes, sont formulées. Elles bénéficient de la robustesse de la poursuite vectorielle en milieux contraints et de la précision de la poursuite scalaire en milieux dégagés. Des résultats expérimentaux montrent que les solutions conçues offrent une meilleure alternative de poursuite et positionnement par rapport aux boucles usuelles de poursuite scalaire et de poursuite vectorielle.

Enfin, la thèse présente des approches de filtrage Bayésien non linéaire pour résoudre le problème de navigation et de poursuite vectorielle. Des stratégies de filtrage itératives et adaptatives appliquées au filtre de Kalman *unscented* sont étudiées. Une nouvelle approche de filtrage particulaire *unscented* dénommée filtre particulaire *unscented* itératif et adaptatif (IAUPF) est formulée. Cette approche exploite les propriétés de convergence des méthodes itératives, l'immunité à la divergence dont jouissent les filtres adaptatifs, et la synergie entre les approches de filtrage particulaire et de Kalman *unscented*. Des simulations de Monte Carlo avec une borne inférieure de Cramér-Rao a posteriori comme référence ainsi que des résultats expérimentaux montrent que l'approche IAUPF a une meilleure performance comparativement aux autres estimateurs Bayésiens présentés.

ACKNOWLEDGEMENTS

I am thankful to Karim Djouani and Anish Kurien, my thesis advisors, for their scientific insights and guidance. I have made a long way with them and they have always been of great support to me. I would like to thank Jean-Rémi De Boer and Willy Vigneau, my M3S industrial supervisors, whose skills and support have been of tremendous value. Thanks are extended to Yacine Amirat for welcoming me at the LISSI Lab. It has been a wonderful experience to interact with many talented researchers.

I am indebted to Vincent Calmettes whose expertise in GNSS has been instrumental to this thesis. Thanks are extended to Marc Pollina, Patricia Hourquet and Christine Bonneil for their support. Fabrice Legrand and Nabil Jardak introduced me to GNSS. I will never forget that. I am thankful to my thesis reviewers, Serge Reboul and Olivier Julien, for their feedback that added a fine touch to this thesis. I am also grateful to the other members of the jury namely François Rocaries, Geneviève Baudouin and Ben Van Wyk for accepting to be examiners of this thesis and for their dedication to the success of this endeavour. Finally, I am grateful to my family and friends who have been a powerful boost to the energy that was required to complete this thesis. Pascaline, Jeanne d'Arc, Alphonsine, Médiatrice, Jean-Pierre, Alain, Patient, Jean-Bosco, Emmanuel, Dauphin, and Vianney; the list is non-exhaustive: Thank You. A special word of thanks is extended to Ponia Pech for his role in this achievement.

DECLARATION

I hereby declare that this thesis is my own work and that all sources that are cited are acknowledged by means of a comprehensive list of references. I further declare that this thesis is submitted at both Université Paris-Est and Tshwane University of Technology as a result of a *cotutelle* programme. This work has not been submitted to any other institution of higher education for a degree, diploma or other qualification whatsoever.

Le travail est un bien de l'homme — il est un bien de son humanité — car, par le travail, non seulement l'homme transforme la nature en l'adaptant à ses propres besoins, mais encore il se réalise lui-même comme homme et même, en un certain sens, «il devient plus homme».

— Jean Paul II

Contents

List of Figures

List of Tables

Acronyms

ADC	Analogue-to-Digital Converter
AGC	Automatic Gain Control
AWGN	Additive White Gaussian Noise
C/A	Coarse Acquisition
CDF	Cumulative Distribution Function
CDMA	Code Division Multiple Access
CFAR	Constant False Alarm Rate
C/N_0	Carrier-to-Noise power ratio
DLL	Delay Locked Loop
DLR	German Aerospace Centre (German)
ECEF	Earth-Centred Earth-Fixed
EKF	Extended Kalman Filter
EKPF	Extended Kalman Particle Filter
EmL	Early-minus-Late
FDE	Fault Detection and Exclusion
FFT	Fast Fourier Transform
FIM	Fisher Information Matrix
FLL	Frequency Locked Loop
FPLL	Frequency-assisted Phase Locked Loop
GLONASS	GLObal NAvigation Satellite System (Russian)
GLRT	Generalized Likelihood Ratio Test
GNSS	Global Navigation Satellite System
GPS	Global Positioning System
GS	Global Sampling
GS-UPF	Global Sampling Unscented Particle Filter
IF	Intermediate Frequency
INS	Inertial Navigation System
IAUKF	Iterated Adaptive Unscented Kalman Filter
IAUPF	Iterated Adaptive Unscented Particle Filter
IUKF	Iterated Unscented Kalman Filter
IUPF	Iterated Unscented Particle Filter
KF	Kalman Filter
LHCP	Left Hand Circularly Polarized
LOS	Line-Of-Sight
MEO	Medium Earth Orbit
M-GLRT	Modified Generalized Likelihood Ratio Test

MISE	Mean Integrated Square Error
MLE	Maximum Likelihood Estimate
MP	Multipath
MSE	Mean Square Error
NCO	Numerically Controlled Oscillator
NLOS	Non-Line-Of-Sight
PCRLB	Posterior Cramér-Rao Lower Bound
PD	Probability of Detection
PDF	Probability Density Function
PF	Particle Filter
PFA	Probability of False Alarm
PLI	Phase Lock Indicator
PLL	Phase Locked Loop
PRN	Pseudorandom Noise
PSD	Power Spectral Density
PVT	Position-Velocity-Time
RAIM	Receiver Autonomous Integrity Monitoring
RHCP	Right Hand Circularly Polarized
RMSE	Root Mean Square Error
RPF	Regularized Particle Filter
SDFLL	Scalar Delay Frequency Locked Loop
SIR	Sampling Importance Resampling
SIS	Sequential Importance Sampling
SNR	Signal to Noise Ratio
STL	Scalar Tracking Loop
UKF	Unscented Kalman Filter
UPF	Unscented Particle Filter
UT	Unscented Transform
VDFLL	Vector Delay Frequency Locked Loop
VDLL	Vector Delay Locked Loop
VGA	Variable Gain Amplifier
VTL	Vector Tracking Loop

Chapter 1

Introduction

> *In science if you know what you are doing you should not be doing it. In engineering if you do not know what you are doing you should not be doing it. Of course, you seldom, if ever, see either pure state.*
>
> — Richard W. Hamming

1.1 Background and Motivation

Navigation can be defined as the skill, art or study that involves determining one's position and orientation. This art has been practised throughout the entire human history. It has evolved from its most elementary form to a more and more sophisticated form. Navigation is used anytime there is a need to move from one place to another whether it is inside a building for instance, or on the way to one's working place, or around an unknown city. Regardless of the form of navigation that is used, the technique behind navigation aims at determining the navigator's position with respect to known locations or patterns. In the most rudimentary form of navigation, the human navigator uses a priori knowledge of the environment in which they are (visual landmarks, mental or actual map), interprets the information provided by their senses (sight, touch), and makes an inference on their position. Thus, unconsciously, the human reproduces the approach that is used by the most sophisticated navigation systems; or better put, the two fundamental steps that are used by modern navigation systems were designed based on the intrinsic and natural human navigation principle. The first step involves sensors that collect noisy measurements indirectly related to the parameters to be estimated. The second step, commonly referred to as filtering, involves the estimation of these parameters based on the collected measurements and, in a Bayesian framework, on an a priori model.

Navigation,—whether on-land, maritime, aeronautic or in-space—, has seen an explosion in usage in the last decades. In fact, apart from the high precision-oriented military and industrial applications, civilian usage of navigation systems has become widespread. Land navigation for instance is a flourishing application where navigation systems are incorporated in private cars, bikes, police vehicles, farming vehicles, firefighter trucks, and so forth. Handheld devices such as cellular phones, pedestrian navigation devices, and health monitoring gadgets represent another

considerable portion of navigation systems users. One of the major technologies that drive these applications is the Global Navigation Satellite System (GNSS), a navigation system that uses satellites to provide absolute geo-spatial positioning. The American *GPS* (Global Positioning System), the Russian *GLONASS*, the European Union *Galileo*, and the Chinese *Compass* are all GNSSs. Some have global coverage already and others are set to reach global coverage soon.

One of the intrinsic shortcomings of GNSS is that it requires line-of-sight (LOS) between the satellites and the receiver antenna. GNSS provides a navigation solution with a good availability in open-sky environments. However, the use of navigation devices extends to harsh environments that do not fulfil this requirement, mainly urban, suburban, heavy foliage, and indoor environments. In these constrained environments, GNSS signals experience extreme conditions (multipaths and LOS signal blockage). Multipath is any signal that has been reflected or diffracted at least once before being incident to the GNSS receiver antenna. These conditions severely attenuate the carrier-to-noise power ratio (C/N_0) and disturb the satellite signal tracking tasks performed by tracking loops on one hand, and the calculation of the navigation solution (position-velocity-time: PVT) on the other hand. The conventional signal tracking method used in GNSS receivers is the scalar tracking loop (STL), in which separate and independent channels are allocated to the signals emitted by different satellites. This independent satellite tracking method does not allow the GNSS receiver to benefit from information on its state and dynamics. In case of prolonged signal unavailability, the scalar tracking-based GNSS receiver must reinitialize its tracking loops by performing signal reacquisition, which is a time-consuming operation. The scalar tracking loops are also sensitive to the receiver dynamics such that high dynamics can lead to their failure.

Different techniques have been proposed to improve the robustness of GNSS receivers in degraded environments: low C/N_0 carrier tracking loops, acquisition/fast-reacquisition techniques, and various multipath processing techniques. However, some of these techniques seldom consider aspects such as precision and integrity of the calculated position (high-sensitivity receivers for instance) privileging availability at the expense of positioning quality.

Vector tracking techniques, pioneered by J.J. Spilker Jr. in [1], have also been devised and have been under study for about two decades now. In vector tracking, the receiver processes different satellite signals together, which allows information exchange between different tracking channels. The receiver thus combines the tracking and navigation tasks in one and the same algorithm, which improves tracking performance in low C/N_0 conditions and reduces the receiver sensitivity to external disturbances and to high dynamics. The principal shortcoming of the vector tracking loop (VTL) comes from its strength i.e. from tracking channels inter-

dependence. The exchange of information between one or more channels that are affected by multipath and healthy channels disturbs all the receiver channels. This disturbance appears in the form of tracking errors propagation among channels and degradation of the calculated navigation solution precision.

The recursive filtering techniques that allow information fusion and combination of tasks as it is done in vector tracking are Bayesian estimation algorithms. The Kalman Filter (KF), introduced in 1960 by Rudolph E. Kalman [2] [3], is part of that family of algorithms. The KF rapidly gained popularity among the algorithms used to estimate the state of a dynamic system. It provides the optimal solution to the filtering problem for linear Gaussian systems as a mean squared error minimizer. However, the vector tracking and navigation problem contains nonlinear models and involves non-Gaussian noises. The Extended Kalman Filter (EKF) [4] [5] is the most commonly used solution in navigation and vector tracking to tackle the nonlinearity problem. The EKF linearizes the filtering model around the most recent system state estimate and then applies KF equations. This is done under the assumption that the only uncertainty in the filtering model lies in the realization of state and measurement noises. However, in practice, the filtering model order and parameters are not known precisely and may vary in time. In the presence of severe nonlinearities, the EKF solution therefore diverges. The Unscented Kalman Filter (UKF) introduced in [6] [7] and Particle Filters (PF) developed independently in [8] [9] [10] [11] [12] [13] are interesting alternatives to the EKF. The UKF is based on a Gaussian approximation. The PF on the other hand does not set any a priori restrictions such as linearity or Gaussianity to the filtering model. The PF has been applied to nonlinear non-Gaussian Bayesian estimation problems in general and moderately to navigation problems in particular. It has not received much attention as alternative to the EKF in the vector tracking problem. Its computational complexity is mainly the cause. However, the ever increasing computational power of the electronic chip is a good motivation to explore such an application.

1.2 PROBLEM STATEMENT

Problems such as the inability of scalar tracking loops to maintain robust tracking and positioning availability in harsh environments, the propagation of tracking errors from a multipath contaminated channel to other channels due to inter-dependence of channels in the vector tracking loops, and the resulting degradation of the positioning solution precision, call for the definition of robust and effective GNSS receiver architectures and the specification of efficient and reliable tracking and positioning algorithms in an attempt to solve them or reduce their impact; and that is the aim of this thesis.

1.2.1 SUB-PROBLEM 1

In harsh environments (urban, suburban, heavy foliage), which are multipath- and signal blockage-prone, scalar tracking loops are unable to maintain robust tracking and positioning availability. However, the fact that scalar tracking loops do not get feedback information from the navigator (PVT estimator) can be exploited in situations where there are enough healthy tracking channels to obtain a PVT solution within acceptable precision ranges.

1.2.2 SUB-PROBLEM 2

In a vector tracking scheme, the tracking loops receive feedback information from the navigator. Channels that are affected by temporary signal outage benefit from the aggregate power of all tracking channels. This advantage comes at a cost because every multipath contaminated channel pollutes the calculated PVT solution and consequently propagates its tracking errors to other channels.

1.2.3 SUB-PROBLEM 3

Most vector tracking solutions in literature are based on the EKF algorithm and some on the UKF algorithm. The underlying assumptions in the EKF-based design are that after linearization of the filtering model that is used for the navigation and vector tracking problems, the realizations of state and measurement noises can account for the nonlinearities and non-Gaussianities associated with the dynamic system. But when severe nonlinearities appear in the system, the EKF solution diverges. The application of particle filtering in vector signal tracking has not received much attention in current literature and is worth investigating.

1.3 THESIS OBJECTIVES

This thesis has four main objectives:

- To investigate the GNSS receiver operation in harsh environments and attempt a solution to the problems of LOS signal blockage (also referred to as non-line-of-sight or NLOS) and multipath.
- To embed the proposed solution into the vector tracking scheme in order to improve the vector tracking loop robustness and PVT integrity through exclusion of fault in the navigator.
- To exploit the strengths and compensate for the weaknesses of both scalar and vector tracking schemes in harsh environments by designing adaptive and conjoint scalar-vector tracking schemes.
- To study and contrast different nonlinear Bayesian filtering approaches to the navigation and vector tracking problem, and propose improvement.

1.4 DELINEATIONS

Although the solutions that are proposed in this thesis are applicable or can be easily extended to any GNSS and other GNSS frequencies, the focus point is on GPS L1. L1 refers to the L-band GPS carrier frequency that equals 1575.42 MHz. This scope restriction is essentially not much in the design principle of the proposed solutions but rather in the testing methodology. Therefore, following the same quintessential principle that is used to design the GPS L1 solutions, the latter can be extended to other GNSSs and frequencies mostly with minor adjustments. In fact, most proposed solutions will have greater significance and impact in a multi-constellation receiver.

The hybridization of GNSS with an inertial navigation system (INS) commonly referred to as GNSS/INS coupling is extensively used to improve navigation in GNSS harsh environments. GNSS uses satellites to provide an absolute drift-free positioning solution. INS on the other hand is an autonomous relative positioning system that does not use external references but computes a position difference from a starting position using information about distance and direction. GNSS/INS coupling is known to provide higher navigation solution output rate. It allows the INS to fill in the gaps between GNSS positioning solutions and to cover GNSS signal outage periods and the GNSS to correct, reset and recalibrate the INS solution. This thesis scope does not include GNSS/INS integration. Instead, hybridization of scalar and vector tracking schemes is considered together with other techniques to deal with multipath and signal blockage. Of course, the proposed hybrid tracking schemes can still be coupled with INS. The interested reader is invited to read [14] for details about INS and GNSS/INS coupling.

Several multipath mitigation techniques based on multipath parameter estimation are used in GNSS. This topic has received much attention in literature. This thesis focuses on multipath detection oriented solutions. Furthermore, in current literature several fault detection and exclusion (FDE) approaches are used in the GNSS navigator. These FDE methods perform measurement consistency checks in general and receiver autonomous integrity monitoring (RAIM) in particular. The interested reader can find details on these topics in [15], [16] and [17]. This thesis scope does not include measurement consistency checks in the navigator. Instead, particular interest is dedicated to providing anticipative solutions, i.e. solutions that can exclude fault in the navigator but from a post-correlator level in the GNSS receiver signal processing chain.

1.5 THESIS OUTLINE

The thesis is organized as follows. *Chapter 1* provides introductory notes. The context and motivation for the thesis are given. This chapter also gives a problem statement, sets the thesis objectives, and states the thesis contributions to solving the problem. *Chapter 2* covers some fundamentals of GNSSs and GNSS receivers. An overview of GNSSs is provided. The chapter then describes the operation of a GPS software receiver. The GPS positioning principle, the GPS observables, the GPS signal acquisition and tracking, the GNSS scalar and vector tracking receiver architectures, and some Bayesian filtering approaches to solving the navigation and vector tracking problem are all succinctly presented.

In *Chapter 3*, the GPS receiver operation in multipath environments is investigated. The chapter provides a theoretical study of multipath induced tracking and positioning errors for the scalar and vector tracking loops. Analytical expressions for the tracking and positioning errors are derived. The chapter scrutinizes GPS correlator outputs in the presence and in the absence of multipath and then proposes correlator-based multipath and NLOS detection techniques. It finally discusses other correlator-based signal quality indicators namely a phase lock indicator (PLI) and some low-complexity C/N_0 estimators.

Chapter 4 is dedicated to adaptive and conjoint scalar-vector tracking loops. A vector tracking scheme that utilizes signal quality indicators (C/N_0 estimator, NLOS detector and multipath detector) to exclude unhealthy satellites from PVT computation in the navigator is described. Moreover, the chapter discusses an adaptive scalar-vector tracking scheme that continuously switches between scalar and vector tracking modes and excludes fault in the navigator using correlator-based signal quality indicators. Finally, a conjoint scalar-vector tracking scheme is presented that performs scalar and vector tracking simultaneously, chooses the measurements to be sent to the navigator and excludes fault in the navigator based on signal quality indicators.

In *Chapter 5*, some nonlinear Bayesian filtering approaches that are used to solve the navigation and vector tracking problem are studied and contrasted. The UKF, iterated UKF (IUKF), iterated adaptive UKF (IAUKF), unscented particle filter (UPF), iterated UPF (IUPF), and iterated adaptive UPF (IAUPF) as applied to GPS navigation and vector tracking are studied and compared theoretically and empirically using the posterior Cramér-Rao lower bound and experimental results. Finally, *Chapter 6* presents a summary of the findings and contributions of this thesis. It also provides suggestions for future studies.

1.6 CONTRIBUTIONS

This thesis has eight main contributions:

- The first contribution, given in *Chapter 3*, is the derivation of models that allow the analysis of GPS code and carrier tracking errors with respect to multipath delay, multipath phase and multipath fading frequency.

- In *Chapter 3*, three correlator-based multipath detectors are proposed with different metrics for the scalar and vector tracking loops. One detector has time-domain metrics and the two others have frequency-domain metrics.

- The third contribution, presented in *Chapter 3*, is the design of a correlator-based NLOS detector that has a frequency domain metric.

- In *Chapter 4*, a vector tracking scheme is devised that uses the proposed multipath detectors as well as a C/N_0 estimator to exclude unhealthy satellites from PVT calculation in the navigator.

- The fifth contribution, described in *Chapter 4*, is the design of an adaptive tracking scheme that commutes between scalar and vector tracking modes using the proposed NLOS detector, a C/N_0 estimator and a PLI, and that excludes unhealthy satellites from PVT computation using the C/N_0 estimator and the proposed multipath detectors.

- Contribution is made in *Chapter 4* by designing a conjoint tracking scheme that maintains simultaneous scalar and vector tracking, uses the C/N_0 estimator, the NLOS detector and the PLI to select the measurements to be fed to the navigator, and exploits the C/N_0 estimator and the specified multipath detectors to exclude fault in the navigator.

- An unscented particle filtering approach, the IAUPF, detailed in *Chapter 5*, is devised with a novel sampling and resampling strategy to reduce UPF complexity. The normal UPF uses the UKF to generate and propagate a Gaussian proposal distribution to each particle, which means using as many UKFs as there are particles. The proposed approach utilizes a single IAUKF with a conditional iteration strategy and uses its state and covariance estimates to form a single Gaussian proposal distribution from which particles are sampled. The proposed resampling strategy is a conditional commutation between stratified and regularized resampling.

- The last contribution, provided in *Chapter 5*, is a comparative study of the navigation and vector tracking solutions of the different Bayesian filters.

The following publications have been made via international peer-reviewed conferences:

- Elie Amani, Jean-Rémi De Boer, Willy Vigneau, Karim Djouani and Anish Kurien, "GPS Multipath Induced Errors for the Vector Tracking Loop: Insight into Multipath Detection", Proc. 2016 European Navigation Conference (ENC 2016), Helsinki, May 2016.

- Elie Amani, Karim Djouani, Anish Kurien, Jean-Rémi De Boer, Willy Vigneau and Lionel Ries, "GPS Multipath Detection in the Frequency Domain", Proc. 2016 European Navigation Conference (ENC 2016), Helsinki, May 2016.

- Elie Amani, Karim Djouani, Jean-Rémi De Boer, Anish Kurien, Willy Vigneau, Thomas Junique, Franck Barbiero and Marion Aubault "Adaptive and Conjoint Scalar-Vector Tracking Loops for GNSS Tracking Robustness and Positioning Integrity", Proc. 2017 European Navigation Conference (ENC 2017/IEEE), Lausanne, May 2017.

Furthermore, the following papers have been submitted to international peer-reviewed journals:

- Elie Amani, Karim Djouani, Jean-Rémi De Boer, Anish Kurien and Willy Vigneau, "A Correlator-Based Multipath Detection Technique for a GPS/GNSS Receiver", submitted to IET Radar, Sonar & Navigation.
- Elie Amani, Karim Djouani, Anish Kurien, Jean-Rémi De Boer, Willy Vigneau, "Performance Evaluation of Nonlinear Bayesian Filtering Approaches for GPS Navigation and Vector Tracking" submitted to IEEE Transactions on Aerospace and Electronic Systems.

Chapter 2

Fundamentals of GNSS and GNSS Receivers

Scientists […] use knowledge primarily to generate more knowledge.

— David P. Billington

2.1 INTRODUCTION

It has been more than thirty-five years since the first satellite of the first Global Navigation Satellite System (GNSS), —the Global Positioning System (GPS)—, was placed in orbit. Since then, tremendous developments have been made in the GNSS and the GNSS receiver design and operation. While a couple of about 50-cm racks of electronic equipment were required then, a small module embedded in a cell phone is enough today to carry out the GNSS receiver processing. With the advent of GNSS software receivers, the signal acquisition and processing tasks of the receiver are almost entirely carried out by reprogrammable software rather than hardware. This chapter intends to provide a synopsis of the GNSSs and the GPS software receiver operation. Details about the GPS receiver operation can be found in [18], [19] and [20]. In this chapter, the architecture of a GPS software receiver is described contrasting scalar and vector tracking schemes. Although information flow in the GPS receiver processing chain goes from the radio frequency (RF) front-end processing to Position-Velocity-Time (PVT) computation through the blocks that allow signal acquisition and tracking, the chapter presents the information in a different order, starting with the positioning principle, describing signal acquisition and tracking and ending with the RF front-end. It is deemed that this presentation order facilitates reading comprehension. The chapter also offers a summary of linear and nonlinear Bayesian filtering algorithms that are used to solve the navigation and vector tracking problem.

2.2 GNSS OVERVIEW

2.2.1 GNSS HISTORY

The launch of the first man-made satellite, *Sputnik 1*, by the Soviet Union in 1957 marked a turning point in navigation. Some American scientists noticed that they could track *Sputnik 1* by monitoring the Doppler shift in radio signals broadcast from the satellite. Very soon after, people noticed that the reversed concept could help them pinpoint their own location. The first space-based navigation systems came from this idea. Some predecessors of the GPS are the U.S. Navy *Transit* and the Russian *Tsikada*. *Transit* became functional to U.S. submarines in 1964 and went commercial in 1967. Both *Transit* and *Tsikada* were not very performant for high dynamic, high velocity vehicles such as aircrafts. The U.S. Navy *Timation* system introduced atomic precision clocks on satellites. Further developments to navigation systems in the 1970s led to the first global navigation system, the American *Navstar GPS* (first launch in 1978, fully operational in 1995) and the Russian *GLONASS* (first launch in 1982, fully operational in 1996, then 2011). The last two decades have seen rapid development of many GNSSs namely the European Union *Galileo* (first test launch in 2005, full operational capability expected in 2019) and the Chinese *Compass* or *Beidou-2* (first launch in 2000, full operational capability expected in 2020).

2.2.2 GPS

The American GPS consists of 3 segments and 5 L-band signals. Only 3 signals are described hereafter.

- **GPS Segments**

Space Segment: this segment is made of 31 operational satellites orbiting in medium earth orbit (MEO) at an altitude of 20200 km above the earth. Additional 3 to 4 inactive satellites can be reactivated when it is necessary [21]. The satellites evolve in 6 equally-spaced orbital planes with 4 satellites each. The orbital planes have an inclination of approximately 55° and are separated by 60°. The orbits are arranged to ensure that at least 6 satellites are in direct line-of-sight from any geographical location on earth. Each satellite broadcasts a navigation message through radio signals that travel at the speed of light.

Control Segment: The segment is made of 5 monitoring stations that are responsible for tracking, monitoring, and maintenance of satellites. These stations are distributed around the world (Colorado Springs, Hawaii, Kwajalein, Ascension Island, and Diego Garcia). The Colorado Springs station is the master station. It gathers data from each of the stations and determines the data to be uploaded (ephemerides,

clock parameters) and the ground stations responsible for transmitting the data to the satellites.

User Segment: it consists of the different radio receivers that use GPS signals to determine their position in real-time. The secure GPS Precise Positioning Service (PPS) is accessible to hundreds of thousands of U.S. and allied military users. The Standard Positioning Service (SPS) is accessible to the general public made of hundreds of millions of civil, commercial and scientific users. About 300 million receivers are in cell phones [22].

- **GPS Signals**

All GPS satellites transmit signals to the user segment at frequencies *L1*=1575.42 MHz, and *L2*=1227.60 MHz. *L1* is accessible to civilians and U.S. military while *L2* is accessible to only U.S. government and military. The satellites use a Code Division Multiple Access (CDMA) spread-spectrum technique whereby carrier signals are modulated by pseudorandom noise (PRN) codes that ensure the immunity of the carried low-rate navigation message (50 bits/s) to external disturbances such as ionospheric effects and weather conditions. The coarse acquisition (C/A) code (1.023 Mchips/s) is modulated on the *L1* carrier while the precise (P) code (10.23 Mchips/s) is modulated on both the *L1* and *L2* carriers. The *L5* signal (1176.45 MHz) with chipping rate 10.23 Mchips/s is part of the modernized GPS and is dedicated to safety of life transportation and other high-performance applications. All these carrier frequencies are generated as multiples of the fundamental satellites clocks frequency, f_0=10.23 MHz.

2.2.3 GLONASS

The Russian GLONASS has 3 segments as well and 3 types of signals.

- **GLONASS Segments**

Space Segment: made of 24 satellites in 3 orbital planes with an inclination of 65°. The orbital planes are separated by 120°. Among these satellites, 21 are active while the others are used as spares. The constellation guarantees that at least 5 satellites are available at any location on earth.

Control Segment: made of the master control centre located in Krasnoznamensk and many tracking, monitoring and measuring stations. Many stations are distributed across the former Soviet Union territory, and a few in Brazil.

User segment: made of the receivers that use GLONASS signals. It provides two types of services, one accessible to the public and the other to reserved users.

- **GLONASS Signals**

GLONASS satellites transmit 2 types of signals to the user segment: a standard-precision signal *L1OF/L2OF* for civil use and a high-precision signal *L1SF/L2SF* for military use. They use a Frequency Division Multiple Access (FDMA) spread-spectrum technique where all satellites use the same spreading code but transmit on different frequencies. The FDMA technique uses frequency channels that span either side from 1602.0 MHz for *L1* and from 1246.0 MHz for *L2*. The signals are modulated by two codes: the C/A code on *L1* only and the P code on both *L1* and *L2*. Each satellite broadcasts a navigation message at 50 bits/s which is immune to external disturbances due to the used spreading code. The *L3* carrier frequency (1204.704 MHz) is used by the new generation *GLONASS-K* satellites and is suitable for safety of life applications.

2.2.4 GALILEO

Galileo is the European Union GNSS. It is still under construction and is expected to reach full operational capacity by 2019.

- **Galileo Segments**

Space Segment: *Galileo* will have a constellation of 30 satellites (27 operational and 3 spare). The satellites are orbiting in MEOs at an altitude of 23222 km, in 3 orbital planes with 56° inclination and separated by 120°. Such an arrangement ensures that at least 6 satellites are in view at any location on the globe.

Ground Segment: made of 2 ground control and mission centres acting as central processing facilities, one located in Oberpfaffenhofen (Germany) and the other in Fucino (Italy). The control centres communicate with 5 tracking and control stations, several uplink stations and several sensor stations.

User Segment: made of all receivers that use *Galileo* signals. *Galileo* will provide five types of services: an open access navigation service, an encrypted commercial navigation service, a safety of life navigation service, an encrypted public regulated navigation service, and a search and rescue service.

- **Galileo Signals**

The *Galileo* signals are transmitted in the frequency ranges 1164 to 1215 MHz (*E5a* and *E5b*), 1215 to 1300 MHz (*E6*) and 1559 to 1592 MHz (*E2-E1*). The frequency range 1544.05 to 1545.15 MHz is defined as search and rescue (SAR) uplink and the range 406.0 to 406.1 MHz as SAR downlink. The spread-spectrum technique is CDMA.

2.2.5 OTHER GNSSS

The Chinese *Compass* or *Beidou-2* navigation system is still under development and is expected to be fully operational by 2020. It will include 35 satellites. Five of them will be geostationary orbit (GEO) satellites, 3 in highly inclined geosynchronous orbits (IGSO) and 27 in MEOs. Compass frequencies are located in 3 bands namely 1575.42 MHz (B1), 1191.795 MHz (B2) and 1268.52 MHz (B3) [23]. The Japanese Quasi Zenith Satellite System (QZSS) and the Indian Regional Navigation Satellite System (IRNSS) are regional navigation systems, the former covering regions in East Asia and Oceania centring on Japan, and the latter covering India and the area extending 1500 km around India.

2.3 GPS SOFTWARE RECEIVER OPERATION

2.3.1 GPS POSITIONING PRINCIPLE

GPS positioning is based on multilateration. Multilateration is the process of calculating the position of a point in space based on its distance from a number of known positions. Multilateration can be performed in two-dimensional (2-D) space or in three-dimensional space (3-D).

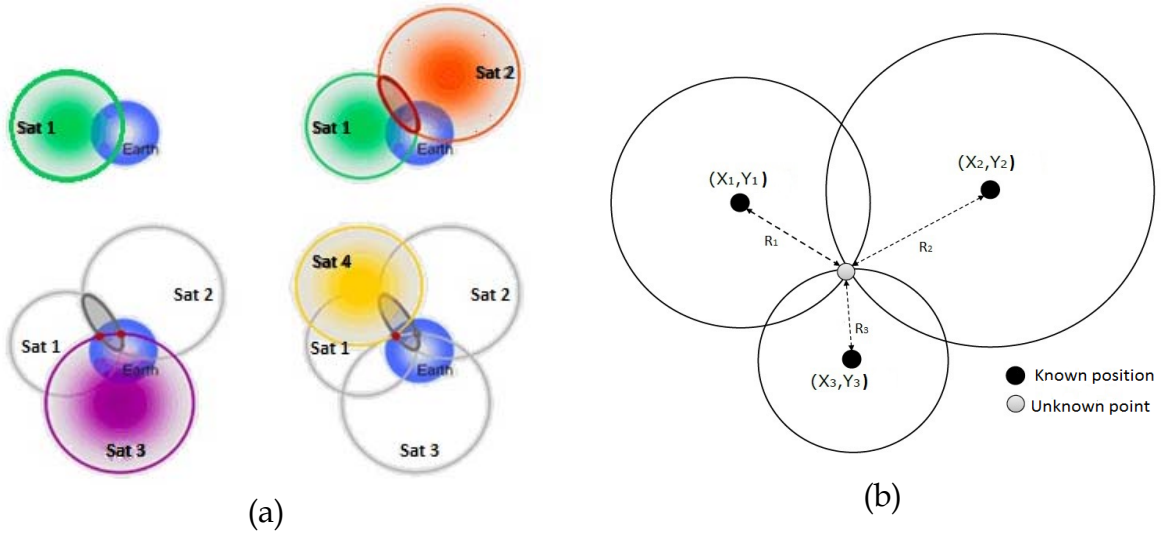

Figure 2.1: (a) Multilateration in 3-D. (b) Multilateration in 2-D

Ideally, if it is assumed that the errors due to the satellite clock bias, the GPS receiver clock bias, atmospheric effects, multipath and other interferences have been corrected, three GPS satellites are required to obtain precise positioning using 3-D multilateration. Figure 2.1 illustrates the GPS positioning principle. If the distance R_1 from the unknown position to a satellite *Sat 1* is available, it is possible to construct a sphere centred about the satellite and having R_1 as radius. The ambiguity to be solved in this case is an infinite number of points constrained to the surface of the sphere. If a second satellite *Sat 2* is added, it is possible to construct two spheres, centred about *Sat 1* and *Sat 2* with respective radii R_1 and R_2, whose intersection is a

circle. The unknown position is still an infinite number of points but ambiguously constrained to the circumference of the circle. A third satellite *Sat 3* allows the construction of a third sphere that intersects the previous circle in two points, thus reducing the ambiguity to two points. If a fourth satellite *Sat 4* is added, the unknown position is unambiguously determined as a single point in space. In the ideal case, the last ambiguity can be solved even without a fourth satellite. Indeed, one of the two intersection points is closer to the surface of the earth than the other is. Thus, by assuming that the GPS receiver is near the surface of the earth, one point is chosen as the position and the other normally far away from the surface of the earth (about 40 000 km away) is rejected.

In practice however, the measured distance between the receiver and the satellite, called pseudorange, deviates from the true range by some error due to ionospheric refraction, tropospheric effects, satellite clock bias with respect to GPS reference time, receiver clock bias with respect to GPS reference time, multipath propagation, receiver measurement noise and more. The measured pseudorange between the receiver and the i^{th} satellite can therefore be written as

$$\rho_i = R_i + \Delta D_i - c(\Delta b_i - \Delta b_r) + c(\Delta T_i + \Delta I_i + v_i + \Delta v_i) + w_i \tag{2.1}$$

where $R_i = \sqrt{(X_i - X)^2 + (Y_i - Y)^2 + (Z_i - Z)^2}$ is the true range, ΔD_i is the satellite position error effect on range, $s_i = (X_i, Y_i, Z_i)$ is the i^{th} satellite Earth-Centred Earth-Fixed (ECEF) position, $r = (X, Y, Z)$ is the receiver ECEF position, c is the speed of light, Δb_i is the satellite clock error, Δb_r is the receiver clock error, ΔT_i is the tropospheric delay error, ΔI_i is the ionospheric delay error, v_i is the receiver measurement noise error, Δv_i is the relativistic time correction, and w_i represents all other sources of error.

Each satellite position is calculated using the orbit parameters included in the navigation message (ephemeris data) sent by the satellite. The receiver uses more parameters in the ephemeris data to account for the satellite clock error. Some models exist to perform tropospheric and ionospheric corrections. Therefore, in practice, the general statement is that at least four satellites are required to calculate the GPS receiver position. In the range measurement settings above, the three spheres that are formed around three satellites would not result in one or two positions to choose from but rather in an ambiguous set of possible positions. The fourth satellite is necessary to correct the receiver clock error. The recursive algorithm that is used to determine the receiver position therefore has to solve a set of four simultaneous equations in four unknowns: the three position coordinates and the receiver clock bias. If the initial position guess is chosen near the surface of the earth, the algorithm converges to the true position.

2.3.2 GPS OBSERVABLES

The basic GPS observables are the pseudorange, the carrier phase and the Doppler frequency measurements.

- **Pseudorange**

The pseudorange was introduced in Section 2.3.1 to explain the GPS positioning principle. This observable is a measure of the distance between the satellite and the receiver's antenna. It is formed by measuring the GPS signal travel time from the satellite to the receiver's antenna. Since the highly accurate and stable atomic clocks of satellites are synchronized, the receiver can tell when a signal is received. The time of transmission is encoded into the satellite signals. The receiver reads this time to have a very accurate record of when the same portion of the different signals was received. The travel time is then calculated. The pseudorange is computed by multiplying the travel time by the speed of light, which is the electromagnetic waves propagation speed.

$$\rho_i = c(t_t - t_{ri}) \tag{2.2}$$

where t_t is the transmission time and t_{ri} is the reception time for satellite i. This reception time is however based on the receiver clock which is of low quality and is offset from the GPS time. This receiver clock bias shows while forming the pseudoranges from tracking results. When all tracking channels have received a synchronized part of the satellite signals, the time delay between different reception times can be computed.

$$\Delta_{ij} = t_{rj} - t_{ri} \tag{2.3}$$

where i and j are different satellites. Pseudoranges are formed by assigning some nominal travel time to the shortest pseudorange, say of satellite 1, usually around 68 ms. The other pseudoranges are then derived by adding the different Δ_{1j} to the nominal pseudorange.

- **Carrier Phase**

The carrier phase can also be used as measurement for positioning purposes. This observable is derived from the phase tracking loop. Although carrier phase is also a measurement of range, it is different from the code phase (pseudorange). Two major differences exist between the two:

- *Precision*: Both the pseudorange and carrier phase are accurate to around 1-2% of the wavelength of the signal. The wavelength of a single code chip is

$$\lambda_{code} = \frac{c}{1.023 \times 10^6} \approx 293\ m \tag{2.4}$$

Similarly, the wavelength of the carrier signal is

$$\lambda_{carrier} = \frac{c}{1575.42 \times 10^6} \approx 19\,cm \tag{2.5}$$

Therefore, the pseudorange is accurate to around 3 to 6 m while the carrier phase is accurate to around 2 to 4 mm.

- *Ambiguity*: The carrier phase is an ambiguous measure while the pseudorange is not. The carrier wave is a simple sinusoid. Each wave peak cannot be distinguished from any other wave peak. Although the carrier phase measurement is very precise, the number of wavelengths between the satellite and the receiver is unknown. This unknown number of wavelengths is called integer ambiguity. An application that uses the carrier phase as range measurement must solve for this ambiguity. The pseudorange, conversely, is not ambiguous. Each code period and code chip can be uniquely determined by its alignment with the data message.

- **Doppler frequency**

The carrier frequency is related to both the velocity of the receiver and the velocity of the transmitting satellite. A Doppler frequency shift from the centre frequency of the signal occurs due to the relative motion between the transmitter and the receiver. This relative motion alters the apparent wavelength received at the antenna. The propagation velocity of a signal that is transmitted can be considered as the speed of light, *c*. A shortening of the distance between the transmitter and the receiver at the rate of *v* implies a shortening of the wavelength. The Doppler relation is given by

$$f_R = f_T\left(1 - \frac{v}{c}\right) \tag{2.6}$$

where f_R is the received (perceived) frequency and f_T is the transmitted frequency. The code is also affected by the Doppler shift but the effect is smaller because code frequency is much lower. The code and the carrier Doppler frequency shifts are related by

$$f_{D,code} = f_{D,carrier} \times \frac{1.023 \times 10^6}{1575.42 \times 10^6} = f_{D,carrier} \times \frac{1}{1540} \tag{2.7}$$

2.3.3 GPS SIGNAL ACQUISITION AND TRACKING

- **GPS Signal Structure**

The net signal transmitted from a GPS satellite, ignoring the modern *L5* carrier, can be modelled as

$$s(t) = \sqrt{2P_C}\,C(t)D(t)\cos(2\pi f_{L1}t) + \sqrt{2P_{PL1}}\,P(t)D(t)\sin(2\pi f_{L1}t) + \sqrt{2P_{PL2}}\,P(t)D(t)\sin(2\pi f_{L2}t) \quad (2.8)$$

where $D(t)$ is the navigation data sequence, f_{L1} and f_{L2} are the *L1* and *L2* carrier frequencies for the signal transmitted from the satellite with powers P_C, P_{PL1} and P_{PL2} for PRN *C/A* code or PRN *P* code, $C(t)$ is the *C/A* code sequence and $P(t)$ is the *P* code sequence.

- **GPS Signal Demodulation**

One of the main purposes of GPS signal acquisition and tracking is to achieve demodulation of the navigation data sequence, meaning the removal of the carrier and the PRN code to extract the navigation data. After band-pass filtering is performed to isolate the *L1* signal and after down-conversion brings the *L1* signal to an intermediate frequency (IF), the analogue signal from one satellite in the GPS receiver front-end before digital conversion can be expressed as

$$\begin{aligned} r(t) = {} & \sqrt{2P_C}\,C(t-\tau)D(t-\tau)\cos\left[2\pi(f_{IF} + f_D)t + \phi\right] \\ & + \sqrt{2P_{PL1}}\,P(t-\tau)D(t-\tau)\sin\left[2\pi(f_{IF} + f_D)t + \phi\right] + \eta(t) \end{aligned} \quad (2.9)$$

where τ is the code propagation delay, f_{IF} is the intermediate frequency, f_D is the Doppler frequency shift, ϕ is the carrier phase shift without the Doppler term, and η is the measurement or thermal noise. For clarity of demodulation process explanation, the Doppler frequency shift, the phase differences, the code propagation delay, and the receiver measurement noise are not explicitly shown in the model hereafter. The received *L1* analogue IF signal from one satellite in Equation (2.9) can be rewritten as

$$r(t) = \sqrt{2P_C}\,C(t)D(t)\cos(\omega_{IF}t) + \sqrt{2P_{PL1}}\,P(t)D(t)\sin(\omega_{IF}t) \quad (2.10)$$

where ω_{IF} is the intermediate radial frequency to which the front-end has down-converted the *L1* carrier frequency. Since only the C/A code signal must be demodulated, the signal in Equation (2.10) is sampled at frequency *fs* by an analogue-to-digital converter (ADC) and a narrow band-pass filter distorts the P code signal and converts it into some negligible noise $\eta(n)$. The signal in Equation (2.10) after ADC conversion therefore becomes

$$r(n) = C(n)D(n)\cos(\omega_{IF}n) + \eta(n) \quad (2.11)$$

where n is in units of $1/fs$ seconds and indicates that the signal is now in discrete-time. Carrier removal is performed by multiplying the above signal with a replica of the carrier. When an exact replica of the carrier in both frequency and phase is obtained, the following result is achieved:

$$\begin{aligned} r(n)\cos(\omega_{IF} n) &= C(n)D(n)\cos(\omega_{IF} n)\cos(\omega_{IF} n) \\ &= \frac{1}{2}C(n)D(n) + \frac{1}{2}\cos(2\omega_{IF} n)C(n)D(n) \end{aligned} \tag{2.12}$$

A low-pass filter with a gain of 2 is used to remove the second term and the signal becomes

$$C(n)D(n) \tag{2.13}$$

The last step is code removal which is performed by correlating the signal with the exact local code replica to obtain

$$\sum_{n=0}^{N-1} C(n)C(n)D(n) = ND(n) \tag{2.14}$$

where $D(n)$ is the navigation message and N is an amplification factor due to the correlation and integration process. Code removal can also be performed before carrier removal. The order in which code and carrier removal are performed does not matter. The block diagram in Figure 2.2 summarizes the demodulation process. In the diagram, the incoming signal is the digitized IF signal. When the local carrier replica coincides with the incoming IF carrier in frequency and phase, $\phi = 0 \quad \therefore \cos(\phi) = 1$ and the navigation message $D(n)$ is obtained in the in-phase arm (I) of the diagram. This block diagram is the Costas carrier tracking loop. The combined code and carrier tracking process is described in the next section.

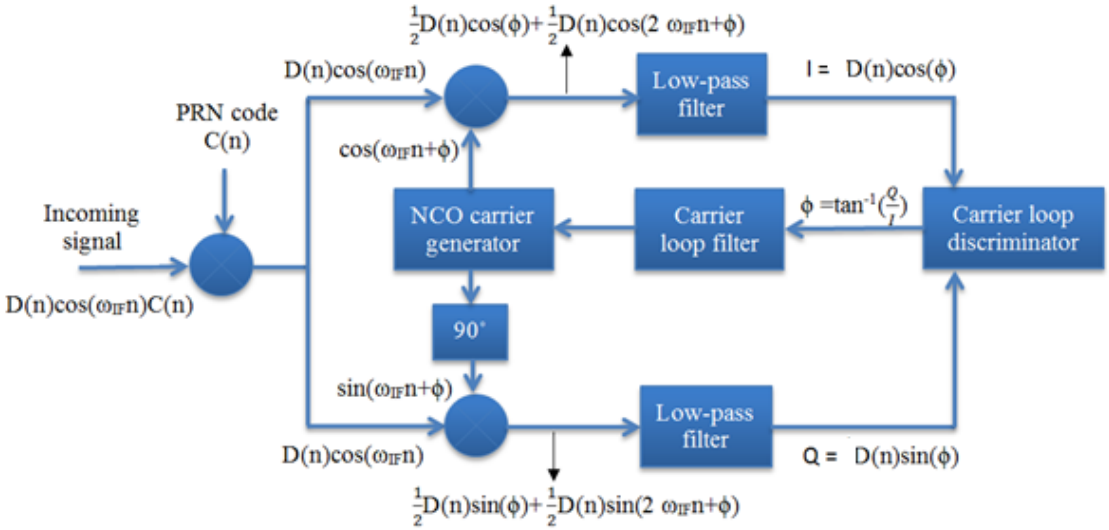

Figure 2.2: Demodulation process: the Costas carrier tracking loop

- **GPS Signal Tracking**

When the GPS receiver is moving with a considerable speed and is frequently changing direction, it experiences a Doppler shift which alters the experienced carrier frequency of the satellite. Similarly, as the satellite moves across the sky, it induces a Doppler shift of its own. The maximum deviation seen from this phenomenon on a receiver is ± 10 kHz. If these frequency deviations are not corrected, the receiver may eventually lose track of the satellite signal and no navigation data will be decoded. Also, the delay due to transmission time must be tracked for each satellite code in the received signal in order to generate a perfectly aligned replica of the code in the receiver. Once the incoming and local code sequences are aligned in time, the receiver must cause its own code chip rate to match the incoming code chip rate as precisely as possible.

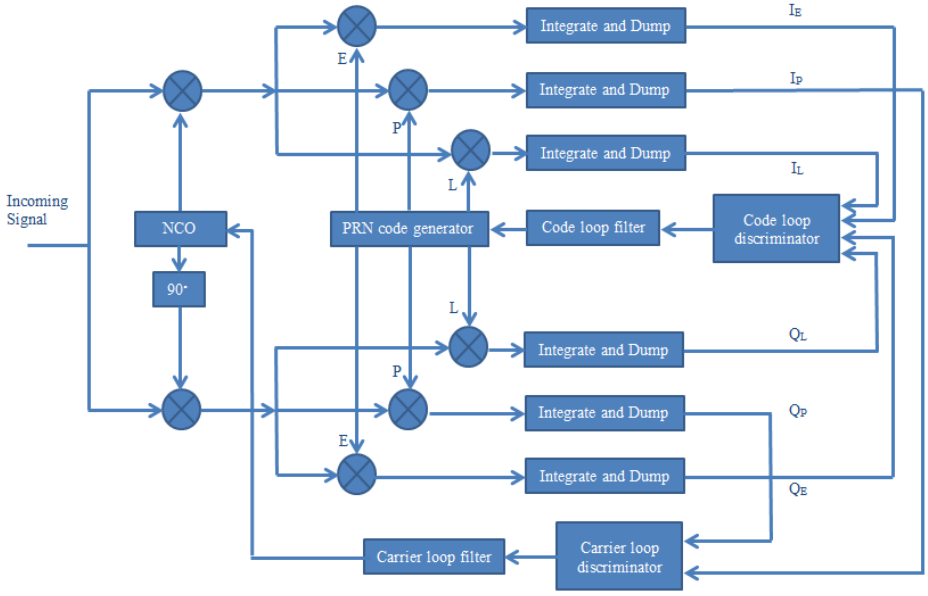

Figure 2.3: GPS receiver scalar tracking loop channel

A scalar tracking loop (STL) such as the one depicted in Figure 2.3 is implemented to track the coarse acquisition (C/A) code and the carrier. The incoming signal in Figure 2.3 is the digitized signal after ADC conversion and after a narrow band-pass filter has removed the P code. A Delay Locked Loop (DLL) is typically used for tracking the C/A code while a Costas Phase Locked Loop (PLL) is commonly used to track the carrier phase. A frequency locked loop (FLL) or Frequency-assisted Phase Locked Loop (FPLL) can be used as well to track the carrier frequency and phase.

In order to track the carrier, a Costas loop requires the generation of an in-phase (I) and quadrature (Q) local replica of the carrier signal, the quadrature signal being a 90° phase-shifted version of the in-phase signal. These two 90° phase-shifted local replicas of the carrier make it possible to evaluate the phase-shift and frequency error between the incoming signal carrier and the in-phase replica using a phase

discriminator and a frequency discriminator respectively. The carrier loop filter transforms the phase and frequency errors into a command for the numerically controlled oscillator (NCO) that is used to generate the local carrier replicas.

In order to properly track the code, the DLL generates a local early (E), prompt (P), and late (L) C/A code signal. When the DLL is initialized, the prompt code replica has the phase shift obtained from the signal acquisition process. The prompt replica is the one that should be kept aligned with the incoming signal code during tracking. The early and late code replicas facilitate the evaluation of code chip error between the incoming signal code and the prompt code replica using a code discriminator. The early and late code replicas have additional phase shifts of $-\partial/2$ and $+\partial/2$ chip respectively from the prompt, ∂ being the correlator chip spacing. The code loop filter transforms the code chip error into a command for the NCO and PRN code generator that are used to generate the local code replicas.

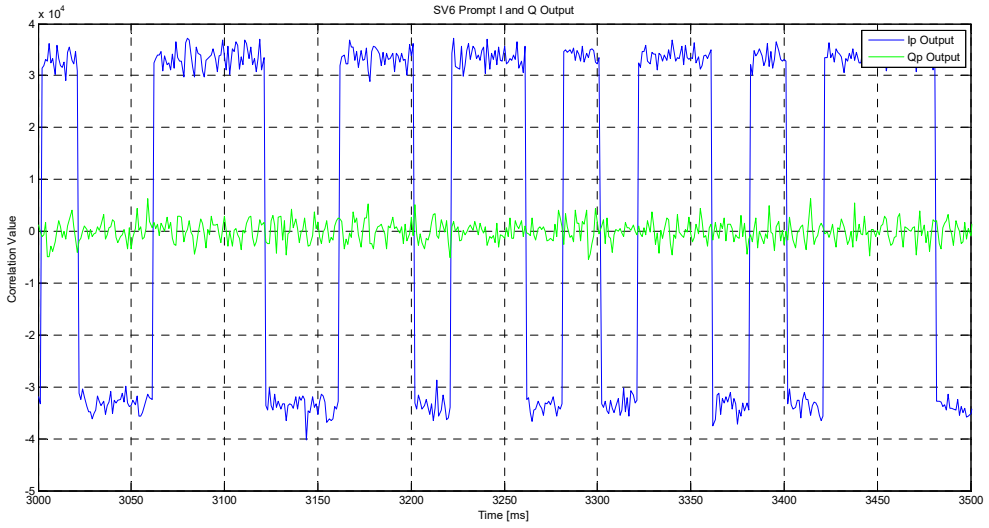

Figure 2.4: GPS SV6 Prompt I and Q outputs: Extract of Navigation Data Sequence

An extract of the navigation data sequence transmitted by a GPS satellite referred to as satellite vehicle (SV) 6 is shown in Figure 2.4. The data is obtained from an incoming signal with IF = 1.25 MHz and *fs* = 5 MHz processed with the DLL and PLL scheme in Figure 2.3 in a channel dedicated to SV6. This data is present on the in-phase prompt arm (Ip) when the code and carrier tracking are successful, meaning when the local code and carrier replicas are well aligned and synchronized with the incoming signal code and carrier. The quadrature prompt arm (Qp) in that case is made of noise whose mean is close to zero.

Some details on the GPS correlation and signal tracking processes are given in Appendix 2.A.

- **GPS Signal Acquisition**

In order to initialize the tracking process, initial local replica guesses for the code and carrier must be generated. The tracking loops process the replicas and generate errors using the discriminators to close the loop. If the replicas are not close in value to the incoming signal, they may not fall in the operating range of discriminators, making the incoming signal impossible to track. The purpose of the signal acquisition process is to obtain initial guesses of the carrier Doppler frequency shift and of the code phase roughly close enough to the incoming signal to make it trackable.

Acquisition must identify all the satellites that are visible to the GPS receiver. It is performed on the digitized IF signal. This signal is a combination of signals from all the available satellites. Let r denote the digitized IF signal and i denote the number of visible satellites.

$$r(n) = r_1(n) + r_2(n) + ... + r_i(n) \tag{2.15}$$

If prior knowledge of possible visible satellites is not available, the acquisition search goes over all satellites known to be in space, meaning that all 31 to 35 possible PRN numbers must be searched for during acquisition. The acquisition process correlates the incoming signal r with the locally generated C/A codes corresponding to the 31 PRN numbers one by one. The nearly zero cross-correlation property between C/A codes from different satellites implies that signals from other satellites are almost removed during the process except the signal of the satellite of interest.

Correlation with the locally generated C/A code is followed by the mixture of the incoming signal with a locally generated carrier wave. The aim is to remove the carrier wave from the received signal. This removal succeeds only if the locally generated signal frequency is close enough to the IF carrier frequency. So, different frequencies within the vicinity of the IF carrier frequency ± the maximum Doppler shift must be tested.

Several acquisition methods exist. There is a trade-off between their speed and their sensitivity. If the signal is strong, the fast and low-sensitivity acquisition method will find it. If the signal is weak, the low sensitivity method will miss it, but the slow and high sensitivity method will find it. Two commonly used acquisition search methods are the serial code phase acquisition and the parallel code phase acquisition. The parallel method which is faster than the serial method is based on Fast Fourier Transform (FFT) search and is illustrated in Figure 2.5.

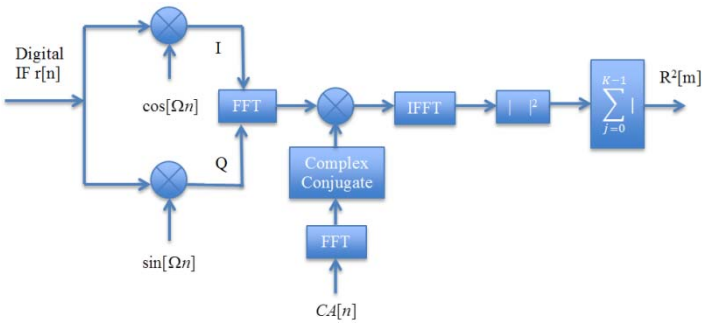

Figure 2.5: FFT-based parallel code phase search acquisition

The FFT algorithm searches for the PRN of interest *CA[n]* over all code phases in the incoming signal *r[n]* with a single pass. Instead of calculating the correlation at each possible code phase of each possible frequency in the search space like the serial method does, this method performs a single shot computation of the correlations in each frequency slice. The correlation operation in the time domain is actually circular convolution which is a multiplication in the frequency domain, such that

$$R[m] = \sum_{n=0}^{L-1} r[n] \cdot CA[(n+m)_L] \qquad (2.16)$$

$$\therefore R[m] = r[n] \otimes CA[-n] = IFFT\left(FFT\left(r[n]\right) \cdot FFT\left(CA[n]\right)^*\right)$$

where *IFFT* and * denote the inverse FFT and conjugate operations respectively. The acquisition process result for an incoming signal with IF = 9.548 MHz and *fs* = 38.192 MHz is illustrated in Figure 2.6. When the PRN code of an available satellite is correlated with the incoming signal, a correlation matrix such as the one in Figure 2.6 is obtained. It exhibits a correlation peak that exceeds the noise power threshold. This peak occurs at the Doppler frequency and code phase of interest. When the PRN that is searched for is not available, only correlation noise is visible in the search matrix.

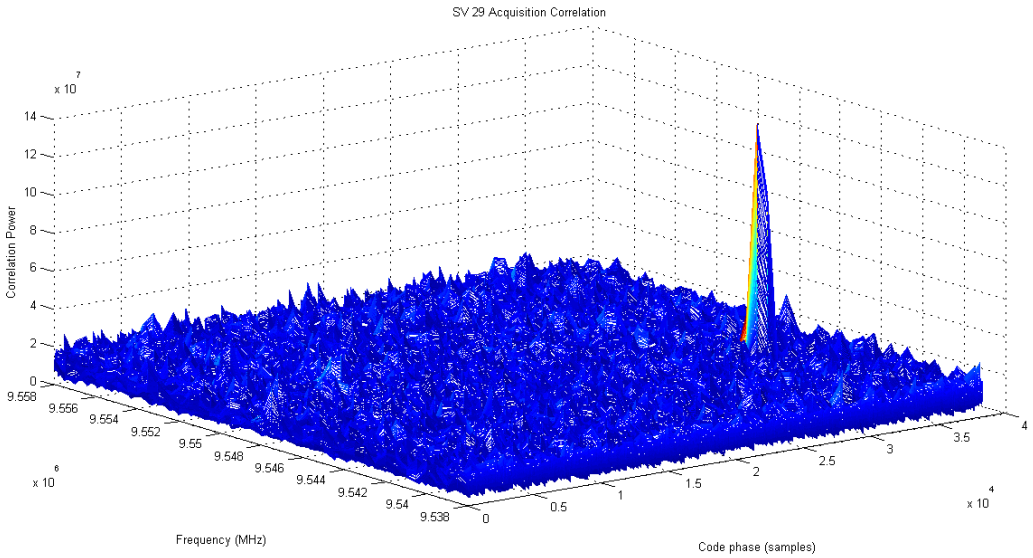

Figure 2.6: GPS SV29 acquisition correlation matrix

2.3.4 GPS RECEIVER FRONT-END

The GPS receiver has a hardware radio-frequency (RF) front-end whose function is to perform down-conversion of the *L*-band carrier frequency signal to an IF signal and digitization thereafter. Down-conversion removes the need to sample at a very high frequency during digitization knowing that the received signal is around 1.5 GHz. The different processing blocks used by the front-end to achieve this are depicted in Figure 2.7.

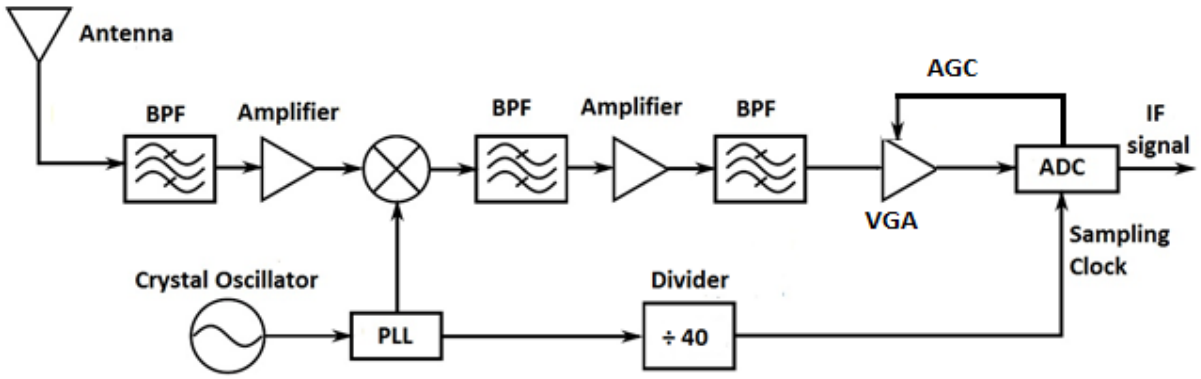

Figure 2.7: GPS receiver front-end

The processing chain starts with an antenna that can be active or passive. Passive antennas are generally appropriate when there is a short distance between the antenna and the signal conditioning circuitry such as in hand held devices. GPS signals are transmitted with right-hand circular polarization (RHCP). In the specular multipath reflection, the GPS signal can be reflected as a left-hand circular polarization (LHCP) signal depending on the angle of incidence, which itself is dependent on the properties of the reflective surface [14]. The conventional receiver antenna is therefore designed to be sensitive to RHCP signals although it does not completely remove LHCP signals, and to have a spatial reception pattern that is near hemispherical to accommodate reception of satellite signals with any azimuth and elevation. Several band-pass filters (BPF) are used at different processing stages to isolate and condition the signal that is wanted for the next stages and to reduce interference. Amplifiers are used to maintain an adequate signal power. A crystal oscillator is used to control the frequency mixing and sampling processes using a phase locked loop (PLL) and a divider. An analogue-to-digital converter (ADC) performs digitization and closes the front-end chain. The ADC's signal sampling and quantization operations induce some losses. These losses are dependent on the ratio between the ADC's quantization threshold, the number of bits that is used, and the incoming signal standard deviation. The automatic gain control (AGC) acts as a variable gain amplifier (VGA). It adjusts the incoming signal's power and optimizes the ratio between the quantization threshold and the signal standard deviation,

keeping quantization losses at minimum. The AGC can adjust to different active antenna gain values.

2.4 GNSS RECEIVER ARCHITECTURE

2.4.1 SCALAR TRACKING RECEIVER

The architecture of the scalar tracking receiver is depicted in Figure 2.8. This is one of several architectural possibilities, its particularity being the use of a local estimator in replacement of code and carrier loop filters. The scalar tracking receiver has independent tracking channels. Each channel tracks one satellite signal independently using a scalar tracking loop (STL). No information is shared among tracking channels and they do not receive any feedback information from the navigator. The operation of the receiver presented in the previous sections can be summarized in the order of information flow as follows. Signals incident on the receiver antenna go through a front-end for filtering, down-conversion and digitization. The digital IF signal is passed to a set of tracking channels initialized via a signal acquisition step. Each tracking channel extracts information from a single satellite signal. This information extraction is called demodulation and is made possible via mixing of the digital IF signal with locally generated code and carrier replica signals in each tracking channel. An integrate-and-dump operation that plays a low-pass filtering role sums up individual samples during an integration period. A set of code and carrier discriminators use the integrated-and-dumped correlator outputs to produce tracking error measurements. A local estimator uses the discriminator outputs to produce refined code and carrier estimates that are then used to adjust the generation of the local code and carrier replicas. In other architectures, the local estimator is replaced by code and carrier loop filters. The local estimator outputs now in a form of range and range rate measurements are also used in the navigator to calculate the PVT navigation solution.

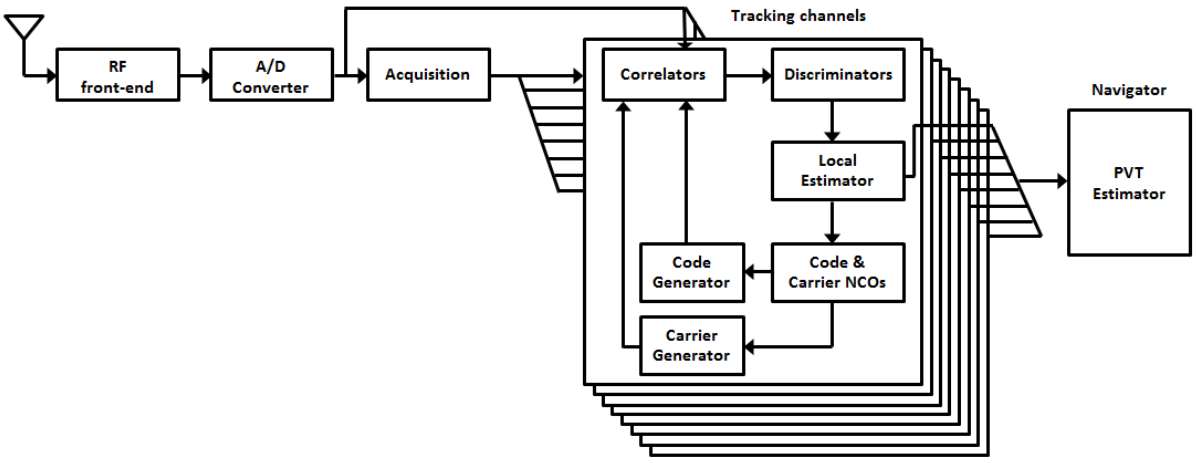

Figure 2.8: GNSS scalar tracking receiver

2.4.2 VECTOR TRACKING RECEIVER

The major difference between a scalar and vector tracking receiver is that there is feedback information from the navigator to the tracking channels in the vector tracking receiver. This makes the tracking channels dependent on one another.

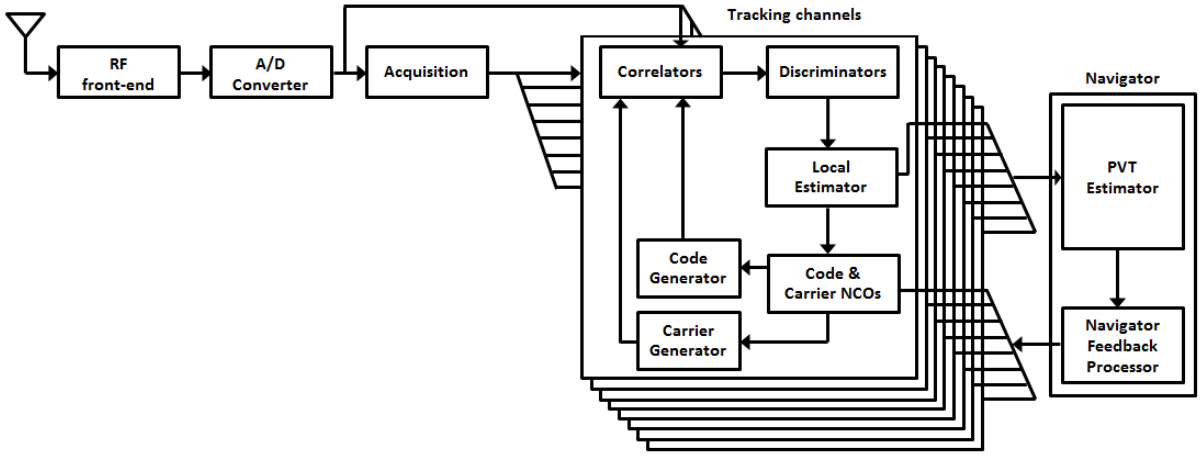

Figure 2.9: GNSS vector tracking receiver

The diagram in Figure 2.9 illustrates the vector tracking receiver architecture corresponding to the scalar tracking architecture of Figure 2.8. Each component retains the role it had in the scalar tracking receiver. But the navigator now has a feedback processor in addition to the PVT estimator. The channels and navigator form the vector tracking loop (VTL). In the VTL, the receiver position, velocity and clock terms are the tracked parameters and they form the states of the Bayesian filtering algorithm that is used for estimation in the navigator. The tracking parameters of all tracking channels with respect to code delay, carrier phase and carrier frequency are generated using these states by translating positions and velocities into line of sight ranges and range rates. Vector tracking therefore has the characteristic of sharing the accuracy and power among the signals which makes it possible to track weakly received satellite signals.

The architecture with a local estimator in each tracking channel is referred to as decentralized architecture. In fact, depending on the type of measurements that are used in the navigator (correlator outputs or discriminator outputs) and on whether each tracking channel has a local estimator or not, GNSS vector tracking receiver architectures can be classified in four main categories: centralized architecture with correlator measurements, centralized architecture with discriminator measurements, decentralized architecture with correlator measurements, and decentralized architecture with discriminator measurements. Table 2.1 contains block diagrams that illustrate the four architecture categories. More details about some of these architectures can be found in [24]. Each type of architecture has its advantages and disadvantages. These are summarized in Table 2.2. The vector tracking architecture

that is chosen for implementation in this thesis is described briefly in *Chapter 3*, then with details in *Chapters 4 and 5*.

Table 2.1: GNSS VTL receiver architectures

	GNSS Measurements	
Architecture	Correlator Outputs	Discriminator Outputs
Centralized	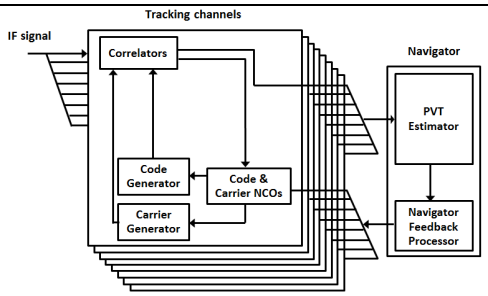	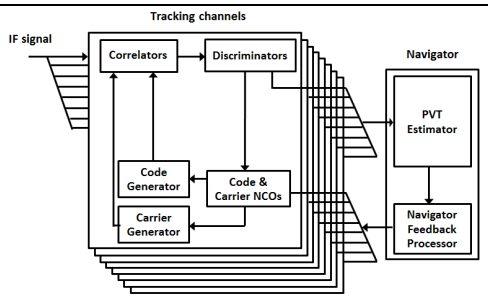
Decentralized	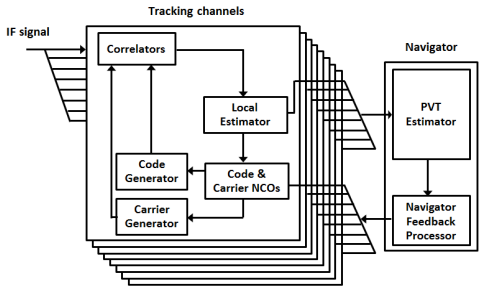	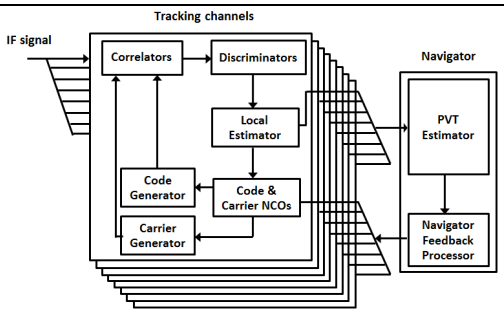

Table 2.2: GNSS VTL receiver architectures: advantages and disadvantages

	GNSS Measurements	
Architecture	Correlator Outputs	Discriminator Outputs
Centralized	*Advantages:* ▪ Good covariance management ▪ Good statistical modelling of non-multipath errors (Gaussianity) *Disadvantages:* ▪ Channel synchronization issues (especially when the integration period varies from one channel to another) ▪ The navigation filter and tracking filter have the same processing frequency ▪ Phase tracking is difficult	*Advantages:* ▪ Good covariance management ▪ Simple measurement model *Disadvantages:* ▪ Channel synchronization issues (especially when the integration period varies from one channel to another) ▪ The navigation filter and tracking filter have the same processing frequency ▪ Phase tracking is difficult ▪ Measurement model is not optimal
Decentralized	*Advantages:* ▪ Possibility of local processing ▪ Reduction of navigation filter order ▪ Tracking filter processing frequency can be different from navigation filter processing frequency ▪ Channel decoupling and/or channel exclusion in the navigator is simple (Easy to fall back to a scalar tracking scheme) ▪ Weighting of measurements based on their power ▪ Good statistical modelling of non-multipath errors (Gaussianity) *Disadvantages:* ▪ …	*Advantages:* ▪ Possibility of local processing ▪ Reduction of navigation filter order ▪ Tracking filter processing frequency can be different from navigation filter processing frequency ▪ Channel decoupling and/or channel exclusion in the navigator is simple (Easy to fall back to a scalar tracking scheme) ▪ Weighting of measurements based on their power ▪ Simple measurement model ▪ Measurement model can be used by STL *Disadvantages:* ▪ Measurement model is not optimal

2.5 SOLVING THE NAVIGATION AND VECTOR TRACKING PROBLEM

Solving the vector tracking problem and the navigation problem requires the use of estimation techniques to find recursively the parameters of interest namely some parameters pertaining to each particular tracking channel (for instance code delay, carrier phase and carrier frequency) and/or directly the navigation parameters (position, velocity and time). Although a technique such as recursive weighted least squares (RWLS) can serve for solving the navigation problem, it is a less accurate estimator than most Bayesian filtering approaches. As the accuracy of the navigation solution impacts the quality of vector tracking, Bayesian filtering techniques rather than the RWLS method are a more appropriate option for solving this problem.

2.5.1 BAYESIAN APPROACH

A brief description of probability theory concepts is given in Appendix 2.B for better understanding of some terms such as probability distribution, probability density function, conditional distribution and joint distribution that are used or applied in this chapter and in *Chapter 5*. The navigation and vector tracking problem, formulated as a Bayesian filtering problem, requires a state equation describing the a priori dynamics of the unknown parameters (system state) and an observation equation that links the unobservable state to the measurements. A state space model formulation is usually adopted in the following form

$$\begin{cases} X_k = f_k\left(X_{k-1}\right) + w_k \\ Z_k = h_k\left(X_k\right) + v_k \end{cases} \tag{2.17}$$

where

- $X_k \in \Re^{N_x}$ is the state vector made of the parameters to be estimated, in navigation of PVT parameters.
- $Z_k \in \Re^{N_z}$ is the measurement vector (also called observation vector) made of the available measurements.
- $w_k \in \Re^{N_x}$ is an additive white noise, an assumption that guarantees the Markovian characteristic of the state process.
- $v_k \in \Re^{N_z}$ is an additive white noise, an assumption that ensures the conditional independence of measurements.
- $f_k : \Re^{N_x} \to \Re^{N_x}$ and $h_k : \Re^{N_x} \to \Re^{N_z}$ are vector-valued functions, eventually nonlinear.

This filtering problem involves the estimation of the state vector X_k at time *k*, given all the measurements up to and including time *k*, which can be denoted by $Z_{1:k}$. This

problem can be formalized as the computation of the conditional probability distribution $P(X_k \in dX_k \mid Z_{1:k})$, also called a-posteriori or posterior distribution of the state vector. All the available information on the state of the system at an instant *k* is contained in the distribution $P(X_k \in dX_k \mid Z_{1:k})$. The solution to the problem is therefore obtained by recursive calculation of the a-posteriori distribution and derivation thereafter of the state estimates. Knowledge of $P(X_k \in dX_k \mid Z_{1:k})$ enables the conceptual calculation of optimal estimates with respect to any criterion such as

- Minimum mean square error (MMSE): $\hat{X}_k^{MMSE} \equiv E(X_k \mid Z_{1:k})$
- Maximum a posteriori (MAP): $\hat{X}_k^{MAP} \equiv \underset{X_k}{\operatorname{argmax}} P(X_k \in dX_k \mid Z_{1:k})$

By assuming that the initial distribution $P(dX_0)$ is known, two steps are applied successively to obtain the distribution of interest at any instant *k*:

Prediction: In the prediction step, $P(X_k \in dX_k \mid Z_{1:k-1})$ is computed from the filtering distribution $P(X_{k-1} \in dX_{k-1} \mid Z_{1:k-1})$ at time *k–1*. $P(X_{k-1} \in dX_{k-1} \mid Z_{1:k-1})$ is assumed to be known due to recursion and $P(X_k \in dX_k \mid X_{k-1})$ is given by the state equation. The prediction of the distribution of interest before the new measurement is available is made using the Chapman-Kolmogorov equation:

$$P(X_k \in dX_k \mid Z_{1:k-1}) = \int_{X_{k-1}} P(X_k \in dX_k \mid X_{k-1}) P(X_{k-1} \in dX_{k-1} \mid Z_{1:k-1}) \tag{2.18}$$

Update (Correction): With the availability of the new measurement, the estimate of the distribution of interest is updated using Bayes Law.

$$P(X_k \in dX_k \mid Z_{1:k}) = \frac{P(Z_k \in dZ_k \mid X_k) P(X_k \in dX_k \mid Z_{1:k-1})}{P(Z_k \in dZ_k \mid Z_{1:k-1})} \tag{2.19}$$

where:

$$P(Z_k \in dZ_k \mid Z_{1:k-1}) = \int_{X_k} P(Z_k \in dZ_k \mid X_k) P(X_k \in dX_k \mid Z_{1:k-1}) \tag{2.20}$$

This solution can however not be evaluated analytically. Equations (2.18) and (2.20) involve intractable integrals. But it is possible to calculate the optimal solution, the Kalman Filter (KF), for some state-space models namely linear Gaussian systems. For nonlinear non-Gaussian systems, sub-optimal solutions are derived: Extended Kalman Filter (EKF), Unscented Kalman Filter (UKF), Particle Filter (PF), and their variants.

2.5.2 SOLUTION TO THE BAYESIAN FILTERING PROBLEM

The Kalman Filter (KF) For linear Gaussian systems, the following state-space model is considered:

$$\begin{cases} X_k = F_k X_{k-1} + w_k \\ Z_k = H_k X_k + v_k \end{cases} \tag{2.21}$$

where the state noise w_k and the measurement noise v_k have Gaussian probability distributions such that $w_k \sim N(0, Q_k)$ and $v_k \sim N(0, R_k)$. If the initial distribution of the state vector is assumed to be Gaussian, it is shown that the a-posteriori distributions of the state vector given the measurements are also Gaussian, such that

$$\begin{array}{c} p(X_k \mid Z_{1:k-1}) \sim N(X_{k|k-1}, P_{k|k-1}) \\ p(Z_k \mid Z_{1:k-1}) \sim N(Z_{k|k-1}, C_k) \\ p(X_k \mid Z_{1:k}) \sim N(X_{k|k}, P_{k|k}) \end{array} \tag{2.22}$$

Here $p(X)$ is the probability density function corresponding to the probability distribution $P(dX)$ such that $P(dX) = p(X)dX$. They will be used interchangeably herein. The Gaussian distributions in (2.22) are completely described by their first- and second-order moments (means and variances) and an analytical solution can be computed iteratively using Equations (2.18) and (2.19). The resulting algorithm is the Kalman Filter (KF). It was introduced for the first time in [2] [3]. Algorithm 2.1 is the KF algorithm.

Algorithm 2.1: Kalman Filter (KF)

Prediction:

$$\begin{aligned} X_{k|k-1} &= F_k X_{k-1|k-1} \\ P_{k|k-1} &= F_k P_{k-1|k-1} F_k^T + Q_k \\ Z_{k|k-1} &= H_k X_{k|k-1} \\ C_k &= H_k P_{k|k-1} H_k^T + R_k \end{aligned}$$

Correction (Update):

$$\begin{aligned} K_k &= P_{k|k-1} H_k^T C_k^{-1} \\ X_{k|k} &= X_{k|k-1} + K_k (Z_k - Z_{k|k-1}) \\ P_{k|k} &= (I - K_k H_k) P_{k|k-1} \end{aligned}$$

The Extended Kalman Filter (EKF) The EKF algorithm is one of the suboptimal solutions obtained for nonlinear systems by linearizing the state space model then applying the equations of the KF. The EKF algorithm (see Algorithm 2.2), discussed in detail in [4] [5], replaces the nonlinear equations by their first-order Taylor series expansion around the most recent system state estimate. The noise is assumed to be Gaussian in order to obtain the a-posteriori distribution and the solution is calculated

recursively using the classical KF equations. The EKF state and observation equations are given by

$$\begin{cases} X_k = f_k(X_{k-1}) + w_k \approx f_k(X_{k-1|k-1}) + F_k(X_{k-1} - X_{k-1|k-1}) + w_k \\ Z_k = h_k(X_k) + v_k \approx h_k(X_{k|k-1}) + H_k(X_k - X_{k|k-1}) + v_k \end{cases} \tag{2.23}$$

where $F_k = \left.\frac{\partial f_k}{\partial X_{k-1}}\right|_{X_{k-1|k-1}}$ and $H_k = \left.\frac{\partial h_k}{\partial X_k}\right|_{X_{k|k-1}}$ are the Jacobian matrices of the functions $f_k(\cdot)$ and $h_k(\cdot)$ respectively.

Algorithm 2.2: Extended Kalman Filter (EKF)

Prediction:

$$\begin{aligned} X_{k|k-1} &= f_k(X_{k-1|k-1}) \\ P_{k|k-1} &= F_k P_{k-1|k-1} F_k^T + Q_k \\ Z_{k|k-1} &= h_k(X_{k|k-1}) \\ C_k &= H_k P_{k|k-1} H_k^T + R_k \end{aligned}$$

Correction (Update):

$$\begin{aligned} K_k &= P_{k|k-1} H_k^T C_k^{-1} \\ X_{k|k} &= X_{k|k-1} + K_k(Z_k - Z_{k|k-1}) \\ P_{k|k} &= (I - K_k H_k) P_{k|k-1} \end{aligned}$$

The Unscented Kalman Filter (UKF) Another solution to the Bayesian filtering problem for nonlinear systems is the UKF, introduced and discussed in detail in [6] [7]. The UKF does not linearize the nonlinear equations of the system. It rather makes use of the unscented transformation which utilizes a set of appropriately chosen weighted points to parameterize the means and variances of the distributions. The unscented transform (UT) calculates the mean and variance of a random variable by propagating it through a nonlinear function. The UKF thus estimates directly the state probability distribution given all the available observations. Let X be a random vector of dimension N with mean $\overline{X}$ and covariance P_x. The UT first calculates a set of $2N+1$ weighted points as follows

$$\chi_0 = \overline{X} \qquad i = 0$$

$$\chi_i = \overline{X} + \left(\sqrt{(N+\lambda)P_x}\right)_i \qquad i = 1,\ldots,N$$

$$\chi_i = \overline{X} + \left(\sqrt{(N+\lambda)P_x}\right)_{i-N} \qquad i = N+1,\ldots,2N$$

$$W_0^{(m)} = \lambda / (N+\lambda)$$

$$W_0^{(c)} = \lambda / (N+\lambda) + (1 - \alpha^2 + \beta)$$

$$W_i^{(m)} = W_i^{(c)} = 1 / 2(N+\lambda) \qquad i = 1,\ldots,2N$$

where $\lambda = \alpha^2(N+\kappa) - N$ is a scaling parameter; α determines the spread of the sigma points around $\bar{X}$ and is generally a small positive value ($10^{-4} \le \alpha \le 1$); κ is a secondary scaling parameter usually set to 0; β is used to incorporate the a-priori distribution of X (for a Gaussian prior, the optimal choice is $\beta = 2$); $\left(\sqrt{(N+\lambda)P_x}\right)_i$ is the i^{th} row or column of the matrix square root of $(N+\lambda)P_x$ and W_i is the weight associated with the i^{th} point. The sigma points are then instantiated through the nonlinear function to yield a set of transformed sigma points such that $Y_i = f(\chi_i)$. The first- and second-order moments of this new set are

$$\bar{Y} = \sum_{i=0}^{2N} W_i^{(m)} Y_i \qquad P_y = \sum_{i=0}^{2N} W_i^{(c)} \left(Y_i - \bar{Y}\right)\left(Y_i - \bar{Y}\right)^T \qquad P_{xy} = \sum_{i=0}^{2N} W_i^{(c)} \left(\chi_i - \bar{X}\right)\left(Y_i - \bar{Y}\right)^T$$

The following state space model can therefore be defined

$$\begin{cases} X_k^a = f_k\left(X_{k-1}^a\right) \\ Z_k = h_k\left(X_k^b\right) \end{cases} \tag{2.24}$$

where $X_k^a = \begin{bmatrix} X_k \\ v_k \\ w_k \end{bmatrix}$ or $X_k^a = \begin{bmatrix} X_k \\ v_k \end{bmatrix}$ and $X_k^b = \begin{bmatrix} X_k \\ v_k \\ w_k \end{bmatrix}$ or $X_k^b = \begin{bmatrix} X_k \\ w_k \end{bmatrix}$ depending on the preferences regarding the augmentation of the state vector with the process and/or measurement noise terms. Algorithm 2.3 summarizes the UKF algorithm.

The Particle Filter (PF) Particle filters, sometimes referred to as sequential Monte Carlo methods, are another solution to the Bayesian filtering problem for nonlinear systems. The generic particle filter algorithm (see Algorithm 2.5) is applicable to any system that can be defined using the following stochastic model:

$$\begin{cases} X_k \sim p\left(X_k \mid X_{0:k-1}\right) \\ Z_k \sim p\left(Z_k \mid X_{0:k}, Z_{0:k-1}\right) \end{cases} \tag{2.25}$$

Particle filters perform a recursive approximation of the conditional probabilities $P\left(X_{0:k} \mid Z_{1:k}\right)$. Here the full posterior distribution $P\left(X_{0:k} \mid Z_{1:k}\right)$ is considered and not the marginal distribution $P\left(X_k \mid Z_{1:k}\right)$. The idea is to approximate the posterior distribution $P\left(X_{0:k-1} \mid Z_{1:k-1}\right)$ at time *k-1* with a weighted set of samples $\left\{X_{0:k-1}^i, w_{k-1}^i\right\}_{i=1}^N$ called particles, and recursively update these particles to obtain an approximation to the posterior distribution $P\left(X_{0:k} \mid Z_{1:k}\right)$ at time *k*. Sequential Monte Carlo methods were already being used in the 1970s to study online dynamic

systems [8]. They have been improved in the 1990s to include a particle selection step. Several algorithms under the generic framework of sequential importance sampling (SIS) have been developed independently such as the bootstrap filter [9], the condensation algorithm [10], particle filtering [11], interacting particle approximations [12], and survival of the fittest [13].

Algorithm 2.3: Unscented Kalman Filter (UKF)

$$
\left.
\begin{aligned}
X^a_{k-1|k-1} &= \begin{bmatrix} X^T_{k-1|k-1} & E[w_k^T]^T \end{bmatrix} \qquad X^b_{k|k-1} = \begin{bmatrix} X^T_{k|k-1} & E[v_k^T]^T \end{bmatrix} \\
P^a_{k-1|k-1} &= \begin{bmatrix} P_{k-1|k-1} & 0 \\ 0 & Q_k \end{bmatrix} \qquad P^b_{k|k-1} = \begin{bmatrix} P_{k|k-1} & 0 \\ 0 & R_k \end{bmatrix} \\
\chi_{0,k-1|k-1} &= X^a_{k-1|k-1} \\
\chi_{i,k-1|k-1} &= X^a_{k-1|k-1} + \left(\sqrt{(N+\lambda)P^a_{k-1|k-1}}\right)_i \qquad i = 1,\ldots N \\
\chi_{i,k-1|k-1} &= X^a_{k-1|k-1} - \left(\sqrt{(N+\lambda)P^a_{k-1|k-1}}\right)_{i-N} \qquad i = N+1,\ldots 2N \\
\chi_{0,k|k-1} &= X^b_{k|k-1} \\
\chi_{i,k|k-1} &= X^b_{k|k-1} + \left(\sqrt{(N+\lambda)P^b_{k|k-1}}\right)_i \qquad i = 1,\ldots N \\
\chi_{i,k|k-1} &= X^b_{k|k-1} - \left(\sqrt{(N+\lambda)P^b_{k|k-1}}\right)_{i-N} \qquad i = N+1,\ldots 2N
\end{aligned}
\right\} \text{Sigma Points}
$$

$$
\left.
\begin{aligned}
\chi^x_{i,k|k-1} &= f_k\left(\chi_{i,k-1|k-1}\right) \\
X_{k|k-1} &= \sum_{i=0}^{2N} W^{(m)}_i \chi^x_{i,k|k-1} \\
P_{k|k-1} &= \sum_{i=0}^{2N} W^{(c)}_i \left(\chi^x_{i,k|k-1} - X_{k|k-1}\right)\left(\chi^x_{i,k|k-1} - X_{k|k-1}\right)^T \\
Z^z_{i,k|k-1} &= h_k\left(\chi_{i,k|k-1}\right) \\
Z_{k|k-1} &= \sum_{i=0}^{2N} W^{(m)}_i Z^z_{i,k|k-1} \\
C_k &= \sum_{i=0}^{2N} W^{(c)}_i \left(Z^z_{i,k|k-1} - Z_{k|k-1}\right)\left(Z^z_{i,k|k-1} - Z_{k|k-1}\right)^T \\
D_k &= \sum_{i=0}^{2N} W^{(c)}_i \left(\chi^x_{i,k|k-1} - X_{k|k-1}\right)\left(Z^z_{i,k|k-1} - Z_{k|k-1}\right)^T
\end{aligned}
\right\} \text{Prediction}
$$

$$
\left.
\begin{aligned}
K_k &= D_k C_k^{-1} \\
X_{k|k} &= X_{k|k-1} + K_k(Z_k - Z_{k|k-1}) \\
P_{k|k} &= P_{k|k-1} - K_k C_k K_k^T
\end{aligned}
\right\} \text{Correction (Update)}
$$

A classical particle filter algorithm has the following two steps: importance sampling and resampling.

Importance sampling: The importance sampling principle aims at approximating a target distribution $P(X)$ using samples drawn from a proposal distribution $Q(X)$. This principle is used generally when it is easier to sample from the proposal distribution than it is to sample from the target distribution itself. To compensate for the discrepancies between the target and proposal distributions, each sample X^i is weighted by $w^i \propto \pi(X^i)/q(X^i)$ where $\pi(X)$ is a probability density function proportional to $p(X)$ and that can be evaluated. The posterior distribution at time *k* using importance sampling is obtained as

$$P(X_{0:k} \mid Z_{1:k}) \approx \sum_{i=1}^{N} w_k^i \delta\left(X_{0:k} - X_{0:k}^i\right) \tag{2.26}$$

where $\delta(\cdot)$ is the delta Dirac function. The weight w_k^i expresses the probability that the particle X^i is the estimated state vector given all the accumulated measurements. The key here is to update the particles $X_{0:k-1}^i$ and their weights w_{k-1}^i so that they would approximate the posterior distribution at time *k*. To achieve that, it is assumed that the proposal distribution can be factorized as

$$Q(X_{0:k} \mid Z_{1:k}) = Q(X_k \mid X_{0:k-1}, Z_{1:k}) Q(X_{0:k-1} \mid Z_{1:k-1}) \tag{2.27}$$

Thus, each of the set of particles $X_{0:k-1}^i$ at time *k-1* can be augmented with a new state X_k^i at time *k* sampled from $Q(X_k \mid X_{0:k-1}, Z_{1:k})$. The weights at time *k* are written as

$$w_k^i \propto \frac{p\left(X_{0:k}^i \mid Z_{1:k}\right)}{q\left(X_{0:k}^i \mid Z_{1:k}\right)} \tag{2.28}$$

Equation (2.28) can be expressed recursively (see proof in Appendix 2.C) as

$$w_k^i \propto w_{k-1}^i \frac{p\left(Z_k \mid X_k^i\right) p\left(X_k^i \mid X_{k-1}^i\right)}{q\left(X_k^i \mid X_{0:k-1}^i, Z_{1:k}\right)} \tag{2.29}$$

The weights are normalized such that $\sum_{i=1}^{N} w_k^i = 1$. It is further assumed that $Q(X_k \mid X_{0:k-1}, Z_{1:k}) = Q(X_k \mid X_{k-1}, Z_k)$ so that the proposal distribution at time *k* only depends on the most recent state and measurement, and thus only X_{k-1}^i needs to be

stored. The particles at step k are generated from $Q\left(X_k \mid X_{k-1}^i, Z_k\right)$. The update equations therefore simplify to

$$\begin{cases} X_k^i \sim Q\left(X_k \mid X_{k-1}^i, Z_k\right) \\ w_k^i \propto w_{k-1}^i \dfrac{p\left(Z_k \mid X_k^i\right) p\left(X_k^i \mid X_{k-1}^i\right)}{q\left(X_k^i \mid X_{k-1}^i, Z_k\right)} \end{cases} \tag{2.30}$$

Resampling: A classical limitation of SIS is the degeneracy problem. Iteration of the update equations in (2.30) will result in only a few particles having a significant weight while all the other particles have very small weights. Degeneracy is typically measured by

$$N_{eff} = \frac{1}{\sum_{i=1}^{N} \left(w_k^i\right)^2} \tag{2.31}$$

A smaller N_{eff} means a larger variance for the weights and therefore more degeneracy. Resampling is performed to deal with degeneracy. The idea is to draw (with replacement) a new set $\left\{X_k^{i\,(*)}\right\}_{i=1}^{N}$ of N particles from the discrete approximation of the filtering distribution $P(X_k \mid Z_{1:k})$ provided by the weighted particles:

$$P\left(X_k \mid Z_{1:k}\right) \approx \sum_{i=1}^{N} w_k^i \delta(X_k - X_k^i) \tag{2.32}$$

Several resampling techniques have been devised. A simplified and efficient technique proposed in [25] guarantees a small variance of the number of descendants per particle. It is described in Algorithm 2.4.

Algorithm 2.4: Stratified Resampling

- Random drawing from a uniform distribution: $u_1 \sim U\left[0, 1/N\right]$
- FOR $i = 2:N$
  - $u_i = u_1 + 1/N \times (i-1)$
  - While $u_i > \sum_{m=1}^{j} w_k^m$
    $j = j + 1$.
  - $X_k^{i\,(*)} = X_k^j$.
- END FOR

Resampling significantly increases the number of particles that efficiently contribute to the state estimation. Particles with large weights are very likely to be drawn multiple times while particles with very small weights are not likely to be drawn at all. However, it is recommended not to apply resampling systematically because of the risk of sample impoverishment that may lead to filter divergence. It is rather advised to apply resampling only if the variance of weights becomes very large. Algorithm 2.5 is the generic particle filter (GPF) algorithm.

Algorithm 2.5: Generic Particle Filter (GPF)

- FOR $i = 1:N$
  - Draw $X_k^i \sim Q\left(X_k \mid X_{k-1}^i, Z_k\right)$
  - Assign a weight:

    $$w_k^i \propto w_{k-1}^i \frac{p\left(Z_k \mid X_k^i\right) p\left(X_k^i \mid X_{k-1}^i\right)}{q\left(X_k^i \mid X_{k-1}^i, Z_k\right)}$$
- END FOR
- Calculate total weight: $\Sigma = \sum_{i=1}^{N} w_k^i$
- FOR $i = 1:N$

  Normalize: $w_k^i = \frac{1}{\Sigma} w_k^i$
- END FOR
- Calculate $N_{eff} = 1 \Big/ \sum_{i=1}^{N} \left(w_k^i\right)^2$
- IF $N_{eff} < N_{Threshold}$

  Resample using Algorithm 2.4.
- END IF

2.6 CONCLUSION

Two GNSSs are global today (the American *GPS* and the Russian *GLONASS*) and two others are set to reach global coverage soon (the European Union *Galileo* and the Chinese *Compass*). The GNSS receiver design and operation has tremendously evolved since the invention of GNSS. The search for more flexibility, adaptability and cost-effectiveness made it possible to fit the entire GNSS receiver processing on a small cell phone module and motivated the invention of GNSS software receivers. The architecture and operation of the GPS software receiver that are described in this chapter set a basis for understanding the investigations and analyses that are performed in the other chapters and for discussing the contributions that are made in this thesis. The non-exhaustive overview that is provided on filtering approaches that are used to solve the navigation and vector tracking problem shows that a precedent has been set upon which any further developments and improvements can be built. The next chapter discusses the problem of GPS/GNSS receiver operation in multipath environments and provides a few solutions.

APPENDIX 2.A: CORRELATION AND SIGNAL TRACKING

Signal tracking is performed in order to extract GPS observables that are used in the GPS receiver navigator from the incoming signal. This is achieved by generating a local replica signal that matches the received signal. Tracking is basically the process of updating the local replica to adapt it to changes in the received signal. Correlators, discriminators, loop filters and numerically controlled oscillators (NCOs) all intervene in the tracking process as shown in Figure 2.3.

CORRELATION

It is not useful to attempt direct estimation of the code delay and carrier phase and frequency from the raw received signal. The latter is generally below the noise floor meaning that its amplitude is lower than that of thermal noise. Thermal noise, unlike other disturbances such as multipath and interference, is always present on signal measurements. The PRN code that is modulated onto the carrier spreads the energy of the signal in the frequency domain keeping it below the noise floor. The correlation process, which is based on multiplication of a locally generated replica of the received PRN code with the received signal, is the reverse process that lifts the received signal power above the noise floor. The received signal onto which the correlation process is performed is the filtered and down-converted intermediate frequency (IF) signal. Correlation is made possible using an in-phase (I) and quadra-phase (Q) correlator. The I correlator is generated using a cosine term at the replica frequency and the Q correlator is generated from a sine term. By ignoring the analogue-to-digital converter (ADC) effect and by assuming that thermal noise is the only external disturbance that is present, the in-phase and quadra-phase local replicas can be modelled as [26]:

$$I(t) = C(t - \hat{\tau})\cos(2\pi f_{IF}\, t + \hat{\phi}) \tag{2.A.1}$$

$$Q(t) = C(t - \hat{\tau})\sin(2\pi f_{IF}\, t + \hat{\phi}) \tag{2.A.2}$$

where $\hat{\tau}$ is the incoming signal code group delay estimate and $\hat{\phi}$ is the carrier phase estimate. The in-phase and quadra-phase replicas are multiplied by the received IF signal *x(t)* and the product is processed by an integrate-and-dump filter. This process can be modelled as [26]:

$$I = \frac{1}{T_{\text{int}}} \int_0^{T_{\text{int}}} x(t) I(t)\, dt \tag{2.A.3}$$

$$Q = \frac{1}{T_{\text{int}}} \int_0^{T_{\text{int}}} x(t) Q(t)\, dt \tag{2.A.4}$$

where T_{int} is the coherent integration time. Assuming that the code delay and carrier phase are quasi-constant during the integration period, that the correlation process is performed within one data bit, and that the front-end filter has one-sided bandwidth, the I and Q correlation outputs can be approximated by:

$$I = \sqrt{\frac{P}{2}} R(\Delta_\tau) D \frac{\sin(\pi \Delta_f T_{\text{int}})}{\pi \Delta_f T_{\text{int}}} \cos(\Delta_\phi) + \eta_I \tag{2.A.5}$$

$$Q = \sqrt{\frac{P}{2}} R(\Delta_\tau) D \frac{\sin(\pi \Delta_f T_{\text{int}})}{\pi \Delta_f T_{\text{int}}} \sin(\Delta_\phi) + \eta_Q \tag{2.A.6}$$

where P is the power of the incoming signal, $R(\cdot)$ is the correlation of the local PRN code with the incoming signal PRN code, D is the sign of the navigation data bit, $\Delta_\tau = \tau - \hat{\tau}$ is the code group delay error, $\Delta_f = f - \hat{f}$ is the Doppler frequency error, $\Delta_\phi = \phi - \hat{\phi}$ is the carrier phase error, η_I and η_Q are independent additive white Gaussian noises with equal power. During signal tracking, if all parameters are correctly estimated, it can be observed from equation 2.A.5 that the navigation data value will appear on the I correlation output.

DISCRIMINATORS

In the tracking algorithm, the discriminator function uses the correlator outputs to generate the error signal. Three general classes of discriminators can be distinguished depending on the tracking loop type: code delay discriminators, carrier phase discriminators, and carrier frequency discriminators. To maintain the local replica aligned, both code and carrier tracking loops are necessary. However, the receiver can maintain either carrier phase lock or carrier frequency lock. In harsh environments, when the incoming signal is weak, the phase locked loop (PLL) is the most vulnerable and most susceptible to loss of lock. However, carrier phase achieves more accuracy when used for range measurement. The frequency locked loop (FLL) ignores the carrier phase and tries to maintain frequency error at zero. It achieves more robust tracking but suffers from less accuracy. Some receivers may implement a frequency-assisted phase locked loop (FPLL). A delay locked loop (DLL) is implemented to keep track of the code phase and to obtain a perfectly aligned replica of the code.

Code tracking is performed using the C/A code correlation peak, which is a function of the relative delay $\Delta\tau$ and is approximated by

$$R(\Delta\tau) = \begin{cases} 1 - \dfrac{|\Delta\tau|}{\partial}, & -\partial \le \Delta\tau \le \partial \\ 0, & \textit{otherwise} \end{cases} \tag{2.A.7}$$

where ∂ is the chip width of a single C/A code value. Correlation of the incoming signal with a perfectly aligned local replica produces maximum correlation value since all samples are perfectly aligned during correlation. To properly generate code tracking error, three replicas of the code are generated. The best guess of the local replica is called the prompt replica. The intentionally advanced and delayed local replicas are called early and late replicas. The DLL is designed to make the prompt replica follow the maximum value of the correlation function. The correlator spacing is the distance between the early and late correlators and is 1 chip for a standard DLL. A perfectly aligned prompt replica is illustrated in Figure 2.10 with ∂=1. The early and late codes have phase shifts of $-\partial/2$ and $+\partial/2$ chip from the prompt. DLL discriminators are either coherent or non-coherent. Some commonly used ones are [18]:

Coherent: $I_E - I_L$: requires a good tracking loop for optimal functionality.

Non-Coherent:

- $\left(I_E^2 + Q_E^2\right) - \left(I_L^2 + Q_L^2\right)$: Early minus Late Power. Its response is almost the same as the coherent discriminator's.
- $\frac{\left(I_E^2 + Q_E^2\right) - \left(I_L^2 + Q_L^2\right)}{\left(I_E^2 + Q_E^2\right) + \left(I_L^2 + Q_L^2\right)}$: Normalized Early minus Late Power. It can keep track of noisy signals with the chip error larger than ½ chip.
- $I_P\left(I_E - I_L\right) + Q_P\left(Q_E - Q_L\right)$: Dot product. It is the only discriminator that uses all six correlators.

where I_E, I_P, I_L are respectively the in-phase early, prompt and late correlator outputs and Q_E, Q_P, Q_L are the quadra-phase early, prompt and late correlator outputs. A DLL that uses a coherent discriminator is optimal when the locally generated carrier wave is locked in phase and frequency. When there is a phase error on the local carrier wave, the signal becomes noisier which makes it difficult for the DLL to keep lock on the code. A non-coherent DLL is designed in such a way as to be independent of the phase of the local carrier wave. If the local carrier wave is in phase with the incoming signal, all the energy will be in the I-arm but if it drifts compared to the input signal the energy switches between the I-arm and Q-arm.

Figure 2.11 illustrates the Early minus Late Power discriminator function. As long as the delay is within half a chip from zero delay, the discriminator output is linear with respect to the delay. This behaviour is very important for proper filtering as the code loop filter is designed based on linear theory. Outside of this range, the output is still meaningful until the delays fall $\frac{3}{2}$ of a chip away. This occurs when either the

early or late correlators fall outside the correlation peak shown in Figure 2.10. In that case their output is zero and makes no contribution to the correction [17].

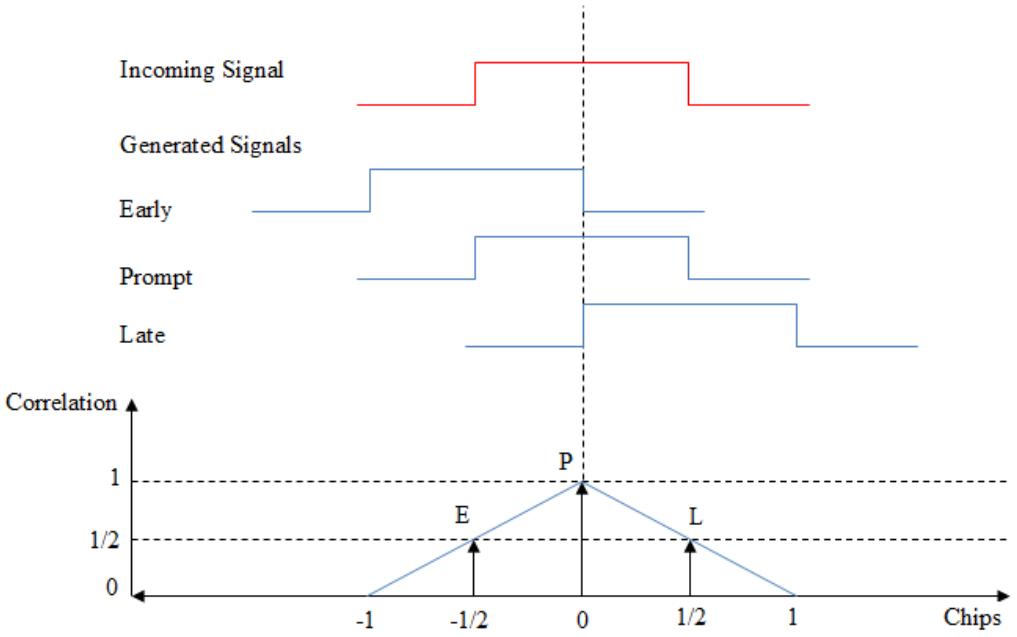

Figure 2.10: Perfectly tuned code tracking loop: highest correlation at prompt output

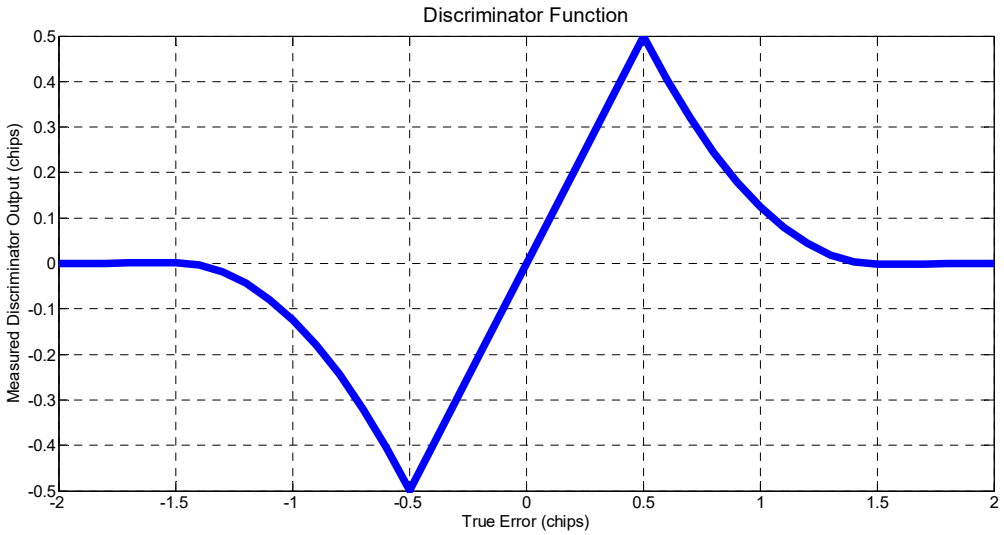

Figure 2.11: Normalized Early minus Late Power Discriminator Function: Linear and Pull-in Regions

The phase tracking error is evaluated using a phase discriminator. The most commonly used phase discriminator is the arctangent discriminator given by:

$$\phi = \arctan\left(\frac{Q_P}{I_P}\right) \tag{2.A.8}$$

where ϕ is the phase error between the local replica and the incoming signal. The discriminator is linear between $-\pi$ and π radians. The arctangent discriminator is also used for evaluating carrier frequency error and is formulated as:

$$\Delta_f = \frac{\arctan(CROSS / DOT)}{2\pi(t_2 - t_1)} \quad \text{with} \quad \begin{aligned} DOT &= I_{P1} \times I_{P2} + Q_{P1} \times Q_{P2} \\ CROSS &= I_{P1} \times Q_{P2} - I_{P2} \times Q_{P1} \end{aligned} \tag{2.A.9}$$

where Δ_f is the frequency error between the local replica and the received signal. *DOT* and *CROSS* use prompt correlator outputs defined between two integrate-and-dump instants t_1 and t_2. More phase and frequency discriminators used for carrier tracking can be found in [20].

LOOP FILTER

The role of a loop filter is to transform a noisy error signal into a filtered signal acting as command to the NCO. Ultimately, the loop filter has to bring the error signal to zero. The design of code and carrier loop filters is similar such that these filters are often presented with the same details but different parameters. The performance of the filter is altered by varying the loop order and associated parameters. The carrier loop filter used for the PLL tracking loop is illustrated in Figure 2.12. The same filter is applicable for the code tracking loop. Its discrete-time equation considering an input $x(n)$ and an output $y(n)$ is derived to obtain

$$y(n) - y(n-1) = (C_1 + C_2)x(n) - C_1 x(n-1) \tag{2.A.10}$$

Applying the z-transform on equation 2.A.10, the transfer function of the filter in the z-domain is found to be

$$H(z) = \frac{Y(z)}{X(z)} = \frac{(C_1 + C_2) - C_1 z^{-1}}{1 - z^{-1}} \tag{2.A.11}$$

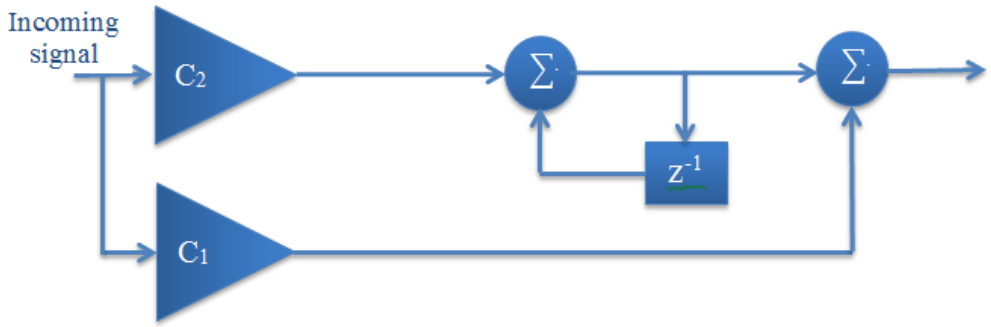

Figure 2.12: Second-order filter: used as code or carrier loop filter

APPENDIX 2.B: PROBABILITY THEORY CONCEPTS

A brief description of probability theory concepts is provided hereafter as an aid to better understand some terms such as probability distribution, probability density function, conditional distribution and joint distribution that are used or applied in this chapter and in *Chapter 5*. For a comprehensive and detailed discussion on probability theory, the reader is advised to consult [27] or [28].

2.B.1 PROBABILITY THEORY

The basic probability theory concepts are the event space S and the events which are subsets of S. The event space S is referred to as the certain event and consists of all possible outcomes of an experiment. The empty set ϕ is the impossible event. Singleton events are denoted ω hereinafter.

- *Axiomatic Definition of Probability*

Let the number $\Pr(A)$ denote the probability of the event A. The following three axioms are defined:

- The probability $\Pr(A)$ of the event A is a positive number assigned to this event.

$$\Pr(A) \geq 0 \tag{2.B.1}$$

- The probability of the certain event equals 1.

$$\Pr(S) = 1 \tag{2.B.2}$$

- If the events A and B are mutually exclusive, i.e. if $A \cap B = \phi$ then

$$\Pr(A \cup B) = \Pr(A) + \Pr(B) \tag{2.B.3}$$

Corollary:

If $A_i \cap A_j = \phi$ for $i \neq j$, then $\Pr\left(\bigcup_{i=1}^{\infty} A_i\right) = \sum_{i=1}^{\infty} \Pr(A_i)$.

- *Conditional Probability*

All of Statistical Inference is based on the concept of conditional probability. The conditional probability of an event A given an event B of nonzero probability $\Pr(B) > 0$ is defined as

$$\Pr(A \mid B) = \frac{\Pr(A \cap B)}{\Pr(B)} \tag{2.B.4}$$

- *Total Probability Theorem*

Let $\{A_1, ..., A_n\}$ be a partition of the event space S and let B be an arbitrary event. It follows that

$$\Pr(B) = \Pr(B \mid A_1)\Pr(A_1) + ... + \Pr(B \mid A_n)\Pr(A_n) \tag{2.B.5}$$

Proof:

It is clear that

$$B = B \cap S = B \cap (A_1 \cup ... \cup A_n) = (B \cap A_1) \cup ... \cup (B \cap A_n) \tag{2.B.6}$$

But the events A_i and A_j are mutually exclusive which entails that the events $B \cap A_i$ and $B \cap A_j$ are also mutually exclusive. It follows from Equations (2.B.3) and (2.B.6) that

$$\Pr(B) = \Pr(B \cap A_1) + ... + \Pr(B \cap A_n) \tag{2.B.7}$$

Therefore,

$\Pr(B) = \Pr(B \mid A_1)\Pr(A_1) + ... + \Pr(B \mid A_n)\Pr(A_n)$, because $\Pr(B \cap A_i) = \Pr(B \mid A_i)\Pr(A_i)$ from Equation (2.B.4), which proves the total probability theorem.

- *Bayes' Theorem*

Let $\{A_1, ..., A_n\}$ be a partition of the event space S and let B and C be two events. It follows that

$$\Pr(C \mid B) = \frac{\Pr(B \mid C)\Pr(C)}{\Pr(B \mid A_1)\Pr(A_1) + ... + \Pr(B \mid A_n)\Pr(A_n)} \tag{2.B.8}$$

Proof:

Since $\Pr(B \cap C) = \Pr(C \cap B) = \Pr(C \mid B)\Pr(B)$, it follows that $\Pr(C \mid B) = \frac{\Pr(B \cap C)}{\Pr(B)}$. Therefore,

$$\Pr(C \mid B) = \frac{\Pr(B \mid C)\Pr(C)}{\Pr(B)} \tag{2.B.9}$$

Substitution of Equation (2.B.5) into Equation (2.B.9) yields Equation (2.B.8) proving Bayes' theorem.

2.B.2 RANDOM VARIABLES

A random variable is a real valued function having as domain the set S of all possible experimental outcomes. Let every outcome ω be assigned a real number $x(\omega)$. The explicit dependency on the event ω can be omitted such that the notation of the random variable can simply be x. The set $\{x \le \chi\}$ is a subset of the event space S consisting of all possible outcomes ω such that $x(\omega) \le \chi$.

The distribution function $P(\chi)$ of the random variable x is the function

$$P(\chi) = \Pr(x \le \chi) \tag{2.B.10}$$

The density function $p(\chi)$ of the random variable x is the derivative of the distribution function $P(\chi)$ and is given by

$$p(\chi) = \frac{dP(\chi)}{d\chi} \tag{2.B.11}$$

The definition of conditional probability can be readily extended to distribution and density functions.

- *Conditional Distribution*

The conditional distribution of a random variable x given an event B of nonzero probability $\Pr(B) > 0$ is

$$P(\chi \mid B) = \Pr(x \le \chi \mid B) = \frac{\Pr(x \le \chi, B)}{\Pr(B)} \tag{2.B.12}$$

The event $\{x \le \chi, B\}$ is the intersection of the event $\{x \le \chi\}$ and B, that is the event consisting of all outcomes ω such that $x(\omega) \le \chi$ and $\omega \in B$.

Similarly, the conditional density is the derivative of $P(\chi \mid B)$ and is given by

$$p(\chi \mid B) = \frac{dP(\chi \mid B)}{d\chi} = \lim_{\Delta\chi \to 0} \frac{P(\chi \le x \le \chi + \Delta\chi \mid B)}{\Delta\chi} \tag{2.B.13}$$

The conditional probability of the event A given an event of zero probability such as $\{x = \chi\}$ is defined through the following limit

$$\Pr(A \mid x = \chi) \approx \lim_{\Delta\chi \to 0} \Pr(\chi \le x \le \chi + \Delta\chi) \tag{2.B.14}$$

The total probability theorem for conditional events of zero probability can therefore be expressed as an infinite sum over the limit in Equation (2.B.14). Consequently, the probability of any event A can be written as

$$\Pr(A) = \int_{-\infty}^{\infty} \Pr(A \mid x = \chi) p(\chi) d\chi \tag{2.B.15}$$

The conditional density of x given the event A is given by

$$p(\chi \mid A) = \frac{\Pr(A \mid x = \chi) p(\chi)}{\Pr(A)} \tag{2.B.16}$$

- *Joint Distribution*

The concepts that apply to scalar random variables can be readily extended to vector valued random variables by considering pairs of scalar variables. The distribution and density functions for the random variable pair (x, y) are given by

$$\begin{aligned} P(\chi, \gamma) &= \Pr(x \le \chi, y \le \gamma) \\ p(\chi, \gamma) &= \frac{\partial^2 P(\chi, \gamma)}{\partial\chi \partial\gamma} \end{aligned} \tag{2.B.17}$$

These functions are referred to as joint distribution and joint density functions respectively.

The definition of conditional distribution and density, given an event B of nonzero probability $\Pr(B) > 0$, similarly extends to pairs of random variables, such that

$$\begin{aligned} P(\chi, \gamma \mid B) &= \frac{\Pr(x \le \chi, y \le \gamma, B)}{\Pr(B)} \\ p(\chi, \gamma \mid B) &= \frac{\partial^2 P(\chi, \gamma \mid B)}{\partial\chi \partial\gamma} \end{aligned} \tag{2.B.18}$$

The conditional density of a random variable y, assuming the value of some other random variable x is known, is often used in statistical inference. However, this

density cannot be directly derived from Equation (2.B.18) because the event $\{x = \chi\}$ generally has zero probability. The density is therefore defined through the following limit:

$$p(\gamma \mid x = \chi) = \lim_{\Delta\chi \to 0} p(\gamma \mid \chi < x \leq \chi + \Delta\chi) \tag{2.B.19}$$

The shorter notation $p(\gamma \mid \chi)$ can be used in place of $p(\gamma \mid x = \chi)$.

- *Bayes' Theorem (Most Common Version)*

The conditional density $p(\chi \mid \gamma)$ can be expressed as

$$p(\chi \mid \gamma) = \frac{p(\gamma \mid \chi)p(\chi)}{p(\gamma)} \tag{2.B.20}$$

The normalizing constant $p(\gamma)$ in the denominator can be expressed using the law of total probability

$$p(\gamma) = \int_{\Re^n} p(\gamma \mid \chi)p(\chi)d\chi \tag{2.B.21}$$

The conditional density function $p(\gamma \mid \chi)$ is called the likelihood, and the parameters density function $p(\chi)$ is called the prior.

Bayes' law in Equation (2.B.20) can be expressed using only the joint density of the random variables x and y as follows

$$p(\chi \mid \gamma) = \frac{p(\gamma, \chi)}{\int_{\Re^n} p(\gamma, \chi)d\chi} \tag{2.B.22}$$

APPENDIX 2.C: DERIVATION OF RECURSIVE EXPRESSION FOR PARTICLE FILTER WEIGHTS

It is discussed in this chapter that the particle filter aims at approximating the posterior distribution $P(X_{0:k-1} \mid Z_{1:k-1})$ at time *k-1* with a weighted set of samples $\{X^{i}_{0:k-1}, w^{i}_{k-1}\}_{i=1}^{N}$ called particles, and recursively updating these particles to obtain an approximation to the posterior distribution $P(X_{0:k} \mid Z_{1:k})$ at time *k*. The weights of the particle filter at time *k* are written as

$$w_k^i \propto \frac{p\left(X^{i}_{0:k} \mid Z_{1:k}\right)}{q\left(X^{i}_{0:k} \mid Z_{1:k}\right)} \tag{2.C.1}$$

Equation (2.C.1) can be expressed recursively as

$$w_k^i \propto w_{k-1}^i \frac{p\left(Z_k \mid X^{i}_{k}\right) p\left(X^{i}_{k} \mid X^{i}_{k-1}\right)}{q\left(X^{i}_{k} \mid X^{i}_{0:k-1}, Z_{1:k}\right)} \tag{2.C.2}$$

Proof:

The proposal probability density function $q(X_{0:k} \mid Z_{1:k})$ can be factorized as

$$q(X_{0:k} \mid Z_{1:k}) = q(X_k \mid X_{0:k-1}, Z_{1:k}) q(X_{0:k-1} \mid Z_{1:k-1}) \tag{2.C.3}$$

Similarly, using Bayes' law, the posterior probability density function $p(X_{0:k} \mid Z_{1:k})$ can be decomposed as

$$\begin{aligned}
p(X_{0:k} \mid Z_{1:k}) &= \frac{p(Z_k \mid X_{0:k} \mid Z_{1:k-1}) p(X_{0:k} \mid Z_{1:k-1})}{p(Z_k \mid Z_{1:k-1})} \\
p(X_{0:k} \mid Z_{1:k}) &= \frac{p(Z_k \mid X_{0:k} \mid Z_{1:k-1}) p(X_k \mid X_{0:k-1} \mid Z_{1:k-1}) p(X_{0:k-1} \mid Z_{1:k-1})}{p(Z_k \mid Z_{1:k-1})} \\
p(X_{0:k} \mid Z_{1:k}) &= \frac{p(Z_k \mid X_k) p(X_k \mid X_{k-1}) p(X_{0:k-1} \mid Z_{1:k-1})}{p(Z_k \mid Z_{1:k-1})}
\end{aligned} \tag{2.C.4}$$

The posterior $p(X_{0:k} \mid Z_{1:k})$ in Equation (2.C.4) can be further approximated by

$$p(X_{0:k} \mid Z_{1:k}) \propto p(Z_k \mid X_k) p(X_k \mid X_{k-1}) p(X_{0:k-1} \mid Z_{1:k-1}) \tag{2.C.5}$$

Substitution of Equations (2.C.3) and (2.C.5) into (2.C.1) yields

$$w_k^i \propto \frac{p\left(X_{0:k}^i \mid Z_{1:k}\right)}{q\left(X_{0:k}^i \mid Z_{1:k}\right)} = \frac{p\left(Z_k \mid X_k^i\right) p\left(X_k^i \mid X_{k-1}^i\right) p\left(X_{0:k-1}^i \mid Z_{1:k-1}\right)}{q\left(X_k^i \mid X_{0:k-1}^i, Z_{1:k}\right) q\left(X_{0:k-1}^i \mid Z_{1:k-1}\right)}$$
$$w_k^i \propto w_{k-1}^i \frac{p\left(Z_k \mid X_k^i\right) p\left(X_k^i \mid X_{k-1}^i\right)}{q\left(X_k^i \mid X_{0:k-1}^i, Z_{1:k}\right)} \tag{2.C.6}$$

Chapter 3

GPS/GNSS Receiver Operation in Multipath Environments

The purpose of analysis is to solve problems, not create pretty theorems.

— George E. Forsythe

To consult the statistician after an experiment is finished is often merely to ask him to conduct a post mortem examination. He can perhaps say what the experiment died of.

— Ronald A. Fisher

3.1 INTRODUCTION

The Global Positioning System (GPS) has been designed in such a way as to use a clear line-of-sight (LOS) between the receiver and the satellites it is tracking to compute the positioning solution. But with the ubiquity of GPS receivers, they are used in more and more constrained environments with signal reflecting and/or blocking obstacles. Such environments include heavy foliage, urban canyon, suburban and indoor areas. Multipath is any signal that has been reflected or diffracted at least once before being incident to the GPS receiver's antenna. The blending of the LOS signal with multipath induces tracking errors in the receiver's channels. Be it specular, diffuse or diffracted, multipath distorts the correlation function used for code phase measurements, and therefore distorts these measurements. This chapter aims at providing theoretical characterization of multipath induced tracking errors in the context of scalar and vector tracking loops (STL and VTL). These tracking errors are derived by modelling the correlator outputs in the presence of multipath then analysing the locking points of both scalar and vector tracking loops in the absence and in the presence of multipath. The chapter then proposes correlator-based multipath detection techniques and a correlator-based non-line-of-sight (NLOS) detection technique. It finally discusses other correlator-based signal quality indicators namely a phase lock indicator (PLI) and some low-complexity C/N_0 estimators.

3.2 GPS MULTIPATH INDUCED ERRORS FOR SCALAR AND VECTOR TRACKING LOOPS

Multipath presents itself as a delayed copy of the LOS signal because the LOS signal always has the shortest transit time from satellite to receiver, its path being the shortest. The blending of the LOS signal with one or more delayed copies induces tracking errors in the receiver's channels. *Chapter 2* has explained that tracking consists of aligning a local replica of the carrier and the spreading code with the incoming signal's carrier and code for the satellite of interest. These alignments are achieved based on correlation between the local replica and incoming signal using scalar tracking loops (code delay, carrier phase and/or frequency locked loops) or vector tracking loops (such as the vector delay frequency locked loop). These loops continuously track the maximum correlation, which indicates that alignment is achieved, by constantly adjusting the locally generated carrier phase and code delay to match the incoming signal's. In the presence of multipath, the loops are not tracking the LOS signal anymore but rather the LOS blended with delayed copies. Thus, multipath contributes significantly to the error induced in the tracking and consequently in the positioning solution. To better design multipath detection and mitigation techniques, it is important to study the characteristics of multipath on a theoretical point of view and devise models that characterize the induced tracking errors.

Code delay, carrier phase and carrier frequency tracking errors are discussed hereafter. Both code and carrier tracking errors are influenced by multipath and the correlator chip spacing. The topic has been extensively covered for STLs in existing literature [29] [30] [31] [32] but not much for VTLs. In [29] and many other publications in literature, only the envelope models are used for code delay errors. The mathematical expressions of the errors under the envelope are presented in [30] [31] and [32]. In [30], the carrier phase tracking error is analysed under the assumption that the code delay tracking error is zero, which is not accurate since the code delay tracking error is nonzero in the presence of multipath. The models in [31] and [32] overcome this weakness. Characterization of the effects of multipath on the VTL with theoretical error expressions is performed in [33]. It is proved in [33] that multipath induced tracking error in one tracking channel is reduced by the VTL algorithm when more than four satellites are tracked. But this reduction can be interpreted merely as the distribution of this single tracking channel error to all tracking channels.

This section reviews models of phase and delay tracking errors under the envelopes for STLs with contrast between narrow and standard correlator chip spacing as well as coherent and non-coherent discriminators. The section makes contribution by

extension from models in [33] to the characterization of multipath induced code delay, carrier phase and carrier frequency tracking errors for VTLs by deriving models that allow the analysis of both code and carrier tracking errors with respect to multipath delay, multipath phase and multipath fading frequency.

3.2.1 CORRELATOR OUTPUTS IN THE PRESENCE OF MULTIPATH

There are several types of multipath reflections: specular, diffuse, diffracted. But two main classes of multipath signals can be distinguished. The first class is diffuse multipaths which are spread in the frequency domain. They affect the received signal quality by degrading the carrier to noise power ratio (C/N_0). The second class is specular multipaths which are localized in frequency. They produce a bias on pseudorange (PR) measurements and delta-range (DR) or range-rate measurements when their frequency is in the frequency band of the receiver. This is particularly true for fixed receivers or receivers moving parallel to the surface that reflects the multipaths. If a specular multipath model with a finite number of multipath signals is considered, the signal entering the code and phase tracking loops, neglecting the low rate data, can be expressed as

$$x(t) = A_0 C(t-\tau_0)\cos(\omega t - \varphi_0) + \sum_{l=1}^{L} A_l C(t-\tau_l)\cos(\omega t - \varphi_l) + w(t) \tag{3.1}$$

where L is the number of multipath signals, A_0 and A_l are the LOS and l^{th} multipath amplitudes respectively, $C(t)$ is the spreading code, τ_0, τ_l, φ_0, φ_l are the code delays and carrier phases induced by the transmission from satellite to receiver for the LOS and l^{th} multipath signals respectively, ω is the nominal GPS L1, L2 or L5 radial frequency, and $w(t)$ is the zero-mean additive white Gaussian noise with variance σ^2. For ease of mathematical derivations that are performed hereinafter, the Doppler shift is included in φ_0 and φ_l in these models. This modelling approach does not affect the derivation results, meaning that a detailed notation for the model could be used and the results would still be essentially the same. The signal at the output of the prompt correlator at an instant of time is modelled as

$$I_P + jQ_p = A_0 R(\Delta\tau)\exp(j\Delta\varphi) + \sum_{l=1}^{L} A_l R(\Delta\tau - \delta_l)\exp[j(\Delta\varphi - \theta_l)] + w_P \tag{3.2}$$

where R is the correlation function, $\Delta\tau$ is the error between the LOS signal delay and the estimated code replica delay, $\Delta\varphi$ is the error between the LOS carrier phase and the estimated carrier replica phase, $\delta_l = \tau_l - \tau_0$ is the delay of the l^{th} multipath with respect to the LOS, $\theta_l = \varphi_l - \varphi_0$ is the phase shift of the l^{th} multipath with respect to the LOS, and w_P is the post-correlation noise. δ_l is always positive since the

multipath signal always arrives later than the LOS signal. Assuming infinite bandwidth, the ideal autocorrelation function for GPS L1 C/A code is approximated by

$$R(\Delta\tau) = \begin{cases} 1 - \dfrac{|\Delta\tau|}{\partial}, & -\partial \le \Delta\tau \le \partial \\ 0, & otherwise \end{cases} \tag{3.3}$$

where ∂ is the early-late correlator chip spacing. Once more, to simplify the notation, it can be assumed that all reflected signals have the same frequency. Thus, the signal entering the code and phase tracking loops can be considered as affected by one specular multipath and can be expressed as

$$x(t) = A_0 C(t-\tau_0)\cos(\omega t - \varphi_0) + A_M C(t-\tau_M)\cos(\omega t - \varphi_M) + w(t) \tag{3.4}$$

where the subscript M refers to the multipath resulting from a vector sum of all multipath signals in presence. It is assumed that the multipaths with a different frequency would contribute to an increase in noise power. With the simplified notation, and if A_M is written as $A_M = \alpha A_0$ the in-phase and quadrature outputs of the prompt correlator in the presence of a specular multipath, at an instant of time, can be written as

$$I_P = A_0 R(\Delta\tau)\cos(\Delta\varphi) + \alpha A_0 R(\Delta\tau - \delta_M)\cos(\Delta\varphi - \theta_M) + w_{I,P} \tag{3.5a}$$

$$Q_P = A_0 R(\Delta\tau)\sin(\Delta\varphi) + \alpha A_0 R(\Delta\tau - \delta_M)\sin(\Delta\varphi - \theta_M) + w_{Q,P} \tag{3.5b}$$

Figure 3.1 depicts the in-phase output of the prompt correlator in the presence of a multipath (normalized correlation, $\alpha = 0.5$, $\delta_M = 0.2046$ chip, $\theta_M = 0^\circ$) with respect to the code delay error on the LOS (error between the incoming LOS signal code delay and the estimated replica code delay in chips). The correlation functions for the LOS and multipath are depicted in green and red respectively. The distorted correlation function which is the sum of the LOS and multipath contributions is shown in blue.

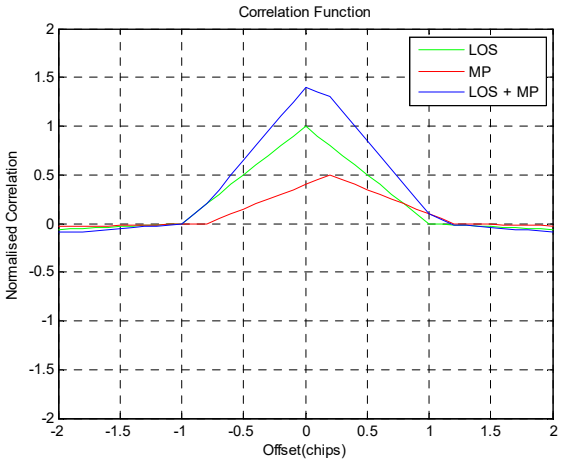

Figure 3.1: Correlation function for LOS signal affected by multipath

The Early and Late in-phase and quadrature correlator outputs are given by

$$I_E = A_0 R(\Delta\tau + d)\cos(\Delta\varphi) + \alpha A_0 R(\Delta\tau - \delta_M + d)\cos(\Delta\varphi - \theta_M) + w_{I,E} \quad (3.6a)$$

$$Q_E = A_0 R(\Delta\tau + d)\sin(\Delta\varphi) + \alpha A_0 R(\Delta\tau - \delta_M + d)\sin(\Delta\varphi - \theta_M) + w_{Q,E} \quad (3.6b)$$

$$I_L = A_0 R(\Delta\tau - d)\cos(\Delta\varphi) + \alpha A_0 R(\Delta\tau - \delta_M - d)\cos(\Delta\varphi - \theta_M) + w_{I,L} \quad (3.7a)$$

$$Q_L = A_0 R(\Delta\tau - d)\sin(\Delta\varphi) + \alpha A_0 R(\Delta\tau - \delta_M - d)\sin(\Delta\varphi - \theta_M) + w_{Q,L} \quad (3.7b)$$

where d is half the Early-Late correlator chip spacing ∂($d = \partial/2$, $0 < \partial \le 1$).

3.2.2 STL CARRIER AND CODE TRACKING ERROR MODELS

3.2.2.1 Coherent Early-minus-Late (EmL) DLL Discriminator

The in-phase and quadrature outputs of the coherent EmL delay locked loop (DLL) discriminator in the presence of a specular multipath are obtained by subtracting Equation (3.7) from Equation (3.6):

$$\begin{aligned} I_{EmL} = {} & A_0\left[R(\Delta\tau + d) - R(\Delta\tau - d)\right]\cos(\Delta\varphi) + \\ & \alpha A_0\left[R(\Delta\tau - \delta_M + d) - R(\Delta\tau - \delta_M - d)\right]\cos(\Delta\varphi - \theta_M) + w_{I,EmL} \end{aligned} \quad (3.8a)$$

$$\begin{aligned} Q_{EmL} = {} & A_0\left[R(\Delta\tau + d) - R(\Delta\tau - d)\right]\sin(\Delta\varphi) + \\ & \alpha A_0\left[R(\Delta\tau - \delta_M + d) - R(\Delta\tau - \delta_M - d)\right]\sin(\Delta\varphi - \theta_M) + w_{Q,EmL} \end{aligned} \quad (3.8b)$$

The task of the tracking loops (phase locked loop: PLL and DLL) is to maintain both phase and code lock on the incoming signal. Phase and code lock are achieved respectively when

$$Q_P = 0 \quad (3.9a)$$

$$I_{EmL} = 0 \quad (3.9b)$$

Equation (3.9a) means that the quadrature arm of the prompt correlator produces a correlation of zero in average, which means that all the energy is in the in-phase arm. Equation (3.9b) means that the correlations in the Early and Late correlators are equal, which implies that the prompt code is aligned with the incoming signal code.

In the absence of multipath, the solution to Equations (3.9a) and (3.9b) is $\Delta\varphi = 0$ and $\Delta\tau$=0 meaning that the estimated carrier replica phase is equal to the LOS carrier phase and the estimated code replica delay is equal to the LOS code delay. This

situation represents errorless phase and code tracking. In the presence of multipath, the locking conditions are still defined by Equations (3.9a) and (3.9b) but the solution to the equations is no longer $\Delta\varphi = 0$ and $\Delta\tau$=0. The loops are no longer tracking the LOS signal but rather a combination of the LOS and reflected signals. Neglecting the correlation noise in Equation (3.5b), phase lock is achieved when

$$A_0 R(\Delta\tau)\sin(\Delta\varphi) + \alpha A_0 R(\Delta\tau - \delta_M)\sin(\Delta\varphi - \theta_M) = 0$$

Algebraic and trigonometric manipulations of the equation above yields that in the presence of a specular multipath, phase lock is achieved with the following phase tracking error [20]:

$$\begin{aligned} \Delta\varphi &= \arctan\left[\frac{\alpha R(\Delta\tau - \delta_M)\sin\theta_M}{R(\Delta\tau) + \alpha R(\Delta\tau - \delta_M)\cos\theta_M}\right], \\ \Delta\varphi &= \arctan\left[\frac{\alpha\beta\sin\theta_M}{1 + \alpha\beta\cos\theta_M}\right], \end{aligned} \tag{3.10}$$

where $\beta = R(\Delta\tau - \delta_M)/R(\Delta\tau)$. Similarly, from Eq. (3.8a), code lock in the presence of multipath is achieved when $I_{EmL} = 0$, meaning when

$$[R(\Delta\tau + d) - R(\Delta\tau - d)]\cos(\Delta\varphi) = -\alpha[R(\Delta\tau - \delta_M + d) - R(\Delta\tau - \delta_M - d)]\cos(\Delta\varphi - \theta_M) \tag{3.11}$$

If the discriminator is considered to be operating within its linear range (i.e. $|\Delta\tau| \le d$), substituting Equations (3.3) and (3.10) into Equation (3.11), with $\partial = 2d \le 1$, the code delay tracking error $\Delta\tau$ in the presence of a specular multipath can be estimated by [30] [31]:

$$\Delta\tau_{EmL} = \begin{cases} \dfrac{\alpha[\alpha\beta + \cos\theta_M]\delta_M}{\alpha[\alpha\beta + \cos\theta_M] + [1 + \alpha\beta\cos\theta_M]}, \text{ for} \\ 0 \le \delta_M < \dfrac{\left[1 + 2\alpha\cos\theta_M + \alpha^2\right]\partial}{2[1 + \alpha\cos\theta_M]}. \\ \dfrac{\alpha[\alpha\beta + \cos\theta_M]\partial}{2[1 + \alpha\beta\cos\theta_M]}, \text{ for } \dfrac{\left[1 + 2\alpha\cos\theta_M + \alpha^2\right]\partial}{2[1 + \alpha\cos\theta_M]} \le \\ \delta_M < 1 - \dfrac{\left[1 - \alpha^2\right]\partial}{2[1 + \alpha\cos\theta_M]}. \\ \dfrac{\alpha[\alpha\beta + \cos\theta_M](1 + d - \delta_M)}{2[1 + \alpha\beta\cos\theta_M] - \alpha[\alpha\beta + \cos\theta_M]}, \text{ for} \\ 1 - \dfrac{\left[1 - \alpha^2\right]\partial}{2[1 + \alpha\cos\theta_M]} \le \delta_M < 1 + d. \\ 0, \text{ for } \delta_M \ge 1 + d. \end{cases} \tag{3.12}$$

Equations (3.10) and (3.11) show that the phase tracking error $\Delta\varphi$ is dependent on the code tracking error $\Delta\tau$ and vice-versa. Equation (3.12) is an implicit expression

because $\beta = R(\Delta\tau_{EmL} - \delta_M)/R(\Delta\tau_{EmL})$. Therefore, $\Delta\tau_{EmL}$ and the corresponding $\Delta\varphi$ are computed iteratively. Figures 3.2 and 3.3 illustrate respectively the carrier phase tracking error and code delay tracking error with respect to the delay δ_M between the multipath and the LOS signal. The ideal autocorrelation function is used with a correlator chip spacing ∂=1(top); $\partial = 0.1$(bottom); and normalized LOS signal amplitude $A_0 = 1$; $\alpha = 0.5$. Also, the following holds $\theta_M = 2\pi f_{L1}\delta_M / R_C$ (where the nominal *L1* frequency $f_{L1} = 1575.42$ MHz and the code chip rate $R_C = 1.023$ Mchips/s).

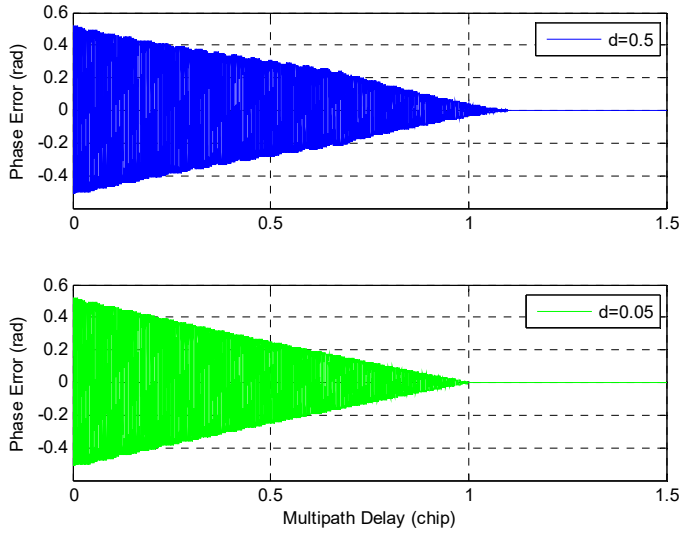

Figure 3.2: Carrier phase tracking error vs. Multipath delay (DLL and PLL in lock). Top: standard correlator, Bottom: narrow correlator.

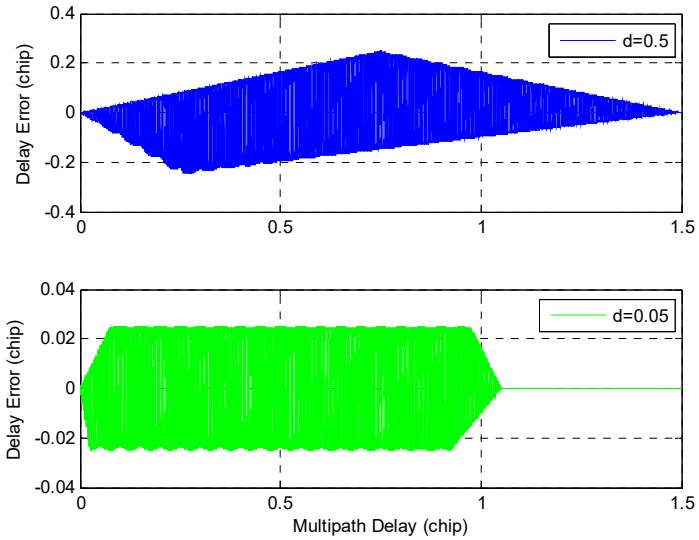

Figure 3.3: Code delay tracking error vs. Multipath delay (EmL, DLL and PLL in lock). Top: standard correlator, Bottom: narrow correlator.

Figures 3.4 and 3.5 show the amplitudes of I_{EmL} and Q_{EmL} in the presence of the same multipath for ∂=1 and $\partial = 0.1$.

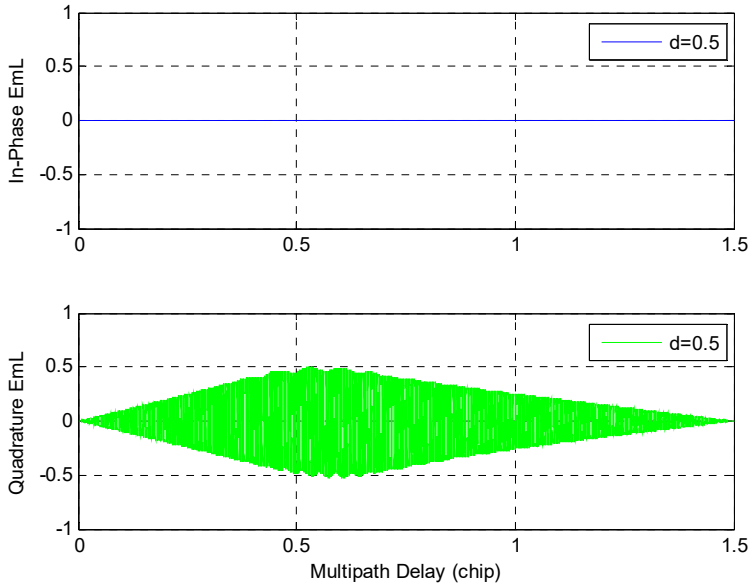

Figure 3.4: I_{EmL} and Q_{EmL} amplitudes vs. Multipath delay (DLL and PLL in lock), standard correlator.

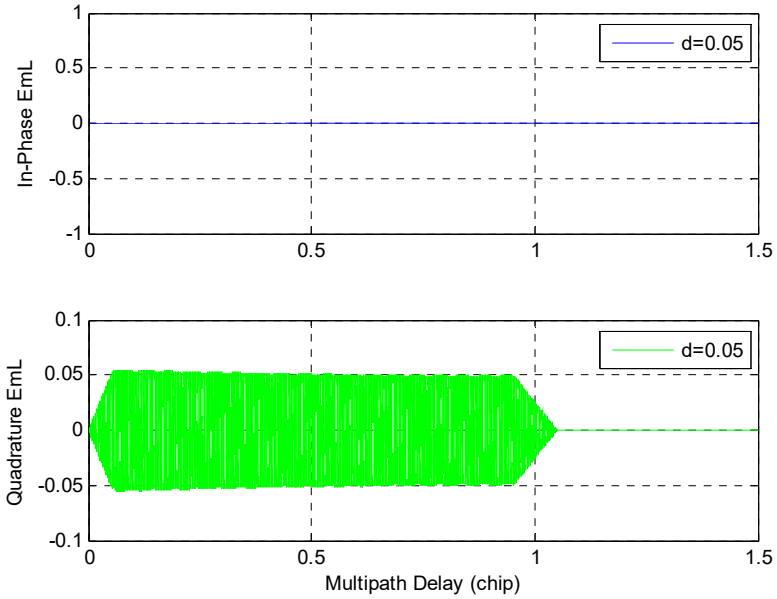

Figure 3.5: I_{EmL} and Q_{EmL} amplitudes vs. Multipath delay (DLL and PLL in lock), narrow correlator.

3.2.2.2 *Non-Coherent Early-minus-Late Power (EmLP) DLL Discriminator*

The EmLP DLL discriminator output in the presence of multipath is

$$EmLP = {I_E}^2 + {Q_E}^2 - {I_L}^2 - {Q_L}^2,$$

$$\begin{aligned} EmLP = {A_0}^2\left[R^2(\Delta\tau + d) - R^2(\Delta\tau - d)\right] + \alpha^2 {A_0}^2\left[R^2(\Delta\tau - \delta_M + d) - R^2(\Delta\tau - \delta_M - d)\right] \\ + 2\alpha {A_0}^2\begin{bmatrix} R(\Delta\tau + d)R(\Delta\tau - \delta_M + d) - \\ R(\Delta\tau - d)R(\Delta\tau - \delta_M - d) \end{bmatrix}\cos\theta_M \end{aligned} \quad (3.13)$$

The EmLP discriminator is capable of overcoming the effect of residual phase error. In fact, it can be observed from Equation (3.13) that code delay tracking error is not affected by the carrier phase tracking error $\Delta\varphi$ or the parameter β. Code lock is achieved when $EmLP = 0$ and phase lock is obtained when $Q_P = 0$. The phase tracking error $\Delta\varphi$ is still defined by Equation (3.10). Again, considering that the discriminator is in its linear range, substituting Equation (3.3) into Equation (3.13) and setting $EmLP = 0$ yields the following code tracking error, which is an explicit expression [30] [31]:

$$\Delta\tau_{EmLP} = \begin{cases} \dfrac{\alpha[\alpha + \cos\theta_M]\delta_M}{1 + 2\alpha\cos\theta_M + \alpha^2}, \text{ for} \\ 0 \le \delta_M < \dfrac{\left[1 + 2\alpha\cos\theta_M + \alpha^2\right]\partial}{2[1 + \alpha\cos\theta_M]}. \\ \dfrac{\left\{\begin{bmatrix}\left[\alpha\cos\theta_M(1-\delta_M) - \alpha^2 d + 1 - d\right]^2 + \\ 2\alpha^2\partial\cos\theta_M\left[\cos\theta_M(1-d) + \alpha(1-\delta_M)\right]\end{bmatrix}^{1/2}\right\}}{-\left[\alpha\cos\theta_M(1-\delta_M) - \alpha^2 d + 1 - d\right]}, \text{ for} \\ 2\alpha\cos\theta_M \\ \dfrac{\left[1 + 2\alpha\cos\theta_M + \alpha^2\right]\partial}{2[1 + \alpha\cos\theta_M]} \le \delta_M < \dfrac{(1 + \alpha\partial\cos\theta_M)(2 - \partial) - \partial\left(1 - d - \alpha^2 d\right)}{\alpha\partial\cos\theta_M + 2 - \partial}. \\ \dfrac{\left\{\begin{bmatrix}\alpha^2{\delta_M}^2\cos^2\theta_M + 2\alpha(2-\partial)(\alpha - \cos\theta_M)\delta_M \\ + 4\alpha^2(\partial^2/4 - \sin^2\theta_M) - 4\alpha^2\delta_M\cos^2\theta_M + \\ (2-\partial)(2 - \partial + 2\alpha\partial\cos\theta_M)\end{bmatrix}^{1/2}\right\}}{+\left(\alpha\cos\theta_M - \alpha^2\right)\delta_M + \alpha^2(1+d) - \alpha\partial\cos\theta_M - 2 + \partial}, \text{ for} \\ 2\alpha\cos\theta_M - \alpha^2 \\ \dfrac{(1 + \alpha\partial\cos\theta_M)(2 - \partial) - \partial\left(1 - d - \alpha^2 d\right)}{\alpha\partial\cos\theta_M + 2 - \partial} \le \delta_M < 1 + d. \\ 0, \text{ for } \delta_M \ge 1 + d. \end{cases} \quad (3.14)$$

The coherent EmL (C-EmL) and non-coherent EmLP (NC-EmLP) discriminators have the same delay tracking error envelopes. In fact, by superimposing the EmL error curves on the EmLP curves, the observed results are exactly as in Figure 3.3. However, the errors within the envelopes are different as indicated by Equations (3.12) and (3.14). Figure 3.6 on the other hand shows that the code tracking architecture definitely influences the phase tracking performance. The NC-EmLP DLL discriminator will result in higher phase tracking error than the C-EmL for a chip spacing ∂=1. The narrow correlator overcomes this shortcoming meaning the NC-EmLP has the same phase error envelope as the C-EmL (see Figure 3.2) for ∂=0.1.

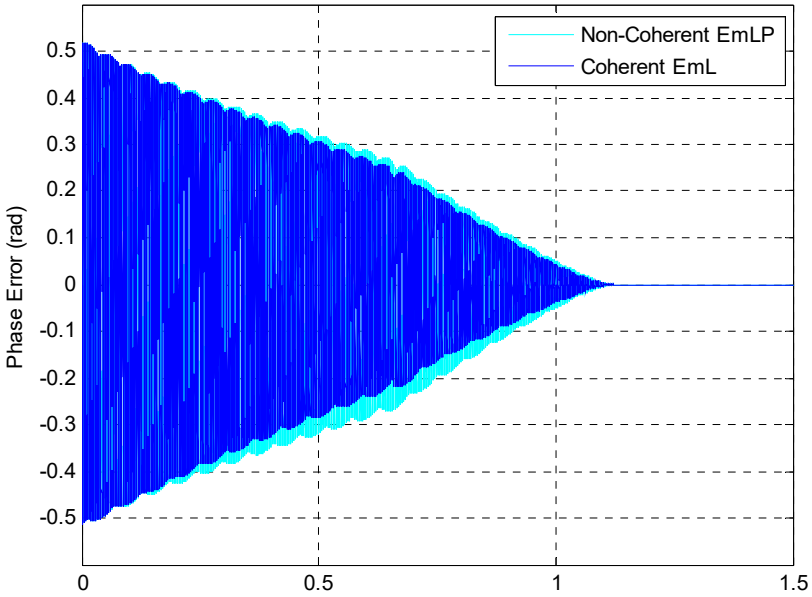

Figure 3.6: Carrier phase tracking error vs. Multipath delay (NC-EmLP and C-EmL, DLL and PLL in lock).

All the illustrated figures so far do not show the oscillatory nature of the errors within the envelopes because there are thousands of oscillations per C/A code chip. If for instance in Figures 3.2 and 3.3 the number of oscillations is reduced and instead of 1575 cycles per C/A code chip for L1, 25 cycles per C/A code chip are considered, the resulting tracking errors are as in Figures 3.7 and 3.8. The reduction of the number of cycles per chip during an analysis is helpful in order to be able to determine the values of multipath delay that induce maximal or minimal code and carrier tracking errors.

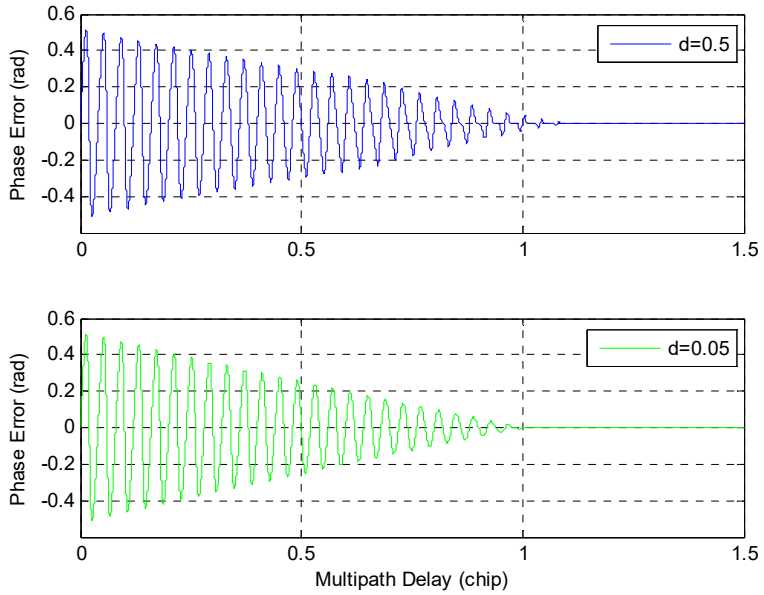

Figure 3.7: Carrier phase tracking error vs. Multipath delay (reduced oscillations). Top: standard correlator, Bottom: narrow correlator.

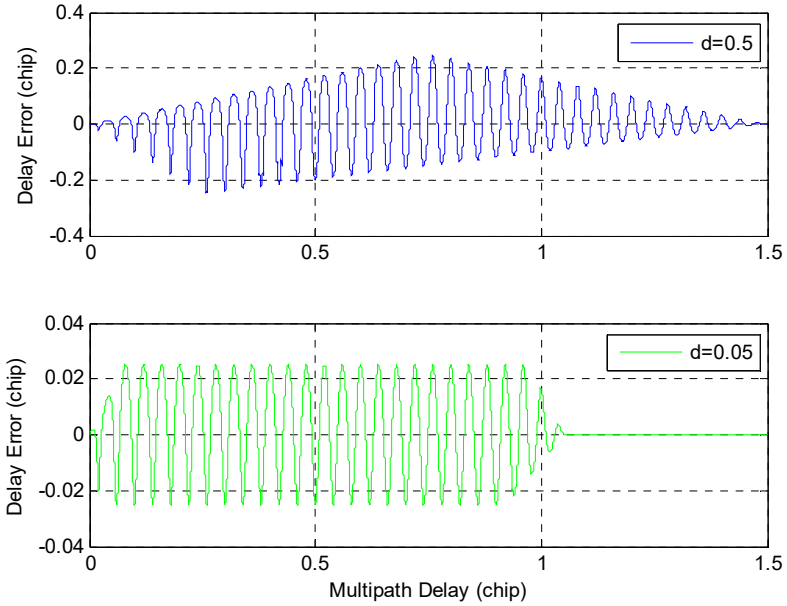

Figure 3.8: Code delay tracking error vs. Multipath delay (reduced oscillations). Top: standard correlator, Bottom: narrow correlator.

3.2.2.3 *Non-Coherent DOT Product DLL Discriminator*

The non-coherent DOT Product DLL discriminator output in the presence of multipath is described by $DOT = I_{EmL} I_P + Q_{EmL} Q_P = (I_E - I_L) I_P + (Q_E - Q_L) Q_P$, meaning that:

$$\begin{aligned} DOT = {} & A_0{}^2 \left[R(\Delta\tau + d) - R(\Delta\tau - d)\right] R(\Delta\tau) + \\ & \alpha A_0{}^2 \left\{ \begin{array}{l} \left[R(\Delta\tau + d) - R(\Delta\tau - d)\right] R(\Delta\tau - \delta_M) + \\ \left[R(\Delta\tau - \delta_M + d) - R(\Delta\tau - \delta_M - d)\right] R(\Delta\tau) \end{array} \right\} \cos\theta_M \\ & + \alpha^2 A_0{}^2 \left[R(\Delta\tau - \delta_M + d) - R(\Delta\tau - \delta_M - d)\right] R(\Delta\tau - \delta_M). \end{aligned} \tag{3.15}$$

Code lock is realized when $DOT = 0$ and phase lock is still achieved when $Q_P = 0$. Letting $DOT = 0$ yields:

$$\begin{aligned} & A_0{}^2 \left[R(\Delta\tau + d) - R(\Delta\tau - d)\right] + \\ & \alpha A_0{}^2 \left\{ \begin{array}{l} \left[R(\Delta\tau + d) - R(\Delta\tau - d)\right] \beta + \\ \left[R(\Delta\tau - \delta_M + d) - R(\Delta\tau - \delta_M - d)\right] \end{array} \right\} \cos\theta_M + \\ & \alpha^2 A_0{}^2 \beta \left[R(\Delta\tau - \delta_M + d) - R(\Delta\tau - \delta_M - d)\right] = 0 \end{aligned} \tag{3.16}$$

with $\beta = R(\Delta\tau - \delta_M) / R(\Delta\tau)$.

Solving for $\Delta\tau$ in Equation (3.16) for a discriminator in its linear range yields the same equation as Equation (3.12) meaning that the coherent EmL and non-coherent DOT product DLL discriminators have the same implicit expression for their code delay errors although Equation (3.16) is not affected by $\Delta\varphi$. An explicit expression for $\Delta\tau_{DOT}$ was derived in [31].

Now that the code delay tracking errors associated with different types of code discriminators have been analysed, it is important to understand the relationship that exist between the code tracking errors and the positioning errors, more specifically the pseudorange errors, on a theoretical point of view. The pseudorange measurement error corresponding to a multipath induced code delay tracking error $\Delta\tau$ is [33] [34]:

$$\Delta\rho = -\frac{c}{R_C} \Delta\tau \tag{3.17}$$

where R_C is the code chip rate and c is the speed of light.

3.2.3 VTL CARRIER AND CODE TRACKING ERROR MODELS

3.2.3.1 PLL Phase Tracking Error for Errorless VDLL

With a vector delay locked loop (VDLL) scheme, the vector tracking is performed for the code delay while scalar tracking is maintained for the carrier phase. It can be noted that even a vector delay frequency locked loop (VDFLL) scheme where code delay and carrier frequency are in vector tracking mode, the scalar tracking of the carrier phase by a PLL can still be conjointly performed to aid in the piloting of the carrier NCOs. With such vector tracking schemes, the steady-state delay tracking error can be assumed to be almost zero ($\Delta\tau \approx 0$) if one presumes that there are sufficient healthy satellites such that the navigator can correctly estimate the receiver position and velocity. This navigation solution allows the precise estimation of the code chip rate of each tracking channel and consequently a proper piloting of the DLL NCOs. If the PLL that is conjointly working with the VDLL or VDFLL does not receive any feedback from the navigation estimator, phase lock is still obtained when the correlation in the quadrature arm of the Prompt correlator is zero ($Q_P = 0$).

In the absence of multipath, vector code lock and scalar phase lock are obtained when $\Delta\tau = 0$ and $\Delta\varphi = 0$. In the presence of multipath, with a locked VDLL ($\Delta\tau \approx 0$), phase lock is achieved when

$$\sin(\Delta\varphi)\left[1 + \alpha R(-\delta_M)\cos\theta_M\right] = \alpha R(-\delta_M)\cos\Delta\varphi\sin\theta_M .$$

The corresponding phase tracking error is given by

$$\Delta\varphi = \arctan\left[\frac{\alpha R(-\delta_M)\sin\theta_M}{1 + \alpha R(-\delta_M)\cos\theta_M}\right] \tag{3.18}$$

When $\Delta\tau \approx 0$, $R(\Delta\tau + d) - R(\Delta\tau - d) \approx 0$ as well. The coherent EmL discriminator outputs in this case are expressed as

$$I_{EmL} = \alpha A_0\left[R(-\delta_M + d) - R(-\delta_M - d)\right]\cos(\Delta\varphi - \theta_M) + w_{I,EmL} \tag{3.19a}$$

$$Q_{EmL} = \alpha A_0\left[R(-\delta_M + d) - R(-\delta_M - d)\right]\sin(\Delta\varphi - \theta_M) + w_{Q,EmL} \tag{3.19b}$$

Equations (3.19a) and (3.19.b) show that, for a VTL (VDLL or VDFLL), when $\Delta\tau \approx 0$, the LOS signal contribution to the discriminator output signal power is negligible whereas the multipath contribution is very significant.

Figure 3.9 illustrates the multipath induced phase tracking error for a PLL and VDLL in lock with an errorless VDLL ($\Delta\tau \approx 0$).

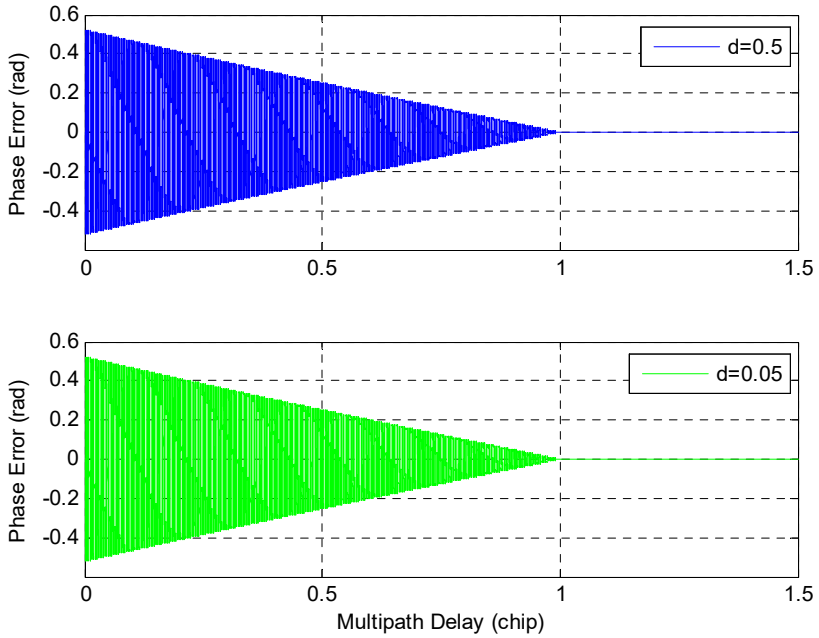

Figure 3.9: Carrier phase tracking error vs. Multipath delay (PLL and VDLL in lock). Top: standard correlator, Bottom: narrow correlator.

Figure 3.10 shows the amplitudes of I_{EmL} , Q_{EmL} and $|EmL| = \sqrt{I_{EmL}{}^2 + Q_{EmL}{}^2}$ in the presence of a multipath ($d = \partial/2 = 0.5$ chip; $A_0 = 1$; $\alpha = 0.5$; $\theta_M = 2\pi f_{L1}\delta_M / R_C$) for a VDLL. Figure 3.11 depicts the same curves for $d = \partial/2 = 0.05$.

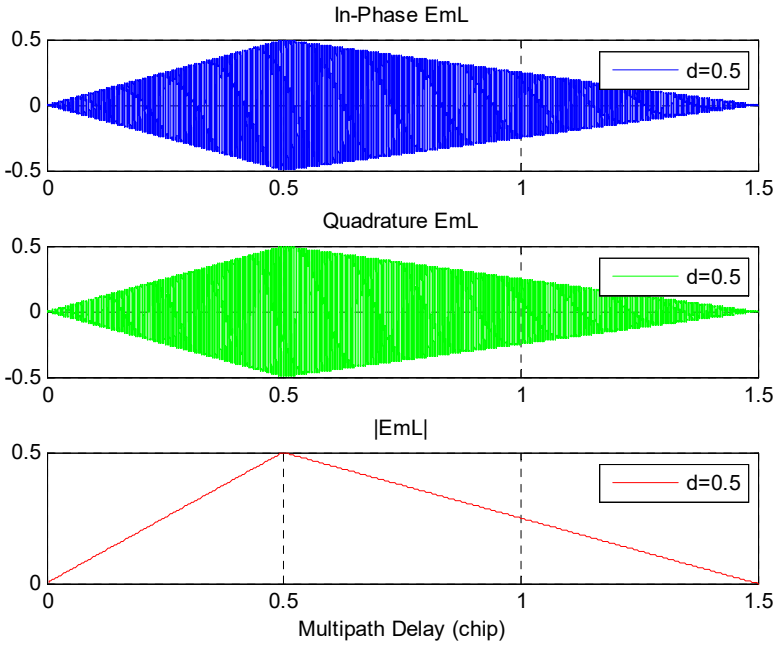

Figure 3.10: I_{EmL}, Q_{EmL}, and $|EmL|$ amplitudes vs. Multipath delay (VDLL in lock), standard correlator.

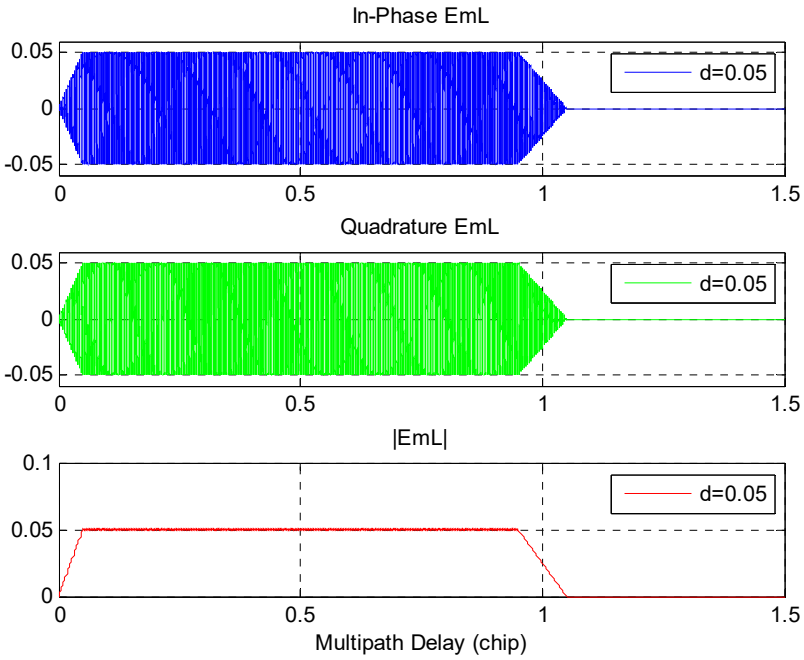

Figure 3.11: I_{EmL}, Q_{EmL}, and $|EmL|$ amplitudes vs. Multipath delay (VDLL in lock), narrow correlator.

3.2.3.2 *Code and Carrier Tracking Errors for a VDFLL*

If an errorless VDLL is no longer assumed, it is better to analyse the code and carrier tracking errors of the VDFLL at two stages, an initial stage and a steady-state stage. An extended Kalman filter (EKF)-based VDFLL that uses code and frequency discriminator outputs as measurements is taken as example. Once the scalar delay frequency locked loop (SDFLL) is locked and the initial position-velocity-time (PVT) solution is calculated, the receiver can switch to VDFLL and use the steady-state SDFLL measurement errors as its initial VDFLL measurement errors. When the tracking loop enters VDFLL mode, both code and carrier tracking errors get smaller and smaller and gradually approach their steady-state values. From the point of view of one multipath contaminated tracking channel working with other healthy channels, the tracking errors obtained from the SDFLL measurements therefore constitute the maximum VDFLL tracking errors.

- **Initial VDFLL Carrier Frequency Tracking Error**

The frequency tracking error that is derived and analysed in this section corresponds to the steady-state frequency tracking error of a scalar frequency locked loop (FLL). The arctangent frequency discriminator generates an estimated Doppler deviation between the received signal and the replica signal using the following expression [35] [36]:

$$Discr(\Delta f) = \frac{\arctan(CROSS / DOT)}{2\pi(t_2 - t_1)} \tag{3.20}$$

where: $\begin{aligned} DOT &= I_{P1} \times I_{P2} + Q_{P1} \times Q_{P2} \\ CROSS &= I_{P1} \times Q_{P2} - I_{P2} \times Q_{P1} \end{aligned}$.

In the absence of multipath, the following Prompt correlator outputs are defined between two Integrate and Dump instants t_1 and t_2 ignoring post-correlation noise:

$$I_{P1} = A_0 R(\Delta\tau)\cos(\Delta\varphi_1) \tag{3.21a}$$

$$I_{P2} = A_0 R(\Delta\tau)\cos(\Delta\varphi_2) \tag{3.21b}$$

$$Q_{P1} = A_0 R(\Delta\tau)\sin(\Delta\varphi_1) \tag{3.21c}$$

$$Q_{P2} = A_0 R(\Delta\tau)\sin(\Delta\varphi_2) \tag{3.21d}$$

The FLL is in lock when the Doppler deviation $Discr(\Delta f) = 0$. Substituting Equations (3.21) into *DOT* and *CROSS* expressions, the ratio *CROSS/DOT* can be expressed as

$$CROSS / DOT = \frac{\sin(\Delta\varphi_2 - \Delta\varphi_1)}{\cos(\Delta\varphi_2 - \Delta\varphi_1)} = \tan(\Delta\varphi_2 - \Delta\varphi_1).$$

Let $\Delta\varphi_2 - \Delta\varphi_1 = 2\pi\Delta f_D T$, where $T = t_2 - t_1$ and Δf_D is the Doppler frequency residual of the LOS signal or the Doppler frequency error between LOS and replica signals.

$$Discr(\Delta f) = 0 \text{ when } \frac{\arctan\left[\tan(2\pi\Delta f_D T)\right]}{2\pi(t_2 - t_1)} = 0, \text{ i.e. } \Delta f_D = 0.$$

In the presence of multipath, the locking conditions remain the same but they induce a different frequency residual. The slope of the curve representing the frequency discriminator operation in its linear range is not 1 anymore. This induces error in the carrier frequency tracking. If the multipath fading effect is considered, the following Prompt correlator outputs are defined between two Integrate and Dump instants t_1 and t_2 ignoring post-correlation noise:

$$I_{P1} = A_0 R(\Delta\tau)\cos(\Delta\varphi_1) + \alpha A_0 R(\Delta\tau - \delta_M)\cos(\Delta\tilde{\varphi}_1 - \theta_M) \tag{3.22a}$$

$$I_{P2} = A_0 R(\Delta\tau)\cos(\Delta\varphi_2) + \alpha A_0 R(\Delta\tau - \delta_M)\cos(\Delta\tilde{\varphi}_2 - \theta_M) \tag{3.22b}$$

$$Q_{P1} = A_0 R(\Delta\tau)\sin(\Delta\varphi_1) + \alpha A_0 R(\Delta\tau - \delta_M)\sin(\Delta\tilde{\varphi}_1 - \theta_M) \tag{3.22c}$$

$$Q_{P2} = A_0 R(\Delta\tau)\sin(\Delta\varphi_2) + \alpha A_0 R(\Delta\tau - \delta_M)\sin(\Delta\tilde{\varphi}_2 - \theta_M) \tag{3.22d}$$

where $\alpha = A_M / A_0$, $\Delta\tilde{\varphi}_1$ and $\Delta\tilde{\varphi}_2$ are affected by a fading frequency component $f_F = \frac{d((\varphi_M)}{dt} \Big/ 2\pi$ due to multipath. Substitution of Equations (3.22) into *DOT* and *CROSS* expressions yields the following equations after trigonometric manipulations:

$$\begin{aligned} DOT &= A_0{}^2 R^2(\Delta\tau)\cos(\Delta\varphi_2 - \Delta\varphi_1) + \alpha^2 A_0{}^2 R^2(\Delta\tau - \delta_M)\cos(\Delta\tilde{\varphi}_2 - \Delta\tilde{\varphi}_1) \\ &+ \alpha A_0{}^2 R(\Delta\tau)R(\Delta\tau - \delta_M)\left[\cos(\Delta\tilde{\varphi}_2 - \Delta\varphi_1)\cos\theta_M + \sin(\Delta\tilde{\varphi}_2 - \Delta\varphi_1)\sin\theta_M\right] \\ &+ \alpha A_0{}^2 R(\Delta\tau)R(\Delta\tau - \delta_M)\left[\cos(\Delta\varphi_2 - \Delta\tilde{\varphi}_1)\cos\theta_M - \sin(\Delta\varphi_2 - \Delta\tilde{\varphi}_1)\sin\theta_M\right] \end{aligned} \tag{3.23a}$$

$$\begin{aligned} CROSS &= A_0{}^2 R^2(\Delta\tau)\sin(\Delta\varphi_2 - \Delta\varphi_1) + \alpha^2 A_0{}^2 R^2(\Delta\tau - \delta_M)\sin(\Delta\tilde{\varphi}_2 - \Delta\tilde{\varphi}_1) \\ &+ \alpha A_0{}^2 R(\Delta\tau)R(\Delta\tau - \delta_M)\left[\sin(\Delta\tilde{\varphi}_2 - \Delta\varphi_1)\cos\theta_M - \cos(\Delta\tilde{\varphi}_2 - \Delta\varphi_1)\sin\theta_M\right] \\ &+ \alpha A_0{}^2 R(\Delta\tau)R(\Delta\tau - \delta_M)\left[\sin(\Delta\varphi_2 - \Delta\tilde{\varphi}_1)\cos\theta_M + \cos(\Delta\varphi_2 - \Delta\tilde{\varphi}_1)\sin\theta_M\right] \end{aligned} \tag{3.23b}$$

Let

$$\Delta\tilde{\varphi}_2 - \Delta\tilde{\varphi}_1 = 2\pi\Delta\tilde{f}_D T \tag{3.24a}$$

$$\Delta\tilde{f}_D = \Delta f_D + f_F \tag{3.24b}$$

$$\Delta\tilde{\varphi}_2 - \Delta\varphi_1 = \Delta\varphi_2 - \Delta\tilde{\varphi}_1 = 2\pi\frac{\Delta f_D + \Delta\tilde{f}_D}{2}T = \pi(\Delta f_D + \Delta\tilde{f}_D)T \tag{3.24c}$$

$$\alpha = \frac{A_M}{A_0} = \frac{\sqrt{2T(C/N_0)_M \sin c^2[\pi(\Delta f_D + f_F)T]}}{\sqrt{2T(C/N_0)\sin c^2(\pi\Delta f_D T)}} = \sqrt{\gamma}\frac{\sin c(\pi\Delta\tilde{f}_D T)}{\sin c(\pi\Delta f_D T)} \tag{3.24d}$$

where $\gamma = M / D$ $(0 < \gamma < 1)$ is the multipath to LOS (direct signal) power ratio, $\Delta\tilde{f}_D$ is the Doppler frequency residual of the multipath signal or the Doppler frequency error between multipath and replica signals, and f_F is the fading frequency due to multipath. Equations (3.23a) and (3.23b) therefore become

$$\begin{aligned} DOT &= A_0{}^2 R^2(\Delta\tau)\cos(2\pi\Delta f_D T) + \alpha^2 A_0{}^2 R^2(\Delta\tau - \delta_M)\cos(2\pi\Delta\tilde{f}_D T) \\ &+ 2\alpha A_0{}^2 R(\Delta\tau)R(\Delta\tau - \delta_M)\cos\left[\pi(\Delta f_D + \Delta\tilde{f}_D)T\right]\cos\theta_M \end{aligned} \tag{3.25a}$$

$$\begin{aligned} CROSS &= A_0{}^2 R^2(\Delta\tau)\sin(2\pi\Delta f_D T) + \alpha^2 A_0{}^2 R^2(\Delta\tau - \delta_M)\sin(2\pi\Delta\tilde{f}_D T) \\ &+ 2\alpha A_0{}^2 R(\Delta\tau)R(\Delta\tau - \delta_M)\sin\left[\pi(\Delta f_D + \Delta\tilde{f}_D)T\right]\cos\theta_M \end{aligned} \tag{3.25b}$$

In the presence of multipath, the FLL is in lock still when the discriminator output is zero, meaning when $Discr(\Delta f) = 0$.

Let $X = CROSS/DOT$. Therefore,

$$X = \frac{\sin(2\pi\Delta f_D T) + \alpha^2\beta^2 \sin(2\pi\Delta\tilde{f}_D T) + 2\alpha\beta \sin\left[\pi(\Delta f_D + \Delta\tilde{f}_D)T\right]\cos\theta_M}{\cos(2\pi\Delta f_D T) + \alpha^2\beta^2 \cos(2\pi\Delta\tilde{f}_D T) + 2\alpha\beta \cos\left[\pi(\Delta f_D + \Delta\tilde{f}_D)T\right]\cos\theta_M}$$

$$X = \frac{\sin(2\pi\Delta f_D T) + \alpha^2\beta^2 \sin\left[2\pi(\Delta f_D + f_F)T\right] + 2\alpha\beta \sin\left[\pi(2\Delta f_D + f_F)T\right]\cos\theta_M}{\cos(2\pi\Delta f_D T) + \alpha^2\beta^2 \cos\left[2\pi(\Delta f_D + f_F)T\right] + 2\alpha\beta \cos\left[\pi(2\Delta f_D + f_F)T\right]\cos\theta_M}$$

$$X = \frac{\begin{bmatrix}\tan(2\pi\Delta f_D T) + \alpha^2\beta^2 \tan(2\pi\Delta f_D T)\cos(2\pi f_F T) + \alpha^2\beta^2 \sin(2\pi f_F T) \\ + 2\alpha\beta \tan(2\pi\Delta f_D T)\cos(\pi f_F T)\cos\theta_M + 2\alpha\beta \sin(\pi f_F T)\cos\theta_M\end{bmatrix}}{\begin{bmatrix}1 + \alpha^2\beta^2 \cos(2\pi f_F T) - \alpha^2\beta^2 \tan(2\pi\Delta f_D T)\sin(2\pi f_F T) \\ + 2\alpha\beta \cos(\pi f_F T)\cos\theta_M - 2\alpha\beta \tan(2\pi\Delta f_D T)\sin(\pi f_F T)\cos\theta_M\end{bmatrix}}$$

$$X = \frac{\tan(2\pi\Delta f_D T) + \dfrac{\alpha^2\beta^2 \sin(2\pi f_F T) + 2\alpha\beta \sin(\pi f_F T)\cos\theta_M}{1 + \alpha^2\beta^2 \cos(2\pi f_F T) + 2\alpha\beta \cos(\pi f_F T)\cos\theta_M}}{1 - \tan(2\pi\Delta f_D T)\dfrac{\alpha^2\beta^2 \sin(2\pi f_F T) + 2\alpha\beta \sin(\pi f_F T)\cos\theta_M}{1 + \alpha^2\beta^2 \cos(2\pi f_F T) + 2\alpha\beta \cos(\pi f_F T)\cos\theta_M}} \tag{3.26}$$

where $\beta = R(\Delta\tau - \delta_M)/R(\Delta\tau)$. Let $\tan\Omega = \dfrac{\alpha^2\beta^2 \sin(2\pi f_F T) + 2\alpha\beta \sin(\pi f_F T)\cos\theta_M}{1 + \alpha^2\beta^2 \cos(2\pi f_F T) + 2\alpha\beta \cos(\pi f_F T)\cos\theta_M}$ and Equation (3.26) subsequently becomes [33]

$$X = \frac{\tan(2\pi\Delta f_D T) + \tan\Omega}{1 - \tan(2\pi\Delta f_D T)\tan\Omega} = \tan(2\pi\Delta f_D T + \Omega) \tag{3.27}$$

With the expressions introduced in Equations (3.24) and the presence of $\beta = R(\Delta\tau - \delta_M)/R(\Delta\tau)$ in X, Equation (3.27) makes it possible to express the vector tracking errors with respect to multipath delay, multipath phase and multipath fading frequency. This is illustrated in the figures that follow hereafter, namely Figures 3.12 to 3.15. The VFLL is in lock when $X = 0$, meaning when $\tan(2\pi\Delta f_D T + \Omega) = 0$, i.e. when

$$2\pi\Delta f_D T + \Omega = 0 \tag{3.28}$$

The associated Doppler frequency error is no longer zero. It is given by

$$\Delta f_D = -\frac{\Omega}{2\pi T} \tag{3.29}$$

It can be observed from Equation (3.26) that the multipath induced frequency tracking error is affected by the parameter β meaning that the frequency tracking error is affected by the delay tracking error.

Figures 3.12 and 3.13 depict the frequency tracking error versus multipath delay for different values of multipath fading frequency. Around 500 Hz fading frequency, the error is maximal. The error is minimal as the fading frequency approaches 1 kHz as well as at frequencies very close to 0 Hz.

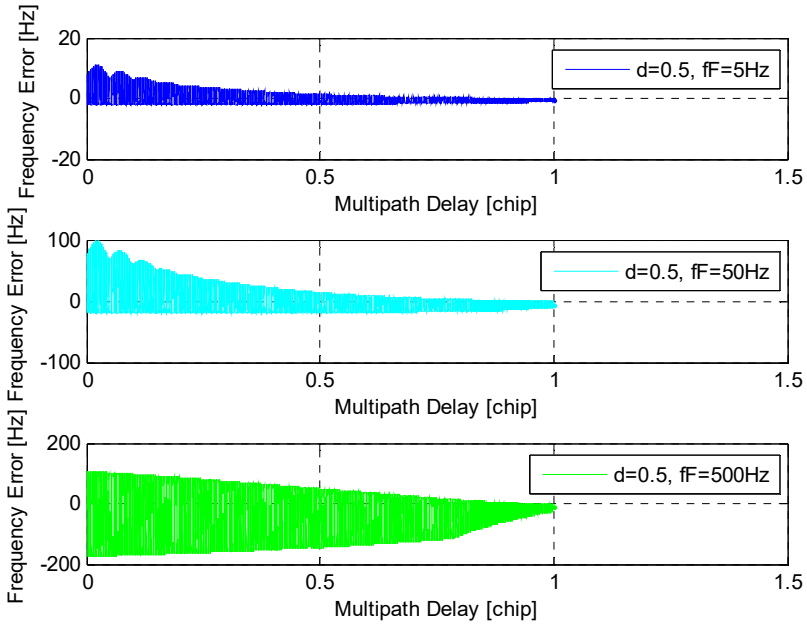

Figure 3.12: Frequency Tracking Error vs. Multipath delay for f_F = *5Hz; 50Hz; 500Hz*, standard correlator.

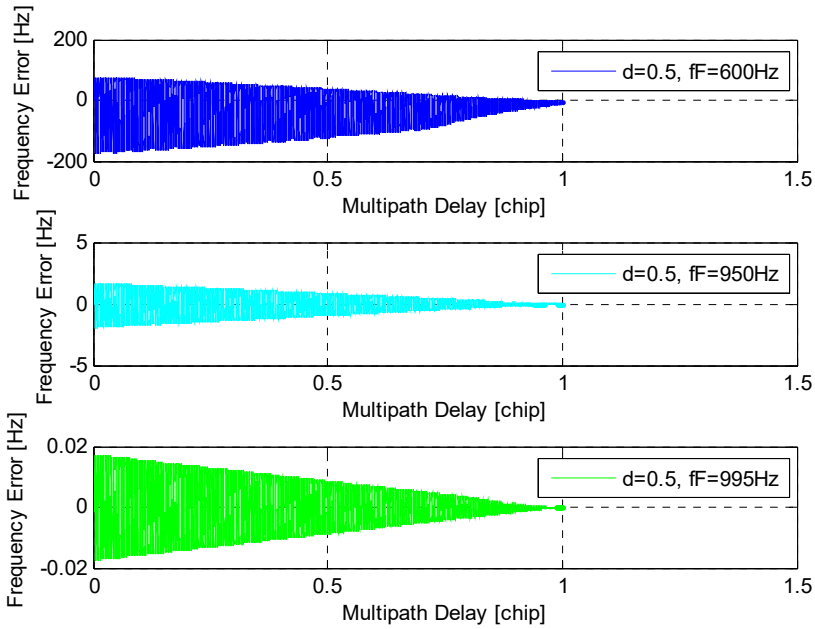

Figure 3.13: Frequency Tracking Error vs. Multipath delay for f_F = *600Hz; 950Hz; 995Hz*, standard correlator.

The pseudorange rate (velocity) measurement error associated with a multipath induced frequency tracking error Δf_D is given by [33] [36]

$$\Delta\dot{\rho} = -\frac{c}{f_L}\Delta f_D \tag{3.30}$$

where f_L is the nominal GPS L1, L2 or L5 carrier frequency.

- **Initial VDFLL Code Delay Tracking Error**

The VDFLL is often implemented with a normalised non-coherent EmL Envelope code discriminator as in Equation (3.31) or a normalized non-coherent EmL Power code discriminator as in Equation (3.32).

$$Discr(\Delta\tau) = \frac{\sum\sqrt{I_E{}^2 + Q_E{}^2} - \sum\sqrt{I_L{}^2 + Q_L{}^2}}{\sum\sqrt{I_E{}^2 + Q_E{}^2} + \sum\sqrt{I_L{}^2 + Q_L{}^2}} \tag{3.31}$$

$$Discr(\Delta\tau) = \frac{(I_E{}^2 + Q_E{}^2) - (I_L{}^2 + Q_L{}^2)}{(I_E{}^2 + Q_E{}^2) + (I_L{}^2 + Q_L{}^2)} \tag{3.32}$$

The DLL locking conditions and multipath induced delay tracking errors for the normalized non-coherent EmLP are the same as the un-normalized EmLP studied in section 3.2.2.2 except that the ratio $\alpha = A_M / A_0$ in Equation (3.14) is now affected by the multipath fading frequency and the frequency tracking error as can be observed in Equation (3.24d).

Figures 3.14 and 3.15 show the frequency and delay tracking errors of the VDFLL and the phase tracking error of the PLL that assists it. The non-coherent EmL Power code discriminator and the standard correlator chip spacing ($d = 0.5$) are used. The errors are displayed versus multipath delay and multipath fading frequency in Figure 3.14 and versus multipath phase and multipath fading frequency in Figure 3.15, with $\theta_M = 2\pi f_{L1}\delta_M / R_C$. The VDFLL is in its initial tracking state. So, theoretically and if the single aggregate specular multipath assumption holds, these errors are the maximum there can be for the given multipath delay, multipath phase, and multipath fading frequency values. The values of delay tracking errors displayed in terms of multipath phase in Figure 3.15 (c) are small because they are computed for multipath delay values very close to zero with the relationship $\theta_M = 2\pi f_{L1}\delta_M / R_C$ taken into account. They evolve in amplitude like in Figures 3.3 and 3.8 for increasing multipath delay values. However, as depicted in Figure 3.15 (c), maximal delay errors occur for multipath phase values of $\theta_M = 0^\circ + k360^\circ$ and $\theta_M = 180^\circ + k360^\circ$, with k being an integer.

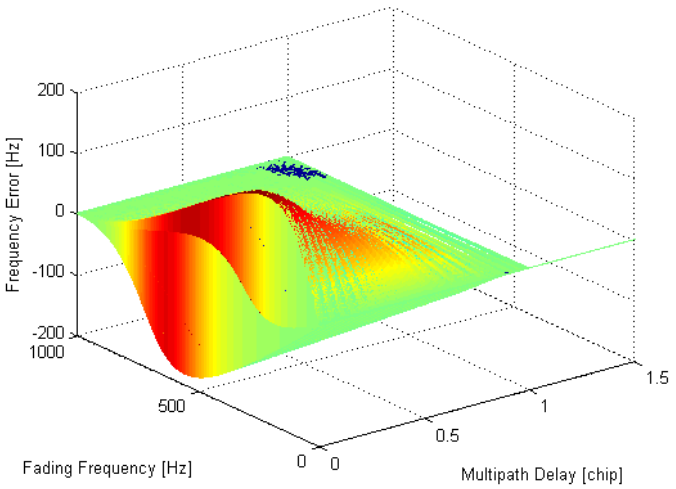

(a)

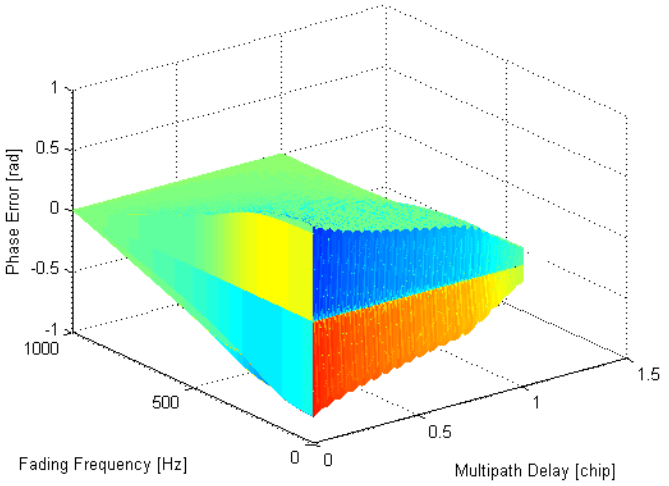

(b)

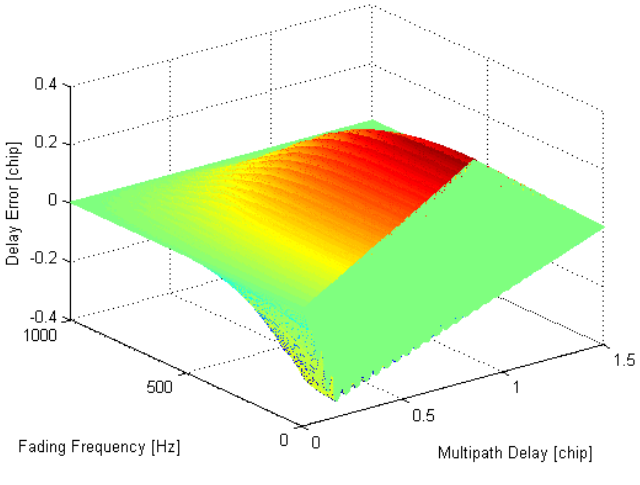

(c)

Figure 3.14: Frequency (a), Phase (b) and Delay (c) Tracking Errors vs. Multipath Delay and Multipath Fading Frequency

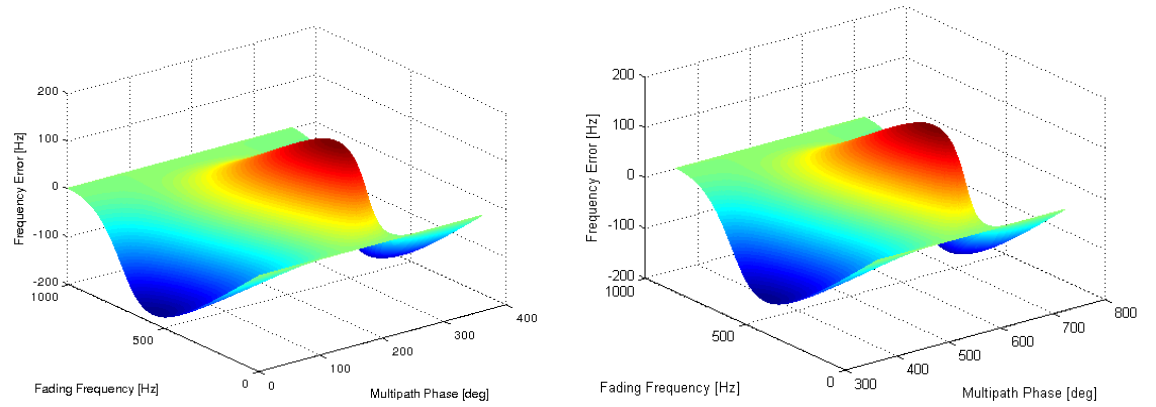

(a)

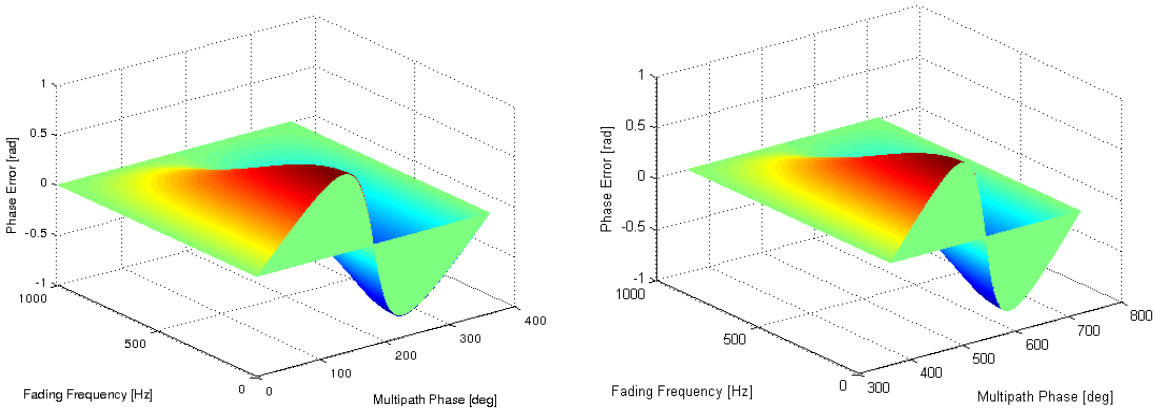

(b)

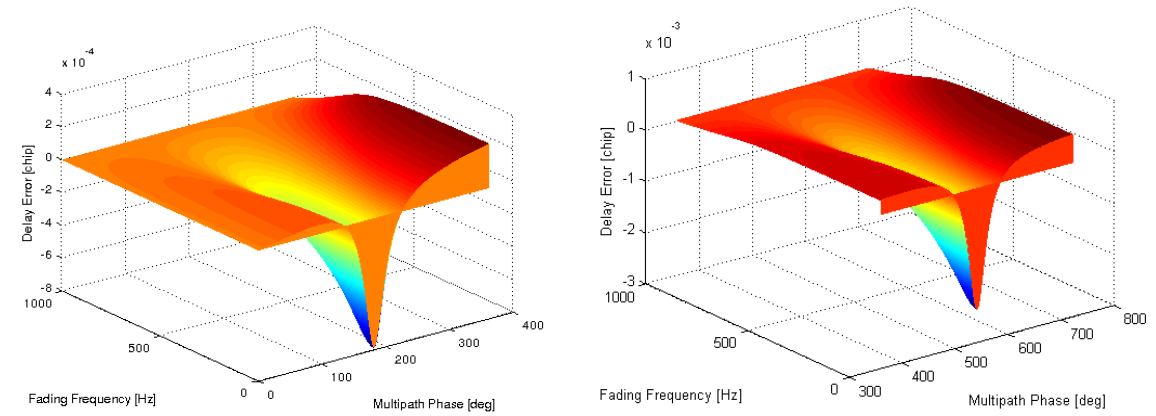

(c)

Figure 3.15: Frequency (a), Phase (b) and Delay (c) Tracking Errors vs. Multipath Phase and Multipath Fading Frequency

- **Steady-state VDFLL Code and Carrier Tracking Errors**

The steady-state code and carrier tracking errors of a VDFLL based on EKF are analysed. Let this VDFLL EKF's state vector be denoted as

$$X = \left[\delta x, \delta y, \delta z, \delta \dot{x}, \delta \dot{y}, \delta \dot{z}, \delta t, \delta \dot{t}\right]^T \tag{3.33}$$

where the vector's elements are the errors in estimating the receiver's position, velocity, clock bias and clock drift. Let the measurement vector be

$$Y = \left[\delta\rho_1, \delta\rho_2, ..., \delta\rho_N, \delta\dot{\rho}_1, \delta\dot{\rho}_2, ..., \delta\dot{\rho}_N\right]^T \tag{3.34}$$

Its elements are the code and frequency discriminators results for the N tracking channels. The system model is given by

$$\begin{aligned} X_k &= \Phi X_{k-1} + W_{k-1} \\ Y_k &= H_k X_k + V_k \end{aligned} \quad \textit{where}$$

$$\Phi = \begin{bmatrix} I_{3x3} & TI_{3x3} & 0_{3x2} \\ 0_{3x3} & I_{3x3} & 0_{3x2} \\ 0_{2x3} & 0_{2x3} & \begin{bmatrix} 1 & T \\ 0 & 1 \end{bmatrix} \end{bmatrix} \quad H = \begin{bmatrix} \hat{a}_1 & 0_{1x3} & -1 & 0 \\ \vdots & \vdots & \vdots & \vdots \\ \hat{a}_N & 0_{1x3} & -1 & 0 \\ 0_{1x3} & \hat{a}_1 & 0 & -1 \\ \vdots & \vdots & \vdots & \vdots \\ 0_{1x3} & \hat{a}_N & 0 & -1 \end{bmatrix} \tag{3.35}$$

T is the update interval, $\hat{a}_i = (s_i - \hat{r}) / \left\| s_i - \hat{r} \right\|$ is a unit vector pointing from the receiver estimated position to the i^{th} satellite; $\left\| s_i - \hat{r} \right\|$ is the estimated distance between the receiver and the i^{th} satellite; $s_i = (x_i, y_i, z_i)$ is the earth-centred earth-fixed (ECEF) coordinates of the i^{th} satellite; $\hat{r} = (\hat{x}_r, \hat{y}_r, \hat{z}_r)$ is the receiver's estimated ECEF coordinates; W_k is a vector of random noise inputs such that $E\{W_k\} = 0, E\left\{W_k W_j^T\right\} = Q_k \delta_{kj}$; V_k is a vector of additive measurement noise such that $E\{V_k\} = 0, E\left\{V_k V_j^T\right\} = R_k \delta_{kj}, E\left\{W_k V_j^T\right\} = 0; \delta_{kj} = 1$ if $k = j$, otherwise $\delta_{kj} = 0$. The EKF algorithm (see *Chapter 2, Algorithm 2.2*) is formulated as follows:

$$\left.\begin{aligned} \hat{X}_{k|k-1} &= \Phi \hat{X}_{k-1} \\ P_{k|k-1} &= \Phi P_{k-1} \Phi^T + Q_k \\ Y_{k|k-1} &= H_k \hat{X}_{k|k-1} \\ C_k &= H_k P_{k|k-1} H_k^T + R_k \end{aligned}\right\} \text{Prediction}$$

$$\left.\begin{aligned} K_k &= P_{k|k-1} H_k^T C_k^{-1} \\ \hat{X}_k &= \hat{X}_{k|k-1} + K_k (Y_k - Y_{k|k-1}) \\ P_k &= (I - K_k H_k) P_{k|k-1} \end{aligned}\right\} \text{Correction} \tag{3.36}$$

After the EKF has converged, the estimated state vector is [33]:

$$\hat{X}_k = P_k H_k^T R_k^{-1} Y_k \tag{3.37}$$

When the VDFLL is in lock, $Y_k \approx 0$ and $\hat{X}_k \approx 0$. Assuming that only the first channel is contaminated by multipath, although $Y_k \approx 0$, the real measurement vector in the presence of multipath should be $Y_k^{'} \approx (\Delta\rho,0,0,...,\Delta\dot{\rho},0,0,...)^T$, where $\Delta\rho = -\frac{c}{R_C}\Delta\tau$ and $\Delta\dot{\rho} = -\frac{c}{f_L}\Delta f_D$ as defined in Equations (3.17) and (3.30). The corresponding real state vector is $X_k^{'} = P_k H_k^T R_k^{-1} Y_k^{'}$.

It is assumed that the SDFLL changes to VDFLL during the transition from time *k-1* to time *k*, with an initial VDFLL EKF's state vector $\hat{X}_{k-1}$. In the absence of multipath, the state vector at time *k* is given by

$$\begin{aligned} \hat{X}_k &= \Phi\hat{X}_{k-1} + K_k(Y_k - H_k\Phi\hat{X}_{k-1}) = \Phi\hat{X}_{k-1} + K_k(-H_k\Phi\hat{X}_{k-1}) \\ \hat{X}_k &= (I - K_k H_k)\Phi\hat{X}_{k-1} \end{aligned} \tag{3.38}$$

In the presence of multipath, the state vector at time *k* is expressed as

$$\begin{aligned} X_k^{'} &= \Phi\hat{X}_{k-1} + K_k(Y_k^{'} - H_k\Phi\hat{X}_{k-1}) \\ X_k^{'} &= (I - K_k H_k)\Phi\hat{X}_{k-1} + K_k Y_k^{'} \end{aligned} \tag{3.39}$$

The difference between the two state vectors in Equations (3.38) and (3.39) is

$$\Delta X_k = X_k^{'} - \hat{X}_k = K_k Y_k^{'} \tag{3.40}$$

The predicted state vector at time *k+1* in the absence of multipath is

$$\hat{X}_{k+1|k} = \Phi\hat{X}_k \tag{3.41}$$

In the presence of multipath, it is

$$X_{k+1|k}^{'} = \Phi(\hat{X}_k + \Delta X_k) \tag{3.42}$$

Thus, the error induced by multipath in the predicted state vector at time *k+1* is

$$\Delta X_{k+1|k} = \Phi\Delta X_k = \Phi K_k Y_k^{'} \tag{3.43}$$

Similarly, the error induced by multipath in the estimated state vector at time *k+1* is

$$\begin{aligned}\Delta X_{k+1} &= (I - K_{k+1}H_{k+1})\Delta X_{k+1|k} + K_{k+1}Y'_{k+1} \\ \Delta X_{k+1} &= (I - K_{k+1}H_{k+1})\Phi K_k Y'_k + K_{k+1}Y'_{k+1}\end{aligned} \tag{3.44}$$

After the SDFLL changes to VDFLL, the code and frequency tracking errors become smaller and smaller and progressively approach their steady-state values. The initial measurement error at the time of the switch from SDFLL to VDFLL is the maximum error. Let $Y'_k \approx (\Delta\rho,0,0,...,\Delta\dot{\rho},0,0,...)^T$ be the initial measurement vector with the maximum measurement errors. The errors induced by multipath in the predicted and estimated state vectors at time k can be written as

$$\begin{aligned}\Delta X_{k|k-1} &= M_{k|k-1}Y'_k \\ \Delta X_k &= M_k Y'_k\end{aligned} \tag{3.45}$$

where

$$M_{k|k-1} = \Phi M_k \quad with\ M_k = (I - K_k H_k)M_{k|k-1} + K_k \tag{3.46}$$

The steady-state matrix M_{ss} is found by iteration of Equation (3.46) until M_k converges to a steady-state value. It is given by

$$\begin{aligned}M_{ss} &= (I - K_{ss}H)\Phi M_{ss} + K_{ss} \\ \therefore &\left[I - (I - K_{ss}H)\Phi\right]M_{ss} = K_{ss} \\ \therefore M_{ss} &= \left[I - (I - K_{ss}H)\Phi\right]^{-1}K_{ss}\end{aligned} \tag{3.47}$$

where K_{ss} is the steady-state Kalman gain matrix. The steady-state measurement vector is

$$Y'_{ss} = H\Delta X_{ss} = HM_{ss}Y'_k \tag{3.48}$$

Equation (3.48) shows that the measurement errors in Y'_k are assigned to each channel following the geometry between the satellites and the receiver to generate the new measurement errors in vector Y'_{ss}. The steady-state multipath induced error in code delay predictions is therefore

$$\Delta\tau = -\frac{R_C}{c}Y'_{ss}(i), i = 1,2,...,N \tag{3.49}$$

The steady-state multipath induced error in carrier Doppler frequency predictions is

$$\Delta f_D = -\frac{f_L}{c}Y'_{ss}(j), j = N+1, N+2,...,2N \tag{3.50}$$

The study conducted in section 3.2 culminates with the following remarks:

- In STL (SDFLL) tracking mode, each channel tracks a satellite independently and is unrelated to other channels. A healthy channel is therefore not affected by and does not assist a multipath-contaminated channel.
- In VTL (VDFLL) tracking mode however, all tracking channels are dependent on one another. When one satellite's signal is affected by a multipath signal, the other healthy channels assist the contaminated channel, and a tracking error in all channels will be induced by that single channel's multipath contamination. If another channel gets also affected by multipath, the code delay and carrier frequency errors assigned by the satellite geometry relationship among channels are directly superimposed on the errors caused by the first channel.
- It was demonstrated in [33] that from the point of view of a single multipath contaminated channel, the total multipath induced VDFLL tracking error is less than that of SDFLL, especially when more than four satellites are visible. The VTL therefore retains an advantage over the STL in multipath prone environments. But from the point of view of a single healthy channel operating with potentially one or more multipath contaminated channels, the STL is more advantageous. There is an attractive way to improve VTL performance if one is able to detect a multipath contaminated channel at post-correlation stage and exclude it from PVT calculation. Section 3.3 introduces and discusses this notion and *Chapter 4* applies it.

3.3 CORRELATOR-BASED MULTIPATH DETECTION TECHNIQUES

3.3.1 CORRELATOR OUTPUTS AND MULTIPATH DETECTION

A thorough analysis of correlator outputs in the absence and in the presence of multipath can lead to the design of multipath detection techniques. In the absence of multipath, the in-phase prompt correlator output carries the LOS signal power. In the presence of a multipath (MP) signal, the prompt correlator output is composed of the sum of the LOS and MP signals (see Figure 3.1 and Equations (3.5)) and the STL locking point is adjusted to this sum. As the tracking loop constantly seeks to bring the quadrature prompt power to zero, the quadrature prompt output will have part of the LOS plus MP signal power only for a short transient time following MP arrival then will get back to zero, unless the MP signal is in phase or opposition of phase with the LOS signal. The situation in the presence of multipath is different however for early and late correlator outputs and consequently for in-phase EmL and quadrature EmL outputs (see Equations (3.8) and Equations (3.19)) as it can be observed in Figures 3.4 and 3.5 for the STL and in Figures 3.10 and 3.11 for the VTL.

For the STL, in the presence of multipath, the signal energy in the quadrature arm of the EmL correlator output during transient and steady-state times following multipath arrival is significantly higher than in the absence of multipath, unless the MP signal is in phase or opposition of phase with the LOS signal. In the absence of multipath, only noise is observed on the quadrature EmL output.

Figure 3.16 represents the curves in Figures 3.4 and 3.10 with a reduced number of oscillations. For the STL, it shows that the Q_{EmL} output is zero for some multipath phase values even in the presence of multipath. More specifically, the Q_{EmL} output is zero when the multipath signal is in phase or opposition of phase ($\theta_M = 0^\circ + k360^\circ$ or $\theta_M = 180^\circ + k360^\circ$) with the LOS signal, with k being an integer. Except for those phase values, the Q_{EmL} output in the presence of multipath oscillates along the different multipath delay values between a maximum and a minimum which depend on the multipath to LOS amplitude ratio α and on the Early-Late correlator chip spacing ∂. These multipath phase values ($\theta_M = 0^\circ + k360^\circ$ and $\theta_M = 180^\circ + k360^\circ$) correspond to multipath delay values $\delta_M = nR_c / f_{L1}$ and $\delta_M = (n + 0.5)R_c / f_{L1}$, with n being an integer, if multipath phase is related to multipath delay using $\theta_M = 2\pi f_{L1}\delta_M / R_C$, i.e. if it is assumed that the multipath phase is only due to the differential path delay. In general, at the moment of reflection or diffraction, the multipath signal undergoes a relative phase θ_M that can be modelled using the differential path delay and reflector and antenna parameters [37] or else can be assumed random [38]. For the VTL, both the I_{EmL} and Q_{EmL} outputs increase in signal power in the presence of multipath and when Q_{EmL} is at zero, I_{EmL} is not and vice versa. This means that for all multipath phase or delay values, the absolute value $|EmL| = \sqrt{I_{EmL}^2 + Q_{EmL}^2}$ increases in amplitude in the presence of multipath.

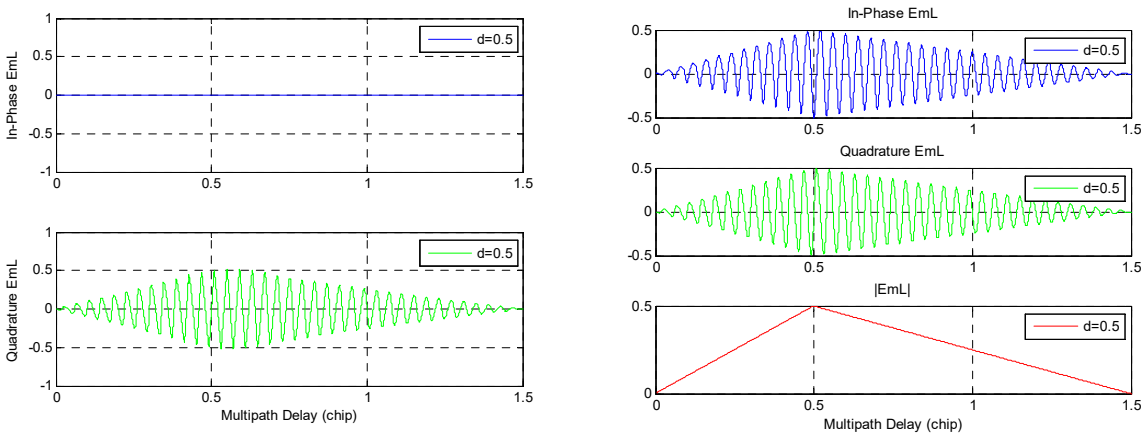

Figure 3.16: I_{EmL} and Q_{EmL} amplitudes vs. Multipath delay for STL in lock (left) and I_{EmL}, Q_{EmL} and $|EmL|$ amplitudes vs. Multipath delay for VTL in lock (right), reduced oscillations, standard correlator.

In order to further illustrate the effects of multipath on correlator outputs and analyse the possibility of devising multipath detection techniques based on them, some simulations are conducted. Consider a signal that is made of the LOS to which a MP having the same frequency as the LOS and constant relative delay and phase values is superimposed after 2 seconds tracking time. The MP maintains these parameter values for the rest of the tracking time. The C/N_0 is taken to be 45 dBHz. Two scenarios are studied: a case where the MP increases the signal power on the Q_{EmL} arm ($\theta_M = 213^\circ, \delta_M = 0.1171\,chip, \alpha = 0.5012$) and a case where it does not ($\theta_M = 0^\circ$, $\delta_M = 0.1623\,chip, \alpha = 0.5012$). Both STL and VTL tracking loops are simulated. The rest of the simulation settings are described in the figures' labels.

Figure 3.17 represents the simulation results of the first scenario for a STL (DLL + PLL) while Figure 3.18 shows the first scenario's results for a VTL (VDLL + PLL). Figure 3.17(c) shows that the MP signal induces an additional delay tracking error of about -0.06 chip and an additional phase tracking error of around 0.6 rad. Figure 3.17(a) shows that after MP arrival, the I_P arm signal power changes from a previous non-zero value to a new non-zero value and maintains its new value for the rest of the tracking period. The Q_P arm signal power on the other hand changes only for a short transient period of time before returning back to its normal value ($Q_P = 0$ for a PLL in lock). Figure 3.17(b) demonstrates that the Q_{EmL} signal power increases (considered an increase in signal power although the Q_{EmL} amplitude value goes from around zero to around -0.15). The I_{EmL} arm in contrast has a short transient-time change of value before returning back to normal ($I_{EmL} = 0$ for a DLL in lock). For a STL, it appears therefore that multipath detection techniques can more easily be formulated based on the Q_{EmL} arm and not the Prompt arms, although the exploitation of I_P in conjunction with Q_{EmL} can be considered.

Figure 3.18(a) for the VTL is almost the same as Figure 3.17(a) for the STL. Figure 3.18(b) proves however that for a VTL, multipath appearance creates a change in signal power on both the I_{EmL} and Q_{EmL} arms, more on the Q_{EmL} than the I_{EmL}, for this scenario and the like. Also, the VTL whose navigator has not been seriously contaminated by multipath generally maintains the delay tracking error to a minimum value (the simulation was set to approach the behaviour $\Delta\tau \approx 0$ for a VDLL in lock). This is observed in Figure 3.18(c). Figure 3.18(c) also shows that multipath induced phase error remains almost as in Figure 3.17(c), i.e. around 0.6 rad because carrier phase is still tracked in STL mode (PLL). Therefore, I_{EmL} and/or Q_{EmL} arms can be used in multipath detection, preferably together and maybe in association with Prompt arms as well, for the VTL. Figure 3.19 displays the simulation results of the second scenario for a STL (DLL + PLL) while Figure 3.20 depicts the second scenario's results for a VTL (VDLL + PLL).

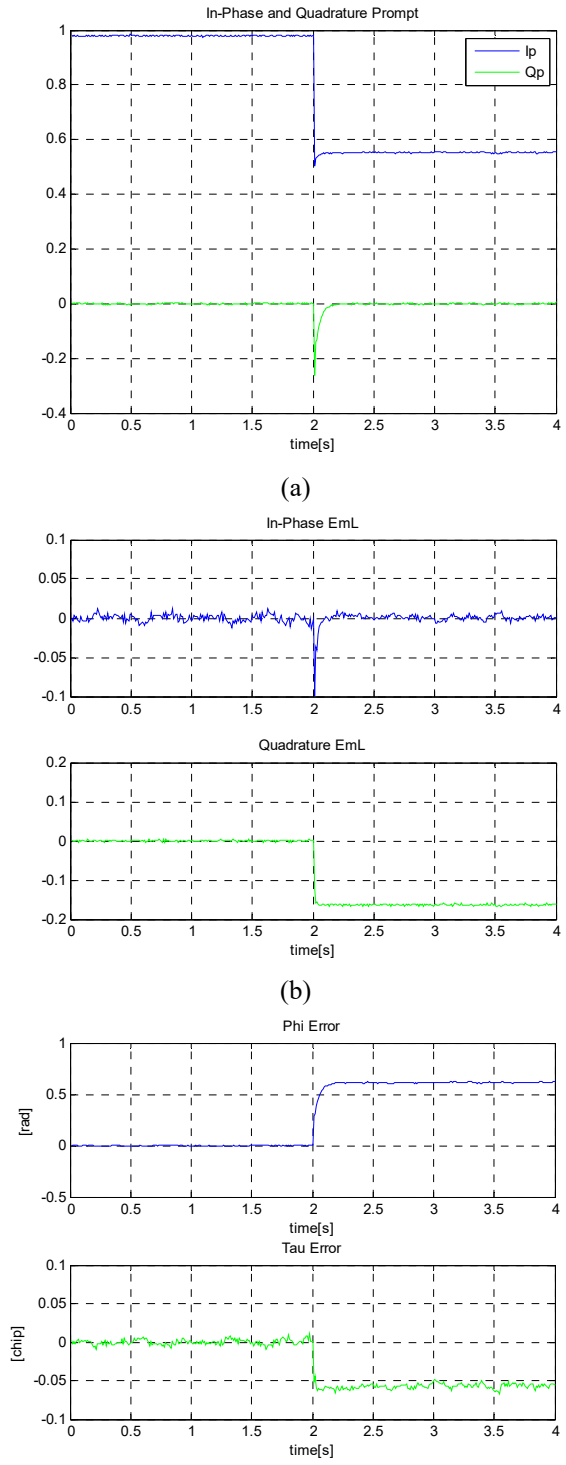

Figure 3.17: Tracking of LOS signal (C/N0=45dBHz) and MP signal ($\theta_M = 213^\circ$, $\delta_M = 0.117 chip$, α=0.501) arriving after 2s tracking time for a STL (second order DLL and PLL, bandwidths of 1 Hz and 10 Hz respectively, coherent EmL DLL discriminator $d = 0.5 chip$, ATAN PLL discriminator, coherent integration time: 10ms). A filtered autocorrelation function is used.

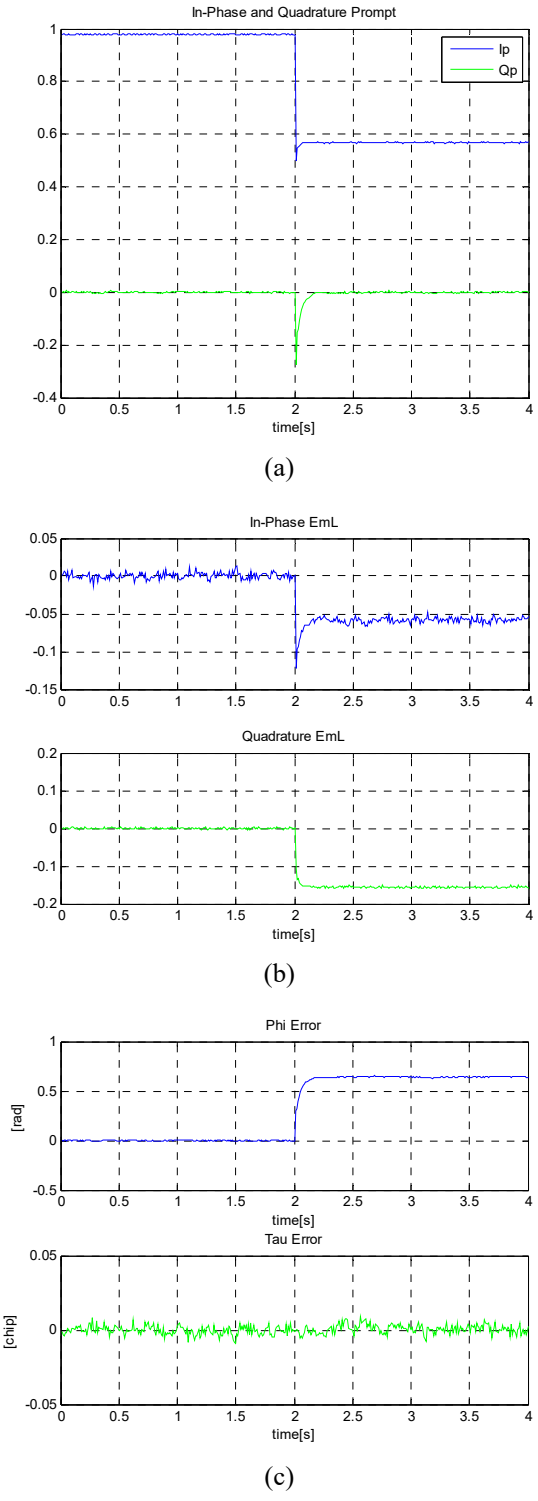

Figure 3.18: Tracking of LOS signal (C/N0=45dBHz) and MP signal ($\theta_M = 213^\circ$, $\delta_M = 0.117 chip$, α=0.501) arriving after 2s tracking time for a VTL (VDLL, second order PLL, bandwidths of 1 Hz and 10 Hz respectively, coherent EmL DLL discriminator $d = 0.5 chip$, ATAN PLL discriminator, coherent integration time: 10ms). A filtered autocorrelation function is used.

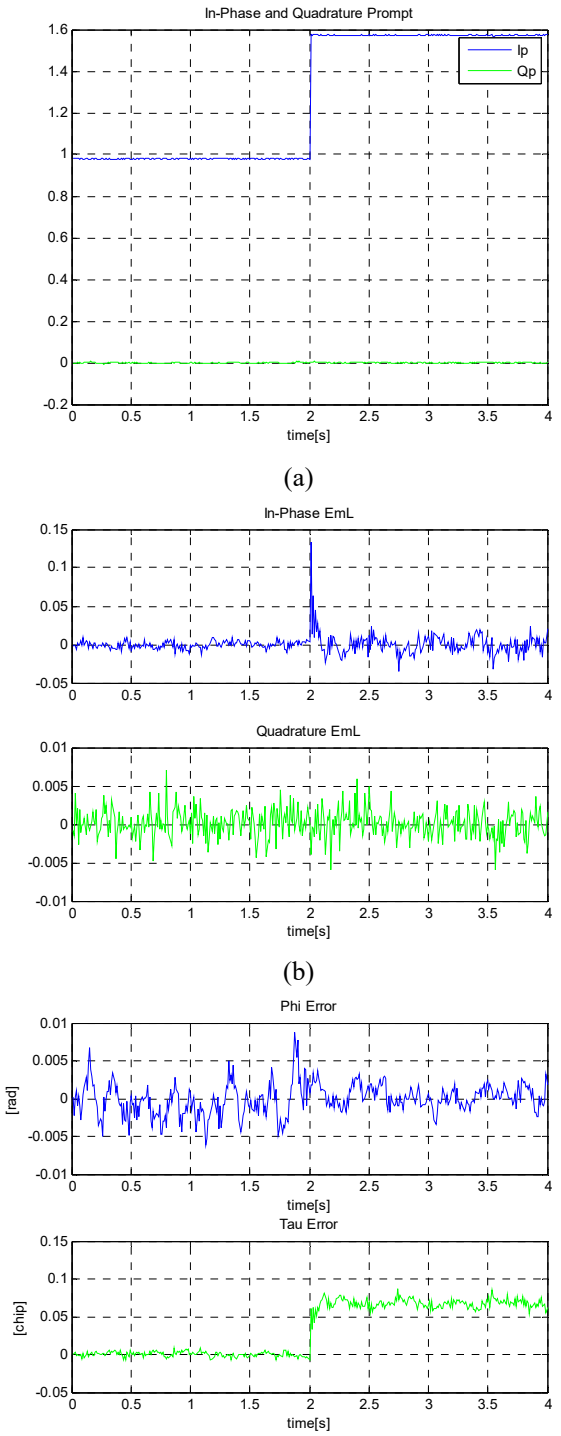

Figure 3.19: Tracking of LOS signal (C/N0=45dBHz) and MP signal ($\theta_M = 0^\circ$, $\delta_M = 0.1623 chip$, α=0.501) arriving after 2s tracking time for a STL (second order DLL and PLL, bandwidths of 1 Hz and 10 Hz respectively, coherent EmL DLL discriminator $d = 0.5 chip$, ATAN PLL discriminator, coherent integration time: 10ms). A filtered autocorrelation function is used.

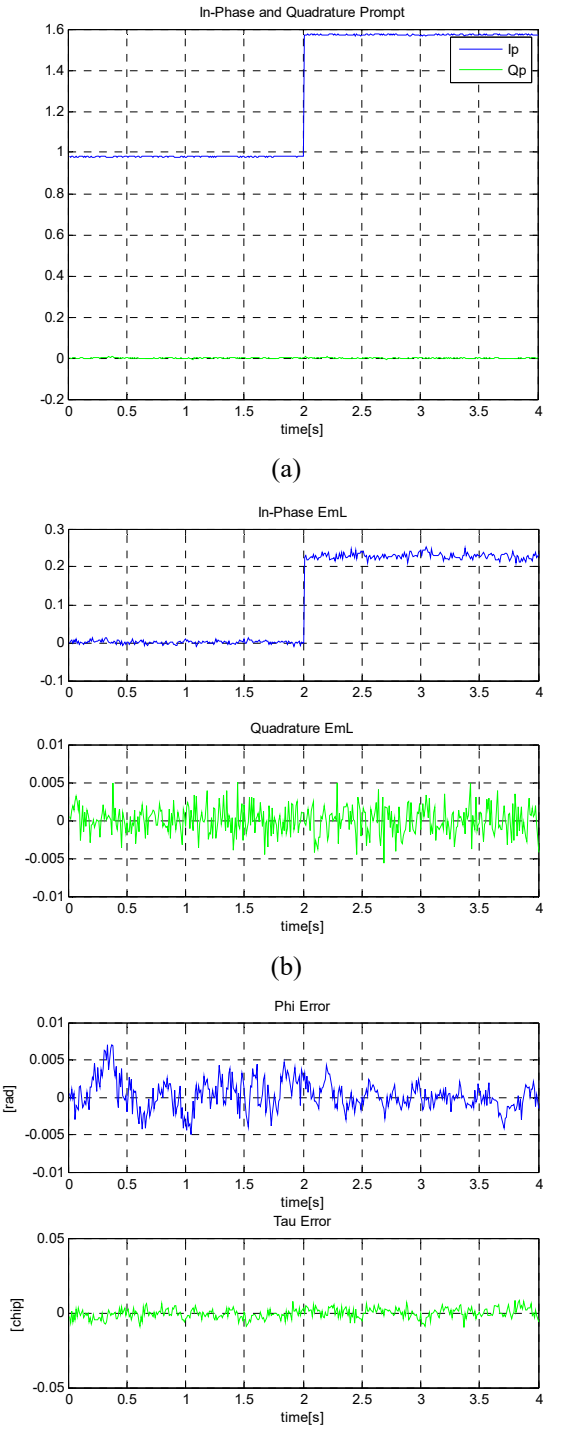

Figure 3.20: Tracking of LOS signal (C/N0=45dBHz) and MP signal ($\theta_M = 0^\circ$, $\delta_M = 0.1623 chip$, α=0.501) arriving after 2s tracking time for a VTL (VDLL, second order PLL, bandwidths of 1 Hz and 10 Hz respectively, coherent EmL DLL discriminator $d = 0.5 chip$, ATAN PLL discriminator, coherent integration time: 10ms). A filtered autocorrelation function is used.

Figures 3.19(a) and 3.20(a) show that I_P has the same behaviour as in the first scenario, but Q_P does not undergo any transient time change in value due to MP. This is due to the fact that the MP signal is in phase with the LOS signal ($\theta_M = 0^\circ$). Figures 3.19(b) and 3.20(b) show that the Q_{EmL} arm for this scenario is blind to MP presence for both STL and VTL, as demonstrated in theory for this MP phase value. The I_{EmL} arm on the other hand undergoes its transient time change of value as expected for the STL, but has a complete increase in signal power during the rest of the tracking period for the VTL as theorized. Figures 3.19(c) and 3.20(c) show that a MP phase of $\theta_M = 0^\circ$ does not induce any additional phase tracking error. However, this MP induces a delay tracking error for the STL case whose significance depends on the MP delay value ($\delta_M = 0.1623\,chip$ here), while the VTL maintains the delay tracking error very close to zero. This second scenario shows that, for the STL, the Q_{EmL} arm is useless in multipath detection if $\theta_M = 0^\circ$ and it is not certain whether the I_P arm can serve some purpose in detection. However, the I_{EmL} or Q_{EmL} for the VTL retain the potential for multipath detection even for $\theta_M = 0^\circ$ or $\theta_M = 180^\circ$, because when these MP phase values drive the Q_{EmL} output value to zero, they do not do so for I_{EmL} and vice versa. The I_P arm in conjunction with I_{EmL} and/or Q_{EmL} arms can also potentially serve some purpose in MP detection for the VTL in this scenario.

3.3.2 MULTIPATH DETECTION TECHNIQUES

Multipath remains one of the main sources of errors in obtaining precise positioning using GPS and all other GNSS. Lately, several signal processing techniques have been developed to deal with errors induced by multipath signals in a GPS receiver. Three classes of techniques can be distinguished. The first class relies on detection of multipath using statistical detection methods [39]. No mitigation is performed but the satellite whose line-of-sight (LOS) signal is absent or severely affected by secondary paths is excluded from calculation of the navigation solution. Some methods that fall under this class are the Early Late Phase (ELP)-based detection [40] [41], the ANOVA-based detection [42], detection based on analysis of Signal-to-Noise Ratio (SNR) fluctuation [43], and detection based on code minus carrier delta-range measurement [44]. One of the ELP-based detection flaws is that its threshold is difficult to define statistically. As for the ANOVA method, it requires a multi-antenna receiver (physical or logical antenna array). With the SNR-based method, the fluctuations occur with a periodicity of 1.5 to 20 minutes for GPS satellites, which requires the multipath detection test to be set over long periods of time (10 minutes in [43]) therefore delaying multipath detection. The second class of techniques alters the receiver tracking loop to make it resistant to multipath signals. The techniques

that fall under this class include the Narrow Correlator [45], the Edge Correlator [46], the Strobe Correlator [46], the High Resolution Correlator (HRC) [47], the Gated Correlator [48], the Multipath Elimination Technology (MET) [49], and the A-Posteriori Multipath Estimation (APME) Technique [50]. The third class is based on joint detection and estimation of the line-of-sight (LOS) and/or multipath signal parameters (amplitude, delay and phase) using statistical estimation methods [51]. Examples include the Multipath Estimating Delay Lock Loop (MEDLL) [52], the Modified RAKE Delay Lock Loop (MRDLL) [53], the Multipath Mitigation Technology (MMT) [54], the Vision Correlator (VC) [55], the Fast Iterative Maximum-Likelihood Algorithm (FIMLA) [56], Deconvolution Approaches [57] [58], and Frequency Domain Processing [59] [60].

The approaches suggested in this section are multipath detection techniques. The major contribution that is made comes from the special use of the Early-minus-Late (EmL) correlator output, and the exploitation of temporal and frequency domains to define the detectors metrics. Some approaches used in detection theory to detect a signal in Gaussian noise are adjusted and applied to multipath detection. Another particularity of the proposed detection tests comes from the fact that they are based on the raw measurements and not the estimated pseudorange. The detectors have constant false alarm rate (CFAR) with respect to noise power, which allows the definition of a threshold that is independent of noise power. They are suitable for a mono or multi antenna receiver and the time delay before the first multipath detection is significantly small (it can be set between 30 ms and 1 sec) in comparison with the time delay of the technique in [43]. After this first delay, the rest of the detection is almost real-time depending on the detector metric calculation cost. No multipath mitigation is performed. Instead, these detection techniques are used to exclude multipath affected satellites from calculation of the position, velocity, and time (PVT) solution. In fact, multipath estimation techniques, especially those based on frequency domain processing, may present a high computational burden in comparison with multipath detection techniques. Adding to this is the fact that many satellite constellations can now be jointly used to obtain the PVT solution in one GNSS receiver. Thus, excluding multipath contaminated satellites instead of spending computational resources to mitigate multipath is sometimes a more suitable approach. The detection tests are proposed for both scalar and vector tracking loops (STL and VTL). The detectors can also be used to switch between STL and VTL tracking modes in a receiver with an adaptive STL-VTL tracking scheme. The test metrics are defined using correlator outputs. For a STL utilizing a coherent EmL discriminator, the EmL correlation output is directly used in the detectors metrics. Indeed, as shown in the previous section, for a STL, depending on the relative phase of the multipath signal, the presence of multipath increases the signal power on the quadrature arm of the EmL correlation point (Q_{EmL}) in comparison

with the power that is usually observed in the absence of multipath. This increase in signal power is used to detect multipath with the specification of a proper threshold. For a VTL using the coherent EmL discriminator, both the in-phase and quadrature arms of the EmL correlation outputs are utilized in the detectors metrics. In fact, for a VTL with a navigator that is not contaminated, the increase in signal power due to the presence of multipath may occur on the in-phase arm (I_{EmL}) and/or on the quadrature arm (Q_{EmL}) of the EmL correlation output depending on the delay and phase of the multipath signal. Two tracking schemes are used for experiments reported in this section: first a vector delay locked loop (VDLL) together with a scalar phase locked loop (PLL); second, a vector delay frequency locked loop (VDFLL) and a phase locked loop (PLL) aided by the navigator, with the possibility to switch to a scalar delay locked loop (DLL) and a frequency-assisted phase locked loop (FPLL).

3.3.2.1 Multipath Detectors for the Scalar Tracking Loop (STL)

The detection tests are defined based on the fact that in the presence of multipath, the signal power on the quadrature arm of the EmL correlator output (Q_{EmL}) increases significantly in comparison with the normal power observed in the absence of multipath.

- **GLRT STL-MP Detector**

The GLRT STL-MP Detector is based on a generalized likelihood ratio test (GLRT). A binary hypothesis test is defined assuming that the multipath exists for a sufficient time and that its amplitude A observed on the Q_{EmL} arm does not change for an observation window of N samples and of initial index n_0.

H_0: $Q_{EmL}(n) = w_{Q,EmL}$
H_1: $Q_{EmL}(n) = A + w_{Q,EmL,}$ with $n \in \{1, \ldots, N\} + n_0$

In other terms, under hypothesis H_0 only noise is observed whereas under hypothesis H_1 a constant term plus noise is observed. The noise is white Gaussian with variance σ^2. Assuming that A and σ^2 are unknown, the maximum likelihood (ML) test to decide for H_0 or H_1 is formulated as

$$N \ln\left[1 + \frac{\overline{Q}^2}{\hat{\sigma}^2}\right] \underset{H_1}{>} \gamma \quad or \quad N \ln\left[1 + \frac{\overline{Q}^2}{\hat{\sigma}^2}\right] \underset{H_0}{<} \gamma \tag{3.51}$$

where $\ln$ denotes natural logarithm, $\overline{Q}$ is the mean of the N samples on the Q_{EmL} arm and $\hat{\sigma}^2$ is the ML estimate of the noise power under hypothesis H_1. N is chosen to be large (typically $N > 30$). The following expressions are used in Equation (3.51):

$$\overline{Q} = \frac{1}{N}\sum_{n=1}^{N} Q_{EmL}(n+n_0) \tag{3.52}$$

$$\hat{\sigma}^2 = \frac{1}{N}\sum_{n=1}^{N}\left(Q_{EmL}(n+n_0) - \overline{Q}\right)^2 \tag{3.53}$$

The detection threshold is

$$\gamma = \left[cdf^{-1}\left(1 - \frac{PFA}{2}\right)\right]^2 \tag{3.54}$$

with cdf being the cumulative distribution function, cdf^{-1} the inverse cumulative distribution function, and PFA the probability of false alarm. The values of *PFA* and N have a great impact on the performance of the GLRT. There is a trade-off between obtaining a high detection capability or a low false alarm rate. Increasing the value of N and/or *PFA* improves the detection capability of the GLRT in theory. However, in practice, increasing the value of N delays the instant when the multipath is detected and may go against the assumption that the amplitude *A* of the multipath remains constant for the duration of N samples. On the other hand, increasing *PFA* may result in many false detections and this may not be beneficial if the objective is to exclude only the multipath contaminated satellites from the navigation solution. If N is assumed sufficiently large ($N > 30$), the probability of detection (*PD*) is given by [39]

$$PD = 2 - cdf\left(cdf^{-1}\left(1 - \frac{PFA}{2}\right) - \sqrt{SNR}\right) - cdf\left(cdf^{-1}\left(1 - \frac{PFA}{2}\right) + \sqrt{SNR}\right) \tag{3.55}$$

where *SNR* is the post-correlation signal to noise ratio and is given by $SNR = \frac{NA^2}{\sigma^2}$.

Appendix 3.A provides a brief discussion on detection theory concepts for proper understanding of the probability of detection (*PD*), probability of false alarm (*PFA*) and probability of missed detection (*PMD*) as used throughout this chapter. The *SNR* for the EmL correlator output depends on the correlator E-L chip spacing as well as the signal carrier-to-noise ratio (C/N_0). The *PD* depends on the chosen *PFA*, on the amplitude *A* of the signal on the Q_{EmL} output, and on the noise power on that output. This noise power is given by $\sigma^2 = \sigma_n{}^2 K(1-r)$ [45] where $\sigma_n{}^2 = N_0 f_S$ is the thermal noise power (N_0 and f_S are noise spectral density and baseband sampling frequency respectively), K is the number of correlation points, and $r = 1-2d$ is the level of correlation between the Early and Late outputs. By taking $A_M = \alpha A_0$ in Equation (3.8b) the amplitude *A* is given by $A = A_0\begin{Bmatrix}\left[R(\Delta\tau + d) - R(\Delta\tau - d)\right]\sin(\Delta\varphi) + \\ \alpha\left[R(\Delta\tau - \delta_M + d) - R(\Delta\tau - \delta_M - d)\right]\sin(\Delta\varphi - \theta_M)\end{Bmatrix}$, where $A_0 = \sqrt{C}K\,\mathrm{sinc}(\pi\Delta f T)$ with

C being the LOS power before correlation, T the coherent integration time ($K = Tf_S$) and Δf the error between the LOS carrier frequency and the estimated carrier replica frequency. The post-correlation SNR at the Q_{EmL} output therefore has the following expression linking it to the C/N_0:

$$SNR = \frac{NA^2}{\sigma^2} = \frac{C}{N_0} NT \frac{\sin c^2(\pi \Delta f T)}{2d} \times \left\{ \begin{array}{l} [R(\Delta\tau + d) - R(\Delta\tau - d)]\sin(\Delta\varphi) + \\ \alpha[R(\Delta\tau - \delta_M + d) - R(\Delta\tau - \delta_M - d)]\sin(\Delta\varphi - \theta_M) \end{array} \right\}^2 \quad (3.56)$$

The GLRT detector approaches optimality when the multipath signal has the same frequency as the LOS signal. In the presence of such MP signal, the Q_{EmL} output does have characteristics close to hypothesis H_1, i.e. it is a signal with constant amplitude combined with noise. This detector will present reduced performance for multipath signals with a frequency different from the LOS signal frequency. However, multipath signals can appear with a frequency different from the LOS frequency. Therefore, there is a need for Fast Fourier Transform (FFT)-based detectors which can detect multipath at any frequency. Figure 3.21 illustrates the probability of detection (PD) given different PFA values for different values of SNR in optimal conditions. It can be observed that a high SNR value increases the PD and theoretically the performance of the GLRT.

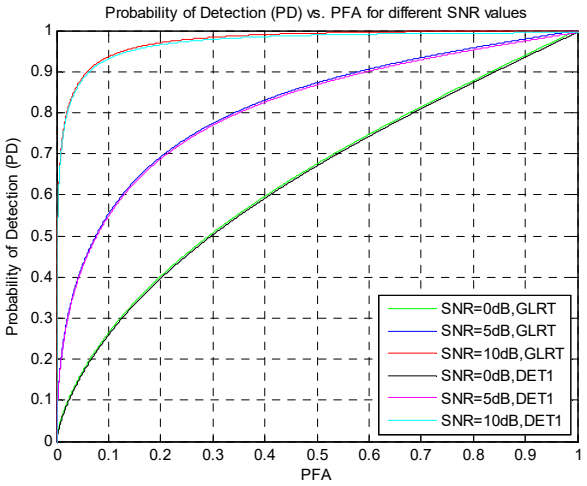

Figure 3.21: Probability of detection versus PFA for different SNRs (GLRT-optimal conditions, Detector I-any conditions)

- **FFT-based STL-MP Detector I**

A binary hypothesis test can be defined as follows for an observation window of N samples and of initial index n_0:

H_0: $Q_{EmL}(n) = w_{Q,EmL}$

H_1: $Q_{EmL}(n) = s(n) + w_{Q,EmL}$, with $n \in \{1, \ldots, N\} + n_0$

In other terms, under hypothesis H_0, no signal is present on the Q_{EmL} output, only noise is observed which implies that no multipath signal is present; whereas under

hypothesis H_1 a signal $s(n)$ plus noise are observed, which implies the presence of multipath. The standard FFT detector [39] [61], used in the sonar and radar systems, which detects the presence of a signal in the frequency domain is modified and applied to GPS multipath detection using the above hypotheses formulation. This detector computes the periodogram given by

$$\Omega(m) = \frac{1}{N}\left|Q_{EmL}(m)\right|^2 \quad where \quad Q_{EmL}(m) = \sum_{n=n_0}^{n_0+N-1} Q_{EmL}(n) e^{-j\frac{2\pi mn}{N}} \tag{3.57}$$

$Q_{EmL}(m)$ is the discrete Fourier transform of $Q_{EmL}(n)$ and is implemented via an N-point FFT algorithm. The detector subsequently chooses the largest value of $\Omega(m)$, divides it by the maximum likelihood estimate (MLE) of noise variance $\hat{\sigma}^2$ and then compares the result against a threshold η. The detection test to decide for H_0 or H_1 is therefore formulated as

$$\frac{\max\left(\Omega(m)\right)}{\hat{\sigma}^2} \underset{H_1}{>} \eta \quad or \quad \frac{\max\left(\Omega(m)\right)}{\hat{\sigma}^2} \underset{H_0}{<} \eta \tag{3.58}$$

where

$$\hat{\sigma}^2 = \frac{1}{N}\sum_{n=1}^{N}\left(Q_{EmL}(n+n_0) - \overline{Q}\right)^2 \quad and \quad \overline{Q} = \frac{1}{N}\sum_{n=1}^{N} Q_{EmL}(n+n_0).$$

Detector I is optimum if $s(n)$ is a sinusoid. This sinusoid may have unknown amplitude, phase and frequency, but optimality requires the frequency to be a bin frequency, i.e. to be equal to $\frac{2\pi m}{N}$, with m being an integer [61]. Optimum detection entails that for a given probability of false alarm (PFA), the detector gives the maximum probability of detection (PD). For a sinusoid $s(n)$, this detector can be considered as a modified generalized likelihood ratio test (M-GLRT). It will have similar performance as the GLRT detector for multipath signals at the same frequency as the LOS, and will have better performance than the GLRT detector for multipath signals with different frequency than the LOS frequency. The derivation of Detector I detection test metric is detailed in Appendix 3.B. This derivation is based on detection of a sinusoid of unknown amplitude, phase and frequency in Gaussian noise. The detection threshold is given by

$$\eta = \exp\left\{\frac{\left[cdf^{-1}\left(1 - PFA/2\right)\right]^2}{N}\right\} - 1 \tag{3.59}$$

with cdf being the cumulative distribution function of the standard normal distribution, cdf^{-1} the inverse cumulative distribution function, and PFA the probability of false alarm. The values of PFA and N have once more a great impact

on the performance of this detector, and there is a trade-off between obtaining a high detection capability or a low false alarm rate. If N is assumed sufficiently large ($N > 32$), theoretically, Detector I probability of detection (PD) in any condition is similar to the GLRT detector PD in optimal conditions (see Figure 3.21):

$$PD = 2 - cdf\left(cdf^{-1}\left(1 - \frac{PFA}{2}\right) - \sqrt{SNR}\right) - cdf\left(cdf^{-1}\left(1 - \frac{PFA}{2}\right) + \sqrt{SNR}\right) \tag{3.60}$$

where *SNR* is the post-correlation signal to noise ratio of the Q_{EmL} output and is given by $SNR = \frac{NA^2}{2\sigma^2}$. Here, *A* is the amplitude of signal *s(n).*

- **FFT-based STL-MP Detector II**

The second MP detector uses the same hypothesis formulation as Detector I and computes an FFT on blocs of 1024 samples at the frequency of correlators. In practice, this 1024-point FFT can be a complex calculation, but for the simplicity of algorithm description, it is chosen. The obtained frequency resolution is ~1 Hz for a coherent integration time of 1 ms. A power spectral density (PSD) estimator is then derived from the FFT bloc output for $|f| \leq 500$ Hz. A periodogram can be used as a PSD estimator. This PSD estimator allows the search for *s(n)* signal frequency in the zone of interest, by measuring the signal power using a sliding window of length 3. More specifically, this PSD estimator makes it possible:

- To estimate the noise power by summing samples of the spectral density for $|f| > 200$ Hz.
- To estimate the power of the signal by summing samples of the spectral density for $|f| < 200$ Hz.
- To estimate a signal to noise power ratio and compare it against a threshold η

Detector II algorithm can therefore be summarized as follows:

- Compute 1024-point FFT on blocs of 1024 samples at the frequency of correlators

$$Q_{EmL}(m) = \sum_{n=n_0}^{n_0+N-1} Q_{EmL}(n) e^{-j\frac{2\pi mn}{N}} \quad where \quad N = 1024 \tag{3.61}$$

- Derive a periodogram (PSD estimator) for $|f| \leq 500$ Hz. Letting m denote the frequency f,

$$\Omega(m) = \frac{1}{N}\left|Q_{EmL}(m)\right|^2 \tag{3.62}$$

- Estimate the noise power

$$NP = \sum_{m=-500}^{-200} \Omega(m) + \sum_{m=200}^{500} \Omega(m) \tag{3.63}$$

- Estimate the signal power

$$SP = \sum_{m=-199}^{199} \Omega(m) \tag{3.64}$$

- Estimate a signal to noise power ratio

$$SNPR = \frac{SP}{NP} \tag{3.65}$$

- Choose H_0 or H_1 using the following test:

$$10\ln(SNPR) \underset{H_1}{\geq} \eta \quad or \quad 10\ln(SNPR) \underset{H_0}{<} \eta \tag{3.66}$$

where $\eta = -\ln(PFA)$ is the detection threshold. The derivation of this threshold is given in Appendix 3.C.

The probability of detection (PD) is given by [39]

$$PD = 1 - CDF\left(2\ln\left(\frac{N/2-1}{PFA}\right)\right) \tag{3.67}$$

where CDF is the cumulative distribution function of the non-central chi-squared distribution with 2 degrees of freedom and non-centrality parameter $\lambda = SNR = \frac{NA^2}{2\sigma^2}$. SNR is the post-correlation signal-to-noise ratio. Figure 3.22 displays Detector II's PD given different PFA values for different SNR values.

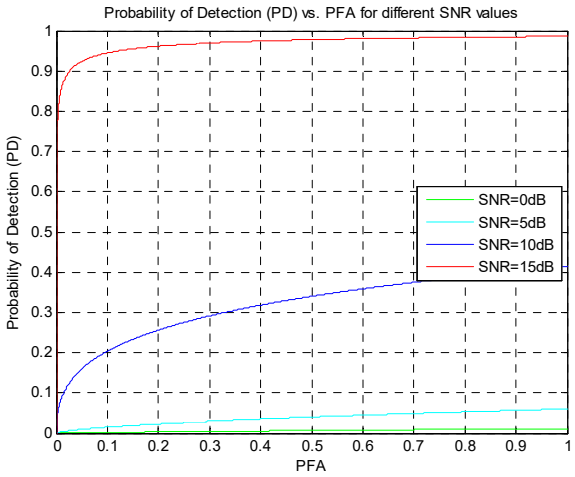

Figure 3.22: Probability of detection versus PFA for different SNRs (Detector II)

3.3.2.2 *Multipath Detectors for the Vector Tracking Loop (VTL)*

For the VTL, the presence of a specular multipath is visible on both the in-phase and quadrature arms of the Early-minus-Late correlation point as long as the navigator is not contaminated. The suggested test is similar to the one defined for the scalar tracking loop but considers the complex output of the EmL correlator output.

- **GLRT VTL-MP Detector**

The binary hypothesis test is again defined assuming that the multipath exists for a sufficient time and that its complex amplitude A does not change for an observation window of N samples and of initial index n_0.

H_0: EmL (n) = w_{EmL}
H_1: EmL (n) = A + w_{EmL}, with n ϵ {1, …, N } + n_0

Assuming that A and σ^2 are unknown, the maximum likelihood test to decide for H_0 or H_1 is formulated as

$$\frac{\left|\overline{EmL}\right|^2}{\hat{\sigma}^2} \underset{H_1}{>} \eta \quad or \quad \frac{\left|\overline{EmL}\right|^2}{\hat{\sigma}^2} \underset{H_0}{<} \eta \tag{3.68}$$

where η is the detection threshold, $\overline{EmL}$ is the mean of the N samples on the EmL correlation point of the VTL and $\hat{\sigma}^2$ is the ML estimate of the noise power under hypothesis H_1. The following expressions are used in Equation (3.68):

$$\overline{EmL} = \frac{1}{N}\sum_{n=1}^{N} EmL(n+n_0) \tag{3.69}$$

$$\hat{\sigma}^2 = \frac{1}{N}\sum_{n=1}^{N}\left|EmL(n+n_0) - \overline{EmL}\right|^2 \tag{3.70}$$

The detection threshold is $\eta = \exp\left\{\frac{\left[cdf^{-1}(1-PFA/2)\right]^2}{N}\right\} - 1$. This threshold is the same as the one in Equation (3.59) used for FFT-based STL-MP Detector I, which is a modified GLRT (M-GLRT). If the logarithmic formulation of the detection test in Equation (3.51) is converted to linear scale, the detection threshold of Equation (3.54) will also be equivalent to that of Equation (3.59). In fact, if a likelihood ratio (LR) test is formulated as $N\ln[1+LR] \underset{H_1}{>} \gamma \quad or \quad N\ln[1+LR] \underset{H_0}{<} \gamma$ with a threshold γ, then it can also be formulated as $LR \underset{H_1}{>} \eta \quad or \quad LR \underset{H_0}{<} \eta$ with a threshold η, where $\eta = \exp\left(\frac{\gamma}{N}\right) - 1$.

- **FFT-based VTL-MP Detector I (M-GLRT)**

A binary hypothesis test can be defined as follows for an observation window of N samples and of initial index n_0:
H_0: EmL (n) = w_{EmL}
H_1: EmL (n) = s(n) + w_{EmL}, with n ϵ {1, …, N } + n_0

As in the STL case, the detector computes the periodogram but this time based on the complex FFT.

$$\Omega(m) = \frac{1}{N}\left|EmL(m)\right|^2 \quad where \quad EmL(m) = \sum_{n=n_0}^{n_0+N-1} EmL(n) e^{-j\frac{2\pi mn}{N}} \tag{3.71}$$

$EmL(m)$ is the discrete complex Fourier transform of $EmL(n) = I_{EmL}(n) + jQ_{EmL}(n)$. The detector then chooses the largest value of $\Omega(m)$, divides it by the MLE of noise variance $\hat{\sigma}^2$ and then compares the result against a threshold η. The detection test to decide for H_0 or H_1 is therefore formulated as

$$\frac{\max\left(\Omega(m)\right)}{\hat{\sigma}^2} \underset{H_1}{>} \eta \quad or \quad \frac{\max\left(\Omega(m)\right)}{\hat{\sigma}^2} \underset{H_0}{<} \eta \tag{3.72}$$

where

$$\hat{\sigma}^2 = \frac{1}{N}\sum_{n=1}^{N}\left|EmL(n+n_0) - \overline{EmL}\right|^2 \quad and \quad \overline{EmL} = \frac{1}{N}\sum_{n=1}^{N} EmL(n+n_0).$$

The detection threshold is still $\eta = \exp\left\{\frac{\left[cdf^{-1}(1-PFA/2)\right]^2}{N}\right\} - 1$.

- **FFT-based VTL-MP Detector II**

The detection test to decide for H_0 or H_1 is formulated as

$$10\ln(SNPR) \underset{H_1}{>} \eta \quad or \quad 10\ln(SNPR) \underset{H_0}{<} \eta \tag{3.73}$$

where $\eta = -\ln(PFA)$ is the detection threshold, and $SNPR$ is obtained as in the test for FFT-based STL-MP Detector II except that the periodogram is calculated for $\left|EmL(n)\right| = \sqrt{\left(I_{EmL}(n)^2 + Q_{EmL}(n)^2\right)}$ and not for $Q_{EmL}(n)$. In other words,

$$EmL(m) = \sum_{n=n_0}^{n_0+N-1} \left|EmL(n)\right| e^{-j\frac{2\pi mn}{N}} \quad where \quad N = 1024 \tag{3.74}$$

and,

$$\Omega(m) = \frac{1}{N}\left|EmL(m)\right|^2 \tag{3.75}$$

3.3.3 EXPERIMENTAL SETUP AND SIMULATION METHODOLOGY

3.3.3.1 GPS Software receiver

For evaluating the performance of the detectors described in section 3.3.2, Matlab simulations are performed using two software tools: a GPS software receiver simulator that uses synthesized GPS signals as input and whose architecture is depicted in Figure 3.23, and a GPS software receiver that utilises real GPS signals as input and whose architecture is shown in Figure 3.24. The GPS receiver simulator that utilises synthesized signals was developed in Matlab by M3 Systems in 2013. The GPS software receiver that uses real GPS signals was developed in Matlab by the author of this PhD thesis in 2014 during an Internship period at M3 Systems. Its development went on during the PhD research period.

The synthesized signals-based GPS receiver simulator is a decentralized architecture meaning that each tracking channel has a local estimator that uses a fixed gain Kalman filter. All channels then deliver their measurements to the navigator, which is the master PVT estimation filter. Thus, this GPS receiver simulator is made of a bank of correlators, code and carrier discriminators, local estimators, code and carrier numerically controlled oscillators (NCOs), and a navigator that is based on an Extended Kalman Filter (EKF) algorithm. The multipath model developed by the German Aerospace Centre (German: Deutsches zentrum für Luft- und Raumfahrt), abbreviated DLR, is utilised in the trajectory and environment simulator used as signal source. This simulator has the potential to perform scalar tracking and vector tracking. The DLR model was developed without taking ionosphere and troposphere propagation into account. In the simulation, it is assumed also that the receiver is not impacted by troposphere and ionosphere errors. This simulation setup ensures proper isolation and study of the impact of multipath disturbance on tracking and positioning. The STL- and VTL-based multipath detectors are tested on synthesized GPS signals using the Early-Late correlator outputs of this GPS receiver simulator. The contributions that are made in this thesis are added to and tested in this GPS receiver simulator, and used to enhance its design and operation.

The real signals-based GPS software receiver is a scalar tracking architecture with a signal acquisition component, a signal tracking component and a navigation component. It uses real GPS signals collected in MP prone environments (urban, suburban, heavy foliage). Its acquisition algorithm is based on parallel FFT search. This GPS software receiver is also made of a bank of correlators, code and carrier discriminators, code and carrier loop filters, code and carrier NCOs, and a navigator that is based on a least squares algorithm. The STL-based multipath detection tests for real GPS signals are performed on the Early-Late correlator outputs of this receiver.

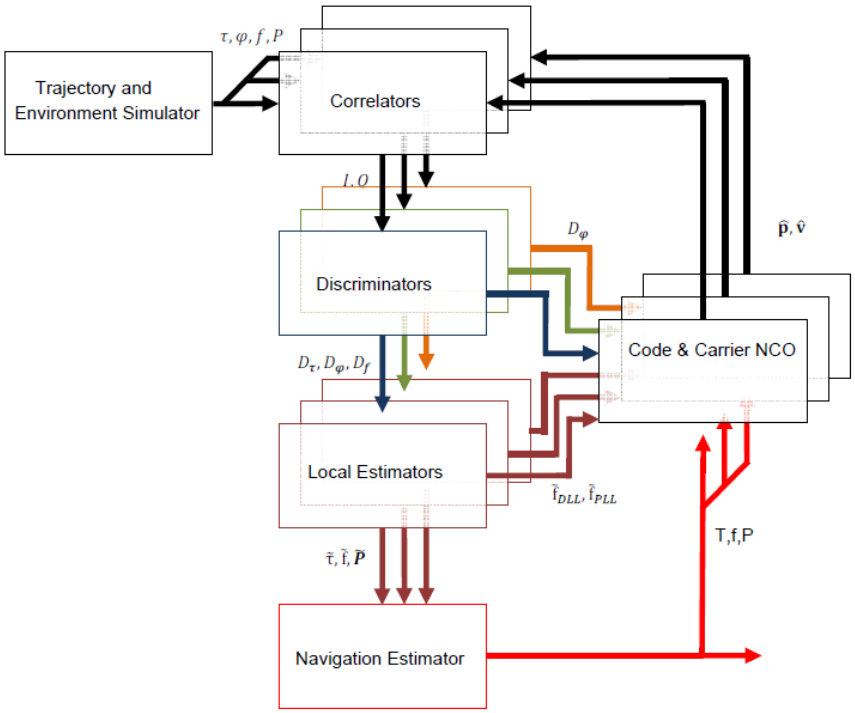

Figure 3.23: GPS software receiver simulator architecture

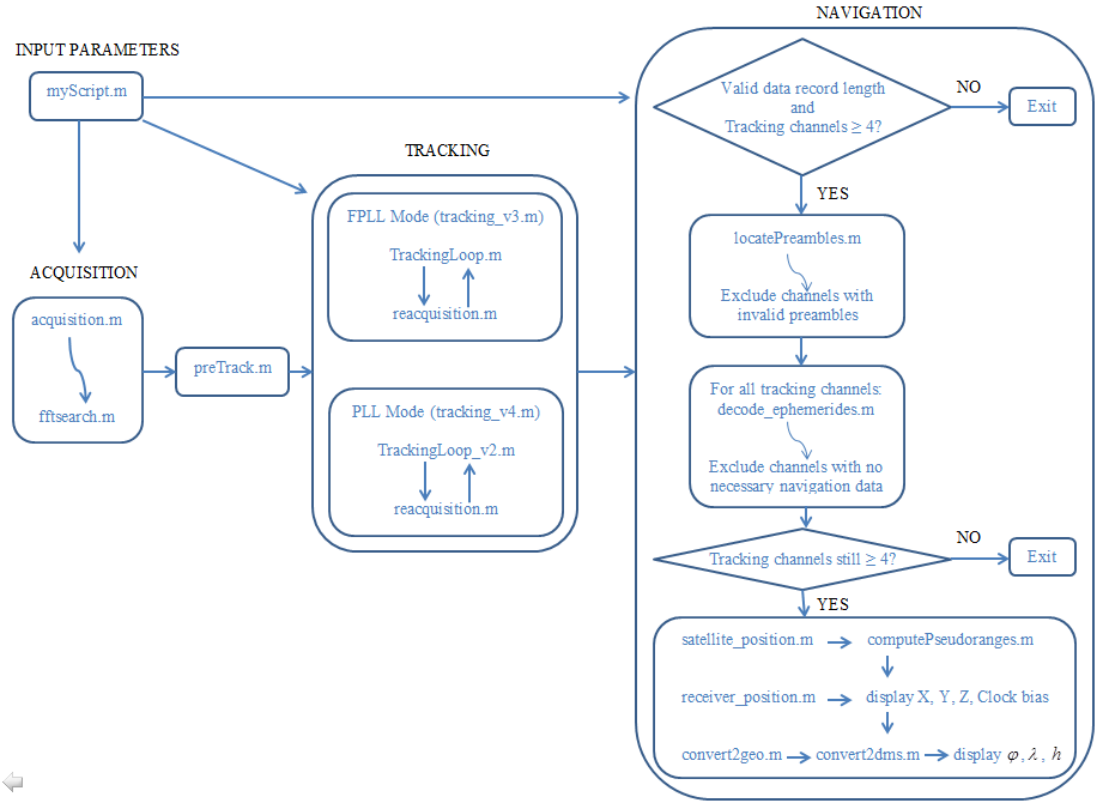

Figure 3.24: GPS software receiver architecture with logic flow between Matlab functions

3.3.3.2 *Multipath Data Used for Experiments*

This sub-section briefly explains how the synthesized multipath data that are used for experiments in this work were generated via simulations using the DLR Multipath Model software. The sub-section also discusses how the GPS real signals were collected.

- **DLR Multipath Model**

The DLR multipath model is a software tool developed under Matlab by the German Aerospace Centre (DLR) to allow characterization of the propagation channel for wideband signals such as GNSS signals. The innovative aspect of this model is the synthesis of statistical data from measurements obtained with deterministic scenarios. Measurements campaigns were performed in Munich in 2002 using wideband signals (100 MHz) modulated on carriers in the GNSS band, specifically between 1460 MHz and 1560 MHz (close to GPS L1). The resulting transmitter was embedded in a Zeppelin that simulated a moving satellite at an altitude of 4 km. A vehicle circulated around Munich's streets from the urban canyon to narrow suburban streets with momentary open sky boulevards, following the Zeppelin displacement. The latter disappeared and appeared behind buildings and obstacles that surrounded the vehicle's trajectory which was assumed to be a straight line locally. The deterministic aspect of the DLR model intervenes in the direct path (LOS) modelling and the calculation of the echoes (multipaths) parameters evolution. The statistical aspect comes from the number of generated echoes, their lifetime, and the position and attenuation factor of reflectors. The echoes lifetime follows a probability distribution whose parameters are deduced from measurements. The attenuation due to a reflector, its bandwidth, its fading factor (Rician factor) and its lifetime (the lifetime of the echo it generates) are statistically determined from the measurements campaigns. The echoes delays and phases evolve following the relative movement of the vehicle with respect to the position of the reflectors. The channel modelling takes into account three elements that are usually found in an urban environment and that are characterized by different parameters:

- *Buildings:* characterized by the presence or absence of the building, its distance from the road's centre, the statistics of the building's height and width, and the statistics of the gap between two buildings (see Figure 3.25).

- *Trees:* characterized by the height, diameter and attenuation of foliage, the length and diameter of the tree trunk, the presence or absence of trees, the statistics of the distance from the road's centre, and the statistics of the gap between two trees (see Figure 3.26).

- *Lamp poles*: characterized by the height and diameter of the poles, the presence or absence of poles, the statistics of the distance from the road's centre, and the statistics of the gap between two lamp poles (see Figure 3.27).

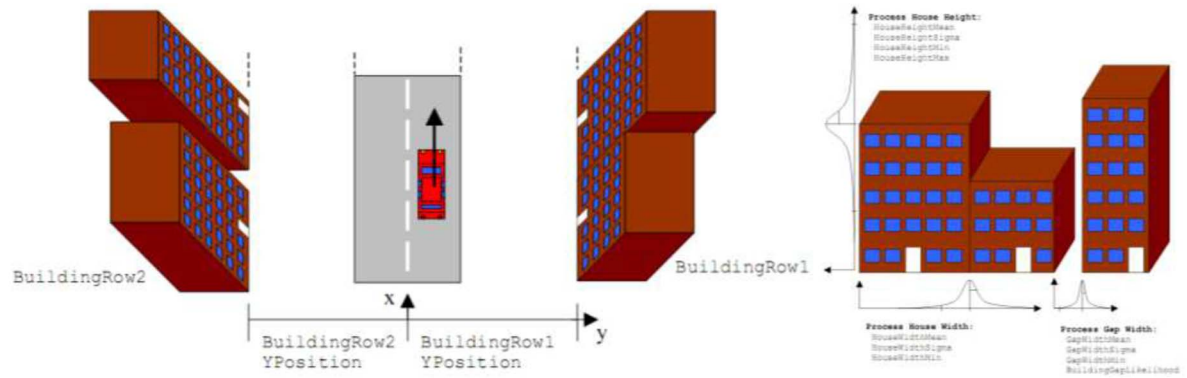

Figure 3.25: Characterization of buildings in the DLR model

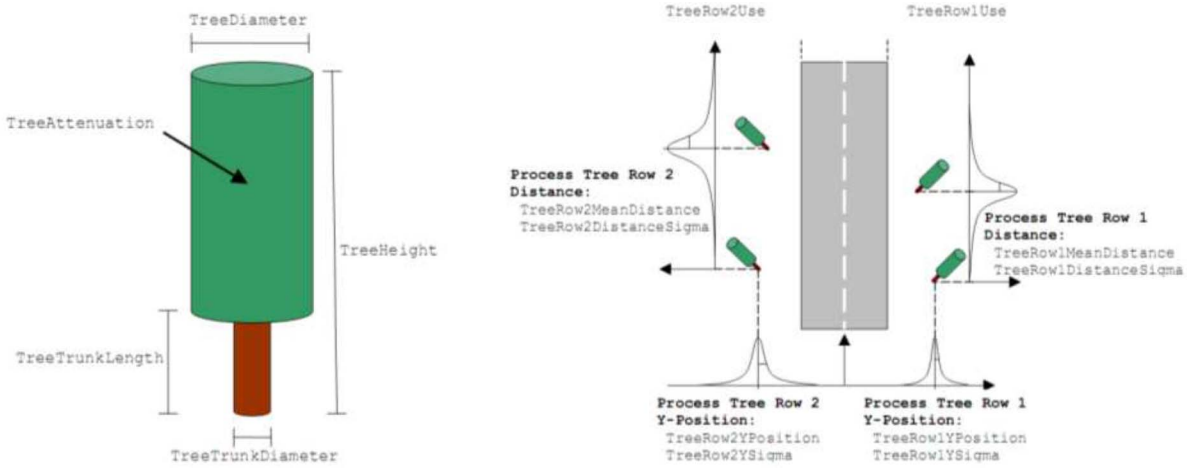

Figure 3.26: Characterization of trees in the DLR model

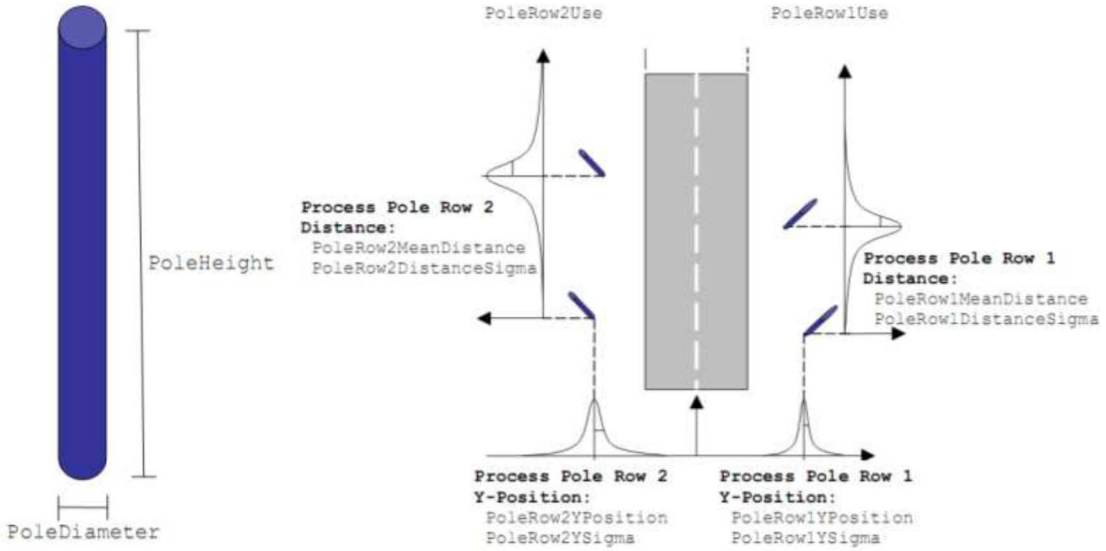

Figure 3.27: Characterization of lamp poles in the DLR model

- **Presentation of Data Simulated by the DLR Software**

An analysis of harsh environments as they can be defined by the DLR model (suburban and urban) for several types of trajectories (fixed point, straight line displacement, displacement with a 90° turn) and for two types of dynamics (pedestrian and vehicle) has been realized by M3 Systems. Simulations of 60s duration have been performed for two real constellations to confirm the statistical validity of results. The constellations details are depicted in Table 3.1.

Table 3.1: Constellations simulated with the DLR model

	Constellation example No 1			Constellation example No 2		
Date and Time	01/03/2013 From 16:50 to 16:58			04/03/2013 From 08:50 to 08:56		
Position	2.23894°E / 48.88341°N			2.23894°E / 48.88341°N		
Visible GPS PRNs	PRN	Elevation	Azimuth	PRN	Elevation	Azimuth
	05	+48.6	198.0	01	+78.5	98.5
	07	+12.1	61.4	17	+32.0	308.9
	15	+41.8	294.5	23	+21.9	183.8
	21	+11.5	307.7	14	+16.2	38.4
	28	+53.7	106.0	28	+12.2	259.1
	08	+41.8	56.5	20	+69.3	252
	09	+55.7	249.4	11	+53.6	137.9
	27	+30.0	248.0	32	+78.9	62.1
	26	+82.9	353.7			

The simulations performed with the DLR model made it possible to reconstruct realistic conditions experienced in harsh environments. Table 3.2 summarizes the statistics of satellites visibility/masking for different environments, dynamics, trajectories and constellations. For each of the two constellations, the number of satellites that undergo either no LOS masking, or partial LOS masking or total LOS masking is shown. For all these cases, multipath is present.

Table 3.2: Summary of satellites visibility/masking statistics

Environment	Dynamics	Trajectory	Constel-lation	No LOS Masking (LOS+MPs)	Partial LOS Masking (LOS+MPs)	Total LOS Masking (MPs)
Suburban	Pedestrian	Fixed Point	No 1	3 (33%)	4 (44%)	2 (22%)
			No 2	1 (12%)	7 (88%)	0
		Straight Line	No 1	4 (44%)	5 (56%)	0
			No 2	4 (50%)	4 (50%)	0
		90° Turn	No 1	4 (44%)	5 (56%)	0
			No 2	4 (50%)	4 (50%)	0
	Vehicle (Car)	Fixed Point	No 1	3 (33%)	5 (56%)	1 (11%)
			No 2	4 (50%)	3 (37%)	1 (12%)
		Straight Line	No 1	3 (33%)	6 (67%)	0
			No 2	3 (37%)	5 (63%)	0
		90° Turn	No 1	5 (56%)	4 (44%)	0
			No 2	3 (37%)	5 (63%)	0
Urban	Pedestrian	Fixed Point	No 1	4 (44%)	3 (33%)	2 (22%)
			No 2	6 (75%)	1 (12%)	1 (12%)
		Straight Line	No 1	3 (33%)	3 (33%)	3 (33%)
			No 2	2 (25%)	6 (75%)	0
		90° Turn	No 1	2 (22%)	7 (78%)	0
			No 2	3 (37%)	5 (63%)	0
	Vehicle (Car)	Fixed Point	No 1	3 (33%)	3 (33%)	3 (33%)
			No 2	4 (50%)	4 (50%)	0
		Straight Line	No 1	3 (33%)	4 (44%)	2 (22%)
			No 2	5 (63%)	2 (25%)	1 (12%)
		90° Turn	No 1	4 (44%)	5 (56%)	0
			No 2	4 (50%)	4 (50%)	0

This analysis has led to the following conclusions:

- Regardless of the trajectory or the receiver dynamics, the harsher the environment, the higher the probability to experience powerful multipaths. However, due to the stochastic nature of parameters related to trees, buildings and lamp posts, sometimes a suburban environment may present some spots that are harsher than urban environment's spots.

- For the particular case of fixed points, the observed differences between several simulations for a given environment show that each simulation can be seen as a unique case or at least as statistically unpredictable.

- For the suburban environment, the satellites statistics are almost the same for the two simulated constellations (4±1 with no masking, 5±1 with partial masking, 0±1 with total masking). For the urban environment, the variability of the statistics for the two simulated constellations is more important (4±2 with no masking, 4±2 with partial masking, 1±2 with total masking). The harsher the environment is, the greater the probability to experience satellite masking.

- For trajectories different than fixed points, and given an environment, the nature of trajectories does not impact the statistics of the satellites much. Thus, no a-priori information on the satellites visibility/masking can be brought forth by the knowledge of the receiver trajectory.

  - **DLR Data Scenarios Used in Experiments**

Table 3.3 summarizes some data scenarios from the DLR model simulations that are used in the experiments that are performed to validate the proposed solutions.

Table 3.3: Scenarios of DLR data used for experiments

	Environment	Trajectory	Dynamics		Scenarios
Constellation No 1	Suburban	Straight Line	Pedestrian	Constant velocity (7km/h)	Scenario 1
				Constant acceleration (0.5 m/s^2)	Scenario 2
			Vehicle (Car)	Constant velocity (50km/h)	Scenario 3
				Constant velocity (90km/h)	Scenario 4
				Constant acceleration (2.5 m/s^2)	Scenario 5
	Urban	Straight Line	Pedestrian	Constant velocity (7km/h)	Scenario 6
				Constant acceleration (0.5 m/s^2)	Scenario 7
			Vehicle (Car)	Constant velocity (50km/h)	Scenario 8
				Constant velocity (90km/h)	Scenario 9
				Constant acceleration (2.5 m/s^2)	Scenario 10

- **Real GPS Signals Data Used in Experiments**

The real GPS signals that are used in the experiments were collected in urban, suburban, and foliage environments. Digitized signals from the radio frequency (RF) front-end of different GPS receivers are used. A receiver with a high gain antenna provides signals with improved carrier to noise ratio (C/N_0) values. A high C/N_0 results in a high post-correlation SNR which increases the probability of multipath detection (PD) and theoretically the performance of the detectors. The different receiver front-ends that are used generate digitized signals at different Intermediate Frequencies (IF) with different sampling frequencies (f_s). The digitized signals are used as signal source to the GPS software receiver described in sub-section 3.3.3.1, figure 3.24. The coherent integration time used during tracking for all signals is 1ms. This means that if a sliding window of *N=64* samples is used to set the detection tests, 64ms time delay results before the very first detection. With the signals synthesized by the DLR multipath model, it is possible to set in experimental simulation at what instant during tracking the multipath signals can be superimposed on the LOS signal. This allows an easy evaluation of the detectors performance. But with real signals, this is not possible as the provided digitized signal from the front-end is a mixture of the LOS and multipath signals already. It is therefore a challenge to know when false alarms or missed detections occur with real signals. The signals are just collected in environments that are prone to generate multipath contaminated signals. The use of fisheye cameras and 3D environment modelling approaches can be beneficial in this case and may be considered for future work.

3.3.4 EXPERIMENTAL RESULTS

Figure 3.28 illustrates the results of simulations used to validate the GLRT detection technique. First, simple simulations that are based on a DLL+PLL/VDLL+PLL tracking scheme and that make use of the two-ray multipath model (LOS + 1 MP) and not the DLR multipath model are performed. A multipath signal with the frequency of the LOS signal is set to appear after 2 seconds tracking time for a STL channel (DLL + second order PLL) and a VTL channel (VDLL + second order PLL) with bandwidths of 1 Hz and 10 Hz respectively. A coherent EmL DLL discriminator ($d = 0.5chip$) and an ATAN PLL discriminator are used. The coherent integration time is 10ms. The C/N_0 is set to 45 dBHz, a value corresponding to good satellite signal reception. PFA of 10^{-7} for the STL and of 10^{-4} for the VTL are used to set the detection thresholds. However, PFAs of 10^{-4} or 10^{-3} are still reasonable for both STL and VTL. A sliding window of $N = 30$ samples (corresponding to 300 ms time delay before the first detection for a coherent integration time of 10 ms) is used to set the detection test.

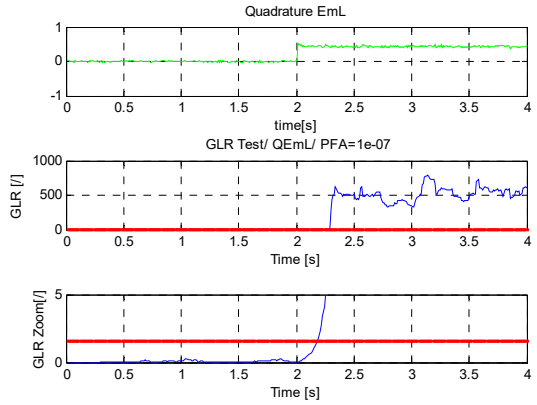

(a) Detection of MP signal ($\theta_M = 94.32^\circ$, $\delta_M = 0.3614 chip$, α=0.501) for a STL (DLL + PLL), C/N0=45dBHz.

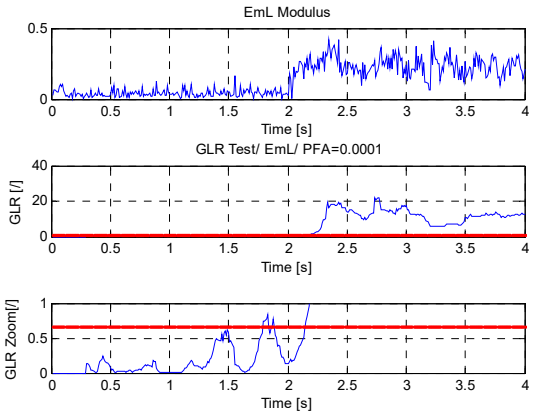

(b) Detection of MP signal ($\theta_M = 0^\circ$, $\delta_M = 0.1623 chip$, α=0.501) for a VTL (VDLL + PLL), C/N0=45dBHz.

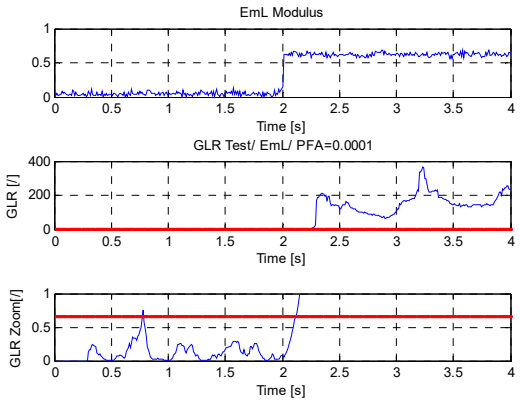

(c) Detection of MP signal ($\theta_M = 94.32^\circ$, $\delta_M = 0.6203 chip$, α=0.501) for a VTL (VDLL + PLL), C/N0=45dBHz.

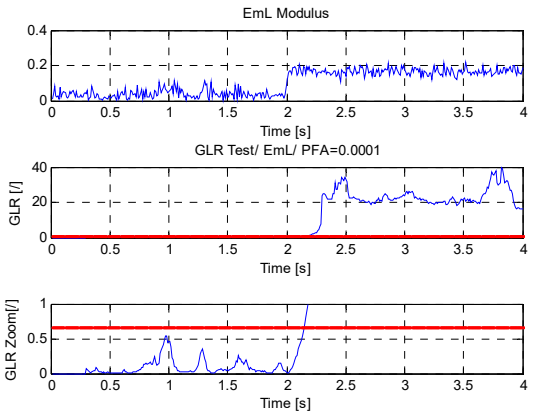

(d) Detection of MP signal ($\theta_M = 213^\circ$, $\delta_M = 0.1171 chip$, α=0.501) for a VTL (VDLL + PLL), C/N0=45dBHz.

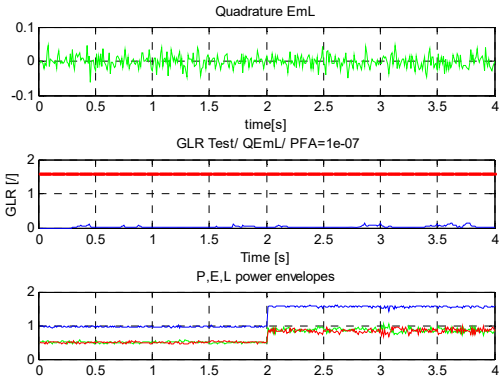

(e) Detection of MP signal ($\theta_M = 0^\circ$, $\delta_M = 0.1623 chip$, α=0.501) for a STL (DLL + PLL), C/N0=45dBHz.

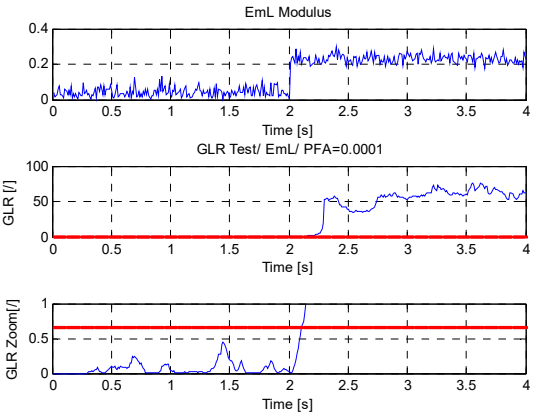

(f) Detection of MP signal ($\theta_M = 180^\circ$, $\delta_M = 0.1623 chip$, α=0.501) for a VTL (VDLL + PLL), C/N0=45dBHz.

Figure 3.28: GLRT detector validation on 2-ray multipath model, STL (DLL+PLL) and VTL (VDLL+PLL)

The suggested GLRT detector metric goes beyond threshold once a multipath signal appears and is superimposed onto the LOS signal (shortly after 2s tracking time) as shown in Figures 3.28(a), 3.28(c) and 3.28(d) proving that the GLRT detector performs well, in these optimum conditions. However, for a multipath arriving in phase ($\theta_M = 0^\circ$) or opposition of phase ($\theta_M = 180^\circ$) with the LOS signal as shown in Figures 3.28(b), 3.28(e) and 3.28(f), the Q_{EmL} output is blind to such MP for a STL. The GLRT detector defined for the STL will therefore not detect such a MP as shown in Figure 3.28(e). For a VTL, with a navigator that is not contaminated, when the Q_{EmL} output is blind to such MP, the I_{EmL} is not, and the GLRT defined for the VTL does detect the MP as illustrated in Figures 3.28(b) and 3.28(f).

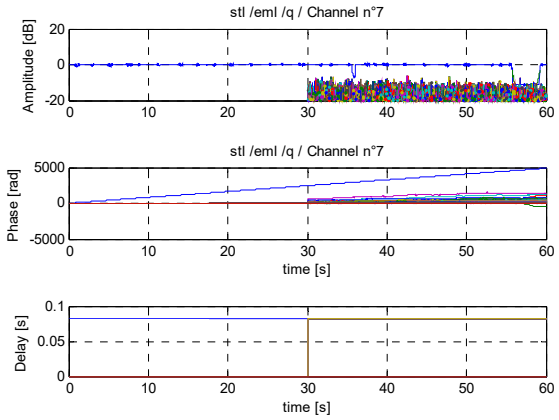

(a) Scenario 9 - Moving vehicle (90km/h) - urban environment, Chan7 (PRN09).

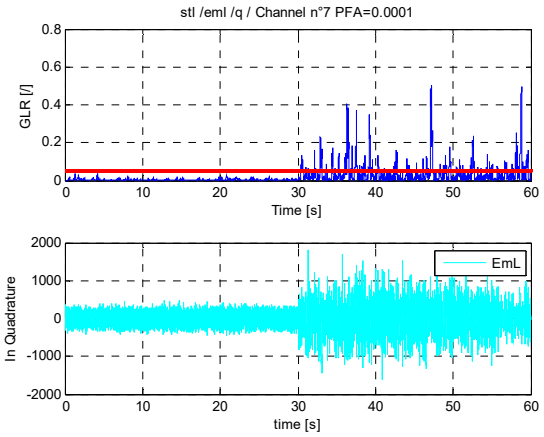

(b) Scenario 9 - Moving vehicle (90km/h) - urban environment, STL, Chan7 (PRN09), GLRT, N=300, PFA=10^{-4}.

Figure 3.29: GLRT detector validation on DLR multipath model, STL (DLL + FPLL)

Simulations are also performed using the GPS receiver simulator in Figure 3.23 with a STL (DLL + FPLL) and a VTL (VDFLL + navigator assisted PLL/FPLL) tracking scheme and the DLR multipath model. The scenarios depicted in the figures hereafter involve a pedestrian or a vehicle moving parallel to the buildings in urban, suburban or unconstrained (open sky) environments.

Figures 3.29(a), 3.30(a), 3.30(c), 3.30(e), 3.31(a), and 3.31(c) depict the parameters (amplitude, phase and delay) of the different signal paths (LOS and/or multipath) for the scenarios and channels under study. Amplitude values are normalized and expressed in dB, with the LOS amplitude having a maximum value of 1 (0 dB). The LOS amplitude is represented in blue in all figures depicting parameters. The LOS phase and delay parameters are represented either in blue or cyan colour. Carrier

phase is expressed in radians and code delay in seconds. Figures 3.29(a) and 3.29(b) show that the GLRT detector does not perform well on DLR MP signals as it does on the 2-ray MP model. The DLR multipaths do not have the same frequency as the LOS signal, thus the GLRT is expected to exhibit performance degradation. The MP parameters in Figure 3.29(a) show that the MP appears around the 30th tracking second out of the 60s tracking duration of the simulation. Figure 3.29(b) shows that there are some missed detections as the Q_{EmL} output in the presence of MP is not a constant signal but rather a signal with +/- fluctuations. However, the GLRT detector can still be used for its very low computational complexity to distinguish between relatively long periods of MP presence or absence.

The FFT-based detectors are analysed in Figures 3.30 and 3.31. Both Detectors I and II perform successfully as illustrated by figures 3.30(b), 3.30(d), 3.30(f), 3.31(b) and 3.31(e). Figure 3.30(a) through the displayed amplitude, phase and delay parameters shows the presence of many multipath signals apart from the LOS signal for a channel (labelled Channel 1) tracking a satellite (with PRN05 position, elevation and azimuth parameters in the DLR simulation) in STL mode for a duration of 60 seconds. Figure 3.30(b) shows the detection tests results for that channel. For simplicity of performance comparison between the two FFT-based detectors, a sliding window of N=1024 samples and PFA values of 10^{-4} (Detector I/M-GLRT) and 10^{-2} (Detector II) are used to calculate the test metric values and set the detection thresholds. The test metric values go above the defined thresholds meaning that the presence of multipath is detected for both Detectors I and II. The signal power observed on the Q_{EmL} arm, whose magnitude is higher than the signal power that would be observed in the absence of multipath (see Figure 3.30(f) for comparison), also confirms the presence of multipath. In fact, in the absence of multipath, only noise is observed on the Q_{EmL} arm. It is important to mention that for the first MP detection to be faster and for lower computational complexity (faster subsequent detections), smaller values of N such as N = 32, 64, 128, 256 can be used for Detector I (M-GLRT), some without compromising the detection capability in low SNR scenarios. N=1024 is used with Detector II for the sake of obtaining a frequency resolution of ~1 Hz, but again smaller values of N may be used with minimal risk of reduced detector performance.

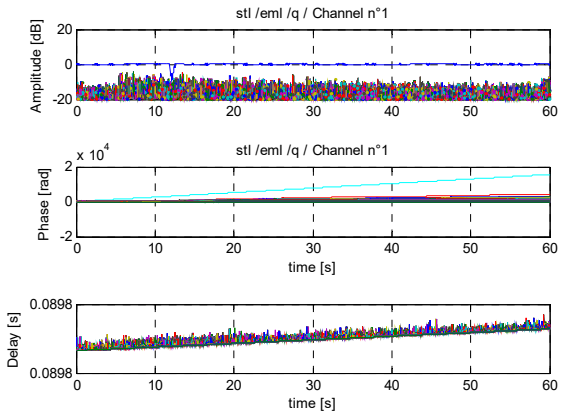

(a) Scenario 9 - Moving vehicle (90km/h) - urban environment, Chan1 (PRN05).

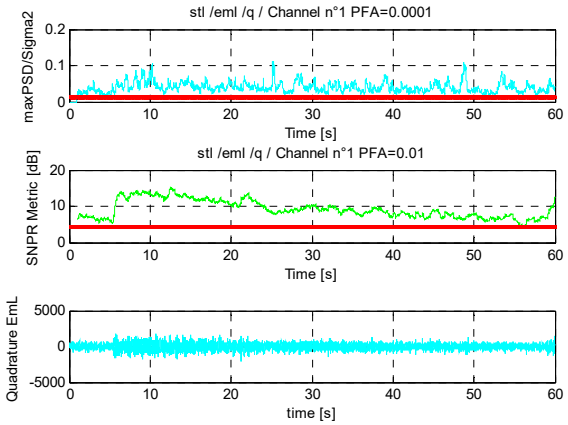

(b) Scenario 9 - Moving vehicle (90km/h) - urban environment, STL, Chan1 (PRN05), PFA=10^{-4} (Detector I/M-GLRT), PFA=10^{-2} (Detector II).

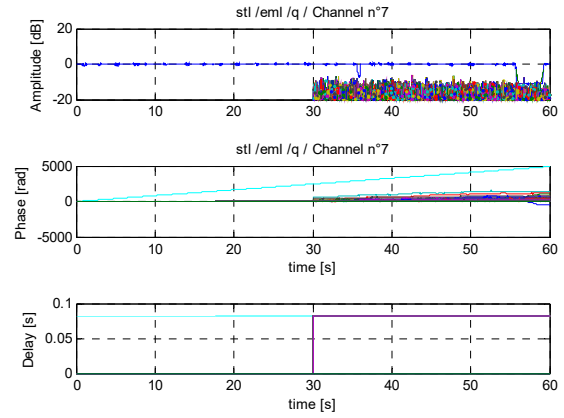

(c) Scenario 9 - Moving vehicle (90km/h) - urban environment, Chan7 (PRN09).

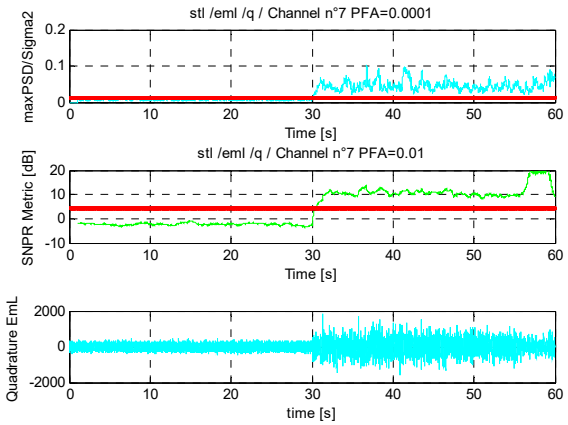

(d) Scenario 9 - Moving vehicle (90km/h) - urban environment, STL, Chan7 (PRN09), PFA=10^{-4} (Detector I/M-GLRT), PFA=10^{-2} (Detector II).

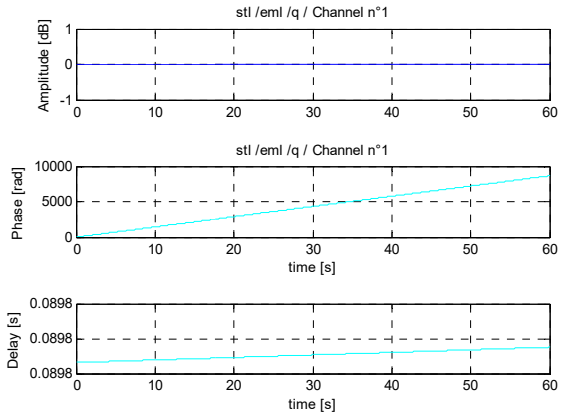

(e) Accelerating vehicle (2.5 m/s²) – open sky environment, STL, Chan1 (PRN05).

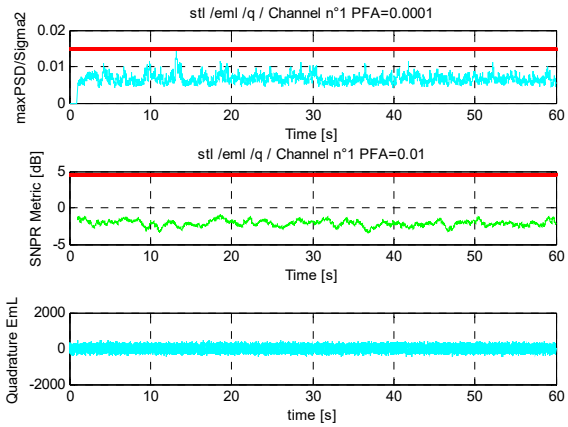

(f) Accelerating vehicle (2.5 m/s²) – open sky environment, STL, Chan1 (PRN05), PFA=10^{-4} (Detector I/M-GLRT), PFA=10^{-2} (Detector II).

Figure 3.30: Detector I (M-GLRT) and Detector II validation on DLR multipath model, STL (DLL + FPLL)

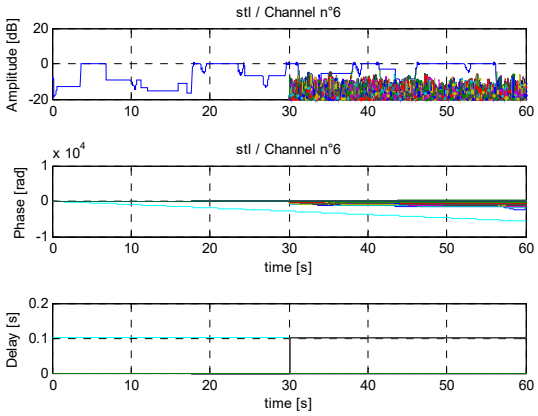

(a) Scenario 4 - Moving vehicle (90km/h) - suburban environment, Chan6 (PRN08).

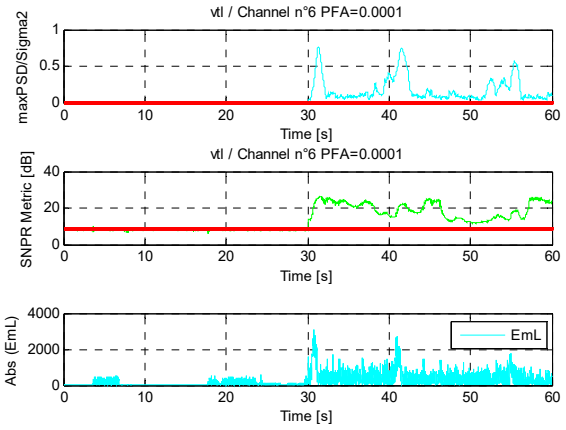

(b) Scenario 4 - Moving vehicle (90km/h) - suburban environment, VTL, Chan6 (PRN08), PFA=10^{-4} (Detector I/M-GLRT), PFA=10^{-4} (Detector II).

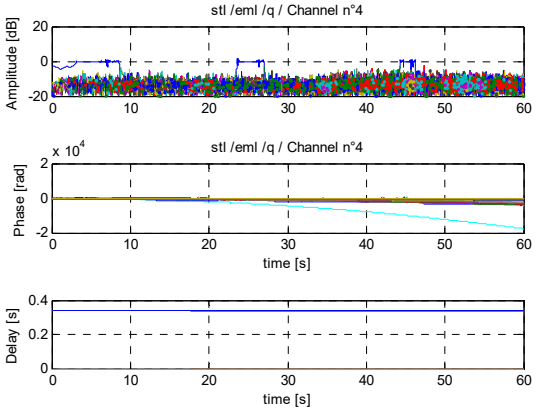

(c) Scenario 7 - Accelerating pedestrian (0.5 m/s^2) - urban environment, Chan4 (PRN21).

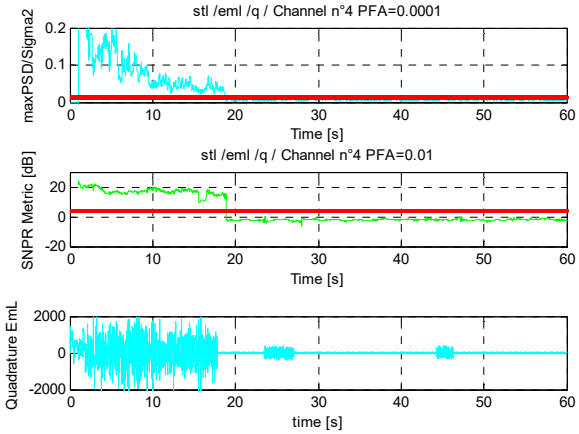

(d) Scenario 7 - Accelerating pedestrian (0.5 m/s^2) - urban environment, STL, Chan4 (PRN21), PFA=10^{-4} (Detector I/M-GLRT), PFA=10^{-2} (Detector II)

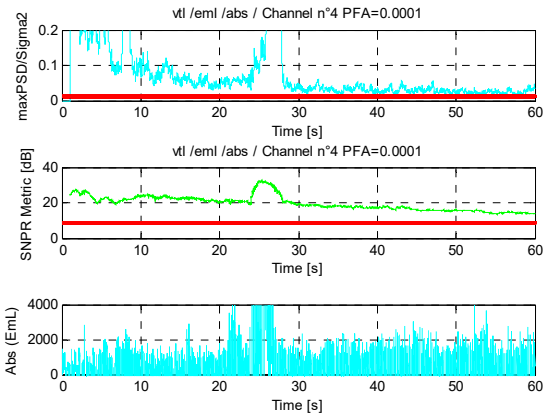

(e) Scenario 7 - Accelerating pedestrian (0.5 m/s^2) - urban environment, VTL, Chan4 (PRN21), PFA=10^{-4} (Detector I/M-GLRT and Detector II)

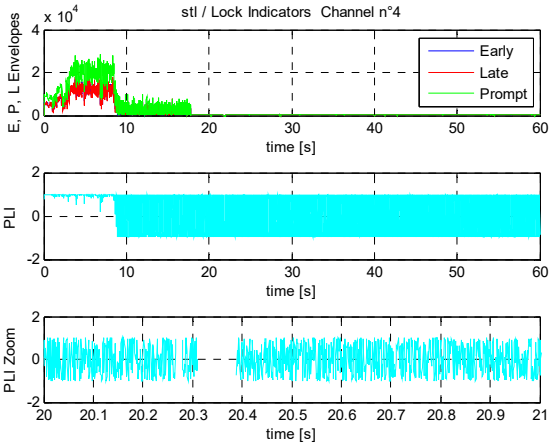

(f) Scenario 7 - Accelerating pedestrian (0.5 m/s^2) - urban environment, STL, Chan4 (PRN21), Lock Indicators

Figure 3.31: Detector I (M-GLRT) and Detector II validation on DLR multipath model, STL (DLL + FPLL), VTL (VDLL + navigator assisted PLL/FPLL)

Two other scenarios from the DLR multipath environment simulator are defined to allow multipath to appear around the 30th tracking second (see Figures 3.30(c) and 3.30(d) for STL - Channel 7 (PRN09) and Figures 3.31(a) and 3.31(b) for VTL - Channel 6 (PRN08)). The detectors perform as expected. The test metric values start below threshold for the 30 tracking seconds where only the LOS signal is present then go above threshold around the 30th second and the rest of the time. This is in accordance with the signal power increase on the Q_{EmL} arm (STL case) and the increase in the absolute value of *EmL* (VTL case) which also occur around the 30th tracking second. Figures 3.30(e) and 3.30(f) are a case of a car accelerating at 2.5 m/s^2 in an unconstrained environment (open sky) and the tracking mode is STL. The test metric values remain below the thresholds for both Detectors I and II, meaning that no multipath is detected as expected. The signal power on the Q_{EmL} arm remains minimal (made of noise only), which confirms the absence of multipath.

Figures 3.31(c), 3.31(d) and 3.31(e) illustrate detection test results for a pedestrian accelerating at 0.5 m/s^2 in an urban environment. They show the case of a channel that is severely affected by multipath. At time intervals where the LOS signal power is so weak in comparison with multipath signals power or where the LOS is absent, the detection tests in STL tracking mode fail to detect the presence of multipath as attested by observing Figures 3.31(a) and 3.31(b). In fact, the STL loses lock, which renders the detection tests useless. This is confirmed by the delay lock indicators and phase lock indicator (PLI) in Figure 3.31(f). The PLI fluctuates between -1 and 1 when phase lock is lost and retains a value around 1 when phase lock is achieved. Similarly, the magnitude of the prompt power envelope is about twice that of the early or late envelopes when delay lock is achieved. Figure 3.31(e) shows that the VTL manages to keep tracking the signal on the same severely affected channel in Figure 3.31(c) even at the time intervals where the LOS signal is absent or has very weak power. Detector I and II tests on the VTL even manage to succeed in detecting multipath where they couldn't with the STL tracking mode. This result is consistent with the VTL tracking robustness in multipath environments in comparison with the STL.

More experiments are conducted for the different DLR multipath scenarios (environment-trajectory-dynamics) in Table 3.3 to statistically formulate the expected percentages of false alarms and percentages of missed detections for both GLRT and FFT-based detectors applied to both STL and VTL tracking schemes. It is worth mentioning that the proposed detectors do not have the ability to evaluate the degree of tracking and positioning error caused by multipath. They are formulated to be able to detect presence or absence of multipath irrespective of the seriousness of the errors caused by the detected multipath. False alarm, missed detection and detection therefore retain the meaning that is given in Appendix 3.A. The step to decide for

hypothesis H_1 (multipath presence) only when multipath impact on positioning is very serious is another study altogether that is worth considering in future studies. Based on the obtained experimental results, the PFAs (thresholds) in Table 3.4 have been chosen as practical for maximizing the detection ability of each detector. These choices are based on empirical observation from examining the results of many different multipath scenarios. A theoretical formulation and justification of the PFA to use in order to define the appropriate threshold can be considered in future work.

Table 3.4: Chosen practical PFA (threshold) values

	PFA (STL)	PFA (VTL)
GLRT Detector	10^{-3} or 10^{-2}	10^{-4} or 10^{-3}
FFT Detector I	10^{-4} or 10^{-3}	10^{-4} or 10^{-3}
FFT Detector II	10^{-2} or 10^{-1}	10^{-4} or 10^{-3}

The recorded percentages of false alarms (% FA) and percentages of missed detections (% MD) with these chosen practical PFA (Threshold Values) used on the different DLR multipath scenarios are summarized in Table 3.5 for both GLRT and FFT-based detectors. It should be mentioned that these results are based on simulations of 60s tracking period to avoid several hours or days of simulation runtime. As the used multipath model has been defined with a probabilistic (statistical) and deterministic component, the variations in environmental factors that create multipath scenarios are significant enough for a duration of 60 seconds to be sufficiently representative of reality. The more variations in environment, trajectory and dynamics are considered in the experiments, the more meaningful the conclusions that are based on these experiments can be even if they only stem from 60s simulations. Of course, to further strengthen the detectors performance evaluation, longer tracking durations can be considered in the experiments.

Table 3.5: Summary of the statistical performances of the detectors

		GLRT		FFT Det. I		FFT Det. II	
Tracking loop		STL	VTL	STL	VTL	STL	VTL
% FA	Pedestrian Urban (0.5 m/s²)	1.39%	3.22%	1.18%	6.95%	0%	1.31%
	Vehicle Urban (90 km/h)	0.95%	0.36%	0.79%	0.20%	0%	0.02%
	Pedestrian Suburban (0.5 m/s²)	0.87%	4.06%	1.14%	9.23%	0%	0%
	Vehicle Suburban (50 km/h)	0.05%	2.05%	0.47%	3.11%	0%	0.08%
	Vehicle Suburban (90 km/h)	0.88%	0%	1.05%	1.12%	0%	7.20%
% MD	Pedestrian Urban (0.5 m/s²)	75.41%	70.09%	4.11%	3.72%	23.97%	7.20%
	Vehicle Urban (90 km/h)	59.31%	42.11%	0.39%	0.29%	1.12%	0.18%
	Pedestrian Suburban (0.5 m/s²)	72.19%	63.41%	0.37%	0.97%	0.85%	1.13%
	Vehicle Suburban (50 km/h)	59.68%	33.58%	0.94%	0.15%	11.10%	2.71%
	Vehicle Suburban (90 km/h)	62.16%	53.76%	0.40%	0.46%	2.14%	1.24%

Table 3.5 shows that the GLRT detector is not efficient enough to provide good performance for real-life scenarios. However, FFT-based detectors can be used effectively to spot multipath effect.

FFT-based Detector I (M-GLRT) is also tested on real GPS signals collected in multipath-prone environments. The GPS receiver in Figure 3.24 only has STL tracking capability (DLL + PLL and DLL+FPLL), so only FFT-based STL-MP Detector I is tested hereafter. Figures 3.32(a), 3.32(b) and 3.32(c) are a case of a moving vehicle in a heavy foliage environment, where the detection test threshold is set with PFA=10^{-1}, PFA=10^{-3} and PFA=10^{-5}. The tracking mode is scalar (STL). A tracking duration of 20 seconds is studied. This is a case of a weak signal (low C/N_0). The probability of multipath detection with a low PFA is low for a low post-correlation SNR. Figure 3.32(c) represents the same channel as Figure 3.32(a) but compares the signal power on the quadrature arm of EmL with that of the in-phase prompt arm. For this scenario, the in-phase prompt arm shows that navigation data demodulation is not achieved which means that low C/N_0 has not made it possible to maintain proper delay and phase lock. The figures show that PFAs of 10^{-3} or 10^{-5} (which are appropriate PFA values to avoid false detections) fail to detect multipath on channels 1 and 2 which are tracking the GPS satellites SV1 and SV20 respectively. With a PFA of 0.1 however, multipath is detected on both channels. A PFA of 0.1 is not recommended because this results in several false detections. It appears however that for a very weak signal, only a high PFA achieves multipath detection for a STL. Depending on whether the number of visible satellites at a given time is enough to compute a navigation solution, a high PFA can be chosen in order to increase the chance of excluding all multipath affected satellites, and a lower PFA may be chosen to more likely exclude only the ones that are severely affected. Figure 3.32(d), 3.33(a) and 3.33(c) show scenarios of a moving vehicle in a suburban environment, and the test is set with PFA=10^{-1}, PFA=10^{-3} and PFA=10^{-5}. The C/N_0 is high enough to get multipath detections with PFA=10^{-3} even with PFA=10^{-5} in some cases on channels 4 and 7 which are tracking satellites SV22 and SV3 respectively.

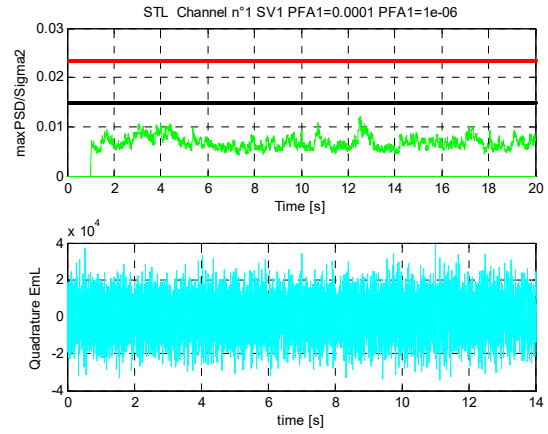

(a) Moving vehicle – foliage environment, STL, SV1, low C/N_0, IF = 0 MHz, f_s = 26 MHz, Detector I.

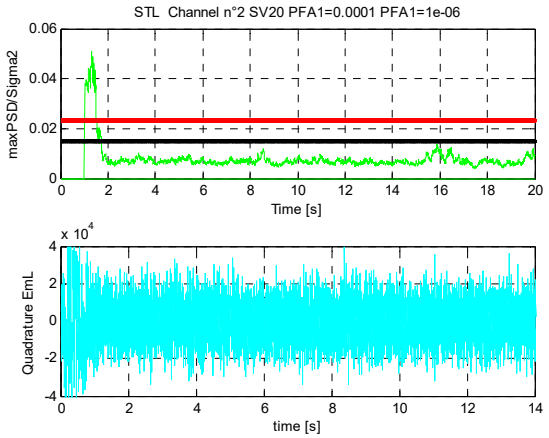

(b) Moving vehicle – foliage environment, STL, SV20, low C/N_0, IF = 0 MHz, f_s = 26 MHz, Detector I.

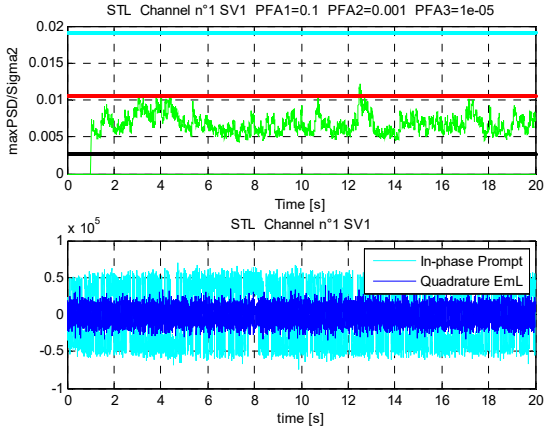

(c) Moving vehicle – foliage environment, STL, SV1, low C/N_0, IF = 0 MHz, f_s = 26 MHz, Detector I.

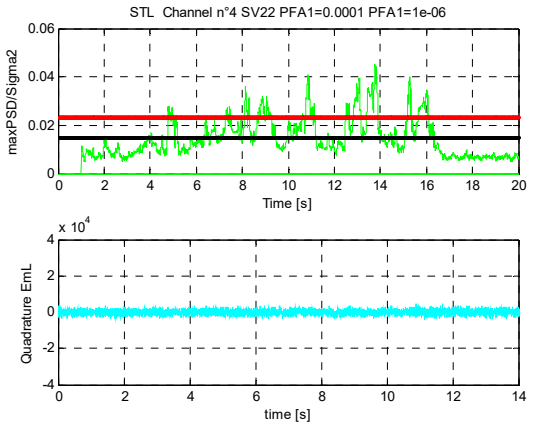

(d) Moving vehicle – suburban environment, STL, SV22, high C/N_0, IF = 9.548 MHz, f_s = 38.192 MHz, Detector I.

Figure 3.32: Detector I (M-GLRT) validation on real GPS multipath signals, STL (DLL + FPLL)

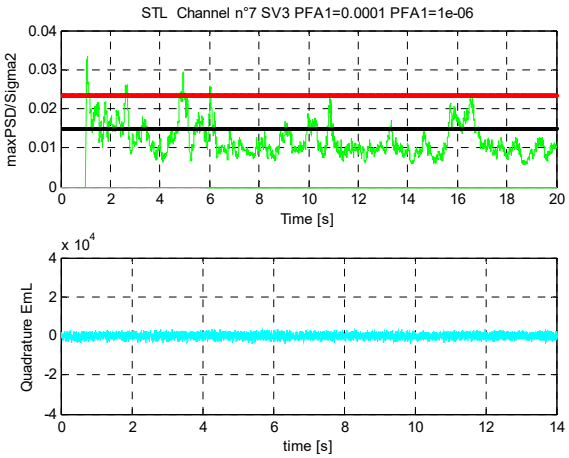

(a) Moving vehicle – suburban environment, STL (DLL + FPLL), SV3, high C/N_0, IF = 9.548 MHz, f_s = 38.192 MHz, Detector I.

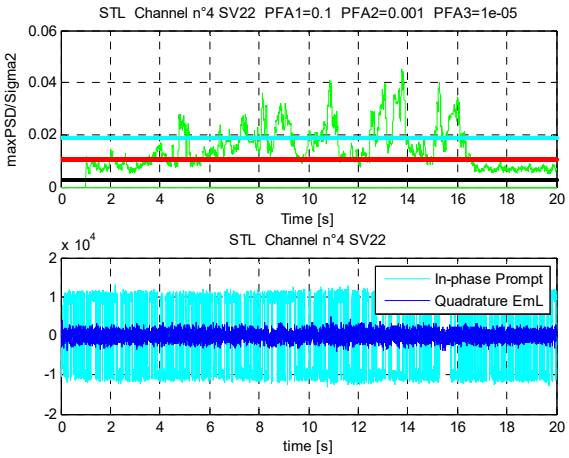

(b) Moving vehicle – suburban environment, STL (DLL + FPLL), SV22, high C/N_0, IF = 9.548 MHz, f_s = 38.192 MHz, Detector I.

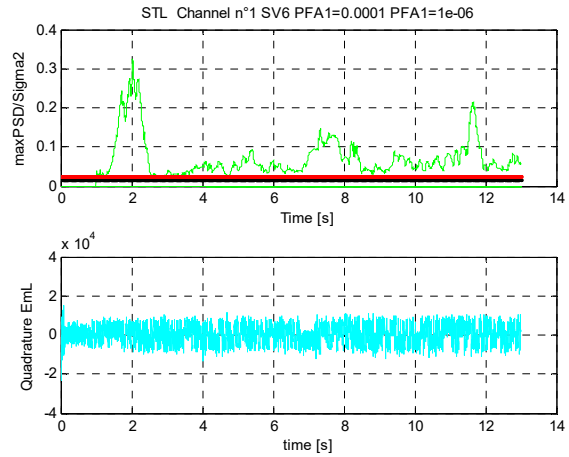

(c) Fixed point – urban environment, STL (DLL + PLL), SV6, high C/N_0, IF = 1.25 MHz, f_s = 5 MHz, Detector I.

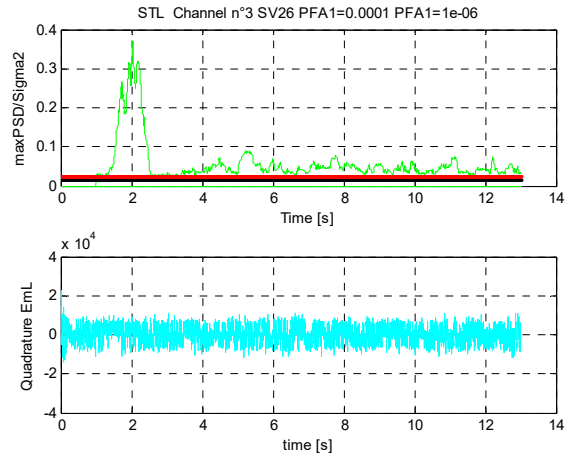

(d) Fixed point – urban environment, STL (DLL + PLL), SV26, high C/N_0, IF = 1.25 MHz, f_s = 5 MHz, Detector I.

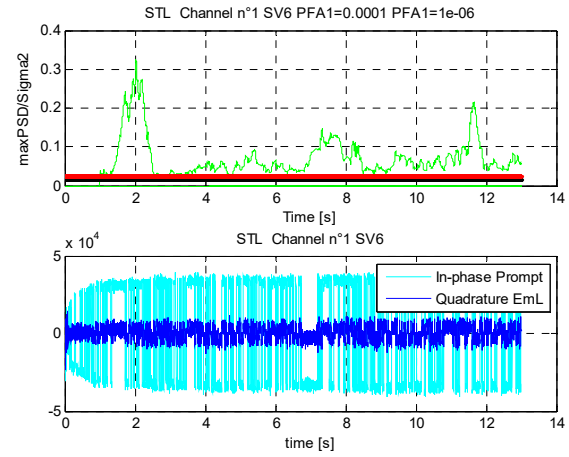

(e) Fixed point – urban environment, STL (DLL + PLL), SV6, high C/N_0, IF = 1.25 MHz, f_s = 5 MHz, Detector I.

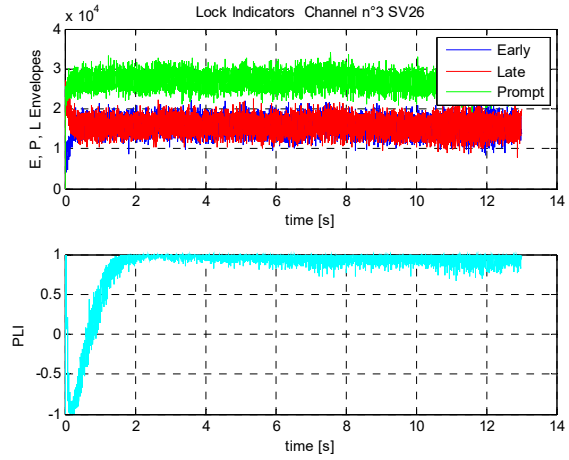

(f) Fixed point – urban environment, STL (DLL + PLL), SV26, high C/N_0, IF = 1.25 MHz, f_s = 5 MHz, Lock Indicators.

Figure 3.33: Detector I (M-GLRT) validation on real GPS multipath signals, STL (DLL + PLL, DLL + FPLL)

Figure 3.33(c), 3.33(d) and 3.33(e) show the results of a fixed point in an urban environment. The processed signal has high C/N_0. PFAs of 10^{-4} and 10^{-6} which are low enough to avoid false detections are used. Multipath is detected almost for the whole 13 seconds tracking duration on channels 1 and 3 tracking satellites SV6 and SV26 respectively. Figure 3.33(f) illustrates the delay and phase lock indicators for the scenario of a fixed point in urban environment of Figure 3.33(d). The prompt, early and late power envelopes show that code delay lock is achieved and maintained. Also, the PLI values remain around 1 which indicates maintained phase lock even though multipath is present.

It was stated earlier in this chapter that diffuse multipaths affect the received signal quality by degrading the C/N_0. The performance analysis of multipath detectors conducted on real GPS signals for the STL shows that a diffuse multipath affected signal that is received with very low C/N_0 may not be easily spotted as multipath contaminated by the suggested detectors unless the threshold is lowered. However, the fact that it is received with very low C/N_0 can be exploited to exclude it from PVT solution calculation using other types of signal quality indicators. The other types of correlator-based signal quality indicators that can be used in conjunction with MP detectors, namely the C/N_0 estimator, the non-line-of-sight (NLOS) indicator, and the phase lock indicator (PLI) are discussed in the next section. Specular multipaths on the other hand produce a bias on pseudorange and delta-range measurements when their frequency is in the frequency band of the receiver. This is particularly true for fixed receivers or receivers moving parallel to the surface that reflects the multipaths. The studied scenarios with real GPS signals for a fixed point have shown that the multipath affected signal is received with high C/N_0, which means that the multipath is more likely to be specular. Therefore, although code and phase lock are maintained, and although navigation data demodulation is achieved, there still is a bias in the measured pseudorange and delta-range. The choice to exclude or use a given satellite from PVT computation will depend on the number of available satellites, as well as the evaluation of the degree of multipath contamination through lowering or rising of detection thresholds. Also, to ensure that good satellite geometry is maintained, a step that involves computation and verification of the dilution of precision after every satellite exclusion can be incorporated in the navigator. The application of the proposed detectors will therefore have greater significance in multi-constellation GNSS receivers. Furthermore, to ensure a good analysis of multipath and NLOS situations on real GPS signals, these detectors can be incorporated in solutions that are based on 3D environment modelling and that use fisheye camera data to improve GPS localization. The works in [62] [63] [64] use fisheye and 3D modelling based approaches.

3.4 Other Correlator-Based Signal Quality Indicators

3.4.1 Non-Line-Of-Sight (NLOS) or LOS Attenuation Detector

NLOS reception occurs when the LOS signal is blocked and only a reflected signal is received. This is frequent in urban environments with very tall buildings. Figure 3.34, which is taken from [65], illustrates the difference between NLOS reception and multipath interference. NLOS reception is another important source of positioning error in GNSS. The NLOS induced ranging measurement error characteristics are different from multipath induced ranging measurement error characteristics. A comparison between NLOS and MP reception is provided in [65]. NLOS and MP require different mitigation techniques. Dual polarization NLOS detection technique is discussed in [66]. This technique correlates the right hand circularly polarized (RHCP) and left hand circularly polarized (LHCP) outputs of a dual-polarization antenna separately and determines a separate C/N_0 for each polarization. It then subtracts the LHCP C/N_0 measurement from the RHCP C/N_0 measurement. The result is positive for directly received signals and negative for most NLOS signals.

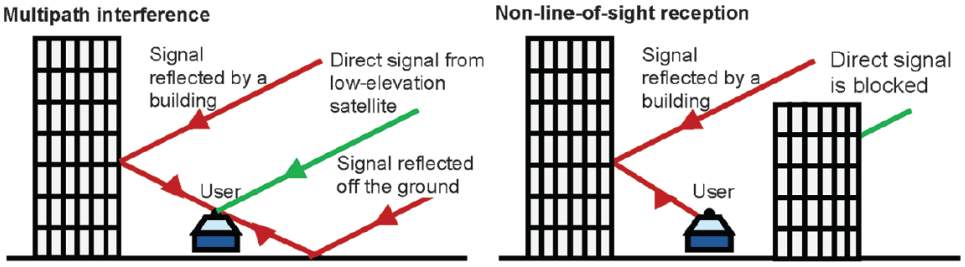

Figure 3.34: Multipath interference and NLOS reception

A LOS attenuation detector is proposed hereafter using the prompt correlator output. The complex prompt correlator output is often used to determine the carrier-to-noise power ratio (C/N_0) as it will be seen in the next sub-section. It can also give an indication on the power of the received LOS signal if the frequency domain is used. In fact, by evaluating the power spectral density (PSD) of the prompt correlator output and using a Fast Fourier Transform (FFT)-based frequency discriminator, it is possible:

- To detect the presence of the LOS signal;
- To measure the frequency error;
- To measure the power of noise and, in the absence of interference, the power of the LOS signal;
- To measure the power of interference and to characterise the frequency distribution of interference.

By assuming absence of interference, the FFT-based detector can be applied to detection of the presence of the LOS signal. Only the in-phase prompt (I_P) correlator output is exploited in the detector metric to reduce the complexity of FFT calculation. However, in-phase and quadra-phase prompt correlator outputs can be conjointly used as they provide information on the LOS signal power especially in case carrier tracking is disturbed and the prompt power switches between the in-phase and quadra-phase arms. The proposed detector computes the periodogram (PSD estimator) on the in-phase prompt output as

$$\Omega(m) = \frac{1}{N}\left|I_P(m)\right|^2 \quad where \quad I_P(m) = \sum_{n=n_0}^{n_0+N-1} I_P(n) e^{-j\frac{2\pi mn}{N}} \tag{3.76}$$

$I_P(m)$ is the discrete Fourier transform of $I_P(n)$ and is implemented via an N-point FFT algorithm. With this approach, the power spectrum density is calculated for each frequency point. The magnitude of $\Omega(m)$ is the power density at the associated frequency point. The point at the maximum magnitude should contain the desired LOS signal while the rest of the points contain noise. In weak signal conditions, the signal could be buried in noise in the time domain. However, in the frequency domain, noise power is spread over the entire frequency band and the single tone signal power is concentrated on a single frequency point. FFT processing makes the power density of the desired signal stronger than that of noise, which makes detection of the LOS signal in the frequency domain possible even when its power is weak. The detector chooses the largest magnitude value of $\Omega(m)$ and compares it against a threshold η. The detection test to decide for H_0 (absence of strong LOS signal) or H_1 (presence of strong LOS signal) is therefore formulated as

$$\max\left(\Omega(m)\right) \underset{H_1}{>} \eta \quad or \quad \max\left(\Omega(m)\right) \underset{H_0}{<} \eta \tag{3.77}$$

This detector therefore can detect NLOS as well as severe LOS attenuation conditions. A properly chosen threshold can indeed consider cases of very weak LOS power as LOS absence. The threshold η can be determined using Monte-Carlo simulations. It can be useful to strengthen the use of this detector by utilizing a C/N_0 estimator in conjunction. The indications on the estimated C/N_0 can confirm whether a decision for absence of LOS is justified or not.

Figure 3.35 illustrates two scenarios where this LOS detection test is applied. The figure represents LOS and MP signals amplitudes as well as the NLOS detector metric. The detection metric is set in dBW/Hz. The study of many scenarios has shown that a threshold of 0 dBW/Hz is able to distinguish between NLOS and LOS situations. In Figure 3.35 a threshold of 0 dBW/Hz is chosen. The LOS presence is detected from 0 to 50 seconds tracking time. After 50 seconds, an NLOS reception is

registered and the detector's metric remains below threshold. In Figure 3.35, for the NLOS condition, the LOS signal amplitude has been set to a very low value.

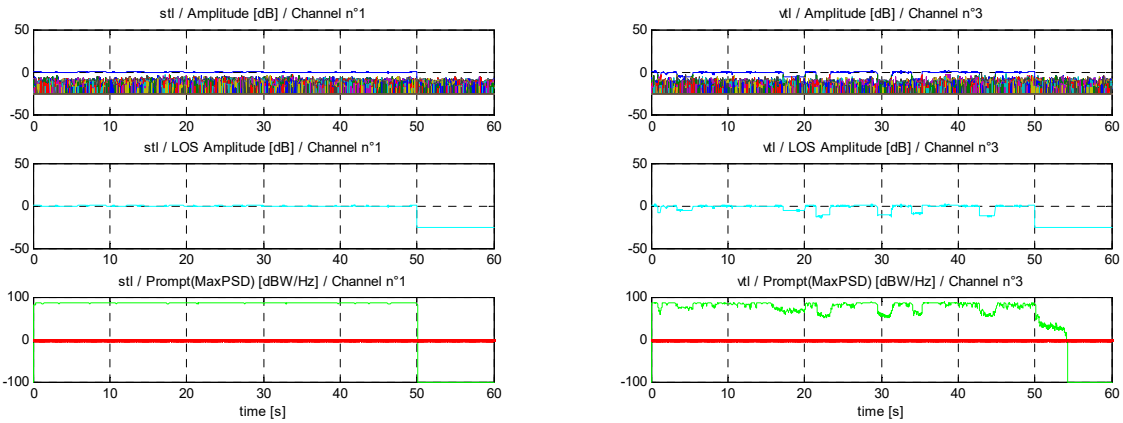

Figure 3.35: NLOS detection.

3.4.2 C/N$_0$ ESTIMATORS

Carrier-to-Noise power ratio (C/N$_0$) estimators can also be used as LOS attenuation indicators. In fact, C/N$_0$ estimates are considered as the most important quality control parameter in GNSS receivers. Apart from its role as a significant parameter to accept or reject satellite observations in the PVT solution, accurate C/N$_0$ estimation is required for the following tasks:

- Quantifying the performance of algorithms proposed for weak GNSS signals.
- Allowing the correct functioning of algorithms that use C/N$_0$ estimates as a measure of thermal noise. These include tracking and positioning algorithms of the Kalman Filter (KF) family.

Three low complexity C/N$_0$ estimators are briefly described hereafter: the Standard Estimator or Narrowband-Wideband Power Ratio Method, the Moments Method, and Beaulieu's Method. The theoretical performance evaluation of these GNSS C/N$_0$ estimators can be found in [67] and [68].

- **Standard Estimator**

It involves the evaluation of the total power of the Prompt correlator output over two different noise bandwidths, a wideband power measurement taken over the noise bandwidth $1/T_{\text{int}}$,

$$WBP_k = \sum_{m=1}^{M}\left(\left(I_p[kM+m]\right)^2 + \left(Q_p[kM+m]\right)^2\right), \quad k = 0,1,\ldots,\left(\frac{N}{M}-1\right) \tag{3.78}$$

and a narrowband power measurement taken over the noise bandwidth $1/MT_{\text{int}}$,

$$NBP_k = \left(\sum_{m=1}^{M} I_p[kM + m] \right)^2 + \left(\sum_{m=1}^{M} Q_p[kM + m] \right)^2, \quad k = 0,1,...,\left(\frac{N}{M} - 1 \right) \tag{3.79}$$

The narrowband to wideband power ratio at discrete time k gives an estimate of the noise power as

$$NP_k = \frac{NBP_k}{WBP_k} \tag{3.80}$$

The C/N_0 estimator is given by

$$\frac{C}{N_0} = \frac{1}{T_{\text{int}}} \frac{\mu_{NP} - 1}{M - \mu_{NP}}, \quad where \quad \mu_{NP} = \frac{M}{N} \sum_{k=0}^{N/M-1} NP_k \tag{3.81}$$

where N is the number of data bit periods over which the averaging is performed, $M = T_{bit} / T_{\text{int}}$ is the number of samples per navigation bit, T_{bit} is the navigation bit duration, and T_{int} is the coherent integration time. For correct implementation, it is necessary that the powers of I-Q outputs are measured in absence of bit transitions; otherwise the estimation might vary significantly, causing an error on the C/N_0 estimate.

- **Moments Method**

It is based on the second- and fourth-order moments of the input process to obtain a separate estimation of the carrier and noise strength in additive white Gaussian noise (AWGN) channels. Let $s[n] = I_p[n] + jQ_p[n]$ be the complex signal (process) at the Prompt correlator output. The theoretical formulations of the 2nd and 4th order moments of this process are $M_2 = E\left\{ |s[n]|^2 \right\}$ and $M_4 = E\left\{ |s[n]|^4 \right\}$. Based on these moments, signal power and noise power are defined respectively as $P_s(M_2, M_4) = \sqrt{2M_2^2 - M_4}$ and $P_n(M_2, M_4) = M_2 - P_s(M_2, M_4)$. The statistical moments M_2 and M_4 are estimated by their respective averages:

$$\hat{M}_2 = \frac{1}{N} \sum_{l=1}^{N} |s[l]|^2 \quad and \quad \hat{M}_4 = \frac{1}{N} \sum_{l=1}^{N} |s[l]|^4 \tag{3.82}$$

And the C/N_0 estimate is therefore given by

$$\frac{C}{N_0} = \frac{\hat{P}_s\left(\hat{M}_2, \hat{M}_4\right)}{\hat{P}_n\left(\hat{M}_2, \hat{M}_4\right)} \tag{3.83}$$

- **Beaulieu's Method**

This method is motivated by an intuitive formulation of the signal and noise power components estimates. The C/N_0 estimator is given by

$$\frac{C}{N_0} = \left[\frac{1}{N} \sum_{l=1}^{N} \frac{\hat{P}_{n,l}}{\hat{P}_{s,l}} \right]^{-1} \tag{3.84}$$

where

$$\hat{P}_{s,l} = \frac{1}{2} \left\{ \left(I_p[l] \right)^2 + \left(Q_p[l] \right)^2 \right\} = \frac{1}{2} \left\{ \left(I_p[l] \right)^2 + \left(I_p[l-1] \right)^2 \right\}$$

$$\hat{P}_{n,l} = \left(\left| I_p[l] \right| - \left| Q_p[l] \right| \right)^2 = \left(\left| I_p[l] \right| - \left| I_p[l-1] \right| \right)^2 .$$

$I_p[l-1]$ is assumed to have the same statistics as $Q_p[l]$ and the factor ½ is due to the 1-dimensional modulation (Binary Phase Shift Keying: BPSK instead of Quadrature Phase Shift Keying: QPSK). Figures 3.36 and 3.37 show C/N_0 estimates using the 3 methods described above. DLR LOS and MP parameters are provided then the associated C/N_0 estimations are displayed. An important observation to make is that MP presence reduces the C/N_0 value (see Figure 3.36). The absence of LOS signal is clearly spotted by the C/N_0 estimators (see Figure 3.37). Here, the estimators are set to return a value of 0 in the absence of a LOS signal.

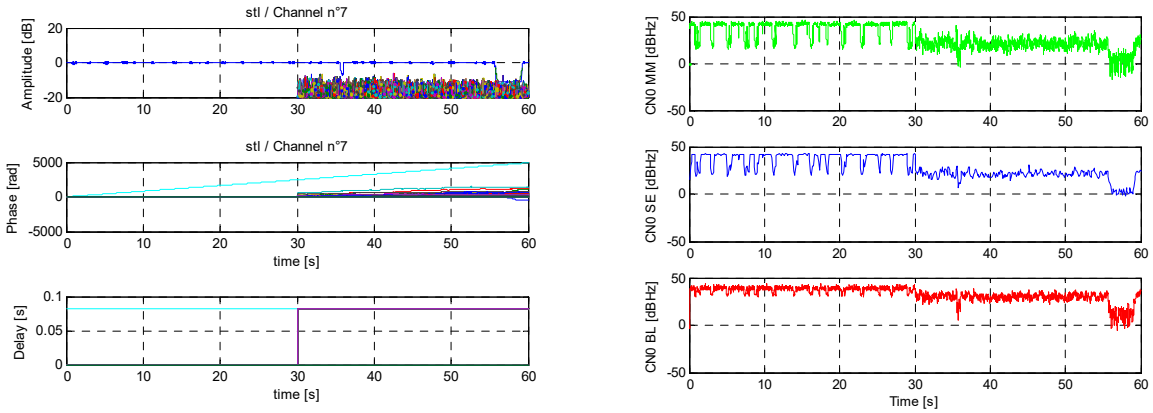

Figure 3.36: LOS + MP Parameters (left), CN_0 estimators (right), Case 1

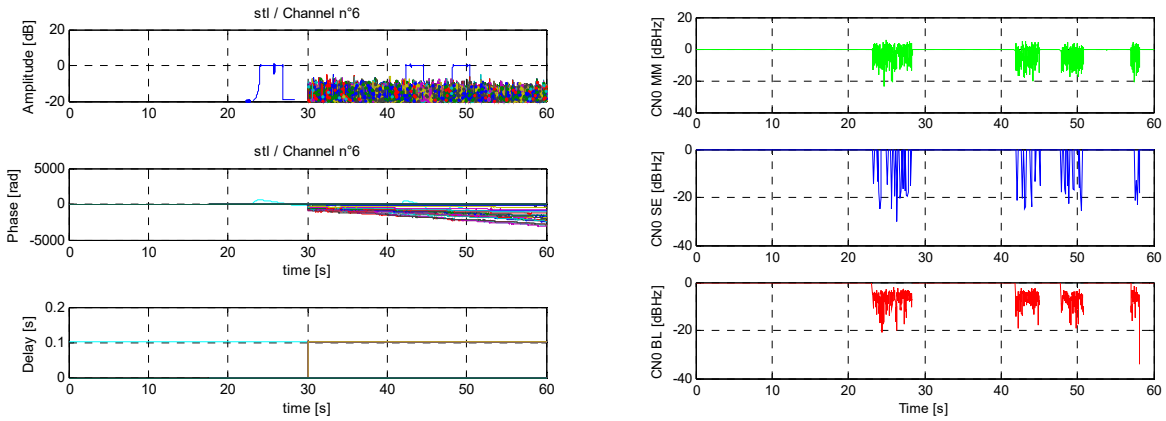

Figure 3.37: LOS + MP Parameters (left), CN_0 estimators (right), Case 2.

3.4.3 PHASE LOCK INDICATOR (PLI)

Phase lock detection is performed using the Prompt correlator output. The standard phase lock indicator (PLI) is defined in [69]. It is based on the fact that when the PLL is tracking the incoming signal's carrier correctly, the in-phase Prompt output has maximum power and the quadrature output has minimum power. This PLI is computed using the normalized estimate of the cosine of twice the carrier phase. To derive the mathematical expression of the PLI, it is important to look at the mathematical expressions of the in-phase (I_P) and quadrature (Q_P) outputs of the Prompt correlator in the PLL. The Costas PLL is illustrated again in Figure 3.38.

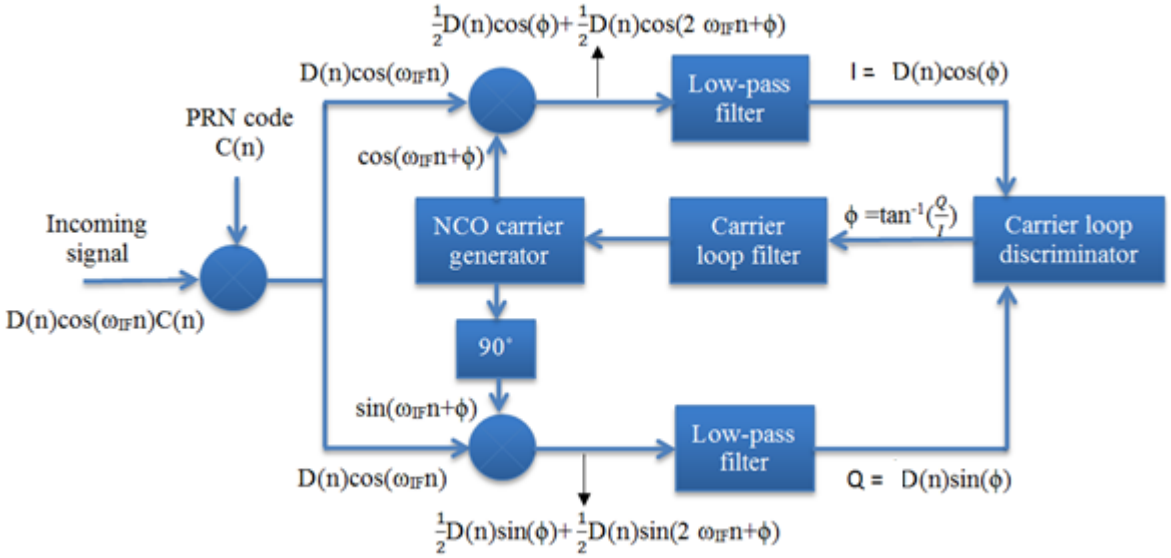

Figure 3.38: Phase locked loop (PLL)

Using the double-angle cosine trigonometric identity, the cosine of twice the carrier phase ϕ is given by

$$\cos(2\phi) = \cos^2\phi - \sin^2\phi \tag{3.85}$$

From Figure 3.38, it is observed that

$$Q_p = D(n)\sin\phi \quad and \quad I_P = D(n)\cos\phi$$

Therefore,

$$I_P^2 - Q_P^2 = D(n)^2\cos^2\phi - D(n)^2\sin^2\phi \quad and \quad I_P^2 + Q_P^2 = D(n)^2\cos^2\phi + D(n)^2\sin^2\phi$$
$$\therefore \quad I_P^2 - Q_P^2 = D(n)^2\left(\cos^2\phi - \sin^2\phi\right) \quad and \quad I_P^2 + Q_P^2 = D(n)^2\left(\cos^2\phi + \sin^2\phi\right) = D(n)^2$$
$$\therefore \frac{I_P^2 - Q_P^2}{I_P^2 + Q_P^2} = \frac{D(n)^2\left(\cos^2\phi - \sin^2\phi\right)}{D(n)^2} = \cos^2\phi - \sin^2\phi = \cos(2\phi)$$

The PLI is therefore given by

$$PLI = \cos(2\phi) = \frac{I_P^2 - Q_P^2}{I_P^2 + Q_P^2} \tag{3.86}$$

Usually in a PLL, the low-pass filter is implemented via an Integrate-and-Dump operation, which means that the I_P and Q_P outputs in Figure 3.38 are normally integrated-and-dumped results. The PLI at time n after an integration of M correlator samples is therefore the ratio between the narrowband difference NBD (i.e. difference of squares of I_P and Q_P) and the narrowband power NBP, as shown in the following expression:

$$PLI(n) = \frac{NBD(n)}{NBP(n)} = \frac{\left(\sum_{i=1}^{M} IP_i\right)_n^2 - \left(\sum_{i=1}^{M} QP_i\right)_n^2}{\left(\sum_{i=1}^{M} IP_i\right)_n^2 + \left(\sum_{i=1}^{M} QP_i\right)_n^2} \tag{3.87}$$

When the PLL is in lock, $\phi \approx 0 \quad \therefore \cos(2\phi) \approx 1$, the PLI value is thus around 1, otherwise the PLI value oscillates between -1 and 1. Figure 3.39 illustrates a tracking channel whose STL tracking is maintained for 60 s, as can be attested by the Prompt, Early and Late power envelopes and the PLI indicator, mainly due to a strong LOS signal. Multipath is present between 30 and 60s. Such a channel is a good candidate for STL or VTL tracking mode. Between 0 and 30 s, it is an excellent candidate for PVT computation. However, between 30 and 60 s, multipath presence makes it a probable candidate for exclusion from PVT computation, depending on whether the multipath

detector can spot this multipath contamination and whether there are enough healthy satellites. Figure 3.40 on the other hand illustrates a channel with very weak LOS power whose STL tracking cannot be maintained, irrespective of multipath presence or absence. The power envelopes and PLI indicator show this clearly. Such a channel is a good candidate for VTL tracking, a good enough candidate for PVT computation in VTL mode between 0 and 30 s as long as the LOS has sufficient power. Due to MP presence and weak LOS power, it is a highly probable candidate for exclusion from PVT computation between 30 and 60 s, depending on the performance of multipath detectors and the number of healthy satellites.

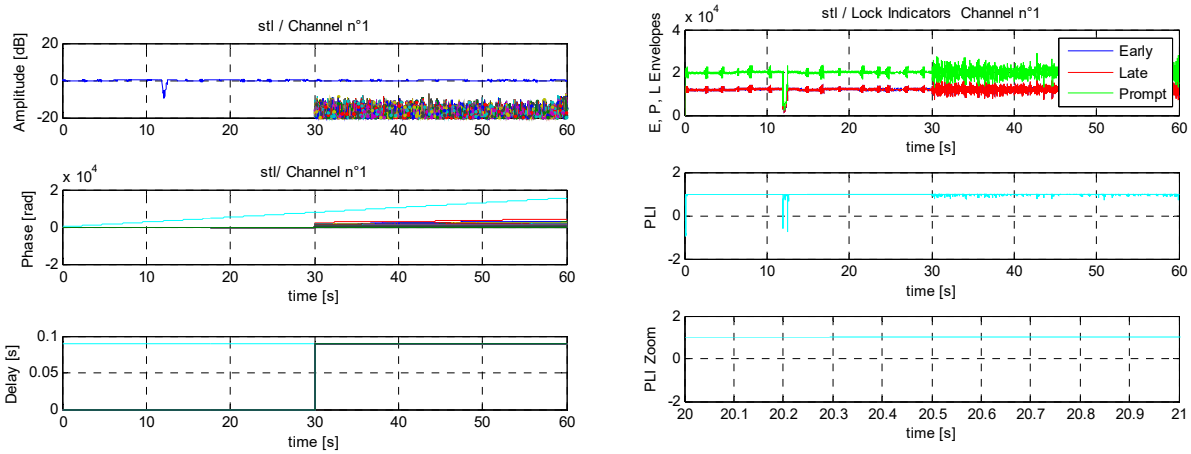

Figure 3.39: LOS + MP Parameters (left), Lock Indicators (right), Case 1.

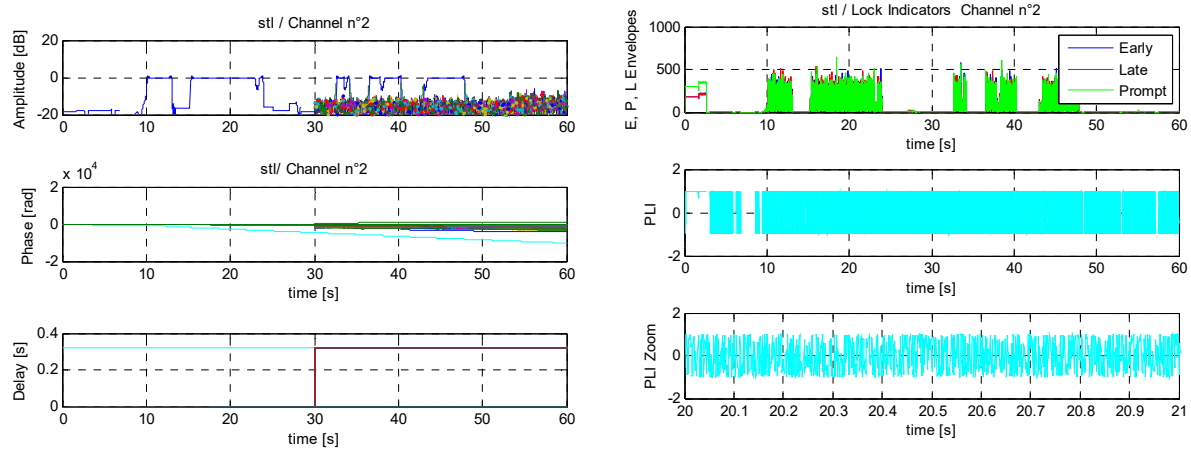

Figure 3.40: LOS + MP Parameters (left), Lock Indicators (right), Case 2.

3.5 CONCLUSION

The GPS receiver does not operate normally in multipath environments. Multipath induces tracking errors in both code and carrier tracking loops. The multipath induced code delay tracking error is directly linked with the multipath induced pseudorange measurement error and hence with the position error. Similarly, the multipath induced carrier frequency tracking error produces delta range measurement errors and consequently velocity errors. This phenomenon is true for both scalar and vector tracking loops but is manifested differently. This chapter has suggested GLRT and FFT-based multipath detection techniques for a GPS receiver. Application of the detection techniques to synthesized signals on correlator outputs of the code and carrier tracking loops (STL or VTL) demonstrate their efficiency in detecting multipath contaminated tracking channels. The GLRT detector is blind to multipath signals that arrive in phase or opposition of phase with the LOS signal for the STL case. This blindness to multipath that is in phase or opposition of phase with the LOS is however not observed in the VTL case. For a VTL, when Q_{EmL} is blind to multipath I_{EmL} is not and vice versa. As both I_{EmL} and Q_{EmL} are used in the VTL detection metrics, the detector's performance is not affected. Also, this blindness is suppressed for the FFT-based detectors due to the use of frequency domain metrics which have a filtering property making it possible to distinguish oscillating signal from noise on Early-Late correlator outputs. The FFT-based detectors exhibit better performance than the GLRT detector in real-life synthesized multipath scenarios. The test of the multipath detectors on real GPS signals shows that other quality indicators need to be used with the multipath detectors to spot or confirm diffuse multipath presence and detect LOS masking. Consequently, the chapter has proposed a correlator-based NLOS detector, and discussed correlator-based C/N_0 estimators and a correlator-based phase lock indicator. All the discussed correlator-based quality indicators can be used to exclude multipath contaminated and low power channels from PVT computation. They can also serve to switch between STL and VTL tracking modes in an adaptive tracking scheme, or to select STL or VTL measurements in a conjoint tracking scheme depending on accuracy and availability needs. Finally, the detection tests can be applied with minor adjustments to other GNSSs such as *Galileo*, *GLONASS* and *Compass*. The next chapter is dedicated to the application of these quality indicators to combating multipath effects in scalar, vector, adaptive and conjoint tracking schemes.

APPENDIX 3.A: DETECTION THEORY CONCEPTS

Let $p(x|\theta)$ or $p(x;\theta)$ be a parametric measurement model, and let Θ_0 and Θ_1 be partitions of the parameter space Θ such that $\Theta_0 \cup \Theta_1 = \Theta$ and $\Theta_0 \cap \Theta_1 = \phi$.

In detection theory, it is wished to make the appropriate decision, i.e. to identify which hypothesis is true:

H_0: $\theta \in \Theta_0$, null hypothesis
H_1: $\theta \in \Theta_1$, alternative hypothesis.

If θ can only take two values, the hypotheses are said to be simple, such that:

$$\Theta = \{\theta_0, \theta_1\}, \quad \Theta_0 = \{\theta_0\}, \quad \text{and} \quad \Theta_1 = \{\theta_1\}.$$

A decision rule (function) $\phi(x): X \to (0,1)$ can be designed with the following characteristics:

$$\phi(x) = \begin{cases} 0, & decide \quad for \quad H_0, \\ 1, & decide \quad for \quad H_1. \end{cases} \tag{3.A.1}$$

The function partitions the data space X, which is the support of $p(x|\theta)$, into two regions:

$$\phi(x): \quad X_0 = \{x : \phi(x) = 0\}, \qquad X_1 = \{x : \phi(x) = 1\}.$$

The probability of false alarm (*PFA*) and probability of missed detection (*PMD*) are defined as follows [39]:

$$PFA = E_{x|\theta}\left[\phi(\mathrm{X})|\theta\right] = \int_{X_1} p(x|\theta)dx \quad for \quad \theta \quad in \quad \Theta_0 \tag{3.A.2}$$

$$PMD = E_{x|\theta}\left[1 - \phi(\mathrm{X})|\theta\right] = 1 - \int_{X_1} p(x|\theta)dx = \int_{X_0} p(x|\theta)dx \quad for \quad \theta \quad in \quad \Theta_1 \tag{3.A.3}$$

Consequently, the probability of detection or the probability of correctly deciding for H_1 is given by [39]:

$$PD = 1 - PMD = E_{x|\theta}\left[\phi(\mathrm{X})|\theta\right] = \int_{X_1} p(x|\theta)dx \quad for \quad \theta \quad in \quad \Theta_1 \tag{3.A.4}$$

APPENDIX 3.B: DERIVATION OF FFT-BASED MP DETECTOR I (M-GLRT) DETECTION METRIC

The Neyman – Pearson theorem [39] states that for a binary hypothesis test between two hypotheses H_0 and H_1, to maximize the PD given a $PFA=\alpha$, H_1 is chosen if

$$L(x)=\frac{p(x;H_1)}{p(x;H_0)}>T \tag{3.B.1}$$

The threshold T is derived from $PFA=\int_{\{x:L(x)>T\}} p(x;H_0)dx=\alpha$. The function $L(x)$ is called the likelihood ratio. It indicates for each value of x the likelihood of H_1 versus the likelihood of H_0. The test of Equation (3.B.1) is called the likelihood ratio test (LRT).

FFT-based MP Detector I metric can be derived by considering that the Early-Late correlator output is a sinusoid, which is the case in general. Given the following sinusoidal detection problem,

$H_0 : x[n]=w[n]$

$H_1 : x[n]=A\cos(2\pi f_0 n+\phi)+w[n]$, with $n\in\{0,1,...,N-1\}$,

where $w[n]$ is white Gaussian noise with known variance σ^2, for unknown amplitude A, phase ϕ and frequency f_0, the GLRT chooses H_1 if

$$\frac{p(x;\hat{A},\hat{\phi},\hat{f}_0,H_1)}{p(x;H_0)}>T \text{ or } \frac{\max_{f_0} p(x;\hat{A},\hat{\phi},f_0,H_1)}{p(x;H_0)}>T \;\therefore \max_{f_0}\frac{p(x;\hat{A},\hat{\phi},f_0,H_1)}{p(x;H_0)}>T$$

$$\therefore \ln\max_{f_0}\frac{p(x;\hat{A},\hat{\phi},f_0,H_1)}{p(x;H_0)}>\ln T$$

$$\therefore \max_{f_0}\ln\frac{p(x;\hat{A},\hat{\phi},f_0,H_1)}{p(x;H_0)}>\ln T \tag{3.B.2}$$

Let $Y(x)=\frac{p(x;\hat{A},\hat{\phi},f_0,H_1)}{p(x;H_0)}$ be the generalized likelihood ratio. For a random value of f_0 that is known, $Y(x)=\frac{p(x;\hat{A},\hat{\phi},H_1)}{p(x;H_0)}$.

$$Y(x)=\frac{\frac{1}{\left(2\pi\sigma^2\right)^{N/2}}\exp\left[-\frac{1}{2\sigma^2}\sum_{n=0}^{N-1}\left(x[n]-\hat{A}\cos\left(2\pi f_0 n+\hat{\phi}\right)\right)^2\right]}{\frac{1}{\left(2\pi\sigma^2\right)^{N/2}}\exp\left[-\frac{1}{2\sigma^2}\sum_{n=0}^{N-1}x^2[n]\right]}.$$

It is shown in [51] that the maximum likelihood estimate (MLE) of $Y(x)$ for large N is approximately

$$\hat{A}=\sqrt{\hat{\beta}_1{}^2+\hat{\beta}_2{}^2}\quad and\quad \hat{\phi}=\tan^{-1}\left(\frac{-\hat{\beta}_2}{\hat{\beta}_1}\right) \tag{3.B.3}$$

$$\text{where } \hat{\beta}_1=\frac{2}{N}\sum_{n=0}^{N-1}x[n]\cos 2\pi f_0 n \text{ and } \hat{\beta}_2=\frac{2}{N}\sum_{n=0}^{N-1}x[n]\sin 2\pi f_0 n.$$

Furthermore,

$$\ln Y(x)=\ln\left\{\exp\left[-\frac{1}{2\sigma^2}\sum_{n=0}^{N-1}\left(x[n]-\hat{A}\cos\left(2\pi f_0 n+\hat{\phi}\right)\right)^2\right]\right\}-\ln\left\{\exp\left[-\frac{1}{2\sigma^2}\sum_{n=0}^{N-1}x^2[n]\right]\right\}$$

$$\ln Y(x)=\left[-\frac{1}{2\sigma^2}\sum_{n=0}^{N-1}\left(x[n]-\hat{A}\cos\left(2\pi f_0 n+\hat{\phi}\right)\right)^2\right]+\left[\frac{1}{2\sigma^2}\sum_{n=0}^{N-1}x^2[n]\right]$$

$$\ln Y(x)=-\frac{1}{2\sigma^2}\left[\sum_{n=0}^{N-1}-2x[n]\hat{A}\cos\left(2\pi f_0 n+\hat{\phi}\right)+\sum_{n=0}^{N-1}\hat{A}^2\cos^2\left(2\pi f_0 n+\hat{\phi}\right)\right]$$

But,

$$\sum_{n=0}^{N-1}x[n]\hat{A}\cos\left(2\pi f_0 n+\hat{\phi}\right)=$$

$$\sum_{n=0}^{N-1}x[n]\cos(2\pi f_0 n)\hat{A}\cos\hat{\phi}-\sum_{n=0}^{N-1}x[n]\sin(2\pi f_0 n)\hat{A}\sin\hat{\phi}$$

Also, $\cos\left(\tan^{-1}(\theta)\right)=\frac{1}{\sqrt{1+\theta^2}}$ and $\sin\left(\tan^{-1}(\theta)\right)=\frac{\theta}{\sqrt{1+\theta^2}}$. By using Equation (3.B.3), $\hat{A}\cos\hat{\phi}=\hat{\beta}_1$ and $-\hat{A}\sin\hat{\phi}=\hat{\beta}_2$. Thus,

$$\sum_{n=0}^{N-1}x[n]\hat{A}\cos\left(2\pi f_0 n+\hat{\phi}\right)=\frac{N}{2}\left(\hat{\beta}_1{}^2+\hat{\beta}_2{}^2\right) \tag{3.B.4}$$

Moreover, by using the formula of the power of a sinusoidal signal, $\sum_{n=0}^{N-1}\cos^2\left(2\pi f_0 n+\hat{\phi}\right)$ can be evaluated. The power of a periodic sinusoid $x[n]=A\cos\left(2\pi f_0 n+\hat{\phi}\right)$ is given by $P_N=\frac{1}{N}\sum_{n=0}^{N-1}A^2\cos^2\left(2\pi f_0 n+\hat{\phi}\right)$.

Furthermore, Euler's formula establishes that

$$\cos\left(2\pi f_0 n + \hat{\phi}\right) = \frac{1}{2}\left[e^{j(2\pi f_0 n+\hat{\phi})} + e^{-j(2\pi f_0 n+\hat{\phi})}\right].$$

For a bin frequency, $2\pi f_0 = 2\pi\frac{m}{N}$, $m = 1,2,...,N-1$. Therefore,

$$P_N = \frac{1}{N}\sum_{n=0}^{N-1} A^2\cos^2\left(2\pi f_0 n + \hat{\phi}\right) = \frac{A^2}{4N}\sum_{n=0}^{N-1}\left(e^{j(2\pi f_0 n+\hat{\phi})} + e^{-j(2\pi f_0 n+\hat{\phi})}\right)^2$$

$$P_N = \frac{A^2}{4N}\left(\sum_{n=0}^{N-1} e^{2j(2\pi f_0 n+\hat{\phi})}\right) + \frac{A^2}{4N}\left(\sum_{n=0}^{N-1} e^{-2j(2\pi f_0 n+\hat{\phi})}\right) + \frac{A^2}{4N}2N,$$

because for $\Omega_0 = 2\pi f_0 = 0$, $x[n] = A\cos\hat{\phi}$ *with* $N = 1$.

Therefore,

$$P_N = \frac{A^2}{2} + e^{2j\hat{\phi}}S_1 + e^{-2j\hat{\phi}}S_2 = \frac{A^2}{2}$$

where:

$$S_1 = \sum_{n=0}^{N-1} e^{2j(2\pi f_0 n)} = \sum_{n=0}^{N-1} e^{2j(2\pi\frac{m}{N}n)}. \quad \textit{Let} \quad z_1 = e^{2j(2\pi\frac{m}{N})}$$

$$\therefore \quad S_1 = \sum_{n=0}^{N-1} z_1^n = \frac{z_1^N - 1}{z_1 - 1} = 0 \qquad \textit{because} \quad z_1^N = 1$$

$$S_2 = \sum_{n=0}^{N-1} e^{-2j(2\pi f_0 n)} = \sum_{n=0}^{N-1} e^{-2j(2\pi\frac{m}{N}n)}. \quad \textit{Let} \quad z_2 = e^{-2j(2\pi\frac{m}{N})}$$

$$\therefore \quad S_2 = \sum_{n=0}^{N-1} z_2^n = \frac{z_2^N - 1}{z_2 - 1} = 0 \qquad \textit{because} \quad z_2^N = 1$$

In summary, for large N (i.e. $N > 2$), the power of the periodic sinusoid $x[n] = A\cos\left(2\pi f_0 n + \hat{\phi}\right) = A\cos\left(2\pi\frac{m}{N}n + \hat{\phi}\right)$ is given by $P_N = \frac{1}{N}\sum_{n=0}^{N-1} A^2\cos^2\left(2\pi f_0 n + \hat{\phi}\right) = \frac{A^2}{2}$

For $A=1$, $x[n] = \cos\left(2\pi f_0 n + \hat{\phi}\right)$ and $P_N = \frac{1}{N}\sum_{n=0}^{N-1}\cos^2\left(2\pi f_0 n + \hat{\phi}\right) = \frac{1}{2}$. Therefore,

$$\sum_{n=0}^{N-1}\cos^2\left(2\pi f_0 n + \hat{\phi}\right) = \frac{N}{2} \tag{3.B.5}$$

Substitution of Equations (3.B.4) and (3.B.5) into $\ln Y(x)$ yields

$$\ln Y(x) = -\frac{1}{2\sigma^2}\left[\sum_{n=0}^{N-1} -2\frac{N}{2}\left(\hat{\beta}_1^2 + \hat{\beta}_2^2\right) + \frac{N}{2}\hat{A}^2\right] = \frac{N}{4\sigma^2}\left(\hat{\beta}_1^2 + \hat{\beta}_2^2\right)$$

But,

$$\hat{\beta}_1^2 + \hat{\beta}_2^2 = \left(\frac{2}{N}\right)^2 \left[\left(\sum_{n=0}^{N-1} x[n] \cos 2\pi f_0 n \right)^2 + \left(\sum_{n=0}^{N-1} x[n] \sin 2\pi f_0 n \right)^2 \right]$$

$$\hat{\beta}_1^2 + \hat{\beta}_2^2 = \frac{4}{N}\frac{1}{N} \left| \sum_{n=0}^{N-1} x[n] \exp(-j2\pi f_0 n) \right|^2 = \frac{4}{N} \Omega(f_0)$$

Therefore, $\ln Y(x) = \frac{N}{4\sigma^2}\frac{4}{N}\Omega(f_0)$.

$$\ln Y(x) = \frac{1}{\sigma^2}\Omega(f_0) \tag{3.B.6}$$

where $\Omega(f_0)$ is the periodogram evaluated at $f = f_0$. Thus, the GLRT decides H_1 if $\max_{f_0} \ln Y(x) > \ln T \;\therefore \max_{f_0} \frac{\Omega(f_0)}{\sigma^2} > \ln T$. Let $\eta = \ln T$ be the threshold and the FFT-based Detector I detection test given in this chapter is obtained as follows:

$$\max_{f_0} \frac{\Omega(f_0)}{\sigma^2} \underset{H_1}{>} \eta \quad or \quad \max_{f_0} \frac{\Omega(f_0)}{\sigma^2} \underset{H_0}{<} \eta \tag{3.B.7}$$

APPENDIX 3.C: DERIVATION OF FFT-BASED MP DETECTOR II DETECTION THRESHOLD

For the FFT-based MP Detector II, it was seen that the probability of detection (PD) is given by

$$PD = 1 - CDF\left(2\ln\left(\frac{N/2-1}{PFA}\right)\right) \tag{3.C.1}$$

where *CDF* is the cumulative distribution function of the non-central chi-squared distribution with 2 degrees of freedom and non-centrality parameter $\lambda = SNR = \frac{NA^2}{2\sigma^2}$.

Let *N* be the FFT size. For such an FFT-based detector, the *PFA* is given by [39]

$$PFA = 1 - \left[1 - \exp\left(-\frac{\gamma'}{\sigma^2}\right)\right]^L \tag{3.C.2}$$

where L is the number of Doppler and range bins examined by the detector and $\gamma' = \sigma^2 \ln T$, with $T > 0$ being a real positive number. For a small *PFA*, $\exp\left(-\frac{\gamma'}{\sigma^2}\right) << 1$. Therefore, using the approximation $(1-x)^L \approx 1 - Lx \quad for \quad x << 1$, the following expression is obtained for *PFA*:

$$PFA = 1 - \left[1 - \exp\left(-\frac{\gamma'}{\sigma^2}\right)\right]^L = 1 - \left[1 - L\exp\left(-\frac{\gamma'}{\sigma^2}\right)\right] = L\exp\left(-\frac{\gamma'}{\sigma^2}\right) \tag{3.C.3}$$

For $L = 1$, $PFA = \exp\left(-\frac{\gamma'}{\sigma^2}\right)$. Both Detector I and Detector II are FFT-based detectors. Therefore, it can be assumed that they have the same quintessential functioning. It was shown that for Detector I, the GLRT decides H_1 if $\max_{f_0} \frac{\Omega(f_0)}{\sigma^2} > \ln T$ with $\eta = \ln T$ being the detection threshold. Let $\eta = \ln T$ be the threshold for Detector II as well. Therefore, $PFA = \exp\left(-\frac{\gamma'}{\sigma^2}\right) = \exp\left(-\frac{\sigma^2 \ln T}{\sigma^2}\right) = \exp(-\ln T) = \exp(-\eta)$ with $\gamma' = \sigma^2 \ln T$. Finally,

$$PFA = \exp(-\eta) \quad \therefore \quad \ln PFA = -\eta \quad \therefore \quad \eta = -\ln PFA \tag{3.C.4}$$

which is the threshold defined in this chapter for FFT-based MP Detector II.

Chapter 4

Adaptive and Conjoint Scalar-Vector Tracking Loops

In science if you know what you are doing you should not be doing it. In engineering if you do not know what you are doing you should not be doing it. Of course, you seldom, if ever, see either pure state.

— Richard W. Hamming

4.1 INTRODUCTION

Maintaining robust tracking and positioning integrity in constrained environments (urban, suburban, heavy foliage) is a real challenge for Global Navigation Satellite Systems (GNSS) such as the Global Positioning System (GPS). In *Chapter 3*, it was shown that problems resulting from those types of environments are mainly the presence of multipath (MP) signals and the masking of the line-of-sight (LOS) signal. Diffuse multipaths are spread in the frequency domain and affect the received signal quality by degrading the carrier to noise power ratio (C/N_0). The estimation of the C/N_0 allows the adjustment of the estimation noise on pseudorange (PR) and delta-range (DR) measurements used in the navigator/position-velocity-time (PVT) estimator. When an algorithm such as weighted least squares or an algorithm of the Bayesian filters family is used in the navigator, it is possible to weigh each measurement depending on its quality. As a result, the impact of a very noisy measurement on the estimated PVT solution is reduced. Specular multipaths on the other hand are localized in frequency. They produce a bias on PR and DR measurements when their frequency is in the frequency band of the receiver. Specular multipaths particularly affect fixed receivers or receivers moving parallel to the surface that reflects the multipaths.

One of the approaches used in literature to mitigate MP effects is based on estimation of the delay and Doppler frequency of MP signals, but this estimation undergoes the measurement errors at the output of discriminators [70] [71] [72]. The vector tracking loop (VTL) has also been extensively studied in recent literature as an alternative to the scalar tracking loop (STL) for achieving robust tracking in harsh environments affected by multipath, scintillations and interference [73] [74] [75] [76]

[77] [78] [79] [80]. Adaptive vector tracking schemes have also been devised with added specific processing to improve tracking loop performance in order to provide reliable PR and DR measurements to the navigator [81] [82] [83]. In a multi-constellation context where the number of potentially available satellites is high, MP detection can be used instead of trying to estimate MP parameters. In fact, MP parameters estimation accuracy depends on the kind of discriminator that is used, the noise bandwidth of tracking loops, and the tracking loop configuration, which do not always take MP presence into account.

This chapter proposes an evolution to the adaptive vector tracking solution in three-fold form as alternative approach to achieve robust tracking and positioning integrity. The first considered solution is a vector tracking loop with the capability to exclude MP contaminated or other disturbed satellites from PVT calculation in the navigator. The contribution is the introduction of a non-line-of-sight (NLOS) detector and correlator-based MP detectors in the receiver architecture. This improves positioning accuracy and tracking performance with the use of a more reliable PVT in the estimation of tracking parameters. The second solution is an adaptive STL-VTL tracking loop with the ability to switch between STL and VTL tracking modes and to exclude unhealthy satellites from PVT calculation. The contribution is the specification of dual-mode NCOs (STL/VTL) and of a tracking mode controller based on different quality indicators. With this solution, the receiver maintains VTL mode when in very harsh conditions and reverts to STL mode in less challenged situations. The third solution that is considered is a conjoint tracking scheme where STL and VTL tracking modes operate conjointly or simultaneously and the PR-DR measurements to be fed to the navigator are selected based on the state of the different signal quality indicators.

4.2 PROPOSED RECEIVER ARCHITECTURES

4.2.1 VECTOR TRACKING ARCHITECTURE

The GNSS receiver architecture of reference from which other evolutions are made is depicted in Figure 4.1.

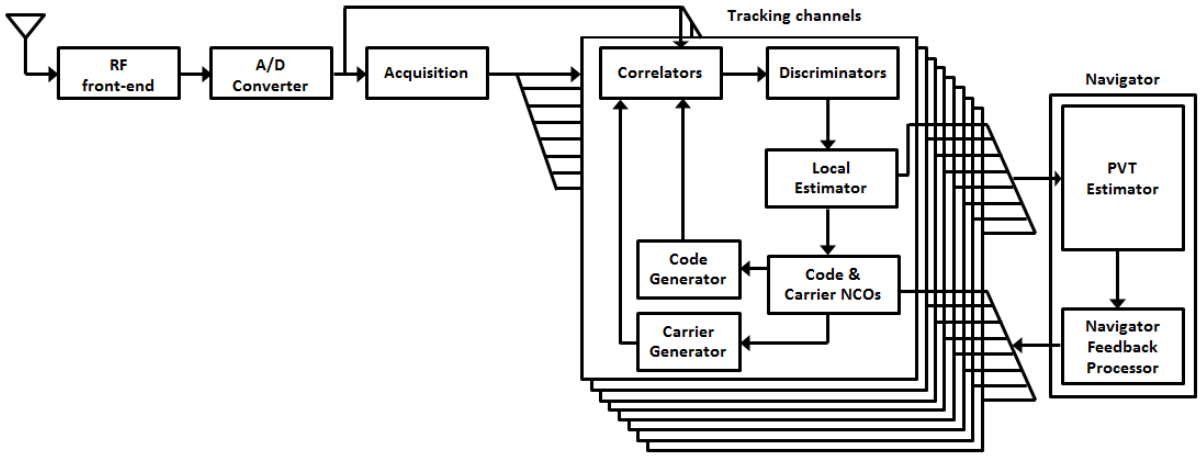

Figure 4.1: GNSS Vector Tracking Receiver Architecture

This is a decentralized (federated) architecture, meaning that each tracking channel has a local estimation filter of the Kalman family, referred to here as a local estimator. All channels deliver their measurements to the navigator, which is the master PVT estimation filter. The receiver is made of a bank of correlators, discriminators, local estimators (based on a fixed gain Kalman filter algorithm), code and carrier numerically controlled oscillators (NCOs), and a navigator based on an Extended Kalman Filter (EKF) algorithm. The navigator provides feedback information to code and carrier NCOs. This vector tracking system is enhanced by adding a NLOS detector, correlator-based MP detectors and a C/N_0 estimator that allow the navigator to exclude unhealthy satellites from PVT computation. This receiver has the potential to perform scalar tracking and vector tracking. As the experiments that are conducted to validate the proposed receiver enhancements require synthesized signals, the GNSS software receiver simulator presented in *Chapter 3* and depicted in Figure 3.23 is used. It has the same architecture as the receiver in Figure 4.1. In the receiver simulator, the DLR multipath model is utilized in the trajectory and environment simulator that is used as multipath signal source in replacement for the signal acquisition block in the receiver of Figure 4.1. Two further evolutions of the architecture in Figure 4.1 are suggested hereafter: an adaptive tracking architecture that switches between STL and VTL tracking continuously depending on the state of quality indicators; and a conjoint tracking architecture that performs STL and VTL tracking simultaneously but chooses PR and DR measurements to be delivered to the navigator (STL or VTL measurements) based on the state of quality indicators.

4.2.2 ADAPTIVE TRACKING ARCHITECTURE

The GNSS receiver based on adaptive tracking is capable of switching the tracking of a particular channel between STL and VTL modes continuously depending on the state of signal quality indicators. Figure 4.2 illustrates a GPS adaptive tracking channel. A channel is considered to be in VTL mode if it receives feedback information from the navigator in the estimation of tracking parameters.

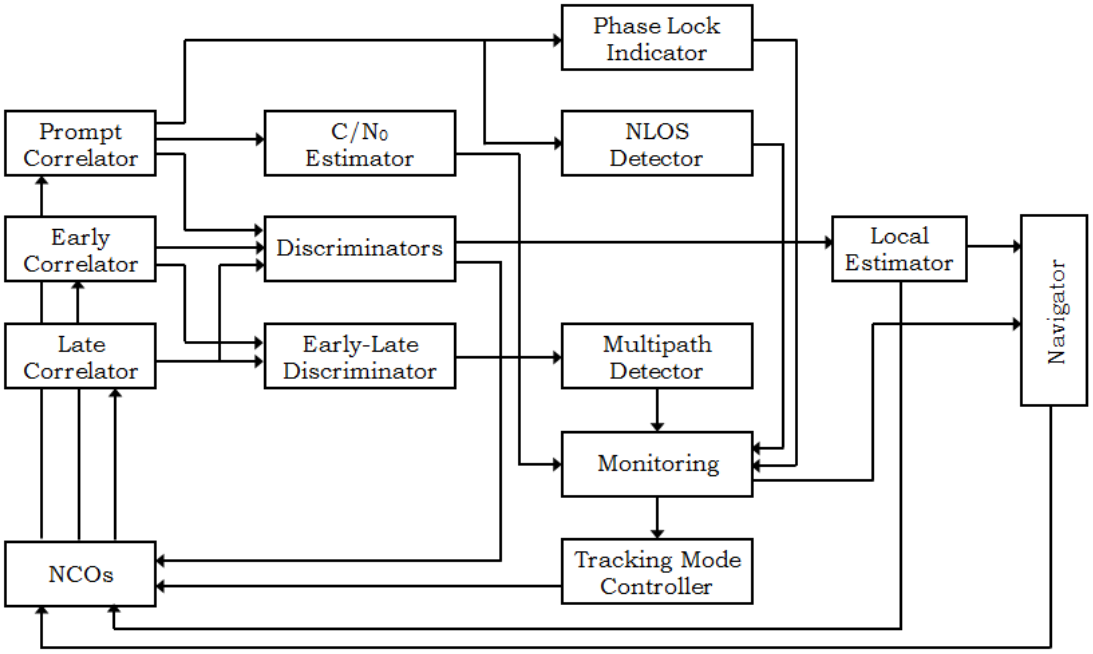

Figure 4.2: GPS Adaptive Tracking Channel Architecture

The STL mode is the tracking mode adopted in conventional receivers. In STL mode, the NCOs that produce the replica signal used in the tracking loop are controlled by the local estimators. The tracking of the signal delivered by the satellite is therefore performed locally (in each channel independently) without any feedback information from the navigator. Feedback information from the navigator is beneficial when the latter has healthy measurements, but can be detrimental when the navigator uses one or many contaminated measurements. The STL configuration here is a delay-locked loop (DLL) working with a frequency-assisted phase-locked loop (FPLL).

In VTL mode, the NCOs that produce the Early, Prompt and Late code replicas used in the code tracking loop are completely controlled by the navigator. The code frequency is deduced from the receiver velocity, projected in the axis of the addressed satellite. The static delay error is obtained from the receiver position by comparison with the position information from the output of the code NCO. For the phase tracking loop in VTL mode, the NCO that produces the carrier replica is controlled by the navigator and the phase discriminator output. The carrier frequency is deduced from the receiver velocity, projected in the axis of the satellite

of interest. The static phase error is delivered by the phase discriminator. In other words, this is a vector delay-frequency-locked loop (VDFLL) working with a phase-locked loop (PLL) aided by the navigator.

The following signal quality indicators are used with the adaptive tracking receiver: a C/N_0 estimator, a phase lock indicator (PLI) that continuously monitors the lock state of the PLL, a NLOS detector that detects LOS masking, and a MP detector. The monitoring block in Figure 4.2 analyses the output of the different detectors (indicators) and delivers to the controller and navigator blocks the information necessary for choosing the tracking mode on one hand or for excluding contaminated measurements on the other hand. The default tracking mode for a channel is STL. If either the NLOS detector indicates an NLOS situation, or the PLI indicates loss of phase lock and the C/N_0 goes below a defined threshold, the tracking mode controller directly switches to VTL mode. The use of these three quality indicators to control STL-VTL commutations guarantees that no disturbance that requires STL to VTL switching is missed. The MP detector can also be optionally used to switch between tracking modes. But its primary function is to exclude MP contaminated channels from PVT computation in the navigator, whether the tracking mode is STL or VTL.

With the adaptive tracking architecture, the quality indication tests performed in VTL mode are made under the assumption that the navigator is not contaminated, i.e. that it does not use contaminated measurements. Thus, this architecture has low complexity but presents a disadvantage: if the navigator is contaminated, the multipath detection tests are no longer valid. The tests may then lead to rejection of healthy measurements.

4.2.3 CONJOINT TRACKING ARCHITECTURE

Figure 4.3 illustrates a more complex architecture but that makes the detection tests more robust, the conjoint tracking architecture. With this architecture, scalar and vector tracking are performed in parallel, i.e. conjointly or simultaneously. One satellite is processed by two channels, a STL channel and a VTL channel. But they remain independent from each other such that a STL channel can lose track of a satellite due to low C/N_0 or multipath but the corresponding VTL channel retains it. Some quality indicators (NLOS detector, phase lock indicator, C/N_0 estimator) then allow the selection of the measurements (STL or VTL measurements) to be delivered to the navigator. Other quality indicators (MP detector, C/N_0 estimator) allow the navigator to exclude unhealthy measurements from the PVT calculation. This architecture is complex as it requires doubling the number of correlators, discriminators, NCOs and local estimators. It presents some advantages: it increases

the performance of the detection tests; and by using the STL and VTL Early-Late discriminator outputs, it is possible to detect navigator contamination.

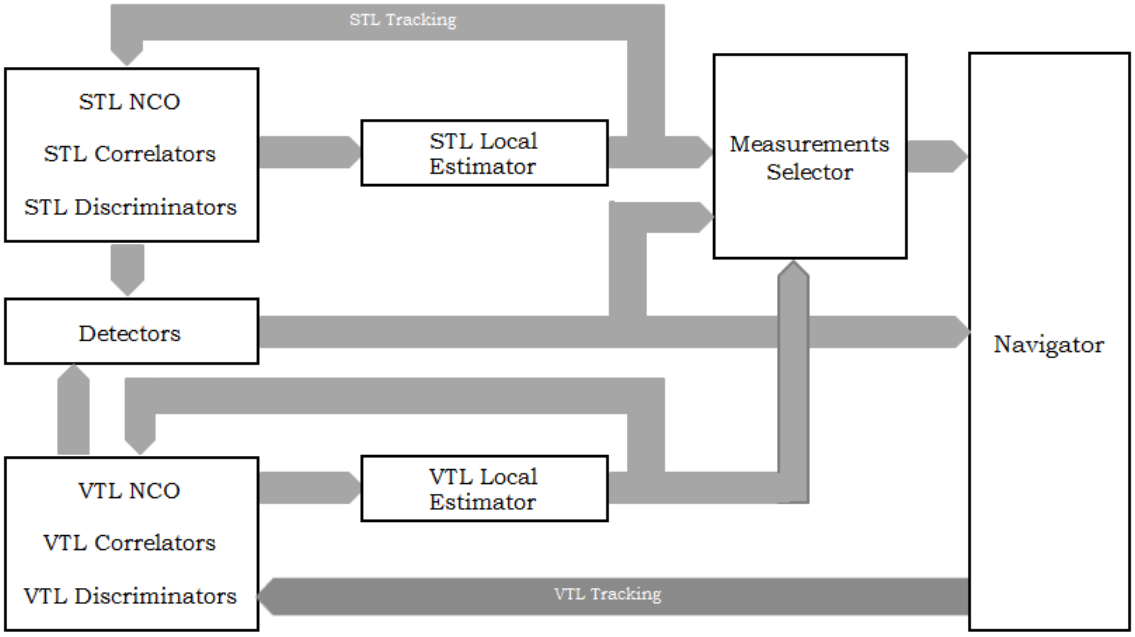

Figure 4.3: Conjoint Tracking Channel Architecture

4.3 DESCRIPTION OF RECEIVER COMPONENTS

For the sake of making this chapter self-contained and as a reminder, some signal quality indicators that have been studied in *Chapter 3* are succinctly discussed again in this section together with other components of the GNSS receiver that are present in the three proposed tracking schemes.

4.3.1 CORRELATORS

The signal that is considered at the input of the GNSS receiver channels block is the complex signal that is a low-pass representation of the received signal. It contains the signals from all N satellites in view and can be expressed as:

$$s(t) = \sum_{k=1}^{N} x_k(t) + w(t) \tag{4.1}$$

where $w(t)$ is the receiver thermal noise and is assumed to be zero-mean additive white Gaussian noise (AWGN) with variance σ^2. In the presence of MP, the signal $x_k(t)$ entering the correlators of a GPS tracking channel (a channel tracks one satellite), neglecting the low rate data, depends on the amplitude, code delay, carrier phase and frequency of LOS and MP signals and can be expressed as

$$x_k(t) = A_0 C(t-\tau_0)\exp\left[j\varphi_0(t)\right] + \sum_{l=1}^{L} A_l C(t-\tau_l)\exp\left[j\varphi_l(t)\right] \tag{4.2}$$

where $\varphi_l(t) = \varphi_l(0) + 2\pi \int_0^t f_l(u)du$, L is the number of multipath signals, $A_0 = \sqrt{2P_0}$ and $A_l = \sqrt{2P_l}$ are the LOS and l^{th} multipath amplitudes, P_0, P_l and f_l are respectively the power of the LOS, the power and frequency of the l^{th} multipath signal, $C(t)$ is the spreading code, τ_0, τ_l, φ_0, φ_l are the time and phase delays induced by the transmission from satellite to receiver for the LOS and l^{th} multipath signals respectively, ω is the nominal GPS L1, L2 or L5 radial frequency. Each tracking channel constitutes a filter that matches the satellite that it is allocated to. This matched filter correlates the received signal, sampled at $F_S = 1/T_s$, with a local replica. The signal at the output of the prompt correlator at an instant of time $t_n = \sum_{m=0}^{n} T_m$, obtained after a coherent integrate-and-dump operation of duration T_n, can be expressed as

$$\begin{aligned} I_P[n] + jQ_p[n] &= \sqrt{2P_0}R(\Delta\tau_{0,n})\frac{\sin(\pi\Delta f_{0,n}T_n)}{\sin(\pi\Delta f_{0,n}T_s)}\exp(j\Delta\varphi_{0,n}) + \\ &\sum_{l=1}^{L}\sqrt{2P_l}R(\Delta\tau_{0,n}-\delta_{l,n})\frac{\sin(\pi\Delta f_{l,n}T_n)}{\sin(\pi\Delta f_{l,n}T_s)}\exp[j(\Delta\varphi_{0,n}-\theta_{l,n})] + w_P[n] \end{aligned} \tag{4.3}$$

where $R(\cdot)$ is the correlation function, $\Delta\tau_{0,n}$ is the error between the LOS signal delay and the estimated code replica delay, $\Delta f_{0,n}$ and $\Delta f_{l,n}$ are the error between the LOS (respectively the l^{th} multipath) carrier frequency and the estimated carrier replica frequency, $\Delta\varphi_{0,n}$ is the error between the LOS carrier phase and the estimated carrier replica phase, $\delta_{l,n}$ is the delay of the l^{th} multipath with respect to the LOS, $\theta_{l,n}$ is the phase shift of the l^{th} multipath with respect to the LOS, and $w_P[n]$ is the post-correlation AWGN. The Early-minus-Late (*EmL*) correlator output, at an instant of time t_n, can be expressed as

$$\begin{aligned} I_{EmL}[n] + jQ_{EmL}[n] &= \sqrt{2P_0}\left[R(\Delta\tau_{0,n}+d)-R(\Delta\tau_{0,n}-d)\right]\frac{\sin(\pi\Delta f_{0,n}T_n)}{\sin(\pi\Delta f_{0,n}T_s)}\exp(j\Delta\varphi_{0,n}) \\ &+\sum_{l=1}^{L}\sqrt{2P_l}\left[R(\Delta\tau_{0,n}-\delta_{l,n}+d)-R(\Delta\tau_{0,n}-\delta_{l,n}-d)\right]\times\frac{\sin(\pi\Delta f_{l,n}T_n)}{\sin(\pi\Delta f_{l,n}T_s)}\exp\left[j(\Delta\varphi_{0,n}-\theta_{l,n})\right]+w_{EmL}[n] \end{aligned} \tag{4.4}$$

where d is half the Early-Late chip spacing $\partial = 2d$ $(0 < \partial \le 1)$.

4.3.2 MP DETECTORS

Chapter 3 has proposed two FFT-based MP detectors, each with a metric variation depending on whether detection is performed on the STL or the VTL. The tracking

architectures in section 4.2 can either utilize FFT-based Detector I (with its STL and VTL options) or FFT-based Detector II (also with STL and VTL options) or both at the same time. Both detectors start with the computation of the periodogram then evaluate MP presence differently. For the PFA values chosen in *Chapter 3*, Table 3.5, it was observed that Detector II exhibited lower false alarm rate than Detector I but displayed higher missed detection percentage than Detector I. Therefore, a design that combines both detectors may benefit from the strengths of both. For instance, if the default detector is Detector I, it might be interesting to confirm a registered MP detection using Detector II. Similarly, if Detector II is the default detector, it might be important to confirm a registered non-MP detection using Detector I. In this way, the two detectors would complement each other. Nonetheless, this chapter will present the results obtained by using one detector individually. In fact, each of the detectors can function independently and present satisfying performance in the different tracking schemes proposed herein.

With Detector I, for the STL, it has been suggested that the detection test to decide for H_0 (MP absence) or H_1 (MP presence) be based on the quadrature arm of the *EmL* correlator output (Q_{EmL}). It is formulated as

$$\frac{\max\left(\Omega(m)\right)}{\hat{\sigma}^2} \underset{H_1}{>} \eta \quad or \quad \frac{\max\left(\Omega(m)\right)}{\hat{\sigma}^2} \underset{H_0}{<} \eta \tag{4.5}$$

where

$$\Omega(m) = \frac{1}{N}\left|Q_{EmL}(m)\right|^2 \quad and \quad Q_{EmL}(m) = \sum_{n=n_0}^{n_0+N-1} Q_{EmL}(n) e^{-j\frac{2\pi mn}{N}}$$

$$\hat{\sigma}^2 = \frac{1}{N}\sum_{n=1}^{N}\left(Q_{EmL}(n+n_0) - \overline{Q}\right)^2 \quad and \quad \overline{Q} = \frac{1}{N}\sum_{n=1}^{N} Q_{EmL}(n+n_0).$$

$\Omega(m)$ is the periodogram based on $Q_{EmL}(m)$, which is the N-point fast Fourier transform (FFT) of $Q_{EmL}(n)$. $\hat{\sigma}^2$ is the maximum likelihood estimate (MLE) of noise variance. For the VTL, it has been proposed that the detection test be based on both in-phase (I_{EmL}) and quadrature (Q_{EmL}) arms of the *EmL* output. The detector computes the periodogram but based on the complex FFT, meaning that:

$$\frac{\max\left(\Omega(m)\right)}{\hat{\sigma}^2} \underset{H_1}{>} \eta \quad or \quad \frac{\max\left(\Omega(m)\right)}{\hat{\sigma}^2} \underset{H_0}{<} \eta$$

with $\Omega(m)=\frac{1}{N}\left|EmL(m)\right|^2$ *where* $EmL(m)=\sum_{n=n_0}^{n_0+N-1}EmL(n)e^{-j\frac{2\pi mn}{N}}$ is the complex FFT of $EmL\,(n)=I_{EmL}\,(n)+jQ_{EmL}\,(n)$. In this case, the MLE of noise variance is $\hat{\sigma}^2=\frac{1}{N}\sum_{n=1}^{N}\left|EmL(n+n_0)-\overline{EmL}\right|^2$ and $\overline{EmL}=\frac{1}{N}\sum_{n=1}^{N}EmL(n+n_0)$. The detection threshold is

$$\eta=\exp\left\{\frac{\left[cdf^{-1}(1-PFA/2)\right]^2}{N}\right\}-1$$

with *cdf* being the cumulative distribution function of the standard normal distribution, cdf^{-1} the inverse cumulative distribution function, and *PFA* the probability of false alarm.

With Detector II, for the STL, the test to choose H_0 (MP absence) or H_1 (MP presence) has been formulated as follows:

$$10\ln(SNPR)\underset{H_1}{>}\eta \quad or \quad 10\ln(SNPR)\underset{H_0}{<}\eta \tag{4.6}$$

where $\eta=-\ln(PFA)$ is the detection threshold, $SNPR=\frac{SP}{NP}$ is the signal to noise power ratio, $SP=\sum_{m=-199}^{199}\Omega(m)$ and $NP=\sum_{m=-500}^{-200}\Omega(m)+\sum_{m=200}^{500}\Omega(m)$ are the signal and noise powers respectively, $\Omega(m)=\frac{1}{N}\left|Q_{EmL}(m)\right|^2$ is the periodogram (power spectrum density) estimated for $|\mathrm{m}|\leq$500 Hz and $Q_{EmL}(m)=\sum_{n=n_0}^{n_0+N-1}Q_{EmL}(n)e^{-j\frac{2\pi mn}{N}}$ is the N-point fast Fourier transform (FFT) of $Q_{EmL}\,(n)$ with $N=1024$ to approach 1 Hz resolution for a coherent integration period of 1 ms. For the VTL, the detection test to decide for H_0 or H_1 has been formulated as

$$10\ln(SNPR)\underset{H_1}{>}\eta \quad or \quad 10\ln(SNPR)\underset{H_0}{<}\eta$$

where $\eta=-\ln(PFA)$ is the detection threshold, and $SNPR$ is obtained as in the test for the STL except that the periodogram is calculated for $\left|EmL\,(n)\right|=\sqrt{\left(I_{EmL}\,(n)^2+Q_{EmL}\,(n)^2\right)}$ and not for $Q_{EmL}\,(n)$. In other words, $EmL(m)=\sum_{n=n_0}^{n_0+N-1}\left|EmL(n)\right|e^{-j\frac{2\pi mn}{N}}$ *where* $N=1024$ and $\Omega(m)=\frac{1}{N}\left|EmL(m)\right|^2$.

4.3.3 NLOS DETECTOR

The FFT-based NLOS detector that was proposed in *Chapter 3* is applied to detection of the presence of the LOS signal through the exploitation of the in-phase prompt correlator output. The detector computes the periodogram

$$\Omega(m) = \frac{1}{N}\left|I_P(m)\right|^2 \qquad where$$
$$I_P(m) = \sum_{n=n_0}^{n_0+N-1} I_P(n) e^{-j\frac{2\pi mn}{N}} \tag{4.7}$$

$I_P(m)$ is the N-point FFT of $I_P(n)$. The detector then chooses the largest value of $\Omega(m)$ and compares it against a threshold η. The detection test to decide for H_0 (absence of strong LOS signal) or H_1 (presence of strong LOS signal) is formulated as

$$\max\left(\Omega(m)\right) \underset{H_1}{>} \eta \quad or \quad \max\left(\Omega(m)\right) \underset{H_0}{<} \eta \tag{4.8}$$

The threshold η can be determined using Monte-Carlo simulations.

4.3.4 C/N$_0$ ESTIMATOR

The used C/N$_0$ estimator is the Moments Method as described in *Chapter 3*. It is based on the 2nd and 4th order moments of the input process to obtain a separate estimation of the carrier and noise strength. Let $s[n] = I_p[n] + jQ_p[n]$ be the complex signal (process) at the prompt correlator output. The theoretical formulation of the 2nd and 4th order moments of this process is $M_2 = E\left\{\left|s[n]\right|^2\right\}$ and $M_4 = E\left\{\left|s[n]\right|^4\right\}$. Based on these moments, signal power and noise power are defined as $P_s(M_2, M_4) = \sqrt{2M_2{}^2 - M_4}$ and $P_n(M_2, M_4) = M_2 - P_s(M_2, M_4)$ respectively. The statistical moments M_2 and M_4 are estimated by their respective averages:

$$\hat{M}_2 = \frac{1}{N}\sum_{l=1}^{N}\left|s[l]\right|^2 \quad and \quad \hat{M}_4 = \frac{1}{N}\sum_{l=1}^{N}\left|s[l]\right|^4 \tag{4.9}$$

And the C/N$_0$ estimate is therefore:

$$\frac{C}{N_0} = \frac{\hat{P}_s\left(\hat{M}_2, \hat{M}_4\right)}{\hat{P}_n\left(\hat{M}_2, \hat{M}_4\right)} \tag{4.10}$$

4.3.5 PHASE LOCK INDICATOR (PLI)

The standard phase lock indicator (PLI) that was discussed in *Chapter 3* is applied here. It is defined as

$$PLI[n] = \frac{I_P[n]^2 - Q_P[n]^2}{I_P[n]^2 + Q_P[n]^2} \tag{4.11}$$

The PLL lock verification test between H_0 (not-in-lock) and H_1 (in-lock) is formulated as

$$std\left(PLI\,[n]\right) \underset{H_1}{<} \eta \quad or \quad std\left(PLI\,[n]\right) \underset{H_0}{>} \eta \tag{4.12}$$

where $std\,(\cdot)$ denotes the standard deviation evaluated over N samples and η is a threshold chosen between 0.5 and 0.6 here.

4.3.6 DISCRIMINATORS

The discriminators use correlator outputs to determine for each tracked satellite the code delay, carrier phase and frequency errors. These errors are used as measurements by the local estimators. The *EmL* discriminator in its dot product [20] form is used as DLL discriminator with spacing $d = 0.4$ chip.

$$D_\tau = (I_E - I_L)I_P + (Q_E - Q_L)Q_P \tag{4.13}$$

The conventional PLL and frequency-locked loop (FLL) discriminators [20] are used:

$$D\varphi = \arctan\left(\frac{Q_P}{I_P}\right) \tag{4.14}$$

$$\begin{aligned} D_f &= \frac{\arctan(CROSS / DOT)}{2\pi(t_2 - t_1)} \\ where \quad & DOT = I_{P1} \times I_{P2} + Q_{P1} \times Q_{P2} \\ & CROSS = I_{P1} \times Q_{P2} - I_{P2} \times Q_{P1} \end{aligned} \tag{4.15}$$

where *DOT* and *CROSS* use prompt correlator outputs defined between two integrate-and-dump instants t_1 and t_2.

4.3.7 LOCAL ESTIMATORS

The local estimators estimate signal parameters for each satellite using discriminators outputs as measurements. They replace the DLL, PLL and FLL loop filters. The state-space system to be solved by local estimators is given by

$$\begin{cases} X_k = \Phi X_{k-1} + w_k \\ Z_k = HX_k + v_k \end{cases} \tag{4.16}$$

where $X_k = \begin{bmatrix} \tilde{\tau} & \tilde{\varphi} & \tilde{f} & \dot{\tilde{f}} \end{bmatrix}^T$, $\Phi = \begin{bmatrix} 1 & 0 & \frac{T}{F_c} & 0 \\ 0 & 1 & 2\pi T & \pi T^2 \\ 0 & 0 & 1 & T \\ 0 & 0 & 0 & 1 \end{bmatrix}$, and $H = \begin{bmatrix} 1 & 0 & 0 & 0 \\ 0 & 1 & 0 & 0 \\ 0 & 0 & 1 & 0 \end{bmatrix}$.

X_k is the vector made of the code delay in *s*, carrier phase in *rad*, carrier frequency in *Hz* and carrier frequency rate in *Hz/s* of the LOS signal, Φ is the transition matrix, H is the matrix of unit vectors, T is the local estimator propagation time, $1/F_c$ is a scaling factor expressing the carrier aid to the DLL.

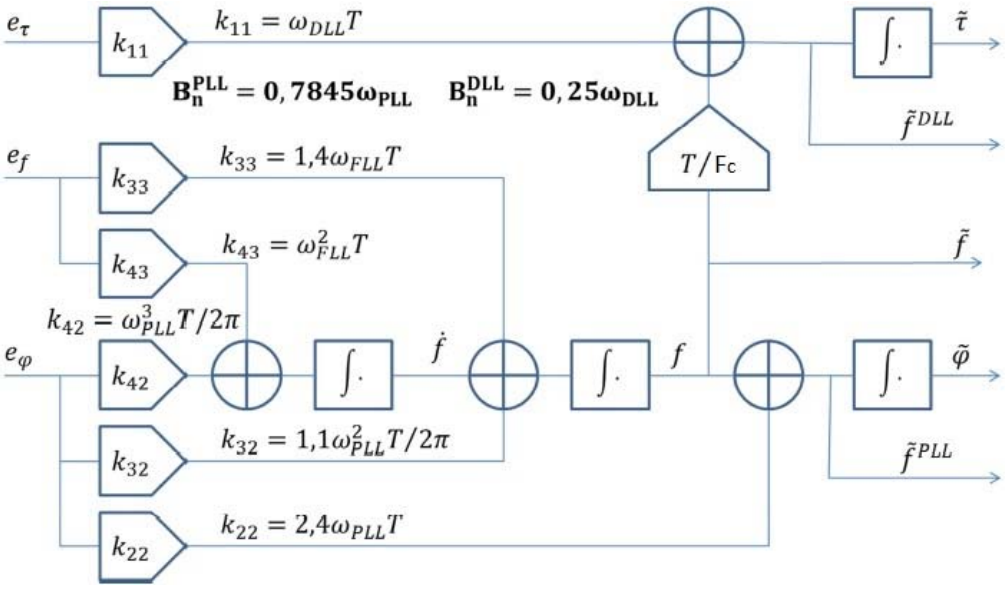

Figure 4.4: Local Estimator Functional Diagram

Traditional loop filters are particular cases of Kalman Filter (KF) for which the gains are not calculated iteratively but fixed and dependent on loop filter parameters. Figure 4.4 depicts a functional diagram of a local estimator. It is implemented using a fixed-gain KF algorithm. The fixed-gain KF algorithm used by the local estimators to solve the system in Equation (4.16) is therefore

$$\left.\begin{aligned} X_{k|k-1} &= \Phi X_{k-1|k-1} \\ Z_{k|k-1} &= H X_{k|k-1} \end{aligned}\right\} \text{Prediction}$$

$$\left.\begin{aligned} K_k &= \begin{bmatrix} \omega_{DLL}T & 0 & 0 \\ 0 & 2.4\omega_{PLL}T & 0 \\ 0 & \frac{1.1\omega_{PLL}^2 T}{2\pi} & 1.4\omega_{FLL}T \\ 0 & \frac{\omega_{PLL}^3 T}{2\pi} & \omega_{FLL}^2 T \end{bmatrix} \\ X_{k|k} &= X_{k|k-1} + K_k(Z_k - Z_{k|k-1}) \end{aligned}\right\} \text{Correction} \qquad (4.17)$$

The elements ω_{DLL}, ω_{FLL} and ω_{PLL} are defined using DLL, FLL and PLL noise bandwidths ($B_n^{DLL} = 0.25\omega_{DLL}$, $B_n^{FLL} = 0.53\omega_{FLL}$ and $B_n^{PLL} = 0.7845\omega_{PLL}$). The correction step is performed only after the discriminators outputs are updated. In fact, $Z_k = \begin{bmatrix} D_\tau + \tau^{NCO} - \tilde{\tau}_{k-1} & D_\varphi & D_f + f^{NCO} - \tilde{f}_{k-1} \end{bmatrix}^T$ where D_τ, D_φ and D_f are DLL, PLL and FLL discriminator outputs, τ^{NCO} and f^{NCO} are the delay and frequency errors from the NCO, $\tilde{\tau}_{k-1}$ and $\tilde{f}_{k-1}$ are previous local estimator delay and frequency estimates.

4.3.8 NAVIGATOR

The state-space system to be solved by the navigator is

$$\begin{cases} X_k = \Phi X_{k-1} + w_k \\ Z_k = HX_k + v_k \end{cases} \tag{4.18}$$

where

$$X_k = \begin{bmatrix} \delta x, \delta y, \delta z, \delta \dot{x}, \delta \dot{y}, \delta \dot{z}, \delta t, \delta \dot{t} \end{bmatrix}^T, \Phi = \begin{bmatrix} I_{3\times 3} & \Delta T \cdot I_{3\times 3} & 0_{3\times 1} & 0_{3\times 1} \\ 0_{3\times 3} & I_{3\times 3} & 0_{3\times 1} & 0_{3\times 1} \\ 0_{1\times 3} & 0_{1\times 3} & 1 & \Delta T \\ 0_{1\times 3} & 0_{1\times 3} & 0 & 1 \end{bmatrix}, Z_k = \begin{bmatrix} \tilde{\tau}_1, \tilde{f}_1, \tilde{\tau}_2, \tilde{f}_2, ..., \tilde{\tau}_N, \tilde{f}_N \end{bmatrix}^T$$

$$H_k = \begin{bmatrix} \hat{a}_1 \frac{1}{c} & 0 & 1 & 0 \\ 0 & -\hat{a}_1 \frac{F_c}{c} & 0 & -F_c \\ \vdots & \vdots & \vdots & \vdots \\ \hat{a}_N \frac{1}{c} & 0 & 1 & 0 \\ 0 & -\hat{a}_N \frac{F_c}{c} & 0 & -F_c \end{bmatrix},$$

X_k is the state vector and is made of the receiver's earth-centred earth-fixed (ECEF) position, velocity, clock bias and clock drift errors; ΔT is the navigator update interval; $\hat{a}_i = (s_i - \hat{r}) / \left\| s_i - \hat{r} \right\|$ is a unit vector pointing from the receiver estimated position to the i^{th} satellite; $\left\| s_i - \hat{r} \right\|$ is the estimated distance between the receiver and the i^{th} satellite; $s_i = (x_i, y_i, z_i)$ is the i^{th} satellite ECEF position; $\hat{r} = (\hat{x}_r, \hat{y}_r, \hat{z}_r)$ is the receiver's estimated ECEF position; F_c is the nominal carrier frequency; c is the speed of light; w_k is a vector of random noise inputs such that $E\{w_k\} = 0, E\{w_k w_j^T\} = Q_k \delta_{kj}$; v_k is a vector of additive measurement noise such that $E\{v_k\} = 0, \quad E\{v_k v_j^T\} = R_k \delta_{kj}, E\{w_k v_j^T\} = 0, \delta_{kj} = 1$ if $k = j$, otherwise $\delta_{kj} = 0$. Z_k is the measurement vector and is made of code delay (pseudorange measurement) and

carrier frequency (delta-range measurement) estimates from the local estimator. The EKF algorithm used by the navigator to solve the system in Equation (4.18) is shown in equation (4.19):

$$\left.\begin{aligned} X_{k|k-1} &= \Phi X_{k-1|k-1} \\ P_{k|k-1} &= \Phi P_{k-1|k-1}\Phi^T + Q_k \\ Z_{k|k-1} &= H_k X_{k|k-1} \\ C_k &= H_k P_{k|k-1} H_k^T + R_k \end{aligned}\right\} \text{Prediction}$$

$$\left.\begin{aligned} K_k &= P_{k|k-1} H_k^T C_k^{-1} \\ X_{k|k} &= X_{k|k-1} + K_k (Z_k - Z_{k|k-1}) \\ P_{k|k} &= (I - K_k H_k) P_{k|k-1} \end{aligned}\right\} \text{Correction (Update)} \tag{4.19}$$

4.3.9 CODE AND CARRIER NCOS

The functional diagram of NCOs is shown in Figure 4.5.

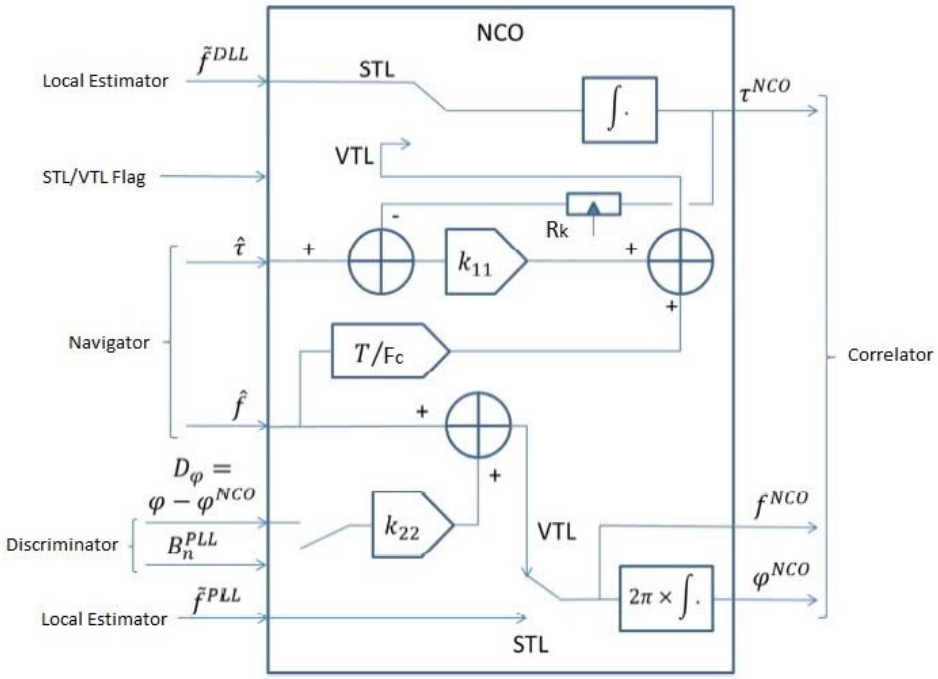

Figure 4.5: NCOs Functional Diagram

In STL mode, the code and carrier NCO outputs are

$$\begin{cases} \tau_k^{NCO} = \tau_{k-1}^{NCO} + T \times \tilde{f}_k^{DLL} \\ \varphi_k^{NCO} = \varphi_{k-1}^{NCO} + 2\pi T \times f_k^{NCO} \\ f_k^{NCO} = \tilde{f}_k^{PLL} \end{cases} \tag{4.20}$$

where T is the NCO update time, $\tilde{f}_k^{DLL}$ and $\tilde{f}_k^{PLL}$ are the DLL and PLL frequencies estimated by the local estimator. In VTL mode, the code and carrier NCO outputs are

$$\begin{cases} \tau_k^{NCO} = \tau_{k-1}^{NCO} + \dfrac{T}{F_c} \times \dfrac{(s_i - \hat{r})}{\|s_i - \hat{r}\|} \times \dfrac{-\hat{v}F_c}{c} + k_{11}\left(\|s_i - \hat{r}\| \dfrac{1}{c} - \tau_{k-1}^{NCO} \right) \\ \varphi_k^{NCO} = \varphi_{k-1}^{NCO} + 2\pi T \times f_k^{NCO} \\ f_k^{NCO} = \dfrac{(s_i - \hat{r})}{\|s_i - \hat{r}\|} \times \dfrac{-\hat{v}F_c}{c} + k_{22} \dfrac{1}{2\pi T} D_{\varphi k} \end{cases} \tag{4.21}$$

where $s_i = (x_i, y_i, z_i)$ is the i^{th} satellite ECEF position, $\hat{r} = (\hat{x}_r, \hat{y}_r, \hat{z}_r)$ is the receiver's estimated ECEF position, $\hat{v}=(\hat{\dot{x}}_r, \hat{\dot{y}}_r, \hat{\dot{z}}_r)$ is the receiver's estimated ECEF velocity, $k_{11} = \omega_{DLL} T$, $k_{22} = 2.4\omega_{PLL} T$, and D_{φ_k} is the current phase discriminator output.

4.3.10 Monitoring and Tracking Mode Controller

The monitoring and tracking mode controller as depicted in the block diagram of Figure 4.6 is present only in the adaptive tracking architecture (see Figure 4.2).

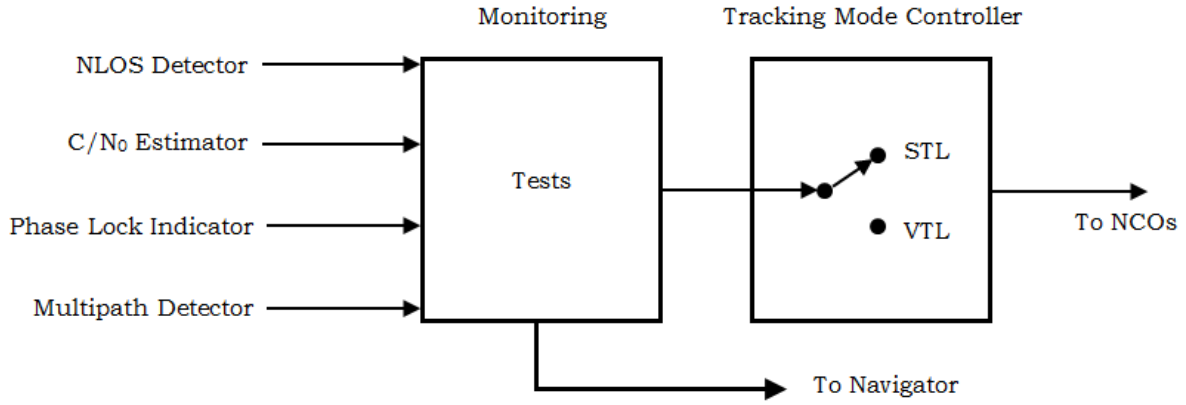

Figure 4.6: Monitoring and Tracking Mode Controller Block Diagram

Figure 4.7 depicts the flow diagram of the components in Figure 4.6. It is shown that the default tracking mode is STL. If either the NLOS detector indicates an NLOS situation, or the PLI indicates loss of phase lock and the C/N_0 goes below a defined threshold, the tracking mode controller directly switches to VTL tracking mode. The MP detector is used to exclude MP contaminated channels from PVT computation in the navigator, whether the tracking mode is STL or VTL.

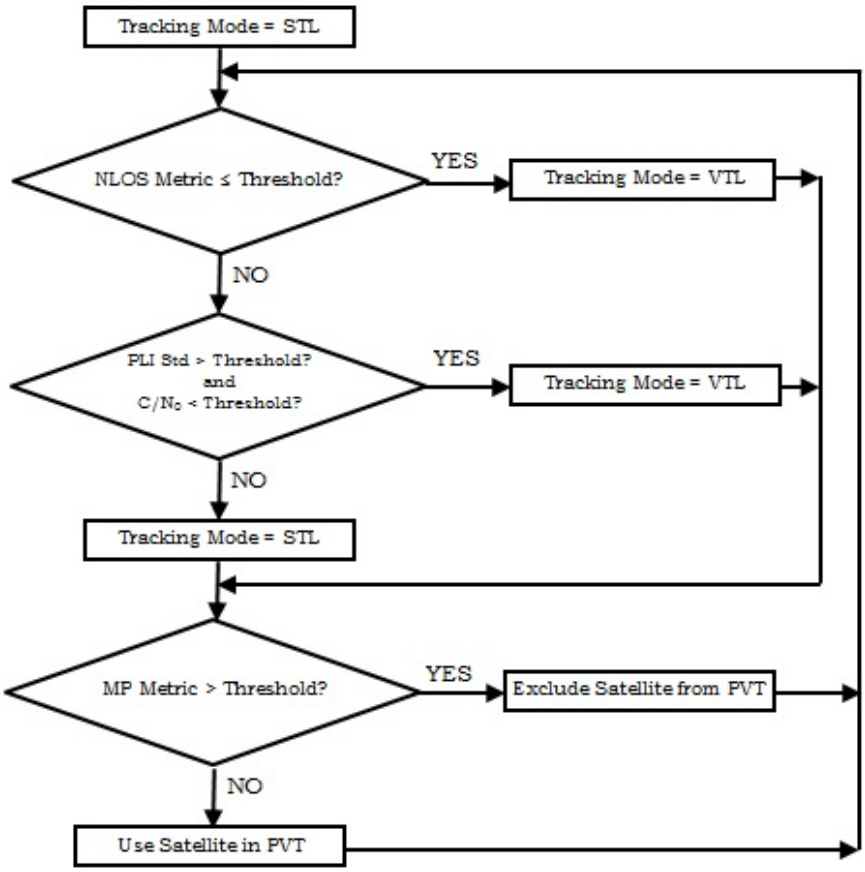

Figure 4.7: Monitoring and Tracking Mode Controller Flow Diagram

4.3.11 MEASUREMENTS SELECTOR

Figure 4.8 illustrates the flow diagram of the Measurements Selector. This component is present only in the conjoint tracking architecture (see Figure 4.3). VTL measurements are selected only if the indicators display a low C/N_0 and LOS absence, or a low C/N_0 and loss of phase lock; otherwise STL measurements are considered.

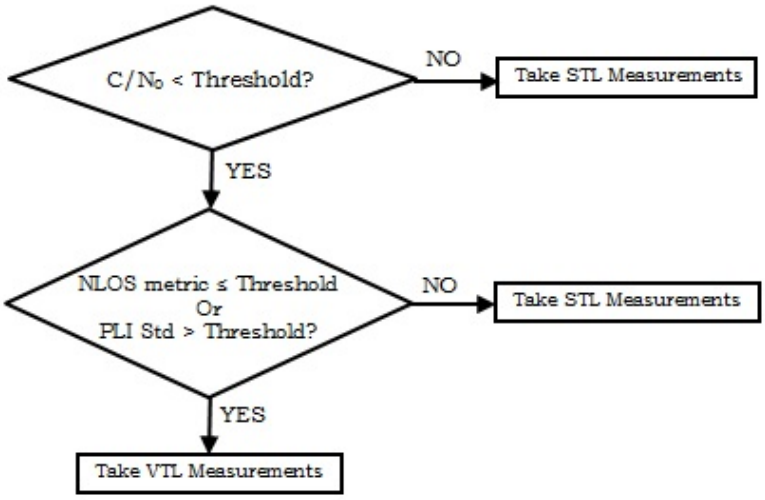

Figure 4.8: Measurements Selector Flow Diagram

4.3.12 TRAJECTORY AND ENVIRONMENT SIMULATOR

The trajectory and environment simulator in Figure 4.9 was described in detail in *Chapter 3*, sub-section 3.3.3.2. It receives as inputs the environment type, the trajectory north-east-down (NED) coordinates, and the constellation characteristics (elevation and azimuth of available satellites). It generates signal data (LOS and MP amplitudes, LOS and MP code propagation delays, LOS and MP carrier phases and frequencies) that are fed to the bank of correlators.

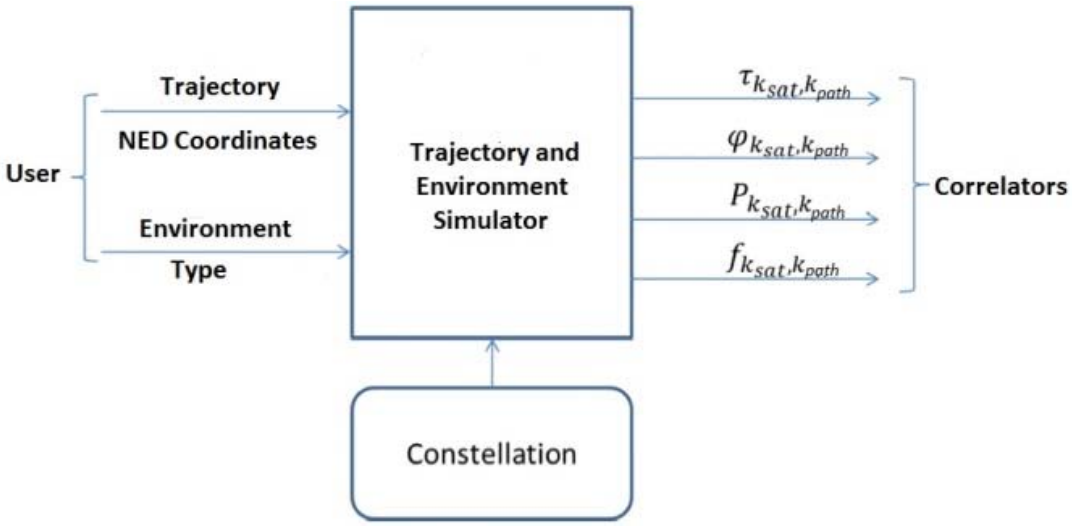

Figure 4.9: Functional Diagram of the Trajectory and Environment Simulator

4.4 DLR DATA SCENARIOS USED IN EXPERIMENTS

Table 4.1 summarizes some data scenarios from the DLR multipath model that are used in the experiments performed to validate the proposed tracking and positioning solutions. More details about data generation are given in *Chapter 3*, sub-section 3.3.3.2.

Table 4.1: Scenarios of DLR data used for experiments

Constellation	Constellation No 1 (see *Chapter 3*, Table 3.1)					
Environment	Suburban			Urban		
Trajectory	Straight Line			Straight Line		
Dynamics	Pedestrian	Vehicle		Pedestrian	Vehicle	
	Constant acceleration (0.5 m/s^2)	Constant velocity (50km/h)	Constant velocity (90km/h)	Constant acceleration (0.5 m/s^2)	Constant velocity (50km/h)	Constant velocity (90km/h)
Scenarios	Scenario 1	Scenario 2	Scenario 3	Scenario 4	Scenario 5	Scenario 6

4.5 EXPERIMENTAL RESULTS

4.5.1 SETTINGS AND TUNINGS

Table 4.2 shows some parameter settings and tunings for the algorithms used in the receiver experimental simulations.

Table 4.2: Settings and tunings in experimental simulations

Algorithm	Parameter	Setting/Tuning
EKF	Measurement noise covariance matrix	$R_k = \begin{bmatrix} \delta_1 & 0 & \cdots & 0 \\ 0 & \delta_2 & \cdots & 0 \\ \vdots & \vdots & \vdots & \vdots \\ 0 & 0 & \cdots & \delta_N \end{bmatrix}_{2N\times 2N}$; $\delta_N = \begin{bmatrix} \sigma_{DLL}^2 & 0 \\ 0 & \sigma_{FLL}^2 \end{bmatrix}$; $\sigma_{DLL}^2 = \frac{B_n^{DLL} d}{2\,C/N_0}$; $\sigma_{FLL}^2 = \frac{B_n^{FLL}}{\pi^2 T_n^2\, C/N_0}$; $B_n^{DLL} = 1Hz$; $B_n^{PLL} = B_n^{FLL} = 10Hz$; $T_n = 1ms$; $d = 0.4chip$; N:number of satellites in view
	Input noise covariance matrix	$Q_k = \begin{bmatrix} u & 0_{2\times2} & 0_{2\times2} & 0_{2\times2} \\ 0_{2\times2} & u & 0_{2\times2} & 0_{2\times2} \\ 0_{2\times2} & 0_{2\times2} & u & 0_{2\times2} \\ 0_{2\times2} & 0_{2\times2} & 0_{2\times2} & \beta \end{bmatrix}_{8\times8}$; $u = \begin{bmatrix} S_p \frac{\Delta T^3}{3} & S_p \frac{\Delta T^2}{2} \\ S_p \frac{\Delta T^2}{2} & S_p \Delta T \end{bmatrix}$; $\beta = \begin{bmatrix} S_c \frac{\Delta T^3}{3} & S_c \frac{\Delta T^2}{2} \\ S_c \frac{\Delta T^2}{2} & S_c \Delta T \end{bmatrix}$; S_p : position noise spectrum density; S_c : clock noise spectrum density; $\Delta T = 1ms$
	Initial estimation error covariance matrix	$P_0 = \begin{bmatrix} \delta P & 0_{3\times3} & 0_{3\times2} \\ 0_{3\times3} & \delta V & 0_{3\times2} \\ 0_{2\times3} & 0_{2\times3} & \delta T \end{bmatrix}_{8\times8}$; $\delta P = \begin{bmatrix} \delta x^2 & 0 & 0 \\ 0 & \delta y^2 & 0 \\ 0 & 0 & \delta z^2 \end{bmatrix}$; $\delta V = \begin{bmatrix} \delta \dot{x}^2 & 0 & 0 \\ 0 & \delta \dot{y}^2 & 0 \\ 0 & 0 & \delta \dot{z}^2 \end{bmatrix}$; $\delta T = \begin{bmatrix} \delta t^2 & 0 \\ 0 & \delta \dot{t}^2 \end{bmatrix}$; $\delta x = \delta y = \delta z = 50m$; $\delta \dot{x} = \delta \dot{y} = \delta \dot{z} = 90/3.6\, m/s$; $\delta t = 10^{-4}\, s$; $\delta \dot{t} = 2\times10^{-5}\, s/s$
MP Detector I	FFT size; Detection threshold	*N = 100* (sliding window)*; PFA = 10-7 (STL); PFA = 10-8 (VTL)*
MP Detector II	FFT size; Detection threshold	*N = 1024* (sliding window)*; PFA = 10-3 (STL); PFA = 10-4 (VTL)*

Table 4.3: Settings and tunings continued

Algorithm	Parameter	Setting/Tuning
NLOS detector	FFT size; Threshold	$N = 100$ (sliding window); $\eta = 50\ dBW/Hz$
PLI indicator	Threshold; Number of samples	$\eta = 0.5$ (PLI standard deviation); $N=100$ (sliding window)
C/N_0 estimator	Threshold; Number of samples	$T = 30dBHz$; $N=40$ (sliding window)

4.5.2 RESULTS

The solutions proposed in this chapter are mostly appropriate for a multi-constellation receiver. In a multi-constellation setting, the number of potentially available satellites is high. Consequently, at a PVT calculation instant of time t_n, there is a high probability to have a reasonable number of satellites that are unaffected by multipath and that can be used in the PVT. If the number of healthy satellites decreases significantly, the MP detector threshold can be momentarily raised or the EKF algorithm can be set to base its PVT on prediction, until better measurement conditions are restored. In the experiments hereafter for instance, the threshold (see Table 4.2) was raised a bit in comparison with the thresholds suggested in *Chapter 3,* Table 3.4, to allow better satellite geometry to be maintained after exclusion of multipath contaminated satellites. Also, as the proposed solutions are tested in a GPS receiver first (see Constellation No 1), in order to create scenarios that will allow comparison between an architecture that uses NLOS and MP detectors and one that does not, Scenarios 1 to 6 (see Table 4.1) are slightly modified in experimental simulations to allow only 4 out of 9 available satellites to undergo MPs. Although the 5 remaining satellites are not MP-affected, they do undergo LOS masking occasionally according to the DLR environment settings.

4.5.2.1 VTL Architecture Performance

In order to validate the suggested VTL architecture, it is first tested in an open sky environment without the use of any signal quality indicators for channel exclusion. Figure 4.10 shows that the position and velocity errors for this unconstrained environment remain at minimum with mean and standard deviation close to zero. Figures 4.11 and 4.12 depict ECEF position and velocity errors for Scenarios 1 and 3 respectively, for the proposed VTL tracking scheme, without the use of the NLOS and MP detectors i.e. without unhealthy channel exclusion from PVT calculation (red

lines) and then with the use of NLOS and MP detectors (MP Detector II metric) i.e. with unhealthy channel exclusion (black lines). Table 4.4 provides numerical values of error means and standard deviations for Scenarios 1 and 3. It can be observed that the magnitude of positioning errors when there is no exclusion is far bigger than when there is exclusion.

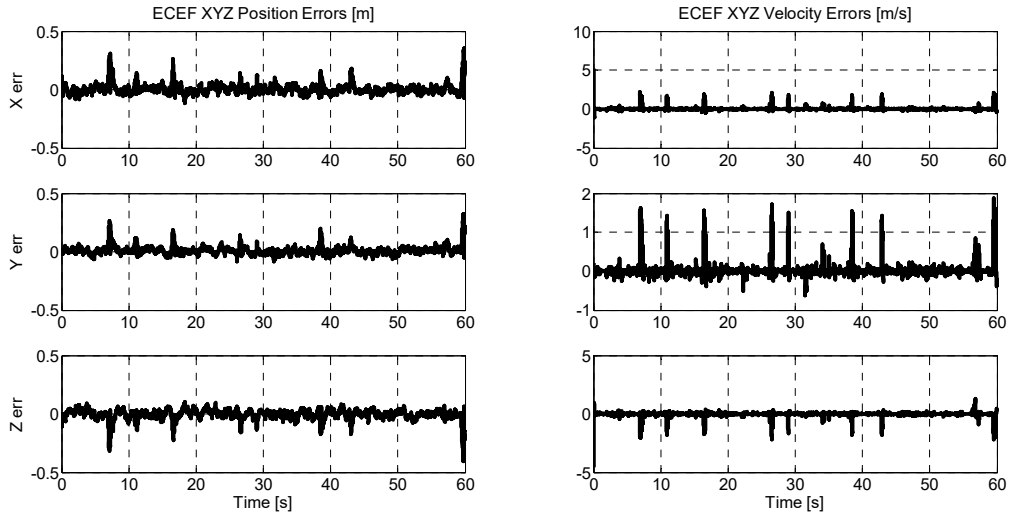

Figure 4.10: VTL ECEF position and velocity errors, open sky, car (50 km/h)

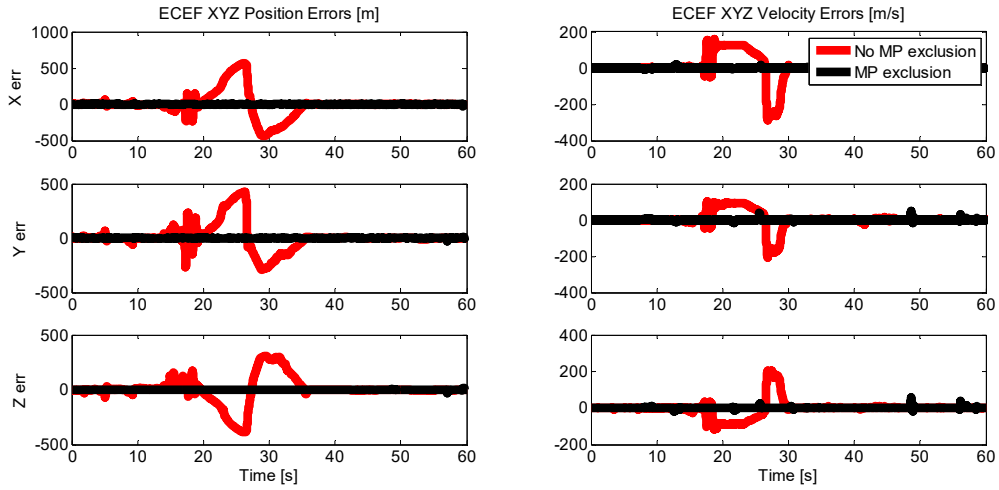

Figure 4.11: Scenario 1, VTL ECEF position and velocity errors

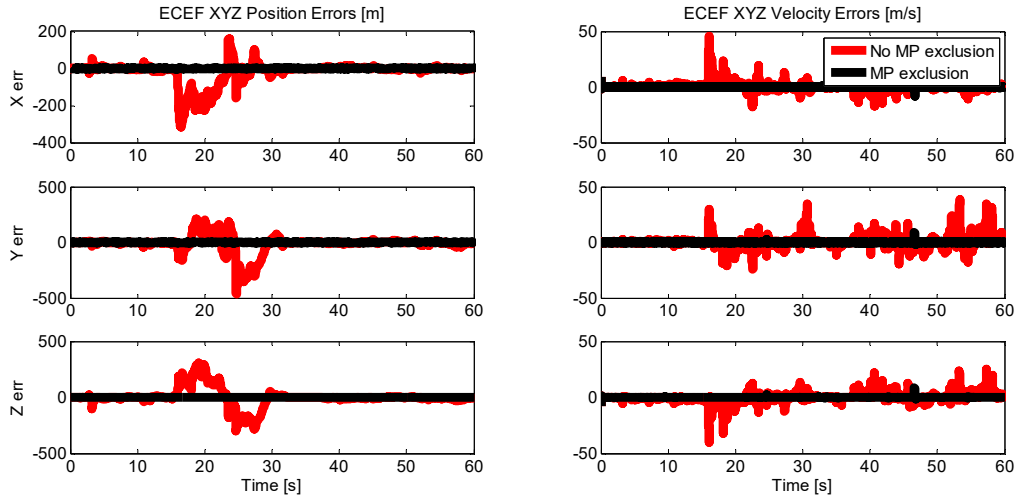

Figure 4.12: Scenario 3, VTL ECEF position and velocity errors

Table 4.4: Scenarios 1 and 3, VTL (NLOS and MP exclusion) versus VTL (No NLOS and No MP exclusion): PVT errors

Error		Scenario 1				Scenario 3			
		Exclusion		No exclusion		Exclusion		No exclusion	
		Mean	STD	Mean	STD	Mean	STD	Mean	STD
Position [m]	X	-0.0958	1.4800	-2.7000	167.8853	-0.0035	0.0540	-18.9066	59.6467
	Y	0.0962	1.0371	6.3050	118.3508	0.0072	0.0674	-14.6505	81.2515
	Z	0.0338	1.4036	6.9688	120.2087	-0.0041	0.0797	0.3135	81.5465
Velocity [m/s]	X	-0.0850	1.2734	5.6048	62.9437	0.0016	0.2334	0.5553	3.5128
	Y	0.1861	2.6874	4.5766	43.2995	0.0054	0.2396	0.7804	5.0903
	Z	0.1978	2.8808	-3.4923	44.2826	0.0011	0.3011	0.0946	3.8671

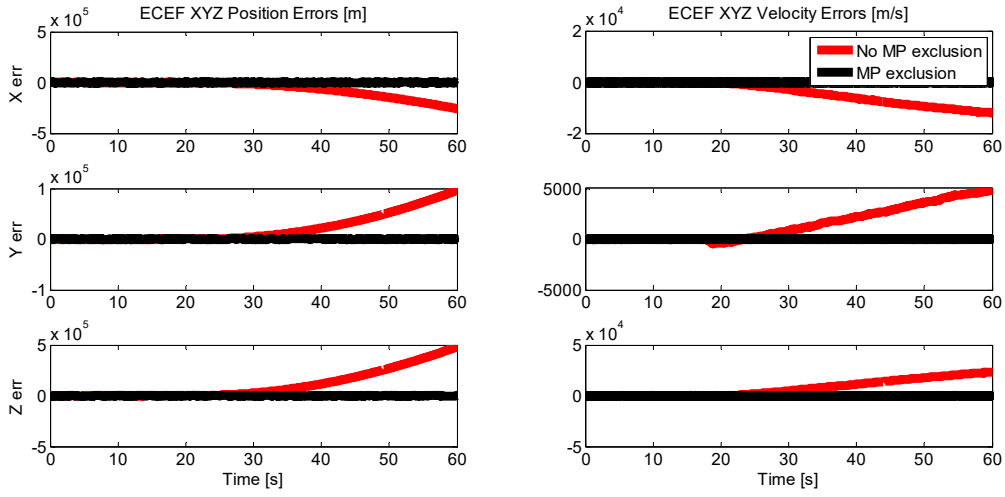

Figure 4.13: Scenario 2, VTL ECEF position and velocity errors

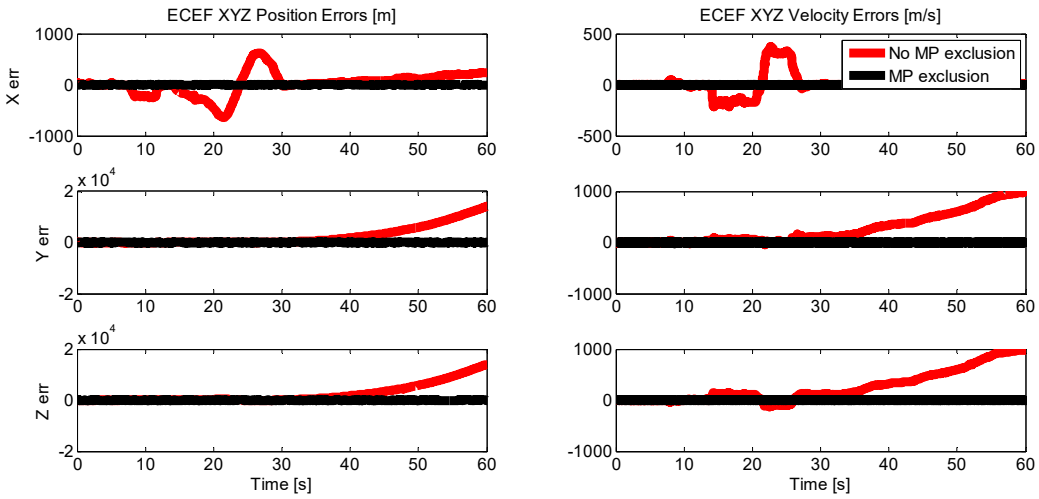

Figure 4.14: Scenario 6, VTL ECEF position and velocity errors

Figures 4.13 and 4.14, which show position and velocity errors for Scenarios 2 and 6 respectively, demonstrate that in very harsh MP conditions, the EKF algorithm in the navigator may diverge. However, the exclusion of low power and MP contaminated satellites from PVT calculation corrects this divergence problem and improves the PVT accuracy from a magnitude of kilometers and kilometers/second to a few meters and meters/sec. Figure 4.15 shows, for Scenario 6, the number of satellites that are considered healthy by the quality indicators at each PVT computation time and that are therefore included in the calculation. Out of the 9 visible satellites of Constellation 1, the number of used satellites is varying between 4 and 9.

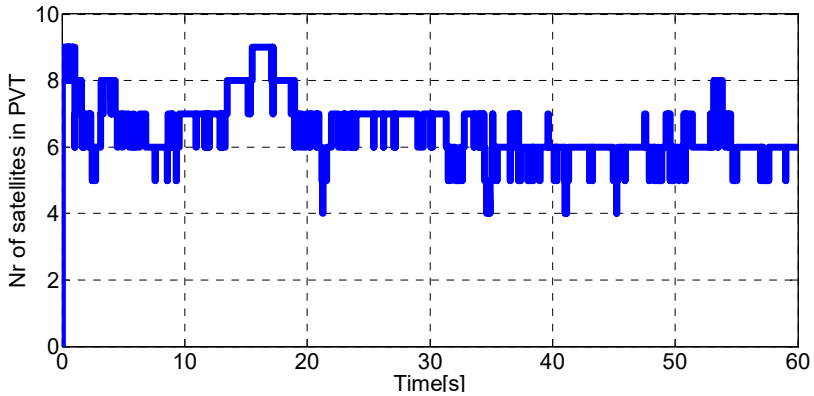

Figure 4.15: Scenario 6, VTL, Number of satellites used in PVT

The improvement of PVT accuracy from exclusion of unhealthy satellites has an interesting consequence: it improves vector tracking performance as it will be demonstrated in the figures hereafter because the estimation of tracking parameters benefits from a more accurate PVT.

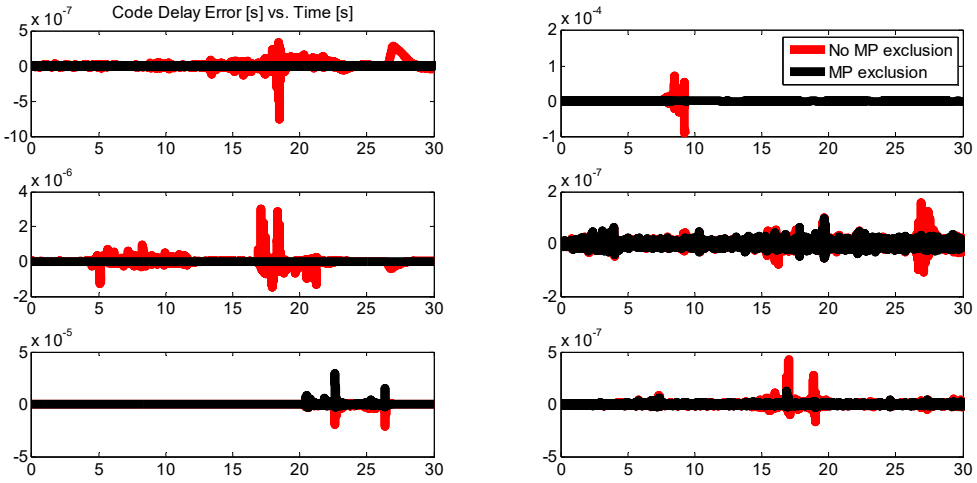

Figure 4.16: Code delay errors before and after unhealthy satellites exclusion from PVT (Top to bottom, left to right: PRN05, PRN15, PRN27, PRN07, PRN09, PRN26; Constellation 1, Scenario 1)

It should be mentioned that although MP contaminated satellites are excluded from PVT calculation, they continue being tracked by the VTL. Figures 4.16, 4.17 and 4.18 illustrate code delay, carrier phase and carrier frequency tracking errors of 6 satellites of Constellation 1 before exclusion of unhealthy satellites from PVT (red lines) and after exclusion (black lines). It is clearly observed that in general the magnitude of tracking errors decreases as PVT accuracy improves. This is particularly noticeable for the phase tracking errors.

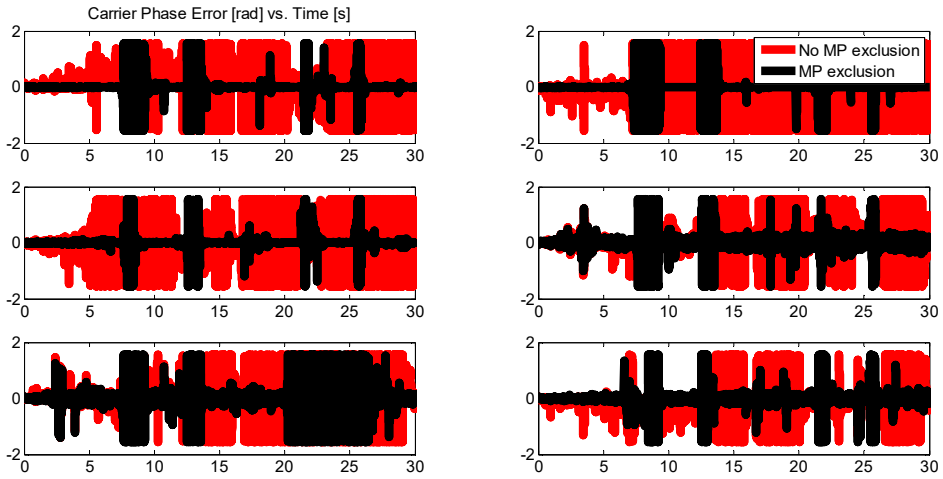

Figure 4.17: Carrier phase errors before and after unhealthy satellites exclusion from PVT (Top to bottom, left to right: PRN05, PRN15, PRN27, PRN07, PRN09, PRN26; Constellation 1, Scenario 1)

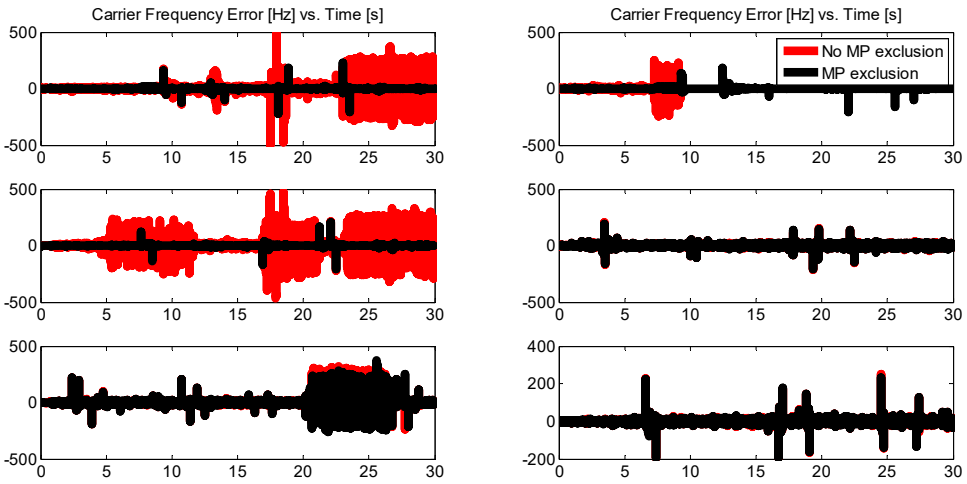

Figure 4.18: Carrier frequency errors before and after unhealthy satellites exclusion from PVT (Top to bottom, left to right: PRN05, PRN15, PRN27, PRN07, PRN09, PRN26; Constellation 1, Scenario 1)

4.5.2.2 Adaptive and Conjoint STL-VTL Architecture Performance

Figures 4.19 and 4.20 show that the channels of the adaptive tracking scheme (A-STL/VTL) switch between STL and VTL modes following the configuration of quality indicators (C/N_0 estimator, NLOS detector and PLI) in Figure 4.7. In Figure 4.19, only the LOS is present. The moments of outage (LOS masking) correspond exactly to the moments where the channel switches to VTL mode. This maintains continuous satellite tracking, which the STL mode cannot do alone. In Figure 4.20, LOS and MPs are present. The A-STL/VTL scheme once more adjusts the tracking mode following the outage conditions. Figures 4.21 and 4.22 also demonstrate that the conjoint tracking scheme (C-STL/VTL) chooses STL or VTL pseudorange and delta-range measurements based on the outage conditions interpreted using the technique in Figure 4.8. The STL C/N_0, PLI and NLOS indicators are used in the tests. It can be seen from Figure 4.21 that the STL loses track of PRN07 around the 7th second due to outage (NLOS) conditions. The VTL maintains PRN07 tracking throughout the outage. Consequently, just after the 7th second, the measurements selector unit of the C-STL/VTL scheme chooses VTL measurements over STL. Figure 4.22 is a case where harsh NLOS and MP conditions do not allow the STL to keep tracking PRN08. Therefore, VTL measurements are selected throughout the 60s simulation time.

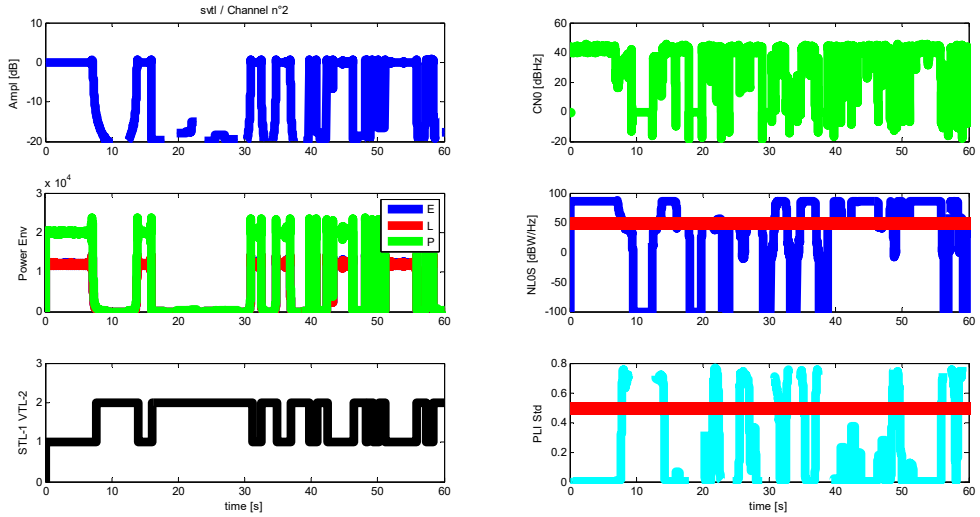

Figure 4.19: Top to bottom, left to right: LOS amplitude (dB), Prompt, Early and Late power envelopes, Tracking mode (STL-1, VTL-2), C/N_0 estimate, NLOS detector, PLI Std. indicator. Constellation 1, PRN07, Scenario 1, Adaptive STL/VTL scheme.

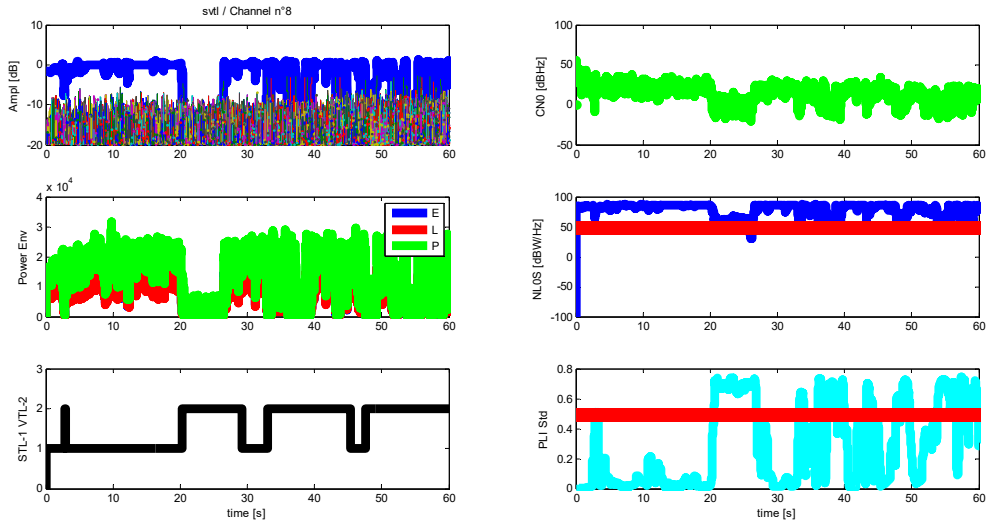

Figure 4.20: Top to bottom, left to right: LOS and MPs amplitudes (dB), Prompt, Early and Late power envelopes, Tracking mode (STL-1, VTL-2), C/N_0 estimate, NLOS detector, PLI Std. indicator. Constellation 1, PRN27, Scenario 1, Adaptive STL/VTL scheme.

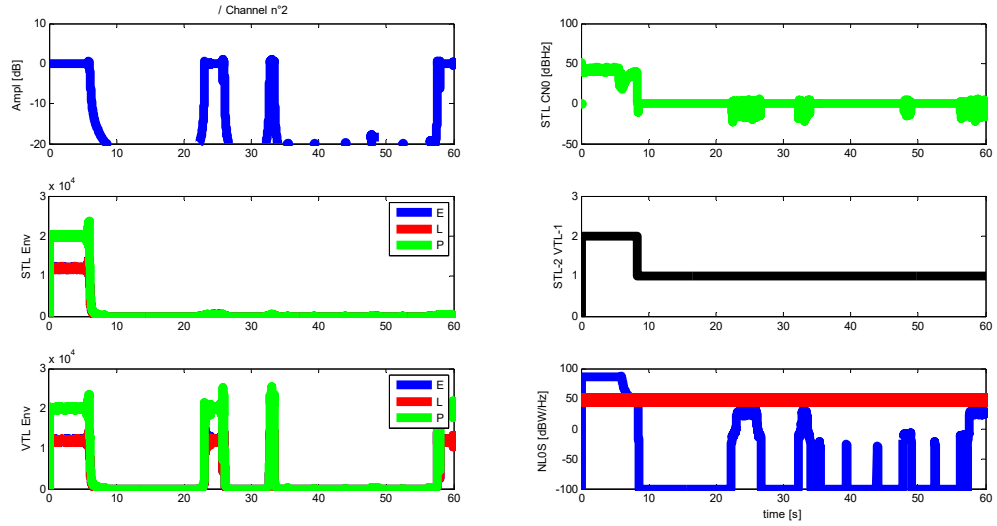

Figure 4.21: Top to bottom, left to right: LOS amplitude (dB), Prompt, Early and Late power envelopes for STL, then for VTL, STL C/N_0 estimate, Selected measurements (STL-2, VTL-1), NLOS detector. Constellation 1, PRN07, Scenario 4, Conjoint STL/VTL scheme.

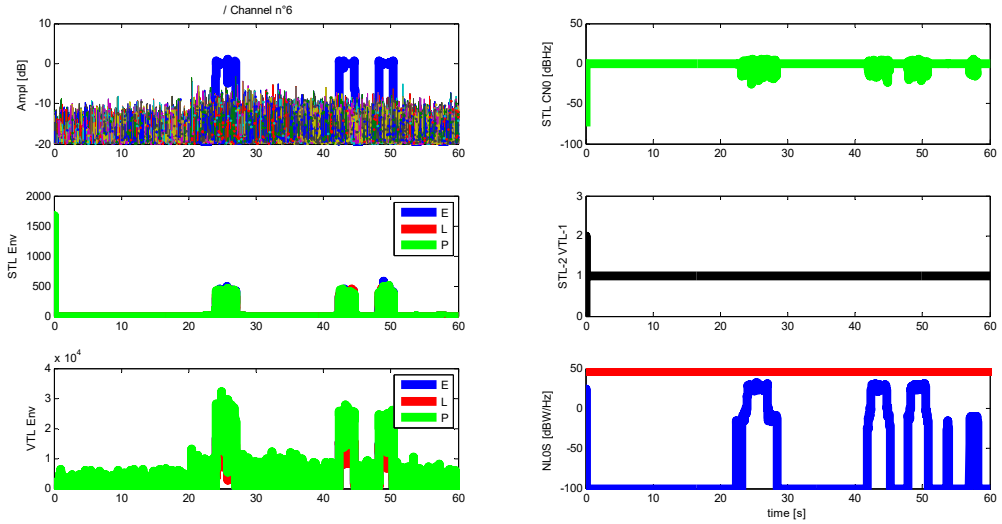

Figure 4.22: Top to bottom, left to right: LOS and MPs amplitudes (dB), Prompt, Early and Late power envelopes for STL, then for VTL, STL C/N_0 estimate, Selected measurements (STL-2, VTL-1), NLOS detector. Constellation 1, PRN08, Scenario 4, Conjoint STL/VTL scheme.

Figures 4.23 and 4.24 depict positioning errors for Scenarios 1 and 3 with the A-STL/VTL scheme, while Figure 4.25 shows errors for Scenario 4 with the C-STL/VTL scheme, before (red lines) and after (black lines) exclusion of unhealthy satellites from PVT calculation. These figures show that the use of quality indicators (C/N_0 estimator, NLOS and MP detectors, PLI) and their proper configuration to ensure continuous satellite tracking and to exclude unhealthy satellites from PVT

computation has the benefit of improving PVT accuracy for both the adaptive and conjoint STL/VTL schemes.

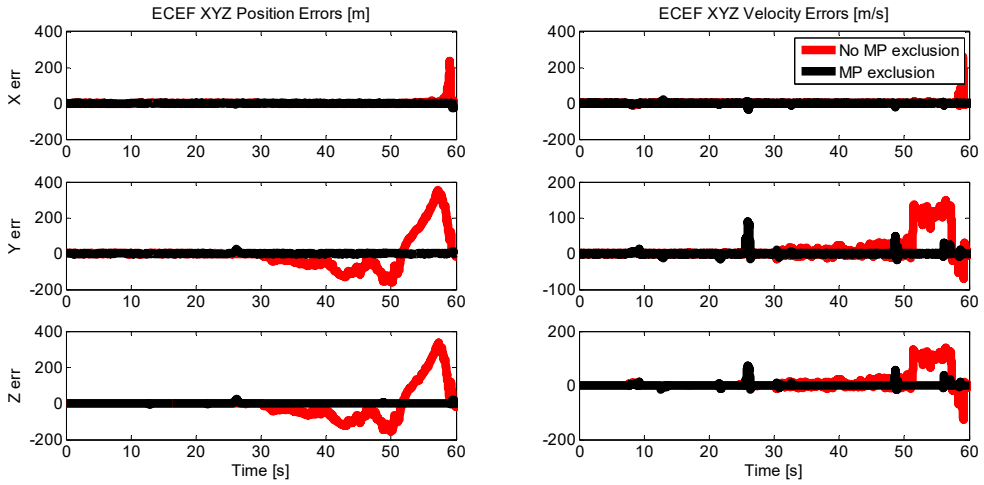

Figure 4.23: Scenario 1, adaptive STL-VTL ECEF position and velocity errors

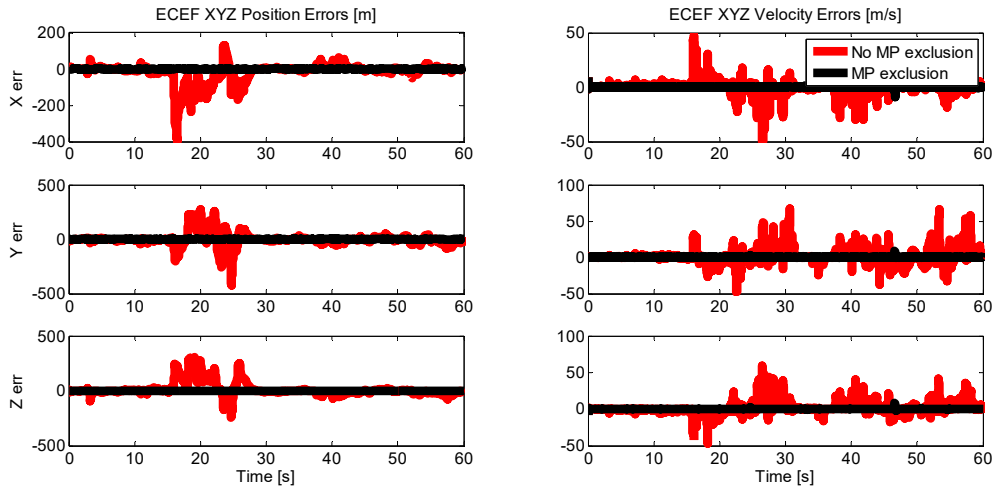

Figure 4.24: Scenario 3, adaptive STL-VTL ECEF position and velocity errors

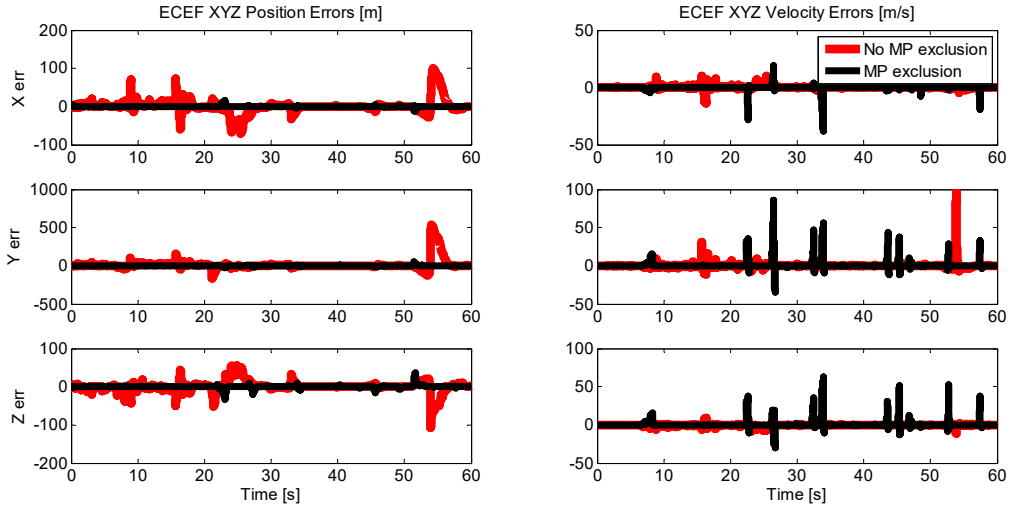

Figure 4.25: Scenario 4, conjoint STL-VTL ECEF position and velocity errors

4.5.2.3 *STL, VTL, Adaptive and Conjoint STL-VTL Performance*

The results hereafter are based on PVT calculation with the use of quality indicators (C/N_0 estimator, MP detectors) to exclude unhealthy satellites. The exclusion is performed for all tracking schemes: STL, VTL, A-STL/VTL and C-STL/VTL. In scenario 4 (Figure 4.26, Figure 4.27 and Table 4.5), the STL has better PVT accuracy than the VTL. This is a direct consequence of good tracking conditions for the STL in this particular situation. This case shows that even in an urban environment, if there are enough healthy satellites and in low dynamic conditions, the STL may still outperform the VTL in terms of PVT accuracy. That is why these hybrid tracking schemes (A-STL/VTL and C-STL/VTL) are proposed to benefit from this type of situation when it arises in harsh environments. The expected behaviour is for the adaptive and conjoint tracking schemes to conform to the STL PVT rather than the VTL PVT and that is exactly what happens. In fact, at each instant of time t_n, quality indicators choose the tracking mode that shows better performance based on the techniques proposed in Figure 4.7 (A-STL/VTL) and Figure 4.8 (C-STL/VTL).

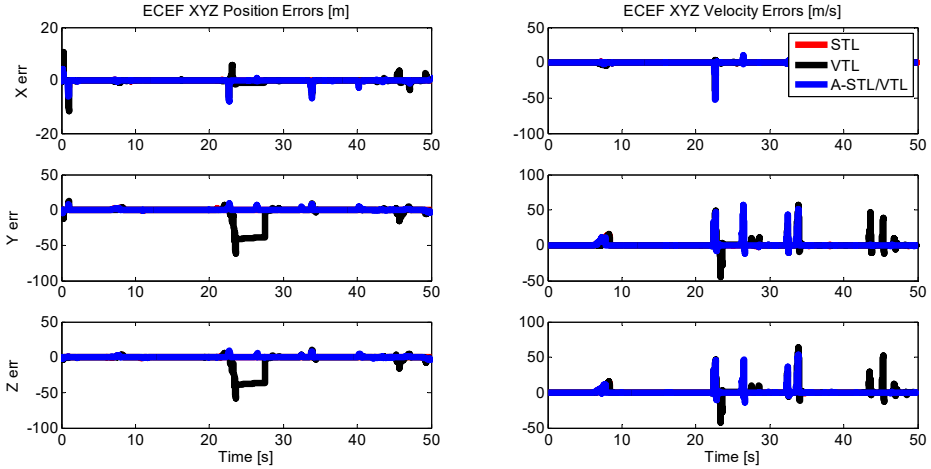

Figure 4.26: Scenario 4, STL, VTL and A-STL/VTL PVT errors

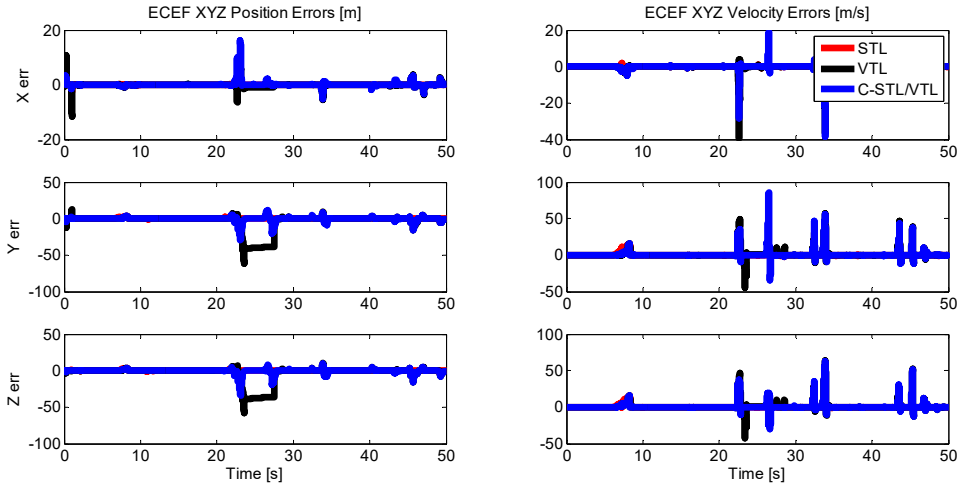

Figure 4.27: Scenario 4, STL, VTL and C-STL/VTL PVT errors

Table 4.5: Scenario 4, STL, VTL, A-STL/VTL, C-STL/VTL: comparison of PVT errors

Error		Scenario 4							
		STL		VTL		A-STL/VTL		C-STL/VTL	
		Mean	STD	Mean	STD	Mean	STD	Mean	STD
Position [m]	X	-0.0074	0.1260	-0.1243	0.6755	-0.0629	0.4827	0.0773	0.9818
	Y	0.0442	0.4726	-3.4503	11.3725	0.1889	0.9656	-0.3825	2.9778
	Z	0.0308	0.4136	-3.2539	10.7194	0.1791	0.9919	-0.4325	3.0129
Velocity [m/s]	X	-0.0013	0.1422	-0.2340	2.1493	-0.2422	2.8286	-0.1931	2.1913
	Y	0.2927	1.7037	0.8137	5.2129	0.7785	4.6677	0.9668	6.1439
	Z	0.2621	1.6248	0.8741	5.4876	0.7066	4.5298	0.7936	5.1347

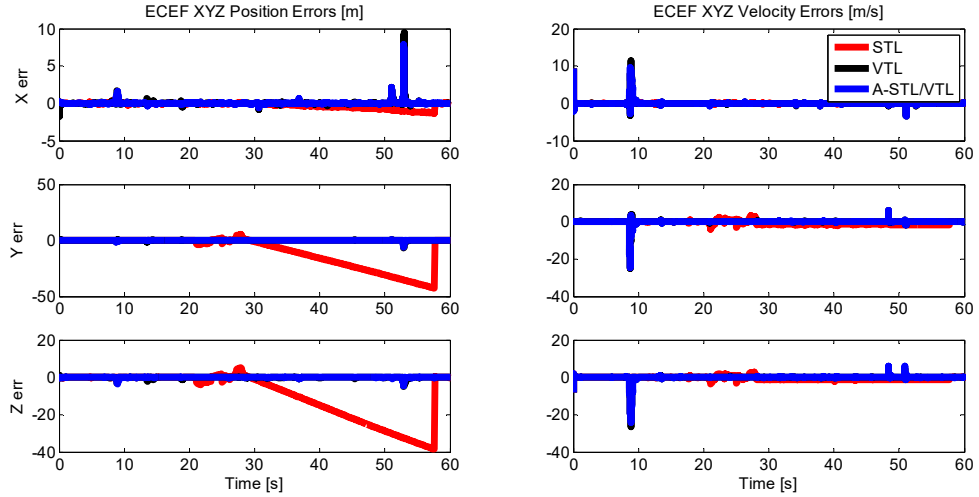

Figure 4.28: Scenario 6, STL, VTL and A-STL/VTL PVT errors

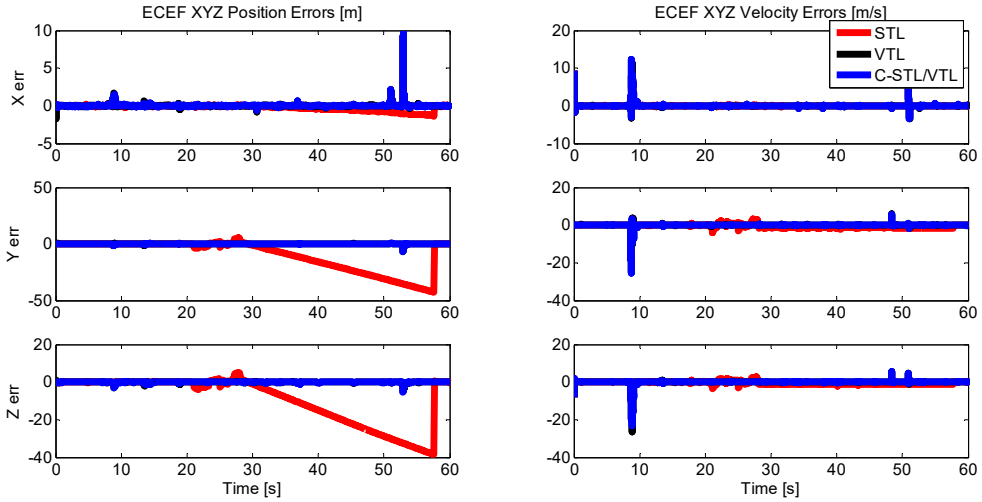

Figure 4.29: Scenario 6, STL, VTL and C-STL/VTL PVT errors

Table 4.6: Scenario 6, STL, VTL, A-STL/VTL, C-STL/VTL: comparison of PVT errors

Error		Scenario 6							
		STL		VTL		A-STL/VTL		C-STL/VTL	
		Mean	STD	Mean	STD	Mean	STD	Mean	STD
Position [m]	X	-0.2658	0.3786	0.0239	0.3376	0.0408	0.3693	0.0298	0.3402
	Y	-9.9858	13.5538	0.0058	0.2640	-0.0050	0.2666	0.0048	0.2591
	Z	-9.2742	12.4969	-0.0682	0.2736	-0.0478	0.2808	-0.0629	0.2959
Velocity [m/s]	X	-0.0120	0.1751	0.0322	0.4912	0.0481	0.5901	0.0469	0.5800
	Y	-0.6867	0.9570	-0.0487	0.8321	-0.0477	0.7013	-0.0486	0.7348
	Z	-0.6335	0.8890	-0.0694	1.0122	-0.0874	1.0835	-0.0914	1.0954

Scenario 6 (Figure 4.28, Figure 4.29 and Table 4.6) is a harsh urban environment case with higher receiver dynamics than Scenario 4. The VTL performs better than the STL as it can be observed from their PVT accuracy. The adaptive (A-STL/VTL) and conjoint (C-STL/VTL) performance conforms to the VTL this time rather than the STL.

The VTL in Scenario 6 (moving car) has better performance than in Scenario 4 (moving pedestrian). The receiver being in a harsh environment for both cases, and as the artificial scenery made of trees, lamp poles and buildings is generated in a stochastic manner, it is possible for a pedestrian to remain in a harsh spot longer than a moving car. If the VTL navigator gets contaminated due to failure to exclude a problematic satellite on time, the positioning and tracking performance of the VTL is affected. In a case of VTL navigator contamination, it is not surprising that the STL outperforms the VTL like in Scenario 4.

Based on the statistics in Tables 4.5 and 4.6, comparison between A-STL/VTL and C-STL/VTL tracking schemes in terms of PVT accuracy shows that they have almost the same performance. Their tracking and navigation performance conforms to the tracking mode from which better performance is expected at a specific time. The key to achieve good performance therefore mainly lies in the proper specification and tuning of the quality indicators that allow commutations between STL and VTL modes for the adaptive tracking scheme or the selection of STL or VTL measurements for the conjoint tracking scheme.

Looking at the statistics in Tables 4.5 and 4.6, in particular cases where the STL (correspondingly the VTL) outperforms the VTL (correspondingly the STL) in terms of PVT accuracy, it also slightly outperforms the hybrid schemes. This comes from

the hybridization. However, in general, taking a broader perspective, the hybrid schemes will both outperform the STL alone and VTL alone, due to their capacity to exploit the advantages and reject the disadvantages of STL and VTL schemes taken alone in harsh environments. This means that when the STL operates alone in harsh environments, it will experience tracking difficulties that the VTL and the hybrid schemes will not. Similarly, the VTL taken alone will experience positioning inaccuracies that the STL and hybrid schemes may overcome. Therefore, although the hybrid schemes have a slightly lower tracking and positioning accuracy than the tracking loop they want to conform to when the latter performs well, they present a good performance compromise that is better than the STL or VTL alone.

4.6 CONCLUSION

The presence of multipath signals and the masking of the LOS signal in harsh environments create problems related to tracking robustness and positioning availability and accuracy when conventional scalar tracking loops are used. This chapter has suggested three tracking and navigation architecture solutions to address these problems simultaneously. Firstly, a VTL scheme that uses signal quality indicators to exclude unhealthy satellites from PVT calculation. Secondly, an adaptive STL-VTL scheme that commutes between STL and VTL modes depending on the state of signal quality indicators. And finally, a conjoint STL-VTL scheme that performs simultaneous STL and VTL tracking and delivers STL or VTL measurements to the navigator based on the indicators state. The proposed VTL scheme shows better tracking and positioning performance when the quality indicators (NLOS and MP detectors, C/N_0 estimator) are used to exclude fault in the navigator. Both adaptive and conjoint schemes retain the robustness of VTL tracking for harshly disturbed satellites and the PVT accuracy of the STL in less challenged situations. In general, both hybrid schemes present a good compromise between STL and VTL advantages and disadvantages, which is better than the STL or VTL schemes alone. The choice of the hybrid scheme to implement depends on preferences as there is a trade-off between low architecture complexity and navigator contamination detection capability. Nonetheless, the low complexity of the adaptive scheme for the performance it can achieve is particularly attractive. The navigator that is used in all the three proposed solutions is Extended Kalman Filter (EKF)-based. The next chapter investigates the use of Unscented Kalman Filter (UKF)-based and Particle Filter (PF)-based navigators in the vector tracking scheme.

Chapter 5

Nonlinear Bayesian Filtering Approaches to the Navigation and Vector Tracking Problem

An approximate answer to the right problem is worth a good deal more than an exact answer to an approximate problem.

— John W. Tukey

5.1 INTRODUCTION

The navigation and signal tracking tasks in a vector tracking scheme of a Global Positioning System (GPS)/Global Navigation Satellite System (GNSS) receiver form a single problem that is tackled in one and the same algorithm. The signal tracking process generates the measurements that are required to calculate the navigation solution and the navigation solution is used to estimate the signal tracking parameters. Due to various phenomena such as atmospheric effects and multipath, the probability densities of measurements and tracking errors become non-Gaussian, asymmetric and often multi-modal. In addition, the measurement model is intrinsically nonlinear. The navigation and vector tracking problem is therefore formulated as a nonlinear, non-Gaussian dynamic system with a state-space model representation. Nonlinear Bayesian estimation algorithms are among the most suitable methods currently known to approach the problem. Several suboptimal solutions have been applied to the problem or theoretically shown to have a high potential as solution to the problem.

The algorithm of the Bayesian estimation family that has been extensively used and documented in literature to tackle the navigation and vector tracking problem in GNSS is the Extended Kalman Filter (EKF). The EKF performs a first-order Taylor series linearization of the filtering model around the most recent system state estimate and then applies Kalman Filter (KF) equations. The underlying assumption behind this successive linearization is that the only uncertainty in the filtering model lies in the realization of state and measurement noises. The EKF is suitable for weakly nonlinear dynamic systems. However, in practice, the filtering model order and parameters are not known precisely and may vary in time. In the presence of

severe nonlinearities, the EKF solution therefore diverges. Several adaptive filtering techniques have been devised to deal with EKF divergence issues. Other techniques that are used to combat multipath and other disturbances in GNSS also help minimize EKF divergence occurrences. The tracking and navigation solutions presented in *Chapter 4* for instance are EKF-based and also contribute to avoiding EKF divergence in nonlinear, non-Gaussian situations as it has been shown.

The Unscented Kalman Filter (UKF) is an alternative to the EKF that does not linearize the nonlinear equations of the system. The UKF is based on a Gaussian approximation of the probability density function of the uncertainties in the state. It makes use of the unscented transformation which utilizes a set of appropriately chosen weighted points to parameterize the means and variances of the probability density function. The UKF is able to accurately capture the mean and covariance estimates up to the third-order of a Taylor series expansion for any nonlinearity with Gaussian inputs [6] [7]. The use of the UKF in various GNSS applications has been investigated in literature with performance comparison with the EKF [84] [85] [86] [87] [88]. Although the UKF is more immune to divergence than the EKF as it approaches the nonlinearities in the system better than the EKF does, it does not apply to general non-Gaussian distributions. It also requires the use of iterative and adaptive filtering strategies to improve its estimation accuracy and prevent it from converging to an incorrect state estimate. Several iterative and adaptive UKF techniques related to GNSS or other applications are documented in literature [89] [90] [91] [92] [93] [94] [95]. The Particle Filter (PF) is another interesting alternative to the EKF that grasps the complexities (nonlinearity, non-Gaussianity) of the dynamic system even better. It assumes general form for the probability density function of the uncertainties in the state. The key idea behind the PF is to find an approximate solution using a complex model rather than an exact solution using a simplified model. In comparison with EKF and UKF, the PF enhances the estimation results but drastically increases the computational cost. This has motivated researchers to develop a synergy of these approaches and has led to the development of the Extended Kalman Particle Filter [96], the Unscented Particle Filter (UPF) [97], and the Gaussian Mixture Particle Filter [98]. Such synergized approaches can achieve robust estimation results with only a small number of particles (50 to 100 particles for instance). A variant of the UPF with a global sampling strategy has been proposed in [99]. Current literature shows that particle filtering has been applied to the GNSS multipath mitigation and navigation problem and moderately to the vector signal tracking problem. Some particle filtering solutions applied to GNSS and GNSS/INS integration are discussed in [70] [100] [101] [102] [103] [104] [105] [106] [107]. The PF is applied to vector code tracking in [108]. Also, a particle filtering approach applied to GPS vector tracking is proposed in [80]. The main reason for moderate attention towards PF approaches especially in industrial applications is their computational

cost. However, the ever-increasing computational capability of the electronic chip is a good motivation to investigate PF application to vector tracking.

This chapter's aim is to apply the UPF approach to the GNSS navigation and vector tracking problem and then compare the EKF with different UKF and UPF approaches. The chapter formulates the problem by describing the state and measurement models that are involved and the navigator feedback that is used to perform vector tracking. The chapter then discusses an adaptive UKF algorithm, an iterated UKF (IUKF) algorithm and the UPF algorithm. The chapter further proposes a novel UPF approach that exploits iterative, adaptive and synergy strategies, the Iterated Adaptive Unscented Particle Filter (IAUPF). The IAUPF has a novel sampling and resampling strategy to reduce UPF complexity. The normal UPF uses the UKF to generate and propagate a Gaussian proposal distribution to each particle, which means using as many UKFs as there are particles. The proposed approach utilizes a single Iterated Adaptive Unscented Kalman Filter (IAUKF) with a conditional iteration strategy and uses its state and covariance estimates to form a single Gaussian proposal distribution from which particles are sampled. The proposed resampling strategy is a conditional commutation between stratified and regularized resampling. The chapter compares the EKF, UKF, IUKF, IUPF, and IAUPF solutions using Monte-Carlo simulations with the posterior Cramér-Rao lower bound (PCRLB) as benchmarking reference, then compares the EKF and IAUPF solutions using experimental results.

5.2 PROBLEM FORMULATION

The algorithms that are used to solve the navigation and vector tracking problem and that are described in this chapter will be based henceforth on the vector tracking receiver architecture described in *Chapter 4* and depicted again in Figure 5.1 below. However, they can be applied to any other type of architecture among the ones shown in *Chapter 2*, Table 2.1 and equally play their role.

The objective is to estimate the receiver's position, velocity, clock bias and clock drift errors using the pseudorange (code delay) and delta-range (carrier frequency) measurements provided by the local estimator; and then utilize the calculated position and velocity to estimate or aid in the estimation of signal tracking parameters namely the code frequency, the static code delay error, and the carrier phase and frequency.

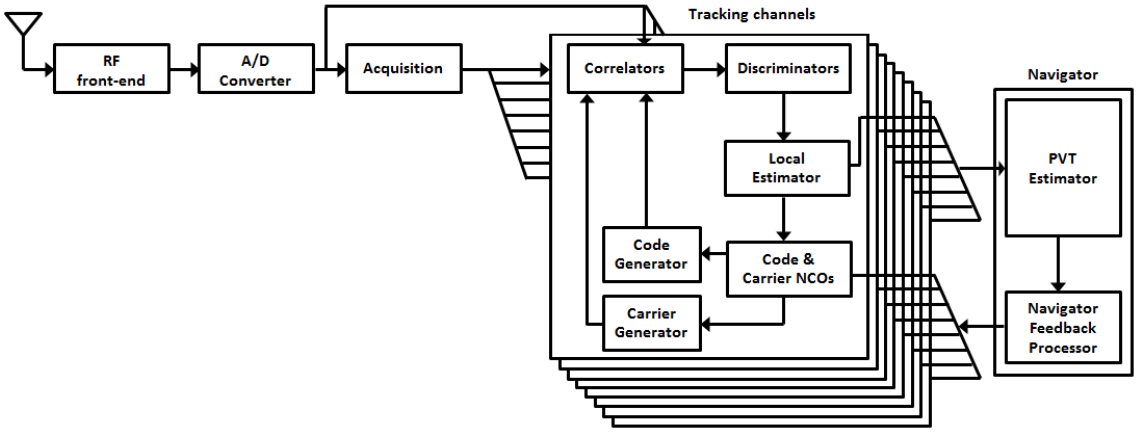

Figure 5.1: GNSS Vector Tracking Receiver Architecture

5.2.1 STATE MODEL

The state vector X_k at time instant k is made of the receiver's earth-centred earth-fixed (ECEF) position, velocity, clock bias and clock drift errors. The receiver acceleration is not included in the vector. In fact, for minimizing the computational load, an evolution model where velocity variations (such as accelerations) are modelled as white noise is used hereafter. This model is suitable for low and medium dynamic users (pedestrians, boats or cars). The discrete-time model that is used to characterise the dynamics of the state can therefore be expressed as follows:

$$X_k = f_k\left(X_{k-1}\right) + w_k \quad or \quad \begin{bmatrix} \delta x_k \\ \delta y_k \\ \delta z_k \\ \delta \ddot{x}_k \\ \delta \ddot{y}_k \\ \delta \ddot{z}_k \\ \delta t_k \\ \delta \dot{t}_k \end{bmatrix} = \begin{bmatrix} 1 & 0 & 0 & \Delta T & 0 & 0 & 0 & 0 \\ 0 & 1 & 0 & 0 & \Delta T & 0 & 0 & 0 \\ 0 & 0 & 1 & 0 & 0 & \Delta T & 0 & 0 \\ 0 & 0 & 0 & 1 & 0 & 0 & 0 & 0 \\ 0 & 0 & 0 & 0 & 1 & 0 & 0 & 0 \\ 0 & 0 & 0 & 0 & 0 & 1 & 0 & 0 \\ 0 & 0 & 0 & 0 & 0 & 0 & 1 & \Delta T \\ 0 & 0 & 0 & 0 & 0 & 0 & 0 & 1 \end{bmatrix} \begin{bmatrix} \delta x_{k-1} \\ \delta y_{k-1} \\ \delta z_{k-1} \\ \delta \ddot{x}_{k-1} \\ \delta \ddot{y}_{k-1} \\ \delta \ddot{z}_{k-1} \\ \delta t_{k-1} \\ \delta \dot{t}_{k-1} \end{bmatrix} + \begin{bmatrix} \left(w_{pos}\right)_{3\times 1} \\ \left(w_{vel}\right)_{3\times 1} \\ \left(w_{bias}\right)_{1\times 1} \\ \left(w_{drift}\right)_{1\times 1} \end{bmatrix} \tag{5.1}$$

where ΔT is the navigator update interval. The process noise w_k is a vector of additive white random noise inputs related to receiver position, velocity, clock bias and clock drift such that $E\{w_k\}=0, E\{w_k w_j^T\}=Q_k$. The process noise covariance matrix Q_k can be expressed as

$$Q_k = \begin{bmatrix} u & 0_{2\times 2} & 0_{2\times 2} & 0_{2\times 2} \\ 0_{2\times 2} & u & 0_{2\times 2} & 0_{2\times 2} \\ 0_{2\times 2} & 0_{2\times 2} & u & 0_{2\times 2} \\ 0_{2\times 2} & 0_{2\times 2} & 0_{2\times 2} & \beta \end{bmatrix}_{8\times 8} \text{ with } u = \begin{bmatrix} S_p \frac{\Delta T^3}{3} & S_p \frac{\Delta T^2}{2} \\ S_p \frac{\Delta T^2}{2} & S_p \Delta T \end{bmatrix} \text{ and } \beta = \begin{bmatrix} S_c \frac{\Delta T^3}{3} & S_c \frac{\Delta T^2}{2} \\ S_c \frac{\Delta T^2}{2} & S_c \Delta T \end{bmatrix};$$

where S_p is the position noise spectrum density and S_c is the clock noise spectrum density. Normally, Q_k is initialized using the specifications of the crystal oscillator in the RF front-end as well as Allan variance parameters [1].

5.2.2 MEASUREMENT MODEL

The measurement vector z_k at time instant k is made of code delay and carrier Doppler frequency estimates from the local estimator for the N satellites that are being tracked.

$$Z_k = \left[\tilde{\tau}_1, \tilde{f}_1, \tilde{\tau}_2, \tilde{f}_2, ..., \tilde{\tau}_N, \tilde{f}_N\right]^T \tag{5.2}$$

The code delay and carrier Doppler frequency are related to the pseudorange and delta-range measurements as follows:

$$\tilde{\tau}_i = \frac{\tilde{\rho}_i}{\lambda_\tau} \quad and \quad \tilde{f}_i = \frac{\tilde{\dot{\rho}}_i}{\lambda_c} \tag{5.3}$$

where $\tilde{\tau}$ is the code delay in chips, $\tilde{\rho}$ is the pseudorange in meters, $\lambda_\tau = cT_c$ is the code chip length in meters, c is the speed of light in meters/second, T_c is the code chip length in seconds, $\tilde{f}$ is the carrier Doppler frequency in Hertz, $\tilde{\dot{\rho}}$ is the delta-range (rate of change of the range) in meters/second, λ_c is the carrier wavelength in meters, and i denotes the satellite number. The measurement vector Z_k depends nonlinearly on the parameters to be estimated (the state vector) according to the following expression:

$$Z_k = h_k(X_k) + v_k \tag{5.4}$$

where X_k is the state vector, h_k is a nonlinear function, and v_k is a vector of additive white measurement noise such that $E\{v_k\} = 0$, $E\left\{v_k v_j^T\right\} = R_k \delta_{kj}$, $E\left\{w_k v_j^T\right\} = 0$, $\delta_{kj} = 1$ if $k = j$, otherwise $\delta_{kj} = 0$. The measurement noise covariance matrix R_k can be expressed as

$$R_k = \begin{bmatrix} \delta_1 & 0 & \cdots & 0 \\ 0 & \delta_2 & \cdots & 0 \\ \vdots & \vdots & \vdots & \vdots \\ 0 & 0 & \cdots & \delta_N \end{bmatrix}_{2N \times 2N} \quad \text{with } \delta_N = \begin{bmatrix} \sigma_{DLL}^2 & 0 \\ 0 & \sigma_{FLL}^2 \end{bmatrix};\ \sigma_{DLL}^2 = \frac{B_n^{DLL} d}{2\,C/N_0};\ \sigma_{FLL}^2 = \frac{B_n^{FLL}}{\pi^2 T_n^2\, C/N_0}$$

where B_n^{DLL}, B_n^{PLL} and B_n^{FLL} are respectively the delay locked loop (DLL), phase locked loop (PLL) and frequency locked loop (FLL) noise bandwidths, T_n is the coherent integration period, d is the DLL chip spacing, N is the number of

satellites in view, and C/N_0 is the carrier to noise power ratio. In Equation (5.4), the classical nonlinear measurement model is used for pseudorange estimation. The measured pseudorange between the receiver and the i^{th} satellite can be written as

$$\rho_i = R_i + \Delta D_i - c(\Delta b_i - \Delta b_r) + c(\Delta T_i + \Delta I_i + v_i + \Delta v_i) + w_i \tag{5.5}$$

where $R_i = \sqrt{(X_i - X)^2 + (Y_i - Y)^2 + (Z_i - Z)^2}$ is the true range, ΔD_i is the satellite position error effect on range, $s_i = (X_i, Y_i, Z_i)$ is the i^{th} satellite Earth-Centred Earth-Fixed (ECEF) position, $r = (X, Y, Z)$ is the receiver ECEF position, c is the speed of light, Δb_i is the satellite clock error, Δb_r is the receiver clock error, ΔT_i is the tropospheric delay error, ΔI_i is the ionospheric delay error, v_i is the receiver measurement noise error, Δv_i is the relativistic time correction, and w_i represents all other sources of error. Tropospheric corrections are usually applied to pseudoranges using a standard refraction model, the Goad and Goodman model [109]. Ionosphere propagation error is mitigated using the classical Klobuchar model [110].

5.2.3 NAVIGATOR FEEDBACK

The vector tracking process requires the navigator to provide feedback information to the tracking channels. The numerically controlled oscillators (NCOs) that produce the Early, Prompt and Late code replicas used in the code tracking loop are completely controlled by the navigator. The code frequency is deduced from the receiver velocity, projected in the axis of the addressed satellite. The static delay error is obtained from the receiver position by comparison with the position information from the output of the code NCO. For the phase tracking loop in VTL mode, the NCO that produces the carrier replica is controlled by the navigator and the phase discriminator output. The carrier frequency is deduced from the receiver velocity, projected in the axis of the satellite of interest. The static phase error is delivered by the phase discriminator. The code and carrier NCO outputs therefore depend on navigator position and velocity estimates and are modelled as

$$\begin{cases} \tau_k^{NCO} = \tau_{k-1}^{NCO} + \dfrac{T}{F_c} \times \dfrac{(s_i - \hat{r})}{\|s_i - \hat{r}\|} \times \dfrac{-\hat{v}F_c}{c} + k_{11}\left(\|s_i - \hat{r}\|\dfrac{1}{c} - \tau_{k-1}^{NCO}\right) \\ \varphi_k^{NCO} = \varphi_{k-1}^{NCO} + 2\pi T \times f_k^{NCO} \\ f_k^{NCO} = \dfrac{(s_i - \hat{r})}{\|s_i - \hat{r}\|} \times \dfrac{-\hat{v}F_c}{c} + k_{22}\dfrac{1}{2\pi T} D_{\varphi k} \end{cases} \tag{5.6}$$

where T is the NCO update time, $s_i = (x_i, y_i, z_i)$ is the i^{th} satellite Earth-Centred Earth-Fixed (ECEF) position, $\hat{r} = (\hat{x}_r, \hat{y}_r, \hat{z}_r)$ is the receiver's estimated ECEF position, $\hat{v} = (\hat{\dot{x}}_r, \hat{\dot{y}}_r, \hat{\dot{z}}_r)$ is the receiver's estimated ECEF velocity, F_c is the nominal carrier frequency; c is the speed of light; $k_{11} = \omega_{DLL} T$, $k_{22} = 2.4\omega_{PLL} T$, and D_{φ_k} is the current

phase discriminator output. ω_{DLL} and ω_{PLL} are defined using DLL and PLL noise bandwidths ($B_n^{DLL} = 0.25\omega_{DLL}$ and $B_n^{PLL} = 0.7845\omega_{PLL}$).

5.3 ADAPTIVE UKF ALGORITHM

Research on adaptive UKF filtering tries to solve the UKF divergence problem. This problem is caused by inaccurate statistical properties of measurement and/or process noises or of the UKF mathematical model itself. Some adaptive filtering techniques aim at estimating unknown system noise recursively. Others perform divergence/convergence tests then apply corrections. An adaptive UKF algorithm that is based on divergence suppression is proposed in [95]. A simplified version of this adaptive UKF approach is described hereafter. Filter divergence is tested using convergence conditions derived from the covariance matching criterion. If the convergence conditions are fulfilled, the standard UKF algorithm is used. However, if divergence occurs, an adaptive weighting coefficient λ_k is calculated through a computational fading factor formula and is applied to correct the state covariance matrix $P_{k|k-1}$. Therefore, the role of the observables is strengthened and the filter divergence is suppressed.

5.3.1 UKF ALGORITHM

The UKF algorithm selects a number of sampling points (sigma points) from the state probability distribution. These points can completely capture the true mean and covariance of the state distribution. The mean and covariance are estimated through the unscented transform process which substitutes sigma points into the nonlinear function to obtain the corresponding nonlinear function point set. The state mean, state variance and measurement variance obtained from the unscented transform are introduced into a recursive Kalman filtering process to obtain the UKF. The UKF algorithm (see *Chapter 2*, Algorithm 2.3) has the following steps:

(I) Initialization

$$\begin{aligned} \overline{X}_0 &= E[X_0] \\ P_0 &= E\left[(X_0 - \overline{X}_0)(X_0 - \overline{X}_0)^T\right] \end{aligned} \tag{5.7}$$

(II) Recursively perform the following:

(1) Compute sigma points

$$\chi_{k-1} = \left[\overline{X}_{k-1} \quad \overline{X}_{k-1} \pm \left(\sqrt{(N+\lambda)P_{k-1}}\right)\right] \tag{5.8}$$

(2) Prediction

$$\chi_{k|k-1} = f\left(\chi_{k-1}\right) \tag{5.9}$$

$$\bar{X}_{k|k-1} = \sum_{i=0}^{2N} W_i^{(m)} \chi_{i,k|k-1} \tag{5.10}$$

$$P_{k|k-1} = \sum_{i=0}^{2N} W_i^{(c)} \left[\chi_{i,k|k-1} - \bar{X}_{k|k-1}\right]\left[\chi_{i,k|k-1} - \bar{X}_{k|k-1}\right]^T + Q \tag{5.11}$$

$$Z_{k|k-1} = h\left(\chi_{k|k-1}\right) \tag{5.12}$$

$$\bar{Z}_{k|k-1} = \sum_{i=0}^{2N} W_i^{(m)} Z_{i,k|k-1} \tag{5.13}$$

(3) Update

$$P_{z_k z_k} = \sum_{i=0}^{2N} W_i^{(c)} \left[Z_{i,k|k-1} - \bar{Z}_{k|k-1}\right]\left[Z_{i,k|k-1} - \bar{Z}_{k|k-1}\right]^T + R \tag{5.14}$$

$$P_{x_k z_k} = \sum_{i=0}^{2N} W_i^{(c)} \left[\chi_{i,k|k-1} - \bar{X}_{k|k-1}\right]\left[Z_{i,k|k-1} - \bar{Z}_{k|k-1}\right]^T \tag{5.15}$$

$$K_k = P_{x_k z_k} P_{z_k z_k}^{-1} \tag{5.16}$$

$$\bar{X}_k = \bar{X}_{k|k-1} + K_k\left(Z_k - \bar{Z}_{k|k-1}\right) \tag{5.17}$$

$$P_k = P_{k|k-1} - K_k P_{z_k z_k} K_k^T \tag{5.18}$$

Here Q is the process noise covariance, R is the measurement noise covariance, K_k is the Kalman gain, and W_i represents the weights of the mean or covariance.

5.3.2 Divergence Suppression Based Adaptive UKF Algorithm

The following convergence conditions are defined [95]:

$$v_k^T v_k \le \beta \cdot Tr\left[E\left(v_k v_k^T\right)\right] \tag{5.19}$$

where $\beta \ge 1$ is an adjustable coefficient presetting, $Tr(\cdot)$ is the matrix trace operation, and v_k is the residual sequence such that $v_k = Z_k - h\left(\bar{X}_{k|k-1}\right)$. $E\left(v_k v_k^T\right)$ can be approximated by

$$S_k = E\left(v_k v_k^T\right) = \frac{1}{N} \sum_{i=k-N+1}^{k} v_k v_k^T \tag{5.20}$$

where N is the size of the estimation window. If the convergence conditions are not met, the covariance $P_{k|k-1}$ is corrected as follows:

$$P_{k|k-1} = \lambda_k \cdot \sum_{i=0}^{2N} W_i^{(c)} \left[\chi_{i,k|k-1} - \overline{X}_{k|k-1} \right] \left[\chi_{i,k|k-1} - \overline{X}_{k|k-1} \right]^T + Q \tag{5.21}$$

Following [95] and using the adaptive fading factor formula, the adaptive weighting coefficient λ_k is calculated as follows:

$$\lambda_k = \begin{cases} \lambda_0 = Tr\left[\dfrac{N_k}{Tr(M_k)} \right] & \lambda_0 \geq 1 \\ 1 & \lambda_0 < 1 \end{cases} \tag{5.22}$$

$$N_k = Tr\left(C_{0,k} - R\right)^T \quad where \quad C_{0,k} = \begin{cases} v_k v_k^T & k = 1 \\ \dfrac{\rho C_{0,k} + v_k v_k^T}{1+\rho} & k > 1 \end{cases} \tag{5.23}$$

$$M_k = Tr\left(\sum_{i=0}^{2N} W_i^{(c)} \left[Z_{i,k|k-1} - \overline{Z}_{k|k-1} \right] \left[Z_{i,k|k-1} - \overline{Z}_{k|k-1} \right]^T \right) \tag{5.24}$$

where ρ $(0 < \rho \leq 1)$ is a forgetful factor (typically around 0.95) used to increase the filter's tracking ability. This adaptive method has a strong tracking capability for sudden status changes. It also maintains tracking in slowly varying state conditions and mutation status changes when the filter reaches steady state.

5.4 ITERATED UKF ALGORITHM

The objective behind the development of the iterated UKF (IUKF) algorithm is to provide a robust algorithm capable of dealing with weak observability and large initial errors. The IUKF algorithm is proposed in [89]. Its steps can be summarized as follows:

(I) For each position-velocity-time (PVT) computation instant k $(k \geq 1)$, evaluate the state estimate $\overline{X}_k$ and state covariance P_k using the standard UKF algorithm steps in Equations (5.7) to (5.18).

(II) Let $\overline{X}_{k,0} = \overline{X}_{k|k-1}$, $P_{k,0} = P_{k|k-1}$, $\overline{X}_{k,1} = \overline{X}_k$, $P_{k,1} = P_k$, $j = 2$ and $g = 1$.

(III) Generate new sigma points

$$\chi_{i,j} = \left[\overline{X}_{k,j-1} \quad \overline{X}_{k,j-1} \pm \left(\sqrt{(N+\lambda) P_{k,j-1}} \right) \right] \tag{5.25}$$

(IV) Recalculate Equations (5.10) to (5.18) as follows

$$\bar{X}_{k|k-1,j} = \sum_{i=0}^{2N} W_i^{(m)} \chi_{i,j} \tag{5.26}$$

$$Z_{i,j} = h\left(\chi_{i,j}\right) \tag{5.27}$$

$$\bar{Z}_{k|k-1,j} = \sum_{i=0}^{2N} W_i^{(m)} Z_{i,j} \tag{5.28}$$

$$P_{zz,k,j} = \sum_{i=0}^{2N} W_i^{(c)} \left[Z_{i,j} - \bar{Z}_{k|k-1,j}\right]\left[Z_{i,j} - \bar{Z}_{k|k-1,j}\right]^T + R_k \tag{5.29}$$

$$P_{xz,k,j} = \sum_{i=0}^{2N} W_i^{(c)} \left[\chi_{i,j} - \bar{X}_{k|k-1,j}\right]\left[Z_{i,j} - \bar{Z}_{k|k-1,j}\right]^T \tag{5.30}$$

$$K_{k,j} = P_{xz,k,j} P_{zz,k,j}^{-1} \tag{5.31}$$

$$\bar{X}_{k,j} = \bar{X}_{k|k-1,j} + g \cdot K_{k,j}\left(Z_k - \bar{Z}_{k|k-1,j}\right) \tag{5.32}$$

$$P_{k,j} = P_{k|,j-1} - K_{k,j} P_{zz,k,j} K_{k,j}^T \tag{5.33}$$

Here the subscript j denotes the j^{th} iterate and $Z_{i,j}$ denotes the i^{th} component of Z_j.

(V) Define the following three equations:

$$\bar{Z}_{k,j} = h\left(\bar{X}_{k,j}\right)$$

$$\tilde{X}_{k,j} = \bar{X}_{k,j} - \bar{X}_{k,j-1}$$

$$\tilde{Z}_{k,j} = Z_k - \bar{Z}_{k,j}$$

(VI) Test for the following inequality:

$$\tilde{X}_{k,j}^T P_{k,j-1}^{-1} \tilde{X}_{k,j} + \tilde{Z}_{k,j}^T R_k^{-1} \tilde{Z}_{k,j} < \tilde{Z}_{k,j-1}^T R_k^{-1} \tilde{Z}_{k,j-1} \tag{5.34}$$

If the inequality holds and $j \le M$ (M being an integer), then set $g = \eta \cdot g$ with η $(0 < \eta \le 1)$ being a decaying factor that affects the convergence speed, $j = j + 1$, and then return to Step (III). If the inequality does not hold, continue to Step (VII).

(VII) Stop if the inequality does not hold or if j is too large ($j > M$) and set $\bar{X}_k = \bar{X}_{k,j}$ and $P_k = P_{k,j}$.

This IUKF algorithm has interesting features. With the termination criteria in Step (VI) the inequality is guaranteed to go up the likelihood surface during the iterations, i.e. the estimates that are obtained during the iterations are guarded to move towards maximum likelihood solution. The decaying factor η $(0 < \eta \leq 1)$ is used to weaken the effect of the latest correction on the prediction state $\bar{X}_{k|k-1,j}$ making two successive iterates $\bar{X}_{k,j}$ and $\bar{X}_{k,j-1}$ become closer as the iterations proceed, and therefore speeding up the iterative convergence. In comparison with the standard UKF, the IUKF has the ability to adjust the state estimate to adaptively approach the true value through corrections of the measurements. Normally, after the iterations terminate, a lower state error is expected. Furthermore, the IUKF can respond to new measurements as fast as possible with state and covariance matrix adjustment. This increases convergence speed in situations where the initial error is large.

5.5 REGULARIZED PF ALGORITHM

Particle filters (PF) are sequential Monte Carlo methods based on point mass or "particle" representations of probability densities. They can be applied to any state-space model as they are a generalization of the traditional Kalman filtering methods. It was seen in *Chapter 2*, section 2.5.2 that particle filters allow the approximation of the posterior probability distribution $P(X_{0:k} \mid Z_{1:k})$ using a set of N weighted samples $\left\{X_{0:k}^{i}\right\}_{i=1}^{N}$ called particles. These samples are drawn from an importance proposal distribution $Q(X_{0:k} \mid Z_{1:k})$. The drawn samples are propagated in time as illustrated in Figure 5.2, which is taken from [111].

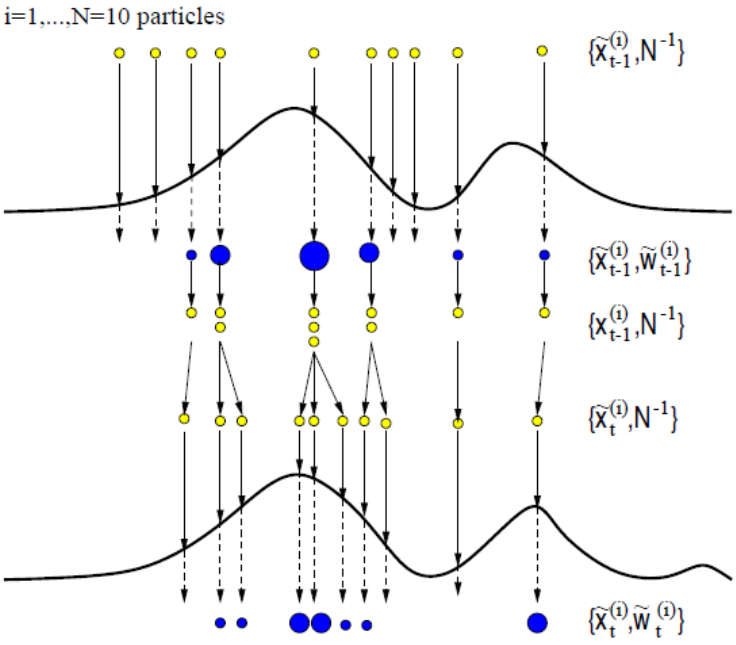

Figure 5.2: PF samples propagation in time

The figure illustrates an example of a particle filter that starts at time *t-1* with an unweighted measure $\left\{\tilde{X}_{t-1}^{i}, 1/N\right\}$ as an approximation of $P(X_{t-1} \mid Z_{1:t-2})$. For each particle, the importance weights are computed based on the information at time *t-1*. The result is the weighted measure $\left\{\tilde{X}_{t-1}^{i}, \tilde{w}_{t-1}^{i}\right\}$ which is an approximation of $P(X_{t-1} \mid Z_{1:t-1})$. To obtain only the fittest particles, a resampling process is performed and results in the unweighted measure $\left\{X_{t-1}^{i}, 1/N\right\}$. The latter is still an approximation of $P(X_{t-1} \mid Z_{1:t-1})$. Finally, the prediction step introduces variety which gives the measure $\left\{\tilde{X}_{t}^{i}, 1/N\right\}$.

This approach makes it possible to map the intractable integrals in the Bayesian estimator (the computations of expectations and marginal distributions) to easy summations. This is done following a rigorous strategy to ensure convergence according to the strong law of large numbers

$$\frac{1}{N}\sum_{i=1}^{N} f_k\left(X_{0:k}^{i}\right) \xrightarrow[N\to+\infty]{a.s} \int f_k(X_{0:k}) P(dX_{0:k} \mid Z_{1:k})$$

where $\xrightarrow{a.s}$ denotes almost sure convergence and $f_k : \Re^{N_x} \to \Re^{N_{f_k}}$ is some function of interest. Resampling is a strategy that is used to combat the degeneracy problem, which is a classical limitation of sequential importance sampling (SIS) in particle filters. It was also mentioned in *Chapter 2* that resampling introduces problems of its own, particularly the loss of diversity among particles. This problem arises because resampling is performed on a discrete distribution rather than a continuous one. If it is left unaddressed, this problem may lead to particle collapse which is a severe case of sample impoverishment where all drawn particles occupy the same point in the state space. This provides a poor representation of the posterior density. The regularized particle filter (RPF) was proposed in [112] as a potential solution to the sample impoverishment problem.

In the sampling importance resampling (SIR) filter, resampling is done from an approximate discrete representation of the posterior probability density function $p(X_k \mid Z_{1:k})$ given by

$$p(X_k \mid Z_{1:k}) \approx \sum_{i=1}^{N} w_k^i \delta(X_k - X_k^i) \tag{5.35}$$

The RPF on the other hand resamples from a continuous approximation of the posterior density $p(X_k \mid Z_{1:k})$ given by [113]

$$p(X_k \mid Z_{1:k}) \approx \sum_{i=1}^{N} w_k^i K_h(X_k - X_k^i) \tag{5.36}$$

where $K_h(X) = \frac{1}{h^{n_x}} K\left(\frac{X}{h}\right)$ is the rescaled Kernel density $K(\cdot)$, $h > 0$ (a scalar parameter) is the Kernel bandwidth, n_x is the dimension of the state vector X, and w_k^i, $i = 1,...,N$ are normalized weights. The Kernel density $K(\cdot)$ and bandwidth h are chosen with the aim to minimize the mean integrated square error (MISE) between the true posterior density $p(X_k \mid Z_{1:k})$ and its regularized empirical representation $\hat{p}(X_k \mid Z_{1:k})$, which is given by the right-hand side of Equation (5.36). $K(\cdot)$ is a symmetric probability density function such that

$$\int XK(X)dX = 0 \quad and \quad \int \|X\|^2 K(X)dX < \infty .$$

The MISE is expressed as

$$MISE(\hat{p}) = E\left[\int [\hat{p}(X_k \mid Z_{1:k}) - p(X_k \mid Z_{1:k})]^2 dX_k\right] \tag{5.37}$$

Algorithm 5.1: Resampling Algorithm

- Initialize the cumulative distribution function (CDF): $c_1 = 0$
- FOR $j = 2 : N$

  Construct the CDF: $c_j = c_{j-1} + w_k^j$
- END FOR
- Start at the bottom of the CDF: $j = 1$
- Draw a starting point: $u_1 \sim U[0, 1/N]$
- FOR $i = 1 : N$
  - Move along the CDF: $u_i = u_1 + 1/N \times (i-1)$
  - While $u_i > c_j$

    $j = j + 1$.
  - Assign sample: $X_k^{i(*)} = X_k^j$
  - Assign weight: $w_k^i = 1/N$
  - Assign parent: $j^{i^k} = j$
- END FOR

In the special case of equally weighted samples, the optimal choice of the Kernel is the Epanechnikov kernel [112] which is given by

$$K_{opt} = \begin{cases} \frac{n_x + 2}{2c_{n_x}}\left(1 - \|X\|^2\right) & if \quad \|X\| < 1 \\ 0, & otherwise \end{cases} \tag{5.38}$$

where c_{n_x} is the volume of the unit hypersphere in $\Re^{n_x}$. Moreover, in the case of a Gaussian underlying density with a unit covariance matrix, the optimal choice for the bandwidth is [112]

$$h_{opt} = AN^{1/(n_x+4)} \tag{5.39}$$

$$A = \left[8c_{n_x}^{-1}(n_x + 4)\left(2\sqrt{\pi}\right)^{n_x} \right]^{1/(n_x+4)} \tag{5.40}$$

Algorithm 5.2: Regularized Particle Filter (RPF)

- FOR $i = 1:N$
  - Draw $X_k^i \sim Q\left(X_k \mid X_{k-1}^i, Z_k\right)$
  - Assign a weight:

    $$w_k^i \propto w_{k-1}^i \frac{p\left(Z_k \mid X_k^i\right) p\left(X_k^i \mid X_{k-1}^i\right)}{q\left(X_k^i \mid X_{k-1}^i, Z_k\right)}$$
- END FOR
- Calculate total weight: $\Sigma = \sum_{i=1}^{N} w_k^i$
- FOR $i = 1:N$

  Normalize: $w_k^i = \frac{1}{\Sigma} w_k^i$
- END FOR
- Calculate $N_{eff} = 1 \Big/ \sum_{i=1}^{N} \left(w_k^i\right)^2$
- IF $N_{eff} < N_{Threshold}$
  - Calculate the empirical covariance matrix S_k of $\left\{X_k^i, w_k^i\right\}_{i=1}^{N}$
  - Compute D_k such that $D_k D_k^T = S_k$
  - Resample using Algorithm 5.1
  - FOR $i = 1:N$
    - Draw $\varepsilon^i \sim K$ from the Epanechnikov Kernel
    - $X_k^i = X_k^i + h_{opt} D_k \varepsilon^i$
  - END FOR
- END IF

The RPF can still be applied to the general case (non-equally weighted particles and non-Gaussian density) and constitute a suboptimal filter. An iteration of the RPF algorithm is summarized in Algorithm 5.2. The calculation of the covariance matrix S_k is performed prior to resampling. S_k is a function of both X_k^i and w_k^i. Algorithm 5.1 is the resampling algorithm [113]. The theoretical disadvantage of the RPF is that it is not guaranteed that the samples asymptotically approximate those from the posterior density. Nonetheless, practically, the RPF outperforms the generic particle filter, i.e. the SIR filter, when sample impoverishment is severe, for instance in case of small process noise.

5.6 UPF ALGORITHM

Particle filters are based on importance sampling and consequently require the design of proposal distributions $Q(X_{0:k} \mid Z_{1:k})$ that can approximate the posterior distribution $P(X_{0:k} \mid Z_{1:k})$ reasonably well. Generally, such proposal distributions are hard to design. Sampling from the probabilistic model of the state evolution (transition prior) fails when the new measurements appear in the tail of the prior or if the likelihood is too peaked in comparison with the prior. To overcome this difficulty, some solutions have been proposed. The EKF Gaussian approximation is used as the proposal distribution for a PF in [96], which yields the Extended Kalman Particle Filter (EKPF). In [97] and [111], the UKF is used to generate the proposal distribution instead of the EKF, which results in the Unscented Particle Filter (UPF). These proposals are better than the transition prior as they incorporate the latest measurements and therefore contain more valuable information for state estimation. In comparison with the EKPF, the UPF can capture the nonlinearity better than the EKPF as it does not linearize the nonlinear equations of the system, and consequently it provides better estimates.

In order to construct the UPF, a UKF operation is applied to each particle to generate and propagate a Gaussian proposal distribution. Thus, as many UKFs as there are particles are used to generate the proposal. This makes the UPF algorithm very computationally expensive in comparison with the general PF. Algorithm 5.3 is the UPF algorithm. A modified version of the UPF that divides the particles into two parts is proposed in [114]. One part is generated from the UKF and another part from the transition prior. By such combination of the general PF and UPF, this method reduces UPF computational complexity but incurs decrease in accuracy. A global sampling (GS) strategy is used in [99] and [104] to reduce UPF complexity without suffering much loss in accuracy. This strategy generates the proposal distribution from the mean and covariance estimates of all particles and not from each particle, thus requiring the use of a single UKF. The resulting UPF is referred to as the GS-UPF. The modified UPF approach that is proposed in section 5.7 exploits this

strategy together with adaptive and iterative strategies to increase the filter immunity against divergence and to speed up convergence in case of large initial errors.

Algorithm 5.3: Unscented Particle Filter (UPF)

(I) Initialisation: $k=1;$ Draw particles $\left\{X^i_{k-1}=X^i_0, w^i_{k-1}=w^i_0=1/N\right\}_{i=1}^{N}$ from the prior $P(X_0)$

(II) Iteratively perform the following for $k \in \{2,\ldots, K\}$:

- FOR $i=1:N$
  - Measure z_k and use the UKF algorithm (Equations 5.7 to 5.18) to evaluate the mean $\overline{X}^i_k$ and covariance P^i_k of the particle $\left\{X^i_{k-1}, w^i_{k-1}\right\}$
  - Draw $X^i_k \sim N\left(\overline{X}^i_k, P^i_k\right)$
  - Assign a weight: $w^i_k \propto w^i_{k-1}\dfrac{p\left(Z_k \mid X^i_k\right)p\left(X^i_k \mid X^i_{k-1}\right)}{N\left(\overline{X}^i_k, P^i_k\right)}$
- END FOR
- Calculate total weight: $\Sigma=\sum_{i=1}^{N} w^i_k$
- FOR $i=1:N$

  Normalize: $w^i_k=\frac{1}{\Sigma}w^i_k$
- END FOR
- Calculate $N_{eff}=1/\sum_{i=1}^{N}\left(w^i_k\right)^2$
- IF $N_{eff} < N_{Threshold}$

  Resample using Algorithm 5.1.
- END IF
- Output the a-posteriori state and covariance estimates:

$$X_k=\sum_{i=1}^{N} w^i_k X^i_k$$

$$P_k=\sum_{i=1}^{N} w^i_k\left(X^i_k-X_k\right)\left(X^i_k-X_k\right)^T$$

5.7 PROPOSED IAUPF ALGORITHM

The benefits of using an iterative approach have been discussed in section 5.4 via the iterated UKF algorithm. The proper and controlled use of an iterative step makes it possible to deal with weak observability and large initial errors. For large initial errors, convergence is speeded up via an iterative strategy. Another approach to combat filter divergence has been argued in section 5.3.2 via the adaptive UKF algorithm. This adaptive strategy performs a divergence test then applies corrections to the state covariance matrix when necessary. By doing so, the adaptive filter increases its tracking capability for sudden status changes as well as for slowly varying state conditions and mutation status changes. Also, the superiority of the particle filter in comparison with the EKF and UKF in dealing with nonlinear and non-Gaussian dynamic systems is well established. Moreover, the UPF provides a UKF-based proposal distribution from which to perform importance sampling, which is a better proposal in comparison with the transition prior. A global sampling (GS) UPF even reduces UPF complexity without suffering much loss in estimation accuracy. Furthermore, by providing a better proposal distribution, the GS-UPF reduces the risks of particle degeneracy which avoids the necessity for resampling. However, in practice, for GNSS applications, some harsh environments might occasionally create conditions that still require the use of resampling. When resampling is occasionally resorted to, there is a possibility of particles impoverishment in case of small process noise. Adopting a regularized resampling strategy avoids particles impoverishment or collapse. However, because the RPF has a theoretical limitation in asymptotical estimation of the posterior distribution, switching between stratified and regularized resampling may be useful. Stratified resampling, described in *Chapter 2*, Algorithm 2.4, guarantees a small variance of the number of descendants per particle.

The modified UPF algorithm that is proposed hereafter is a synergy of strategies. It exploits iterative and adaptive methods, global sampling, regularized resampling, and stratified resampling. This version of the UPF, called Iterated Adaptive Unscented Particle Filter (IAUPF) uses a single iterated adaptive UKF (IAUKF) with a conditional iteration strategy and uses its state and covariance estimates to form a global Gaussian proposal distribution from which particles are sampled. When useful, resampling is performed using a conditional commutation between stratified and regularized resampling approaches. The proposed IAUPF algorithm is illustrated in Algorithm 5.4. This algorithm maintains almost the same computational cost as the GS-UPF but benefits from the divergence suppression methods (iterative and adaptive methods) as well as the synergized resampling approaches (regularized and stratified resampling).

Algorithm 5.4: Iterated Adaptive Unscented Particle Filter (IAUPF)

(I) Initialisation: $\bar{X}_0 = E[X_0]$ *and* $P_0 = E\left[(X_0 - \bar{X}_0)(X_0 - \bar{X}_0)^T\right]$

(II) Iteratively perform the following for $k \in \{1,\ldots, K\}$:

(1) Draw sigma points: $\chi_{k-1} = \left[\bar{X}_{k-1} \quad \bar{X}_{k-1} \pm \left(\sqrt{(N+\lambda)P_{k-1}}\right)\right]$

(2) Prediction

$$\chi_{k|k-1} = f(\chi_{k-1});\ \bar{X}_{k|k-1} = \sum_{i=0}^{2N} W_i^{(m)} \chi_{i,k|k-1};$$

$$P_{k|k-1} = \sum_{i=0}^{2N} W_i^{(c)} \left[\chi_{i,k|k-1} - \bar{X}_{k|k-1}\right]\left[\chi_{i,k|k-1} - \bar{X}_{k|k-1}\right]^T + Q;$$

$$Z_{k|k-1} = h(\chi_{k|k-1});\ \bar{Z}_{k|k-1} = \sum_{i=0}^{2N} W_i^{(m)} Z_{i,k|k-1}$$

(3) Update

$$P_{z_k z_k} = \sum_{i=0}^{2N} W_i^{(c)} \left[Z_{i,k|k-1} - \bar{Z}_{k|k-1}\right]\left[Z_{i,k|k-1} - \bar{Z}_{k|k-1}\right]^T + R$$

$$P_{x_k z_k} = \sum_{i=0}^{2N} W_i^{(c)} \left[\chi_{i,k|k-1} - \bar{X}_{k|k-1}\right]\left[Z_{i,k|k-1} - \bar{Z}_{k|k-1}\right]^T$$

$$K_k = P_{x_k z_k} P_{z_k z_k}^{-1};\ v_k = Z_k - \bar{Z}_{k|k-1};\ \bar{X}_k = \bar{X}_{k|k-1} + K_k v_k$$

IF $v_k^T v_k \le \beta \cdot Tr\left[E\left(v_k v_k^T\right)\right]$ IS NOT SATISFIED

$$\lambda_k = \begin{cases} \lambda_0 = Tr\left[\dfrac{N_k}{Tr(M_k)}\right] & \lambda_0 \ge 1 \\ 1 & \lambda_0 < 1 \end{cases}$$

$$P_{k|k-1} = \lambda_k \cdot \sum_{i=0}^{2N} W_i^{(c)} \left[\chi_{i,k|k-1} - \bar{X}_{k|k-1}\right]\left[\chi_{i,k|k-1} - \bar{X}_{k|k-1}\right]^T + Q$$

END IF

$$P_k = P_{k|k-1} - K_k P_{z_k z_k} K_k^T$$

(4) Let $\bar{X}_{k,0} = \bar{X}_{k|k-1}$, $P_{k,0} = P_{k|k-1}$, $\bar{X}_{k,1} = \bar{X}_{k|}$, $P_{k,1} = P_{k|}$, $j = 2$, $g = 1$

(5) WHILE $j \le M$

Generate new sigma points:

$$\chi_{i,j} = \left[\bar{X}_{k,j-1} \quad \bar{X}_{k,j-1} \pm \left(\sqrt{(N+\lambda)P_{k,j-1}}\right)\right]$$

Recalculate the UKF Equations as follows:

$$\bar{X}_{k|k-1,j} = \sum_{i=0}^{2N} W_i^{(m)} \chi_{i,j};\ Z_{i,j} = h(\chi_{i,j});\ \bar{Z}_{k|k-1,j} = \sum_{i=0}^{2N} W_i^{(m)} Z_{i,j};$$

$$P_{zz,k,j} = \sum_{i=0}^{2N} W_i^{(c)} \left[Z_{i,j} - \bar{Z}_{k|k-1,j}\right]\left[Z_{i,j} - \bar{Z}_{k|k-1,j}\right]^T + R_k;$$

$$P_{xz,k,j} = \sum_{i=0}^{2N} W_i^{(c)} \left[\chi_{i,j} - \bar{X}_{k|k-1,j}\right]\left[Z_{i,j} - \bar{Z}_{k|k-1,j}\right]^T;\ K_{k,j} = P_{xz,k,j} P_{zz,k,j}^{-1};$$

$$\bar{X}_{k,j} = \bar{X}_{k|k-1,j} + g \cdot K_{k,j}\left(Z_k - \bar{Z}_{k|k-1,j}\right);\ P_{k,j} = P_{k|,j-1} - K_{k,j} P_{zz,k,j} K_{k,j}^T$$

Algorithm 5.4 continued: Iterated Adaptive Unscented Particle Filter (IAUPF)

Define the following three equations:

$\bar{Z}_{k,j} = h\left(\bar{X}_{k,j}\right)$; $\tilde{X}_{k,j} = \bar{X}_{k,j} - \bar{X}_{k,j-1}$ and $\tilde{Z}_{k,j} = Z_k - \bar{Z}_{k,j}$

IF $\tilde{X}_{k,j}^T P_{k,j-1}^{-1} \tilde{X}_{k,j} + \tilde{Z}_{k,j}^T R_k^{-1} \tilde{Z}_{k,j} \geq \tilde{Z}_{k,j-1}^T R_k^{-1} \tilde{Z}_{k,j-1}$

BREAK;

END IF

Set $g = \eta \cdot g$ and $j = j + 1$

(6) END WHILE

(7) Set $\bar{X}_k = \bar{X}_{k,j}$ and $P_k = P_{k,j}$

(8) FOR $i = 1:N$

- Draw $X_k^i \sim N\left(\bar{X}_k, P_k\right)$
- Assign a weight:

$$w_k^i \propto w_{k-1}^i \frac{p\left(Z_k \mid X_k^i\right) N\left(X_k^i \mid \bar{X}_{k|k-1,j}, P_{k|,j-1}\right)}{N\left(X_k^i \mid \bar{X}_k, P_k\right)}$$

(9) END FOR

(10) Calculate total weight: $\Sigma = \sum_{i=1}^N w_k^i$

(11) FOR $i = 1:N$

Normalize: $w_k^i = \frac{1}{\Sigma} w_k^i$

(12) END FOR

(13) Calculate $N_{eff} = 1 \Big/ \sum_{i=1}^N \left(w_k^i\right)^2$

(14) IF $N_{eff} < N_{Threshold}$

IF $N_{eff} < 0.3 N_{Threshold}$

Calculate the empirical covariance matrix S_k of $\left\{X_k^i, w_k^i\right\}_{i=1}^N$

Compute D_k such that $D_k D_k^T = S_k$

Resample using Algorithm 5.1

FOR $i = 1:N$

Draw $\varepsilon^i \sim K$ from the Epanechnikov Kernel

$X_k^i = X_k^i + h_{opt} D_k \varepsilon^i$

END FOR

ELSE

Resample using Algorithm 2.4

END IF

(15) END IF

(16) Output the a-posteriori state and covariance estimates:

$$\bar{X}_k = \sum_{i=1}^N w_k^i X_k^i \; ; \; P_k = \sum_{i=1}^N w_k^i \left(X_k^i - \bar{X}_k\right)\left(X_k^i - \bar{X}_k\right)^T$$

The expression that is used in Algorithm 5.4 for particle weights is given by:

$$w_k^i \propto w_{k-1}^i \frac{p\left(Z_k \mid X_k^i\right) N\left(X_k^i \mid \overline{X}_{k|k-1,j}, P_{k|,j-1}\right)}{N\left(X_k^i \mid \overline{X}_k, P_k\right)}$$

where:

$$p\left(Z_k \mid X_k^i\right) \approx \frac{1}{\sqrt{(2\pi)^m \left\|R_k\right\|}} \exp\left\{-\frac{\left[\left(Z_k - h_k(X_k^i)\right)^T R_k^{-1}\left(Z_k - h_k(X_k^i)\right)\right]}{2}\right\}$$

$$N\left(X_k^i \mid \overline{X}_{k|k-1,j}, P_{k,j-1}\right) = \frac{1}{\sqrt{(2\pi)^n \left\|P_{k,j-1}\right\|}} \exp\left\{-\frac{\left[\left(X_k^i - \overline{X}_{k|k-1,j}\right)^T R_k^{-1}\left(X_k^i - \overline{X}_{k|k-1,j}\right)\right]}{2}\right\}$$

$$N\left(X_k^i \mid \overline{X}_k, P_k\right) = \frac{1}{\sqrt{(2\pi)^n \left\|P_k\right\|}} \exp\left\{-\frac{\left[\left(X_k^i - \overline{X}_k\right)^T R_k^{-1}\left(X_k^i - \overline{X}_k\right)\right]}{2}\right\}$$

Here the likelihood density $p\left(Z_k \mid X_k^i\right)$ is described as Gaussian distributed. In case the statistics of the non-Gaussian distributed measurement errors are known, they can be used instead of the Gaussian approximation.

Moreover, the calculation of the state covariance matrix $P_k = \sum_{i=1}^{N} w_k^i \left(X_k^i - \overline{X}_k\right)\left(X_k^i - \overline{X}_k\right)^T$ in Step (16) of Algorithm 5.4 should be skipped in case particle degeneracy occurs (i.e. $N_{eff} < N_{Threshold}$). After degeneracy, the particles have very low covariance and the use of the covariance matrix resulting from that calculation may create mathematical inconsistencies in the IAUKF algorithm used to provide a Gaussian distributed proposal to the IAUPF algorithm. In this case, the state covariance matrix previously calculated by the IAUKF algorithm should be used as a-posteriori covariance estimate instead.

Furthermore, if the particle filtering steps (Steps 8 to 16) are removed from Algorithm 5.4, the IAUKF algorithm is obtained. If the divergence suppression adaptive steps are removed from the state covariance matrix update in Step 3 of the IAUKF algorithm, the IUKF algorithm is obtained. If the IUKF algorithm is used to provide a Gaussian distributed proposal to the particle filter, the result is the IUPF algorithm. The next section derives a state estimation error bound that is used for benchmarking purposes, i.e. for comparing the performance of the algorithms.

5.8 POSTERIOR CRAMER-RAO LOWER BOUND FOR BAYESIAN ESTIMATORS

To evaluate the performance of unbiased estimators, many variance lower bounds have been used in literature. These bounds are divided into two main categories: classical and Bayesian bounds. Classical bounds apply to a non-random parameter of interest while Bayesian bounds consider that the parameter of interest is drawn from a given distribution [105]. In the Bayesian framework, the most popular bounds are the Posterior Cramér-Rao Bound (PCRB) [115] [116], the weighted PCRB [117], the Bayesian Bhattacharyya Bound [116], the Bobrovsky-Zakai Bound [117] [118] [119], and the Weiss-Weinstein Bound [120]. The PCRB is one of the most used bounds in statistical signal processing to assess the performance of parameter estimation algorithms although it is less tight than its counterparts [51]. The reason behind this is that it is easier to evaluate. The PCRB is derived herein and used for performance benchmarking between different Bayesian estimators. It is deemed that it provides a tight enough bound to serve its benchmarking purpose. The derivation of other bounds can be considered for future work.

5.8.1 NONLINEAR DYNAMIC MODEL

Consider the following discrete-time nonlinear system:

$$\begin{cases} X_k = f_k\left(X_{k-1}\right) + G_k w_{k-1} \\ Z_k = h_k\left(X_k\right) + v_k \end{cases} \tag{5.41}$$

where the nonlinear vector-valued functions $f_k \in \Re^n$ and $h_k \in \Re^m$ are used to model the state kinematics and measurements respectively, $X_k \in \Re^n$ is the state vector, $Z_k \in \Re^m$ is the measurement vector, the input noise $w_k \in \Re^n$ is assumed to be a random vector with zero-mean and known covariance Q_k, $G_k \in \Re^{n \times n}$ is the input matrix and is assumed to be stationary over time, $v_k \in \Re^m$ is assumed to be a zero-mean white measurement noise with known covariance R_k.

5.8.2 POSTERIOR CRAMÉR-RAO LOWER BOUND

In the context of Bayesian estimators, the posterior CRLB (PCRLB) inequality [121] states that the mean square error (MSE) matrix associated with the estimate $\hat{X}_{0:k}$ of the state vector $X_{0:k}$ for the entire trajectory up to time step *k* is lower bounded by

$$E\left\{\left[X_{0:k} - \hat{X}_{0:k}\right]\left[X_{0:k} - \hat{X}_{0:k}\right]^T\right\} \geq \left[J\left(X_{0:k}\right)\right]^{-1} \tag{5.42}$$

where the matrix $J(X_{0:k})$ is the Fisher information matrix (FIM). The proof of this inequality is provided in Appendix 5.A. The FIM is the inverse of the PCRLB and is derived from the joint probability density $p(X_{0:k}, Z_{1:k})$ of states and measurements. Let ∇ and Δ denote the operators for the first and second order partial derivatives as follows

$$\nabla_{X_k} = \left[\frac{\partial}{\partial X_k(1)}, ..., \frac{\partial}{\partial X_k(n)}\right]^T \text{ and } \Delta_{X_{k-1}}^{X_k} = \nabla_{X_{k-1}} \nabla_{X_k}^T .$$

The FIM is generally defined as [121]

$$J(X_{0:k}) = E\left\{-\Delta_{X_{0:k}}^{X_{0:k}} \log\ p(X_{0:k}, Z_{1:k})\right\} \tag{5.43}$$

where the expectation is taken with respect to the joint distribution of the states and measurements. An alternative expression for the FIM is obtained by expressing the joint probability density as

$$p(X_{0:k}, Z_{1:k}) = p(X_{0:k} \mid Z_{1:k}) p(Z_{1:k}).$$

Since $p(Z_{1:k})$ is assumed to be independent of the states, the FIM for the state vector $X_{0:k}$ from time *0* to time *k* is given by [122]

$$J(X_{0:k}) = E\left\{-\Delta_{X_{0:k}}^{X_{0:k}} \log\ p(X_{0:k} \mid Z_{1:k})\right\} = -\int \Delta_{X_{0:k}}^{X_{0:k}} \log\ p(X_{0:k} \mid Z_{1:k}) p(X_{0:k}, Z_{1:k}) dX \tag{5.44}$$

where the expectation is taken with respect to $p(X_{0:k}, Z_{1:k})$ and the integration is multidimensional and depends on the dimensions of the states.

Following [121] [123] , the trajectory FIM can be decomposed as

$$J(X_{0:k}) = \begin{bmatrix} A(k) & B(k) \\ B(k)^T & C(k) \end{bmatrix} = \begin{bmatrix} E\left\{-\Delta_{X_{0:k-1}}^{X_{0:k-1}} \log P(k)\right\} & E\left\{-\Delta_{X_{0:k-1}}^{X_k} \log P(k)\right\} \\ E\left\{-\Delta_{X_k}^{X_{0:k-1}} \log P(k)\right\} & E\left\{-\Delta_{X_k}^{X_k} \log P(k)\right\} \end{bmatrix} \tag{5.45}$$

where $P(k) = p(X_{0:k} \mid Z_{1:k})$. The FIM $J(X_k)$ associated with the estimate $\hat{X}_k$ is the inverse of the $n \times n$ lower-right square block of $\left[J(X_{0:k})\right]^{-1}$. As in [123], the matrix inversion lemma is used to derive $J(X_k)$:

$$\begin{bmatrix} A & B \\ B^T & C \end{bmatrix}^{-1} = \begin{bmatrix} D^{-1} & -A^{-1}BE^{-1} \\ -E^{-1}B^T A^{-1} & E^{-1} \end{bmatrix} \tag{5.46}$$

where A, B, C are submatrices with the appropriate dimensions, $D = A - BC^{-1}B^T$ and $E = C - B^T A^{-1} B$. The FIM $J(X_k)$ at epoch *k* is given by

$$J(X_k) = C(k) - B(k)^T A(k)^{-1} B(k) \tag{5.47}$$

As an alternative, instead of using a procedure that requires computing the inverse of $J(X_{0:k})$ or of any other large matrix such as $A(k)$ in Equation (5.47), the FIM $J(X_k)$ is calculated recursively as derived in [121]

$$J(X_k) = D_k^{22} - D_k^{21}\left[J(X_{k-1}) + D_k^{11}\right]^{-1} D_k^{12} \tag{5.48}$$

where:

$$\begin{aligned}
D_k^{11} &= E\left\{-\Delta_{X_{k-1}}^{X_{k-1}} \log p(X_k \mid X_{k-1})\right\} \\
D_k^{12} &= E\left\{-\Delta_{X_{k-1}}^{X_k} \log p(X_k \mid X_{k-1})\right\} = D_k^{21^T} \\
D_k^{21} &= E\left\{-\Delta_{X_k}^{X_{k-1}} \log p(X_k \mid X_{k-1})\right\} \\
D_k^{22} &= E\left\{-\Delta_{X_k}^{X_k} \log p(X_k \mid X_{k-1})\right\} + E\left\{-\Delta_{X_k}^{X_k} \log p(Z_k \mid X_k)\right\}
\end{aligned}$$

The initial FIM $J(X_0) = E\left\{-\Delta_{X_0}^{X_0} \log p(X_0)\right\}$. The proof of this recursive expression is given in Appendix 5.B.

5.8.3 Approximated Gaussian Form

In order to compute the D-terms in Equation (5.48), the conditional probability density functions (PDF) $p(X_k \mid X_{k-1})$ and $p(Z_k \mid X_k)$ are both assumed to be Gaussian such that

$$\begin{aligned}
p(X_k \mid X_{k-1}) &\approx N\left(X_k \mid F_k X_{k-1}, G_k Q_{k-1} G_k^T\right) \\
p(Z_k \mid X_k) &\approx N(Z_k \mid H_k X_k, R_k)
\end{aligned} \tag{5.49}$$

where $F_k = \nabla_{X_k} f_k\left[X_k{}^T\right]^T = \left[\dfrac{\partial f_k(X_k)}{\partial X_k}\right]_{n\times n}$ and $H_k = \nabla_{X_k} h_k\left[X_k{}^T\right]^T = \left[\dfrac{\partial h_k(X_k)}{\partial X_k}\right]_{n\times m}$ are the Jacobian matrices of the vector-valued functions $f_k \in \Re^n$ and $h_k \in \Re^m$ and G_k is the input matrix. With these assumptions, the resulting lower bound may not be the tightest possible. Nevertheless, it is a good-enough approximated lower bound. The analytic expressions of the conditional densities can therefore be expressed as

$$\begin{aligned}
p(X_k \mid X_{k-1}) &\approx \frac{1}{\sqrt{(2\pi)^n \left\| G_k Q_{k-1} G_k^T \right\|}} \exp\left\{-\frac{\left[X_k - F_k X_{k-1}\right]^T \left(G_k Q_{k-1} G_k^T\right)^{-1} \left[X_k - F_k X_{k-1}\right]}{2}\right\} \\
p(Z_k \mid X_k) &\approx \frac{1}{\sqrt{(2\pi)^m \left\| R_k \right\|}} \exp\left\{-\frac{\left[Z_k - H_k X_k\right]^T (R_k)^{-1} \left[Z_k - H_k X_k\right]}{2}\right\}
\end{aligned} \tag{5.50}$$

The log-PDFs of state and measurements can consequently be formulated as

$$\begin{aligned}\log p(X_k \mid X_{k-1}) &= -\frac{n}{2}\log(2\pi) - \frac{1}{2}\log\left\|G_k Q_{k-1} G_k^T\right\| \\ &\quad -\frac{1}{2}[X_k - F_k X_{k-1}]^T \left(G_k Q_{k-1} G_k^T\right)^{-1}[X_k - F_k X_{k-1}] \\ \log p(Z_k \mid X_k) &= -\frac{m}{2}\log(2\pi) - \frac{1}{2}\log\|R_k\| - \frac{1}{2}[Z_k - H_k X_k]^T (R_k)^{-1}[Z_k - H_k X_k]\end{aligned} \tag{5.51}$$

The following partial derivative expressions are obtained:

$$\begin{aligned}\Delta_{X_{k-1}}^{X_{k-1}} \log p(X_k \mid X_{k-1}) &= \nabla_{X_{k-1}}\left[\nabla_{X_{k-1}}^T \log p(X_k \mid X_{k-1})\right] \\ &= \nabla_{X_{k-1}}\left\{F_k^T \left(G_k Q_{k-1} G_k^T\right)^{-1}[X_k - F_k X_{k-1}]\right\} = -F_k^T \left(G_k Q_{k-1} G_k^T\right)^{-1} F_k\end{aligned}$$

$$\begin{aligned}\Delta_{X_{k-1}}^{X_k} \log p(X_k \mid X_{k-1}) &= \nabla_{X_{k-1}}\left[\nabla_{X_k}^T \log p(X_k \mid X_{k-1})\right] \\ &= \nabla_{X_{k-1}}\left\{-\left(G_k Q_{k-1} G_k^T\right)^{-1}[X_k - F_k X_{k-1}]\right\} = \left(G_k Q_{k-1} G_k^T\right)^{-1} F_k\end{aligned}$$

$$\begin{aligned}\Delta_{X_k}^{X_{k-1}} \log p(X_k \mid X_{k-1}) &= \nabla_{X_k}\left[\nabla_{X_{k-1}}^T \log p(X_k \mid X_{k-1})\right] \\ &= \nabla_{X_k}\left\{F_k^T \left(G_k Q_{k-1} G_k^T\right)^{-1}[X_k - F_k X_{k-1}]\right\} = F_k^T \left(G_k Q_{k-1} G_k^T\right)^{-1}\end{aligned}$$

$$\begin{aligned}\Delta_{X_k}^{X_k} \log p(X_k \mid X_{k-1}) &= \nabla_{X_k}\left[\nabla_{X_k}^T \log p(X_k \mid X_{k-1})\right] \\ &= \nabla_{X_k}\left\{-\left(G_k Q_{k-1} G_k^T\right)^{-1}[X_k - F_k X_{k-1}]\right\} = -\left(G_k Q_{k-1} G_k^T\right)^{-1}\end{aligned}$$

$$\begin{aligned}\Delta_{X_k}^{X_k} \log p(Z_k \mid X_k) &= \nabla_{X_k}\left[\nabla_{X_k}^T \log p(Z_k \mid X_k)\right] \\ &= \nabla_{X_k}\left\{H_k^T R_k^{-1}[Z_k - H_k X_k]\right\} = -H_k^T R_k^{-1} H_k\end{aligned}$$

The *D*-terms are therefore expressed as

$$\begin{aligned}D_k^{11} &= E\left\{-\Delta_{X_{k-1}}^{X_{k-1}} \log p(X_k \mid X_{k-1})\right\} = F_k^T \left(G_k Q_{k-1} G_k^T\right)^{-1} F_k \\ D_k^{12} &= E\left\{-\Delta_{X_{k-1}}^{X_k} \log p(X_k \mid X_{k-1})\right\} = -\left(G_k Q_{k-1} G_k^T\right)^{-1} F_k = D_k^{21^T} \\ D_k^{21} &= E\left\{-\Delta_{X_k}^{X_{k-1}} \log p(X_k \mid X_{k-1})\right\} = -F_k^T \left(G_k Q_{k-1} G_k^T\right)^{-1} \\ D_k^{22} &= E\left\{-\Delta_{X_k}^{X_k} \log p(X_k \mid X_{k-1})\right\} + E\left\{-\Delta_{X_k}^{X_k} \log p(Z_k \mid X_k)\right\} = \left(G_k Q_{k-1} G_k^T\right)^{-1} + H_k^T R_k^{-1} H_k\end{aligned}$$

The FIM $J(X_k)$ is consequently given by

$$\begin{aligned} J(X_k) &= D_k^{22} - D_k^{21}\left[J(X_{k-1}) + D_k^{11}\right]^{-1} D_k^{12} \\ J(X_k) &= \left(G_k Q_{k-1} G_k^T\right)^{-1} + H_k^T R_k^{-1} H_k - F_k^T \left(G_k Q_{k-1} G_k^T\right)^{-1} \\ &\quad \times \left[J(X_{k-1}) + F_k^T \left(G_k Q_{k-1} G_k^T\right)^{-1} F_k \right]^{-1} \left(G_k Q_{k-1} G_k^T\right)^{-1} F_k \end{aligned} \tag{5.52}$$

The Posterior Cramér-Rao Lower Bound is therefore $PCRLB = \left[J(X_k)\right]^{-1}$.

If the evolution equation $X_k = f_k(X_{k-1}) + w_k$ suggested in the state model of sub-section 5.2.1 is considered instead of the more general evolution equation $X_k = f_k(X_{k-1}) + G_k w_{k-1}$ of the dynamic system in subsection 5.8.1, the input matrix G_k is replaced by the identity matrix I in the expression of Equation (5.52). The FIM $J_m(X_k)$ for this modified version is therefore expressed as

$$\begin{aligned} J_m(X_k) &= D_k^{22} - D_k^{21}\left[J_m(X_{k-1}) + D_k^{11}\right]^{-1} D_k^{12} \\ J_m(X_k) &= (Q_{k-1})^{-1} + H_k^T R_k^{-1} H_k - F_k^T (Q_{k-1})^{-1} \times \left[J_m(X_{k-1}) + F_k^T (Q_{k-1})^{-1} F_k\right]^{-1} (Q_{k-1})^{-1} F_k \end{aligned} \tag{5.53}$$

The corresponding Posterior Cramér-Rao Lower Bound is $PCRLB_m = \left[J_m(X_k)\right]^{-1}$.

5.9 ALGORITHMS PERFORMANCE EVALUATION

This section is dedicated to the evaluation of the performance of the different algorithms that are discussed in this chapter. First, the PCRLB that is derived in section 5.8 is used as benchmark for performance comparison by running Monte Carlo simulations based on one static suburban navigation scenario. Only positioning solutions are compared via PCRLB. Then, many experiments are conducted using DLR urban and suburban multipath data for various receiver dynamics and trajectories and the obtained empirical results are utilized to compare the navigation and vector tracking performance of the different filtering approaches. The multipath and non-line-of-sight (NLOS) detection methods and the associated satellite exclusion techniques that are discussed in *Chapters 3 and 4* are not applied in this chapter. The implementations in this chapter aim at comparing the navigation and vector tracking performance of the Bayesian filtering approaches without aid of multipath and NLOS detection/mitigation techniques.

5.9.1 PCRLB-BASED PERFORMANCE EVALUATION

The positioning solutions of five algorithms are compared hereafter: the Extended Kalman Filter (EKF), the Unscented Kalman Filter (UKF), the Iterated Unscented Kalman Filter (IUKF), the Iterated Unscented Particle Filter (IUPF), and the proposed Iterated Adaptive Unscented Particle Filter (IAUPF). A realistic GPS satellite constellation geometry is used in the simulations. It is depicted in the sky plot of Figure 5.3. Four satellites are visible. The azimuth and elevation angles of the four satellites are as follows (in degrees):

Azimuth = [53.7808, 72.4364, 52.8083, 312.6718]

Elevation = [74.8819, 33.6936, 57.3134, 39.9328]

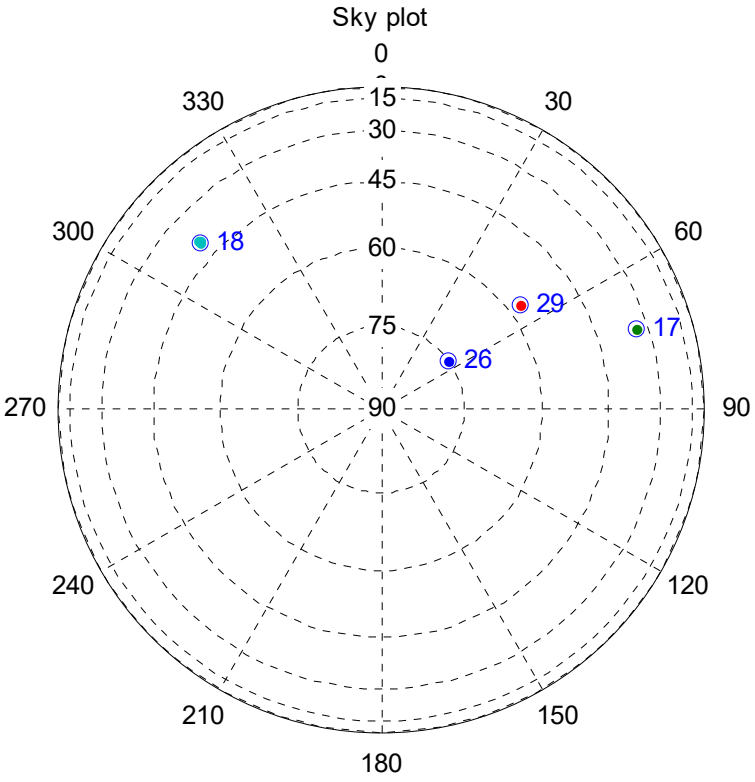

Figure 5.3: Constellation geometry (sky plot) used in the simulations.

A suburban environment scenario with a static receiver is recreated. Satellite positions and pseudorange measurements data are available for a period of 25 seconds. The positioning solutions of the five algorithms are provided for the 25 seconds duration with the navigator operating at a frequency of 1 Hz. Fifty Monte Carlo runs are performed.

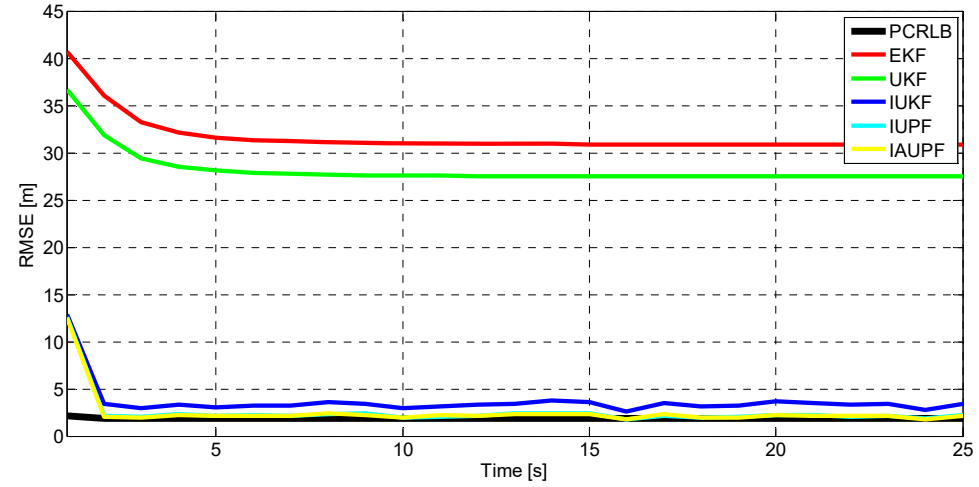

(a)

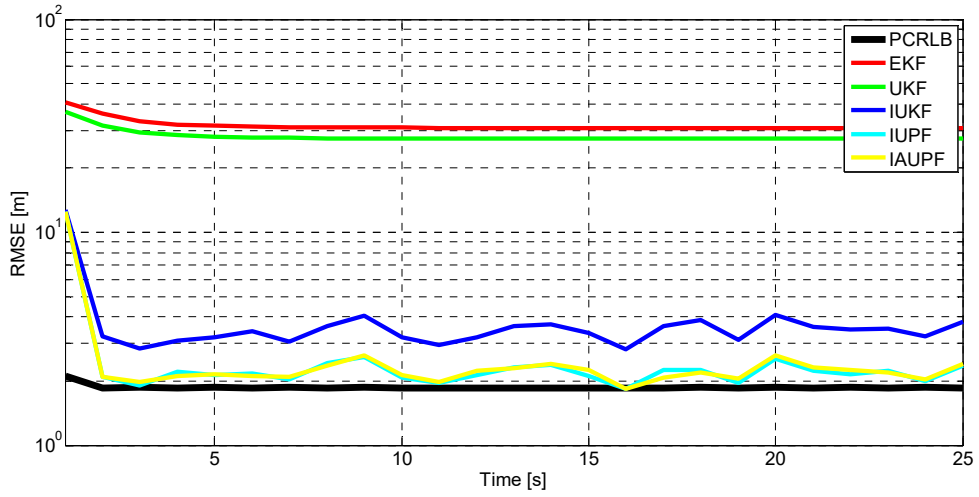

(b)

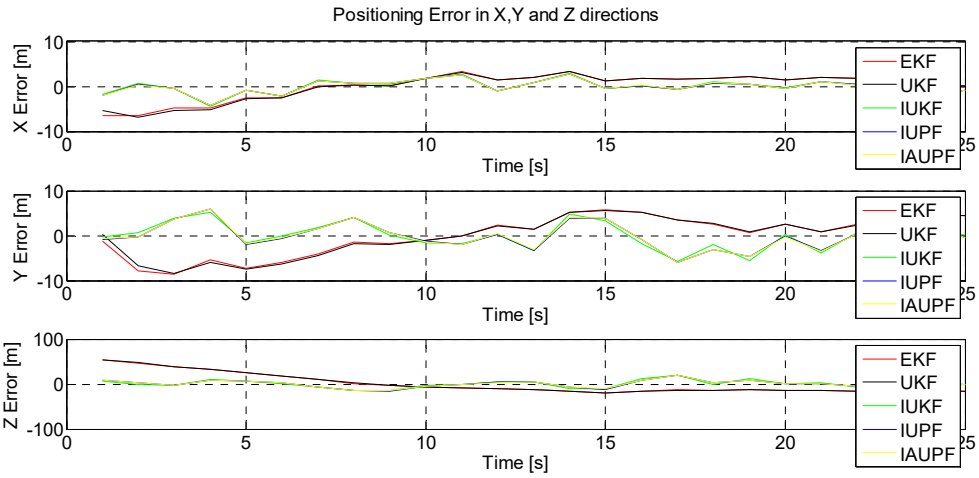

(c)

Figure 5.4: Performance evaluation for EKF, UKF, IUKF, IUPF, and IAUPF. (a) Algorithms RMSE vs. PCRLB, linear scale (b) Algorithms RMSE vs. PCRLB, logarithmic scale (c) ECEF XYZ Positioning Errors

The algorithms performance is evaluated based on the root mean square error (RMSE) of their position estimations. The curves that are provided give a measure of the algorithms convergence time and show their asymptotic behaviour. The figures are based on the mean square error (MSE) value of the three-dimensional position vector defined as follows:

$$\sigma_p^2 = E\left\{(p-\hat{p})^T(p-\hat{p})\right\} = \sigma_x^2 + \sigma_y^2 + \sigma_z^2 \tag{5.54}$$

where σ_x^2, σ_y^2 and σ_z^2 are the mean square errors of the ECEF X, Y and Z position coordinates respectively. The root mean square error is therefore computed as $RMSE = \sqrt{\sigma_p^2}$. A corresponding root PCRLB that is based on the XYZ position coordinates is similarly computed using the simulation results of the PCRLB expression in Equation (5.53). This $\sqrt{PCRLB}$ is used as reference for performance evaluation.

Figure 5.4 (a) and Figure 5.4 (b) illustrate the RMSE curves for the five algorithms as well as the root PCRLB. Clearly, the EKF algorithm is the least performant. It is the furthest from the PCRLB. The linearization of the measurement equation does not play in its favour when measurements exhibit strong nonlinearities. The EKF performance is however close to the UKF performance in terms of convergence time. Both EKF and UKF converge slower than the iterative algorithms. In fact, the IUKF, IUPF and IAUPF converge faster and are closer to the PCRLB in terms of estimation accuracy. The particle filtering approaches, namely the IUPF and the proposed IAUPF, have similar performance. They have the highest performance of the five algorithms as they are the closest to the PCRLB. In other terms, the particle filtering methods present better convergence properties and their density $\hat{p}(X_{0:k} \mid Z_{1:k})$ approximates the true posterior density $p(X_{0:k} \mid Z_{1:k})$ better than the other algorithms. This performance improvement is attributed not only to the standard particle filtering approach but also to the use of iterative and adaptive methods with the UKF algorithm to build the proposal distribution and the use of the novel sampling and resampling approaches in the UPF algorithm. Figure 5.4 (c) illustrates the ECEF XYZ positioning errors of the five algorithms for the scenario under study. The superior performance of the iterative and particle filtering methods is also visible from this figure.

However, this performance improvement comes with a high computational cost. Normally, for a state vector of size n_x, the EKF and UKF algorithms are said to have approximately $O\left(n_x^3\right)$ complexity, while the generic PF has $O\left(N_p n_x^2\right)$ complexity, with N_p being the number of particles used in the PF calculations [124]. From this

perspective, the PF is a factor N_p/n_x computationally more expensive than the EKF and UKF. If the iterative steps are added to the UKF, the complexity increases depending on the average number of iterations that are required to have the inequality in Equation (5.34) not hold anymore. This number of iterations varies from case to case but reduces significantly, sometimes down to one, when the algorithm has converged. If the average number of UKF iterations required in the IAUKF is denoted N_i, then the IAUKF algorithm complexity is approximately $O\left(N_i n_x^3\right)$ and the proposed IAUPF algorithm complexity can be approximated to $O\left[\left(N_i n_x + N_p\right) n_x^2\right]$. The IAUPF is consequently a factor $\left(N_i n_x + N_p\right)/n_x$ computationally more expensive than the EKF and UKF. Nonetheless, this complexity order is still low compared to the standard UPF algorithm that generates a UKF-based Gaussian proposal distribution for each particle thus requiring as many UKFs as there are particles. The standard UPF complexity is thus approximately $O\left(N_p n_x^5\right)$ and is a factor $N_p n_x^2$ computationally more demanding than the EKF and UKF.

5.9.2 Performance Evaluation Based on DLR Multipath Data Experiments

Further validation of the proposed particle filtering approach, the IAUPF, is performed first by utilizing simple, unconstrained, open sky scenarios from the DLR model, with the simulation of Constellation No 1 (see *Chapter 3*, Table 3.1). These mild scenarios allow proper validation of the algorithm implementation in a vector tracking loop (VTL) scheme before evaluating its performance in harsh, constrained scenarios. The GNSS software receiver simulator presented in *Chapter 3* and depicted in Figure 3.23 is used in the experiments. This receiver simulator has the same architecture as the VTL-based receiver depicted in Figure 5.1. The settings and tunings of Table 4.2 (*Chapter 4*) regarding the measurement noise covariance matrix, the input noise covariance matrix, and the initial estimation error covariance matrix, are re-used for the EKF and IAUPF. For the IAUPF algorithm, 100 particles are used. The possibility to achieve good performance with a small number of particles is among the benefits of unscented particle filters in comparison with the standard particle filters. Figures 5.5 and 5.7 depict the EKF ECEF position and velocity errors in an open sky environment for a static pedestrian and a moving car (50 km/h) respectively. Figures 5.6 and 5.8 on the other hand depict the IAUPF ECEF position and velocity errors for the same two scenarios.

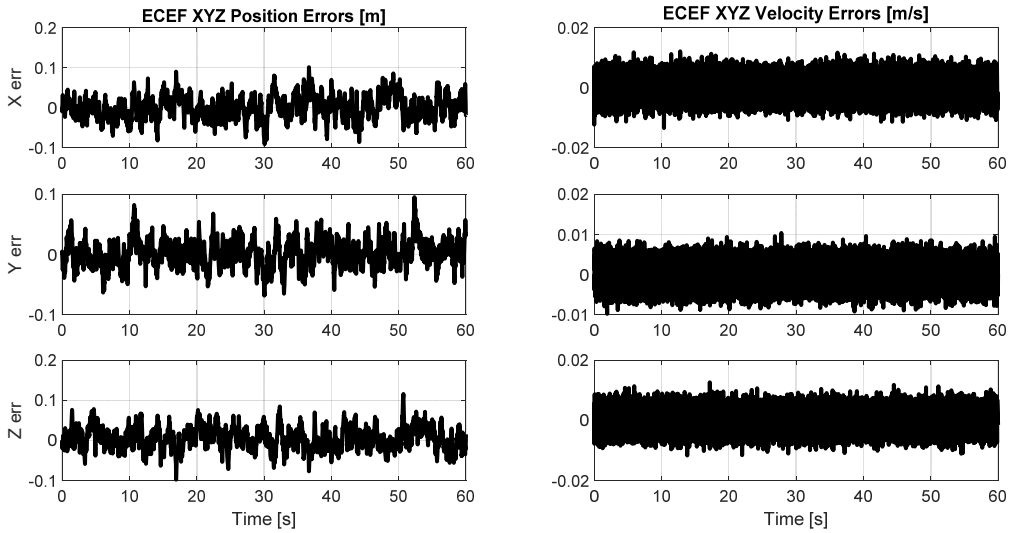

Figure 5.5: Open sky, static pedestrian, EKF ECEF position and velocity errors

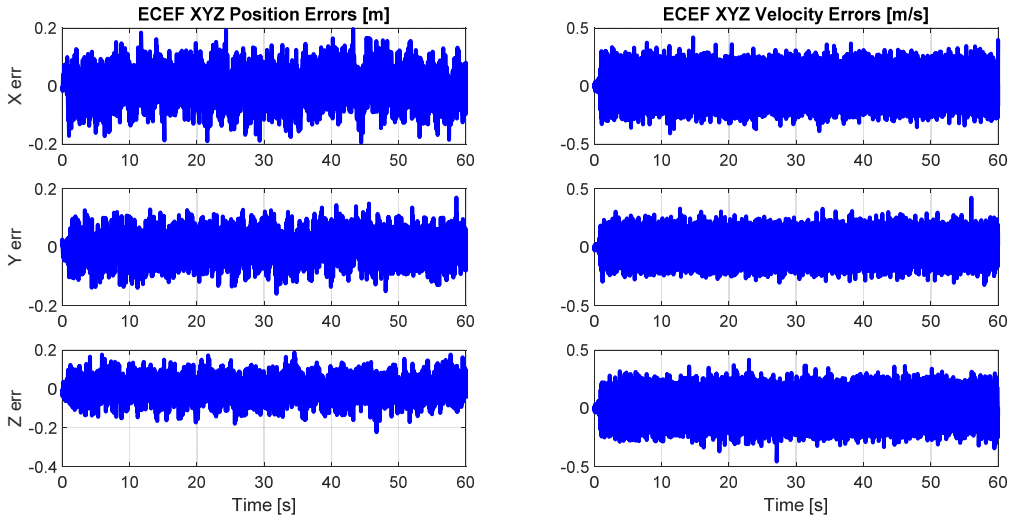

Figure 5.6: Open sky, static pedestrian, IAUPF ECEF position and velocity errors

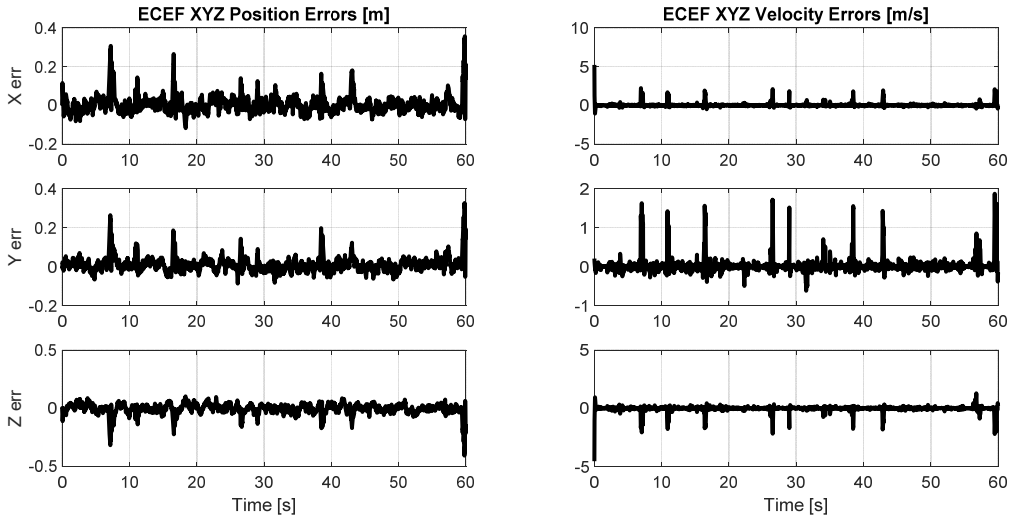

Figure 5.7: Open sky, moving car (50 km/h), EKF ECEF position and velocity errors

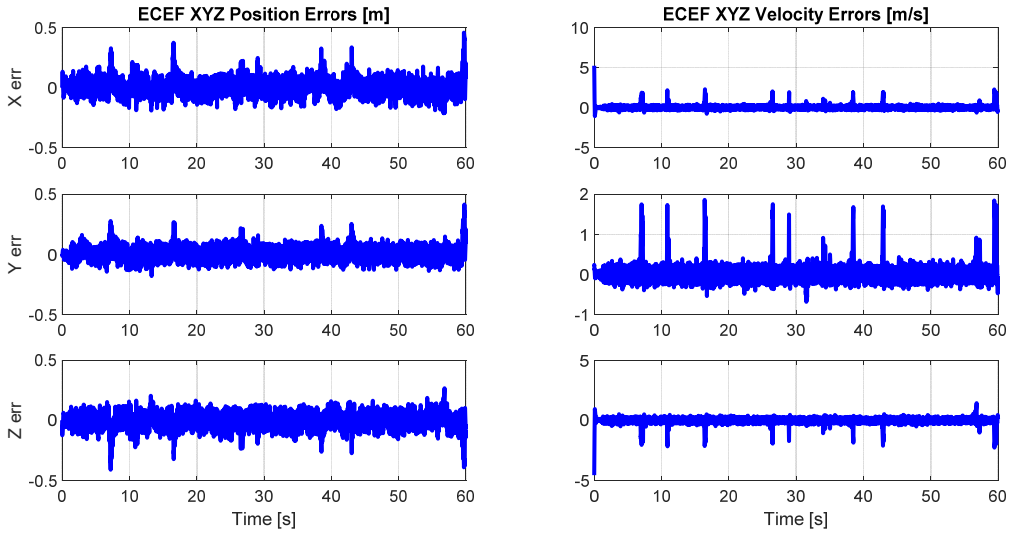

Figure 5.8: Open sky, moving car (50 km/h), IAUPF ECEF position and velocity errors

It can be observed that for these open sky scenarios, both the EKF and IAUPF maintain positioning errors at minimum, the EKF having slightly better performance than the suggested IAUPF. The absolute value of the mean IAUPF position error has a maximum of $|0.0112|$m for the two scenarios. The absolute value of the IAUPF position error standard deviation has a maximum of $|0.0633|$m for the two scenarios under study. These results, which are obtained by comparing the estimated PVT solution to the PVT solution of a reference trajectory, show that both EKF and IAUPF algorithms are correctly implemented.

Table 5.1 contains the DLR multipath scenarios that are used in the experiments conducted to further evaluate the performance of the algorithms. These are harsh environments scenarios (suburban and urban) with high probability of multipath presence and with a dynamic receiver. It is very likely for the probability densities of measurements and tracking errors to be non-Gaussian, asymmetric and multi-modal. Also, severe nonlinearities are likely to appear in the measurements.

Table 5.1: DLR multipath scenarios used in the experiments

Constellation	Constellation No 1 (see *Chapter 3*, Table 3.1)				
Environment	Suburban		Urban		
Trajectory	Straight Line				
Dynamics	Vehicle (Car)				
	Constant velocity (50km/h)	Constant acceleration (2.5 m/s^2)	Constant velocity (50km/h)	Constant velocity (90km/h)	Constant acceleration (2.5 m/s^2)
Scenarios	Scenario 1	Scenario 2	Scenario 3	Scenario 4	Scenario 5

Here, the EKF-based and the proposed IAUPF-based vector tracking and navigation solutions are compared. No multipath exclusion strategy is implemented in either EKF or IAUPF approaches here. The objective is to first compare the Bayesian filtering approaches alone. The use of multipath and NLOS detection/mitigation techniques is left for future work. The navigation (positioning) performance and the vector tracking performance are evaluated. With respect to the navigation solution, two performance indicators are of interest: the immunity to divergence in harsh conditions, and the positioning accuracy. With respect to the vector tracking solution, the code delay, carrier phase and carrier frequency tracking errors are used as performance indicators.

Figure 5.9 and Figure 5.10 display the ECEF position and velocity errors for the EKF and IAUPF algorithms for Scenario 1 and 2 respectively, which are suburban scenarios. The EKF solution diverges between the 20^{th} and 30^{th} tracking second for Scenario 1 and a bit earlier for Scenario 2. This makes the position and velocity accuracy deteriorate seriously. The numerical figures in Table 5.2 for Scenarios 1 and 2 show how significantly the EKF divergence affects its PVT solution accuracy. When compared with the IAUPF solution, the departure from the reference trajectory is very substantial. No divergence is registered for the IAUPF. This confirms that the use of iterative and adaptive strategies to speed up convergence and to combat divergence has a positive impact. Although the IAUPF solution accuracy is not as high as the EKF solutions of *Chapter 4* that incorporate multipath detection and exclusion and that are based on robust adaptive and conjoint tracking architectures, it is within reasonable ranges for these very harsh multipath environments where no mitigation is implemented. Here is a quick EKF versus IAUPF performance comparison of the ECEF XYZ position errors for Scenarios 1 and 2: the absolute value of the mean IAUPF position error varies between |6.5553|m and |-136.375|m while the mean EKF position error varies between |-8.3207|km and |105.910|km. Similarly, the absolute value of the IAUPF position error standard deviation goes from |99.7265|m to |258.4733|m against |8.5137|km to |139.400|km for the EKF. The deviation between the EKF and IAUPF velocity errors is of the same order of magnitude.

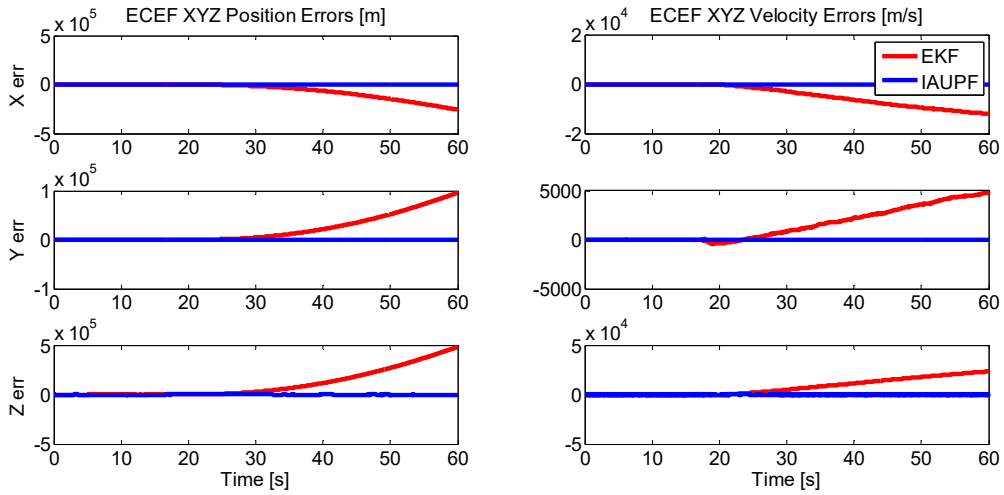

Figure 5.9: Scenario 1, VTL ECEF position and velocity errors

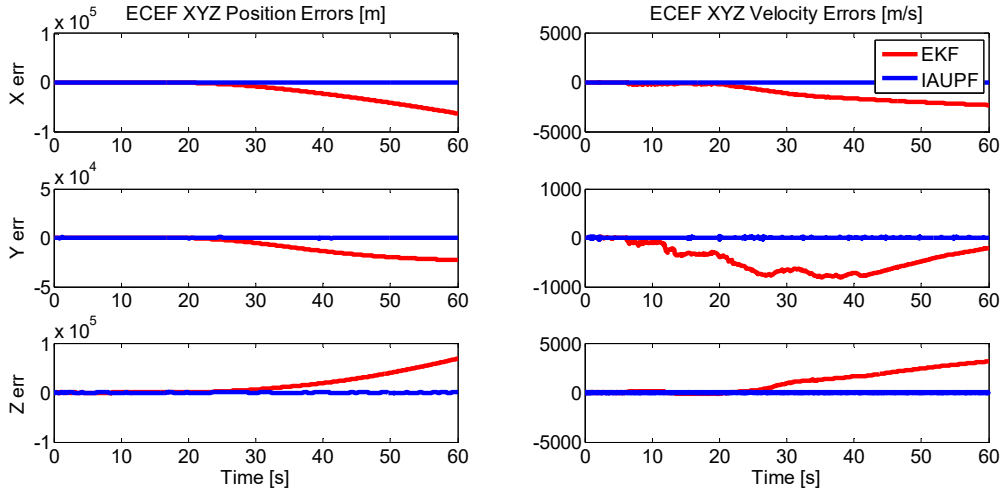

Figure 5.10: Scenario 2, VTL ECEF position and velocity errors

Table 5.2: Scenarios 1 and 2 ECEF position and velocity errors

Error		Scenario 1				Scenario 2			
		EKF		IAUPF		EKF		IAUPF	
		Mean	STD	Mean	STD	Mean	STD	Mean	STD
Position [m]	X	57621	74954	-136.375	258.4733	-17029	19503	16.4024	99.7265
	Y	20398	27486	50.6002	131.1174	-8320.7	8513.7	6.5553	167.9596
	Z	105910	139400	87.7732	182.2220	16283	19981	-17.2044	183.9363
Velocity [m/s]	X	-4075.3	4139.9	0.7177	6.8512	-1035.8	826.2602	0.1843	2.2841
	Y	1464.7	1659.5	-0.1889	3.2327	-441.6726	259.6769	0.1268	3.0251
	Z	7598.3	7970.9	-0.5167	4.7322	1058.7	1095.3	0.0183	2.8706

Looking at the code delay, carrier phase and carrier frequency tracking errors as depicted in Figures 5.11, 5.12 and 5.13, the IAUPF positioning advantage over the EKF is extended to vector tracking performance as well. These figures examine Scenario 2, which represents a suburban vehicle accelerating at 2.5 m/s^2. The tracking errors of six satellites are displayed. The most significant deviations are observed in carrier phase and carrier frequency tracking errors. The velocity errors obviously are mirrored onto the carrier tracking errors. However, the EKF and IAUPF code delay tracking errors remain relatively close in value for this scenario. This example shows that the IAUPF-based vector tracking loop is more robust than the EKF-based.

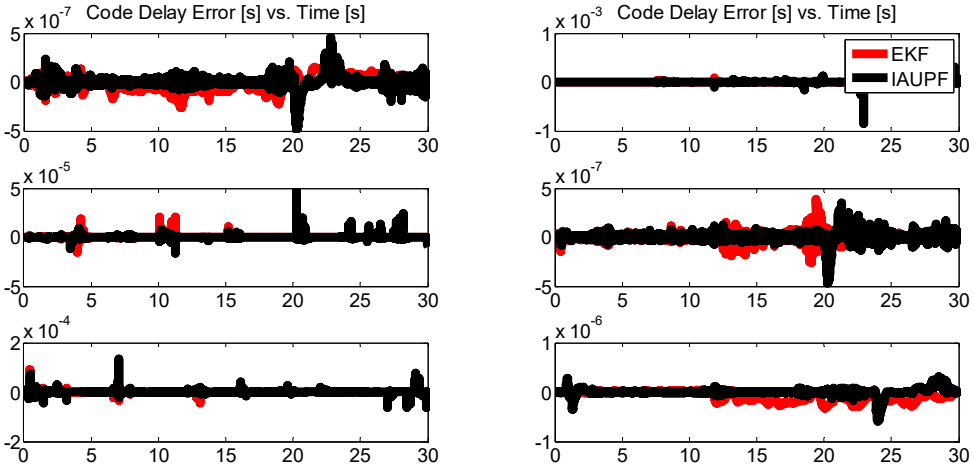

Figure 5.11: Code delay errors (Top to bottom, left to right: PRN05, PRN15, PRN27, PRN07, PRN09, PRN26; Constellation 1, Scenario 2)

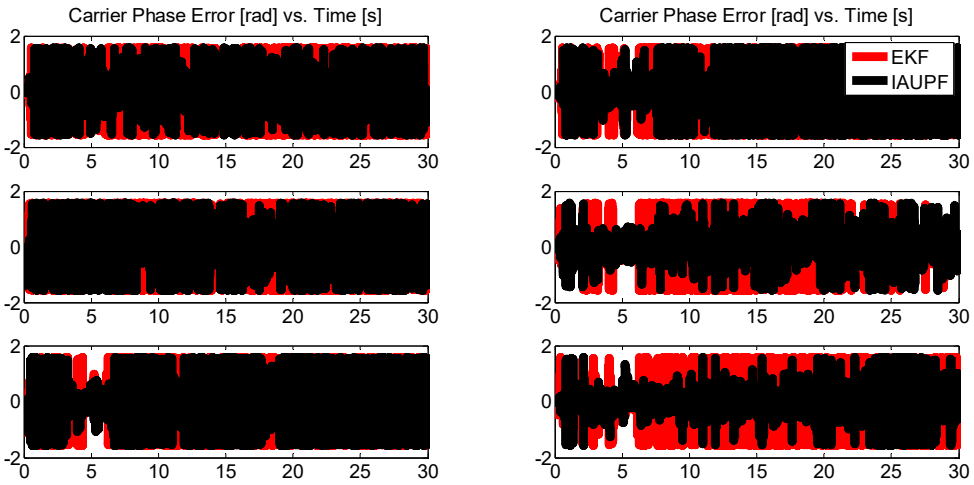

Figure 5.12: Carrier phase errors (Top to bottom, left to right: PRN05, PRN15, PRN27, PRN07, PRN09, PRN26; Constellation 1, Scenario 2)

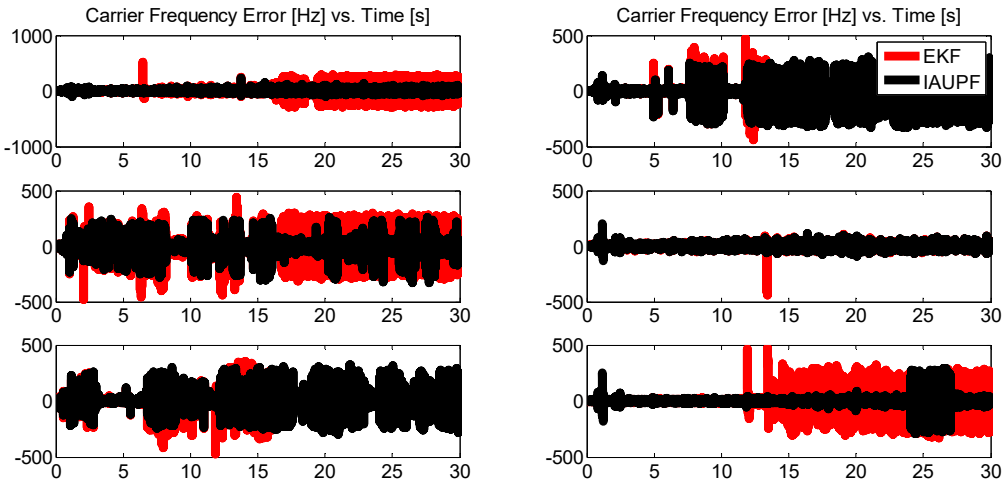

Figure 5.13: Carrier frequency errors (Top to bottom, left to right: PRN05, PRN15, PRN27, PRN07, PRN09, PRN26; Constellation 1, Scenario 2)

It is interesting to consider the EKF and IAUPF position and velocity errors for the 3 urban scenarios as well. For scenario 3 (see Figure 5.14), which is a relatively low dynamic scenario (a vehicle with constant velocity of 50 km/h), the deviation between the EKF and the IAUPF PVT solutions is not significant. In both cases, no divergence due to potential nonlinearities and non-Gaussianity from multipath or other disturbances is registered. Table 5.3 contains numerical values of means and standard deviations of ECEF position and velocity errors for this scenario. The absolute value of the mean IAUPF position error varies between |0.9185|m and |84.8699|m while the mean EKF position error varies between |-3.8530|m and |-113.1665|m. The absolute value of the IAUPF position error standard deviation is between |36.3960|m and |246.2487|m against |11.811|m and |206.9052|m for the EKF. The velocity errors are also very close between EKF and IAUPF solutions. For this urban scenario, no major disturbances susceptible of putting the IAUPF at an advantage in comparison with the EKF have been registered.

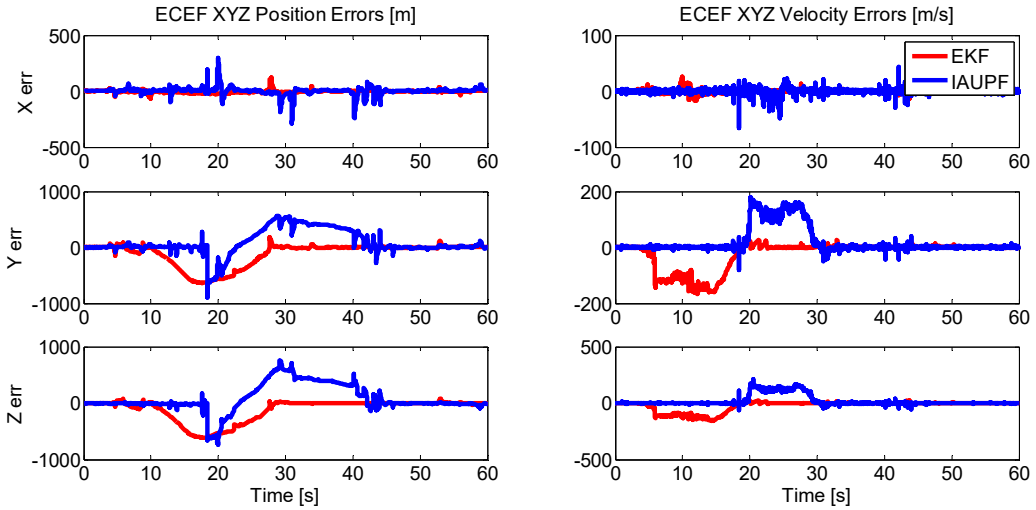

Figure 5.14: Scenario 3, VTL ECEF position and velocity errors

Table 5.3: Scenario 3 ECEF position and velocity errors

Error		Scenario 3			
		EKF		IAUPF	
		Mean	STD	Mean	STD
Position [m]	X	-3.8530	11.8111	0.9185	36.3960
	Y	-112.6100	206.9052	84.8699	220.2445
	Z	-113.1665	197.3757	80.4924	246.2487
Velocity [m/s]	X	-0.4602	2.0733	-0.1513	4.2399
	Y	-23.1180	49.6731	20.1360	47.7934
	Z	-21.9280	46.4157	19.3796	46.1786

Looking at the curves in Figures 5.15 and 5.16 as well as the numerical values in Table 5.4, for scenarios 4 and 5, the IAUPF maintains its superior performance vis-à-vis the EKF especially in scenario 4. Scenario 4 is a car moving at a constant velocity of 90km/h and scenario 5 is a car accelerating at 2.5 m/s^2. Once more, the EKF solutions diverge as a result of disturbances in the urban environment while the IAUPF solution does not. While the performance deviation between the EKF and IAUPF PVT solutions is very significant for scenario 4, the EKF performance in scenario 5 is moderately lower than the IAUPF performance. The recurrent flaw in the EKF solution is divergence. This is a confirmation of the theoretical projections that place the EKF algorithm at a disadvantage in comparison with other Bayesian filtering solutions that do not linearize the filtering model, among which the proposed IAUPF algorithm appear.

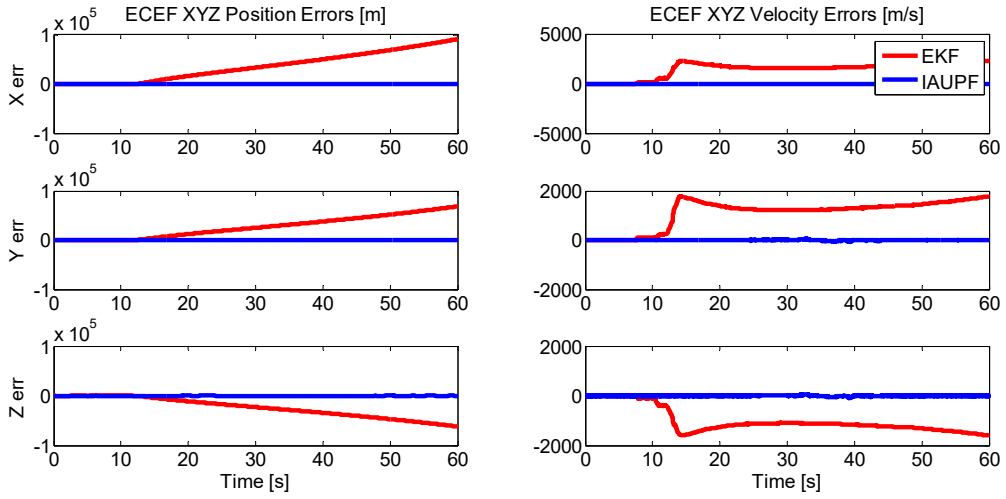

Figure 5.15: Scenario 4, VTL ECEF position and velocity errors

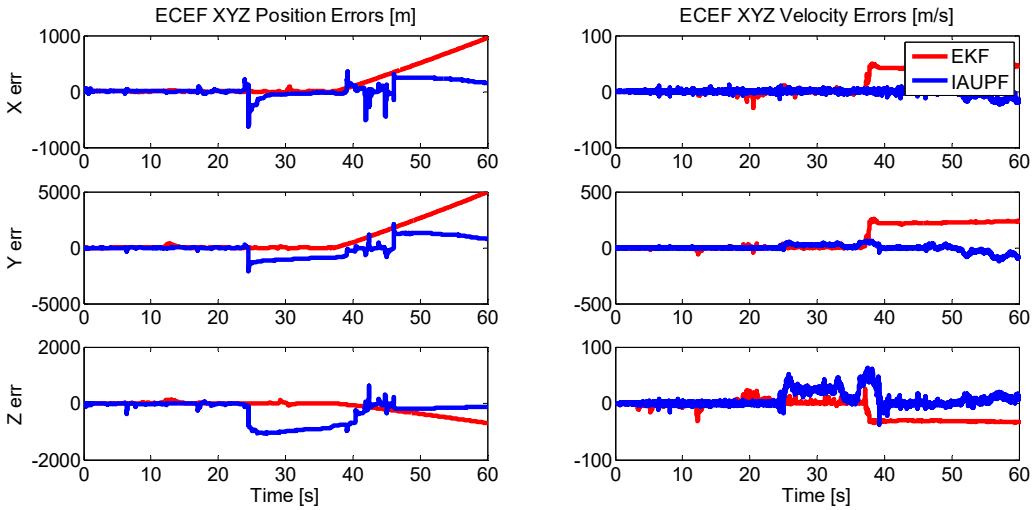

Figure 5.16: Scenario 5, VTL ECEF position and velocity errors

Table 5.4: Scenarios 4 and 5 ECEF position and velocity errors

Error		Scenario 4				Scenario 5			
		EKF		IAUPF		EKF		IAUPF	
		Mean	STD	Mean	STD	Mean	STD	Mean	STD
Position [m]	X	35385	28683	22.5866	69.8603	174.2370	279.5656	38.5148	120.2649
	Y	26595	21517	-140.8633	268.1811	908.7674	1448.1	-1.3792	766.0523
	Z	-24068	19481	-227.3580	282.3275	-121.0491	208.7806	-297.2182	386.3266
Velocity [m/s]	X	1497.1	739.7758	0.1524	1.7481	16.1356	21.2806	-1.1949	4.6799
	Y	1114.8	566.9724	-0.2639	13.6096	84.9352	108.6557	-1.5287	28.5328
	Z	-1015.3	500.3373	-0.4947	13.8766	-11.3221	15.9723	7.1236	12.7855

5.10 CONCLUSION

This chapter has studied various Bayesian filtering algorithms, namely the unscented Kalman filter (UKF), the iterated UKF (IUKF), the adaptive UKF (AUKF), the iterated AUKF (IAUKF), the regularized particle filter (RPF), and the unscented particle filter (UPF). A novel particle filtering approach, the iterated adaptive unscented particle filter (IAUPF) has been devised. This novel algorithm exploits the convergence benefits of iterative and adaptive filtering methods. It also exploits the synergy of regularized and stratified resampling therefore dealing with particle degeneracy while avoiding particle impoverishment or collapse. Furthermore, it reduces the complexity of the standard UPF algorithm by using a single IAUKF to provide a

Gaussian proposal distribution from which particles are globally sampled. However, it remains a factor $\left(N_i n_x + N_p\right)/n_x$ computationally more expensive than the EKF and UKF, with N_i, n_x, and N_p being respectively the average number of iterations required for the IAUKF to converge to a good state estimate, the size of the state vector, and the number of particles used in the IAUPF algorithm. A performance evaluation based on Monte Carlo simulations with a posterior Cramér-Rao lower bound (PCRLB) as benchmarking reference and based on experiments with DLR multipath data has demonstrated the advantages of the IAUPF in terms of convergence speed, divergence suppression, vector tracking and positioning accuracy in comparison with the other filters. In particular, Monte Carlo simulations of the EKF, UKF, IUKF, IUPF and IAUPF algorithms as applied to a static suburban navigation problem have shown that iterative and adaptive strategies, when applied to either UKF or UPF filters, improve convergence speed and immunity against divergence. From the Monte Carlo simulations, it has been also observed that the particle filtering approaches are the closest in performance to the PCRLB. They have the best convergence and estimation accuracy. The experiments with DLR multipath data for dynamic suburban and urban scenarios have particularly revealed the EKF proclivity to diverge in harsh environments where disturbances are likely to create severe nonlinearities and non-Gaussianity in the measurements errors. The proposed IAUKF algorithm on the other hand has demonstrated a strong immunity to divergence in these conditions and a better PVT estimation accuracy. If computational complexity is not an issue, this novel approach can be implemented in the robust tracking architectures that have been designed in *Chapter 4*. The benefits obtained from these architectures with an EKF-based implementation would be magnified with this particle filtering approach.

APPENDIX 5.A: PROOF OF PCRLB INEQUALITY

For a Bayesian estimator, the mean square error (MSE) matrix or error covariance matrix (ECM) associated with the estimate $\hat{X}_{0:k}$ of the state vector $X_{0:k}$ for the entire trajectory up to time step *k* is lower bounded according to the following inequality:

$$\mathrm{M}_{\mathrm{cov}} = E\left\{\left[X_{0:k} - \hat{X}_{0:k}\right]\left[X_{0:k} - \hat{X}_{0:k}\right]^{T}\right\} \geq \left[J(X_{0:k})\right]^{-1} \tag{5.A.1}$$

where the matrix $J(X_{0:k})$ is the Fisher information matrix (FIM). The Posterior Cramér-Rao Lower Bound (PCRLB) is the inverse of the FIM: $PCRLB = \left[J(X_k)\right]^{-1}$.

Proof:

Bayesian estimators are considered to be asymptotically unbiased. This asymptotic unbiasness assumption can be exploited to prove the inequality in Equation (5.A.1).

- *Assumption*

The asymptotic unbiasness assumption states that [125]

$$\begin{gathered}\lim_{X_j(i)\to\chi_i^{+}} B(X_{0:k})p(X_{0:k}) = \lim_{X_j(i)\to\chi_i^{-}} B(X_{0:k})p(X_{0:k}) \\ \forall j \in \{0,\ldots,k\} \quad and \quad \forall i \in \{0,\ldots,n\}\end{gathered} \tag{5.A.2}$$

Here $B(X_{0:k})$ is the bias associated with the estimation of $X_{0:k}$, χ_i is the domain of $X_j(i)$ for all j in $\{0,\ldots,k\}$ and $\left\{\chi_i^{-},\chi_i^{+}\right\}$ are its bounds, n is the number of elements in the state vector X_j at time step j. The bias $B(X_{0:k})$ is defined as

$$B(X_{0:k}) = E\left\{\left(X_{0:k} - \hat{X}_{0:k}\right) \middle| X_{0:k}\right\} \tag{5.A.3}$$

$B_{ij}(X_{0:k})$ is the bias associated with the estimation of $X_j(i)$ such that

$$B_{ij}(X_{0:k}) = E\left\{\left[X_j(i) - \left(\hat{X}_{0:k}\right)_{ij}\right] \middle| X_{0:k}\right\} \tag{5.A.4}$$

For an unbiased estimator, the bias $B(X_{0:k})$ is almost surely equal to zero.

- *Lemmas*

Lemma 1: The FIM $J(X_{0:k})$ is given by

$$J(X_{0:k}) = E\left\{-\Delta_{X_{0:k}}^{X_{0:k}} \log\ p(X_{0:k}, Z_{1:k})\right\} \tag{5.A.5}$$

Lemma 2: Let M be a symmetric matrix such that $M = \begin{bmatrix} A & C \\ C^T & B \end{bmatrix}$, where A is an non-negative real symmetric matrix, B is a positive real symmetric matrix, and C is a real matrix. It follows that

$$M \geq 0 \quad implies \quad A - CB^{-1}C^T \geq 0 \tag{5.A.6}$$

- *Proof*

Based on the lemmas above, a matrix $M = \begin{bmatrix} A & C \\ C^T & B \end{bmatrix}$ is built such that $A = \mathrm{M}_{\mathrm{cov}}$, $B = J(X_{0:k})$, and $C = E\left\{\left(X_{0:k} - \hat{X}_{0:k}\right)\nabla_{X_{0:k}}^T \log(X_{0:k}, Z_{1:k})\right\}$.

With this construction, proving the inequality in Equation (5.A.1) is equivalent to simply proving that C is the identity matrix I. Matrix C is expressed as

$$\begin{aligned} C &= E\left\{\left(X_{0:k} - \hat{X}_{0:k}\right)\nabla_{X_{0:k}}^T \log(X_{0:k}, Z_{1:k})\right\} \\ C &= \int \left(X_{0:k} - \hat{X}_{0:k}\right)\nabla_{X_{0:k}}^T p(X_{0:k}, Z_{1:k}) d(X_{0:k}, Z_{1:k}) \end{aligned} \tag{5.A.7}$$

C is a square matrix. By applying integration by parts to the integral in Equation (5.A.7), an element of matrix C can be expressed as [125]

$$\begin{aligned} C(ij, i'j') &= I(ij, i'j') + \int \left[\left(X_j(i) - (\hat{X}_{0:k})_{ij}\right)p(X_{0:k}, Z_{1:k})\right]_{\chi_{i'}^-}^{\chi_{i'}^+} d\left(X_{0:k}^{-i'j'}, Z_{1:k}\right) \\ C(ij, i'j') &= I(ij, i'j') + \int \left[\left(X_j(i) - (\hat{X}_{0:k})_{ij}\right)p(X_{0:k}, Z_{1:k}) dZ_{1:k}\right]_{\chi_{i'}^-}^{\chi_{i'}^+} dX_{0:k}^{-i'j'} \end{aligned} \tag{5.A.8}$$

Here the expression $X_{0:k}^{-ij}$ represents the entire trajectory except for the element $X_j(i)$. The bias definition in Equation (5.A.4) yields:

$$C(ij, i'j') = I(ij, i'j') + \int \left[B_{ij}(X_{0:k})p(X_{0:k})\right]_{\chi_{i'}^-}^{\chi_{i'}^+} dX_{0:k}^{-i'j'} \tag{5.A.9}$$

From the asymptotic unbiasness assumption defined in Equation (5.A.2), the following result is obtained

$$C(ij, i'j') = I(ij, i'j') \tag{5.A.10}$$

which proves the PCRLB inequality.

APPENDIX 5.B: PROOF OF FIM RECURSIVE EXPRESSION

The FIM $J(X_{k+1})$ is calculated recursively as

$$J(X_{k+1}) = D_{k+1}^{22} - D_{k+1}^{21}\left[J(X_k) + D_{k+1}^{11}\right]^{-1} D_{k+1}^{12} \tag{5.B.1}$$

where:

$$\begin{aligned}
D_{k+1}^{11} &= E\left\{-\Delta_{X_k}^{X_k} \log p(X_{k+1} \mid X_k)\right\} \\
D_{k+1}^{12} &= E\left\{-\Delta_{X_k}^{X_{k+1}} \log p(X_{k+1} \mid X_k)\right\} = D_{k+1}^{21\,T} \\
D_{k+1}^{21} &= E\left\{-\Delta_{X_{k+1}}^{X_k} \log p(X_{k+1} \mid X_k)\right\} \\
D_{k+1}^{22} &= E\left\{-\Delta_{X_{k+1}}^{X_{k+1}} \log p(X_{k+1} \mid X_k)\right\} + E\left\{-\Delta_{X_{k+1}}^{X_{k+1}} \log p(Z_{k+1} \mid X_{k+1})\right\}
\end{aligned}$$

The initial FIM $J(X_0) = E\left\{-\Delta_{X_0}^{X_0} \log p(X_0)\right\}$.

Proof:

Following [121], the joint probability density of measurements and states can be expressed as follows

$$\begin{aligned}
p(X_{0:k+1}, Z_{1:k+1}) &= p(X_{0:k}, Z_{1:k})\, p(X_{k+1} \mid X_{0:k}, Z_{1:k})\, p(Z_{k+1} \mid X_{k+1}, X_{0:k}, Z_{1:k}) \\
&= p(X_{0:k}, Z_{1:k})\, p(X_{k+1} \mid X_k)\, p(Z_k \mid X_k)
\end{aligned} \tag{5.B.2}$$

From the decomposition of $J(X_{0:k})$ into submatrices that is given in Equation (5.45), the D-terms expressions in the recursive formula of Equation (5.B.1), and the joint density expression of Equation (5.B.2), the FIM $J(X_{0:k+1})$ can be written in block form as

$$J(X_{0:k+1}) = \begin{bmatrix} A(k) & B(k) & 0 \\ B(k)^T & C(k) + D_k^{11} & D_k^{12} \\ 0 & D_k^{21} & D_k^{22} \end{bmatrix} \tag{5.B.3}$$

The FIM $J(X_{k+1})$ is the inverse of the $n \times n$ lower-right submatrix of $\left[J(X_{0:k+1})\right]^{-1}$:

$$\begin{aligned}
J(X_{k+1}) &= D_k^{22} - \begin{bmatrix} 0 & D_k^{21} \end{bmatrix} \begin{bmatrix} A(k) & B(k) \\ B(k)^T & C(k) + D_k^{11} \end{bmatrix} \begin{bmatrix} 0 \\ D_k^{12} \end{bmatrix} \\
J(X_{k+1}) &= D_k^{22} - D_k^{21}\left[C(k) + D_k^{11} - B(k)^T A(k)^{-1} B(k)\right]^{-1} D_k^{12}
\end{aligned} \tag{5.B.4}$$

According to Equation (5.47), $J(X_k) = C(k) - B(k)^T A(k)^{-1} B(k)$, which when substituted into Equation (5.B.4) gives the following:

$$J(X_{k+1}) = D_k^{22} - D_k^{21} \left[D_k^{11} + J(X_k) \right]^{-1} D_k^{12} \tag{5.B.5}$$

which is the desired result.

Chapter 6

Conclusion

> *The engineer is concerned to travel from the abstract to the concrete. He begins with an idea and ends with an object. He journeys from theory to practice. The scientist's job is the precise opposite. He explores nature with his telescopes or microscopes, or much more sophisticated techniques, and feeds into a computer what he finds or sees in an attempt to define mathematically its significance and relationships. He travels from the real to the symbolic, from the concrete to the abstract. The scientist and the engineer are the mirror image of each other.*
>
> — Gordon L. Glegg

6.1 SUMMARY OF CONTRIBUTIONS

This thesis aim was to contribute towards finding a solution to a multi-fold problem related to Global Navigation Satellite Systems (GNSS) inherent shortcomings, the principal shortcoming being that GNSS was designed to operate in clear line-of-sight (LOS) environments. The multi-fold problem pertains to the conventional scalar tracking approach inability to maintain robust tracking and positioning availability in multipath and non-line-of-sight (NLOS) prone environments (urban, suburban, heavy foliage), as well as to the modern vector tracking approach proclivity to propagate multipath induced tracking errors from channel to channel and thus compromise the positioning solution integrity in such environments. It is a matter of fact that robust and well-designed GNSS receiver architectures as well as efficient tracking and positioning algorithms can both contribute towards alleviating the problems related to the GNSS inherent shortcomings. Grounded on these premises, the thesis contribution was sought to have architectural as well as algorithmic orientation. Stemming from the fact that both scalar tracking and vector tracking solutions have advantages as well as disadvantages when navigating in harsh environments, it was deemed useful to have the proposed architectural solutions exploit the strengths of both scalar and vector tracking while minimizing their weaknesses. Furthermore, in order to fit the multipath and NLOS mitigation strategy into the proposed architectures with minimal additional architectural and algorithmic burden, multipath and NLOS detection techniques have been privileged over multipath estimation techniques and have been designed based on correlator outputs. The mitigation is performed by excluding unhealthy channels from the position-velocity-time (PVT) solution calculation in the navigator. Moreover,

considering the fact that the PVT solution accuracy depends on the algorithm that is used in the navigator and directly impacts the vector tracking performance, Bayesian filtering methods that better approach the nonlinear and non-Gaussian nature of the GNSS navigation and vector tracking problem have been explored and some improvements have been suggested. After this succinct review of the rationale behind the orientation and nature of this thesis' contributions, these contributions are summarized hereafter in three main parts.

- **Correlator-based signal quality indicators**: An investigation into the Global Positioning System (GPS) receiver operation in multipath environments has been performed and has resulted in a contribution of this thesis to the modelling of multipath induced tracking errors. This investigation has been done with the objective to propose a solution to the multipath and NLOS problems. Three multipath detection techniques have been proposed. Their working principle is based on the fact that in the presence of multipath, the early-minus-late (EmL) correlator output exhibits an increase in signal power in comparison with the signal power that is usually observed in the absence of multipath. By assuming that the signal at the EmL output in the presence of multipath has constant amplitude (DC level signal), a first detector using time-domain metrics and based on the Generalized Likelihood Ratio Test (GLRT) for a binary hypothesis has been defined. It is referred to as GLRT-based Detector. However, this detector performs well only for scenarios where the multipath (MP) and LOS signals have the same frequency and for the two-ray (LOS + MP) multipath model. Its poor performance in realistic scenarios has motivated the design of better MP detectors. By assuming that the signal at the EmL output in the presence of MP is a sinusoidal signal this time, two detectors using frequency domain metrics i.e. based on Fast Fourier Transform (FFT) have been proposed. They are referred to as FFT-based Detector I and FFT-based Detector II. FFT-based Detector I is also called modified GLRT (M-GLRT) Detector as it also steams from GLRT. Both FFT-based detectors have proved to be performant in detecting multipath contaminated signals. Realistic experimental scenarios using synthesized and real GPS signals have been used to evaluate and validate the performance of these MP detectors in harsh environments. As harsh environments create NLOS problems in addition to MP problems, a correlator-based NLOS detector has been designed to operate hand-in-hand with the MP detectors. It principally acts as a LOS power attenuation detector but with a proper threshold setting it makes it possible to distinguish LOS from NLOS situations.

- **Adaptive and conjoint scalar-vector tracking loops**: As a first evolution and contribution to the vector tracking solutions in literature, this thesis has proposed a vector tracking loop that utilizes the proposed MP and NLOS detectors as well as a C/N_0 estimator to exclude unhealthy channels from PVT computation in the navigator. In comparison with fault detection and exclusion (FDE) methods that perform consistency checks and integrity monitoring in the navigator, this technique excludes fault in the navigator but from a post-correlator level in the GNSS signal processing chain thus providing an anticipative solution. This does not preclude using FDE methods in conjunction with the proposed vector tracking scheme and therefore obtaining some benefit in redundancy. The experiments that have been conducted on DLR synthesized signals in urban and suburban environments have shown the ability of this vector tracking scheme to improve positioning and tracking performance in multipath environments in comparison with a standard vector tracking scheme. The second proposed evolution to existing tracking solutions is an adaptive scalar-vector tracking loop. The latter uses the proposed NLOS detector, a Phase Lock Indicator (PLI) and a C/N_0 estimator to continuously switch between scalar and vector tracking modes depending on tracking and positioning availability and accuracy needs. This adaptive tracking scheme also uses the proposed MP detectors and a C/N_0 estimator to exclude unhealthy satellites from PVT calculation. Another proposed hybrid tracking solution and the third evolution is the conjoint scalar-vector tracking loop. This tracking scheme maintains simultaneous scalar and vector tracking and uses the proposed NLOS detector, a PLI and a C/N_0 estimator to continuously select which between the scalar and vector tracking measurements are to be sent to the navigator. The conjoint tracking scheme excludes unhealthy satellites from the PVT computation using the proposed MP detectors and a C/N_0 estimator. Many experiments using DLR multipath data have been conducted and have indicated that the hybrid schemes (adaptive and conjoint tracking schemes) tend to conform to the best between the scalar tracking loop and the vector tracking loop, i.e. to the tracking scheme that provides the best positioning accuracy or tracking robustness at a given time. Looking at the two hybrid schemes, the adaptive tracking architecture is less complex than the conjoint counterpart, while the conjoint tracking architecture has the potential to open a way for detecting navigator contamination thus rendering the MP detection tests more robust. If coupling with an Inertial Navigation System (INS) is to be considered without aberration in architectural complexity, the low complexity of the adaptive tracking scheme is particularly attractive.

- **Nonlinear Bayesian filtering approaches:** The GNSS positioning and vector tracking problem is nonlinear and potentially non-Gaussian in nature. Among the Bayesian filtering methods used to solve this problem, the Extended Kalman Filter (EKF) linearizes the filtering model around the most recent state estimate then applies the standard Kalman filter equations. This linearization is problematic when severe nonlinearities appear in the system leading to the EKF solution divergence. This thesis has investigated iterative and adaptive methods as applied to the Unscented Kalman Filter (UKF). The UKF does not linearize the filtering model but provides a Gaussian approximation for the state mean and covariance. The iterative and adaptive methods allow rapid filter convergence in case of large initial errors and are able to combat filter divergence. The thesis has further proposed a novel Unscented Particle Filtering (UPF) approach, the Iterated Adaptive UPF (IAUPF). Particle filters do not set a priori restrictions such as linearity or Gaussianity to the filtering model which theoretically makes them the Bayesian filtering approach with the potential for the best estimation of the posterior distribution. The IAUPF exploits the iterative and adaptive methods and uses the Iterated adaptive UKF (IAUKF) to provide a Gaussian proposal distribution from which particles are sampled. The proposed IAUPF uses a synergized resampling strategy that is based on regularized and stratified resampling, switching between the two depending on the degree of particle degeneracy. A regularized resampling strategy avoids particles impoverishment or collapse. Switching between stratified and regularized resampling has been used because the regularized particle filter has a theoretical limitation in asymptotical estimation of the posterior distribution. Stratified resampling ensures that a small variance of the number of descendants per particle is obtained. A posterior Cramér-Rao lower bound (PCRLB) has been derived for benchmarking purposes. Performance evaluation of the different algorithms, namely EKF, UKF, IUKF, IUPF and IAUPF, based on Monte-Carlo simulations and using the derived PCRLB as benchmarking reference has shown that particle filtering approaches are the closest to the PCRLB, i.e. they provide the best convergence properties and the best position estimation accuracy. This PCRLB-based performance benchmarking has also demonstrated that the iterative and adaptive methods do have a great impact on convergence and estimation accuracy. To provide further validation to the IAUPF algorithm, its positioning and vector tracking solution has been compared with the EKF solution using experiments that are based on the DLR multipath model data. The obtained experimental results for five dynamic scenarios in suburban and urban environments have demonstrated the superior vector tracking and positioning performance of the IAUPF in comparison with the EKF.

6.2 FUTURE WORK

The multipath detectors that have been proposed in *Chapter 3* exploit the Early-minus-Late (EmL) correlator output. They are thus based on the detection of a bias on the estimated code delay. The detection of these biases is facilitated in vector tracking mode when the navigator is not contaminated. For the case of low receiver dynamics in particular, the impact of these biases may be attenuated in a receiver that utilizes a narrow discriminator (which requires the use of a high sampling frequency), and that operates in vector tracking mode and in tight coupling with an INS. For the case of high receiver dynamics, the code delay errors are spread in the frequency domain as the receiver velocity is high. Power measurements that are obtained from a power spectral density (PSD) estimator, such as the one present in the FFT-based multipath detectors, are therefore interesting. The PSD estimator being able to spot power increase on the EmL output, a detector based on it may therefore rightly be utilized to exclude contaminated measurements from the navigator or to control the covariance matrix of delay and Doppler measurements in the navigator. It is also worthy to mention that the impact of these multipaths can be attenuated by reducing the tracking loops noise bandwidths. This is particularly efficient if an increase in the receiver cost is not an issue (use of stable oscillator, INS coupling, and more).

A question however may arise as to how the proposed multipath detectors would distinguish between multipath and other disturbances that distort phase tracking and that can also have an effect on the EmL correlator output, such as non-multipath interference or ionospheric scintillation. The fact that the EmL output is a discriminator on its own reduces somehow the effects of some kind of interference but that depends on the Early-Late chip spacing. This is true for some correlation interval that depends on the autocorrelation function shape and on the value of the Early-Late chip spacing. But, multipath on its own is a type of interference. Depending on whether it is specular or diffuse, it impacts the C/N_0 as narrowband or wideband interference. The FFT-based detectors basically suggest excluding any channel that is contaminated by interference. Further work needs therefore to be done to be able to clearly distinguish between the types of interference (multipath or non-multipath). But in general, multipath interference will be the one mostly mirroring its effects on the EmL output as attested by the DLR experimental results in this thesis.

Also, it is worth examining a possibility to characterize the proposed detectors further by defining a mathematical relationship between their detection metric and the multipath induced positioning error. In this way, multipath that does not induce great errors on pseudorange measurements could be ignored in the channel

exclusion process. A possible approach to define this mathematical relationship would be to go from empirical results and build a database of multipath detection scenarios and their corresponding pseudorange errors. Using a large population of data, quantile regression or machine learning may be considered to derive a mathematical model linking the detector's metric to the induced pseudorange error but this is very tedious work. The work in this thesis has limited the detectors characterization to a binary decision process whereby it is assumed that detection of multipath on a channel implies that the channel is unhealthy for PVT calculation and therefore should be excluded. Of course, it was mentioned in this thesis that further verification can be included in the decision process, such as the verification of the induced dilution of precision (DOP) after exclusion of a particular channel (satellite) from PVT calculation. There is therefore more work to be done in the future regarding these issues.

Another case to be further examined would be that of multipath emanating from reflection on a building when the LOS is masked, i.e. in NLOS situation. This type of multipath arrives with a delay that depends on the building position and a frequency that depends on the building orientation. This type of multipath can be exploited by the navigator if a 3D map of the environment is available. The works in [62] [63] [64] and many more already exploit 3D environment maps and may be useful for investigating this case. Furthermore, the NLOS detector/LOS attenuation detector that has been suggested in *Chapter 3* does not have a mathematical expression for the threshold. The threshold that has been used is based on empirical observation. Further theoretical analysis coupled with Monte-Carlo simulations may be useful for the derivation of a threshold expression.

Furthermore, with respect to the tracking and navigation solutions proposed in *Chapter 4*, these will have greater significance in a multi-constellation receiver as they use satellite exclusion. Therefore, extending the receiver architecture to accommodate the acquisition, tracking and further processing of signals from *GLONASS*, *Galileo* and *Compass* constellations may be considered. Additionally, in the conjoint scalar-vector tracking scheme, the mechanism to reinitialize the scalar tracking loop (STL) of a channel that has lost track of a satellite when the latter becomes trackable again has not been implemented. A straightforward way to implement this STL tracking re-initialization would be to base it on the tracking parameter values of the corresponding vector tracking loop (VTL) channel and not on re-acquisition as it is traditionally done in literature for a receiver that does not incorporate conjoint STL-VTL tracking.

Finally, *Chapter 5* has suggested better Bayesian filtering algorithms than the EKF but they come with additional computational cost. These alternative algorithms can be

implemented in the receiver architectures proposed in *Chapter 4*. For instance, the combination of the adaptive, iterative, and particle filtering techniques with multipath detection and exclusion techniques as suggested in this thesis and their incorporation within the robust tracking architectures that have been proposed is an orientation worth investigating in future studies. However, other particle filtering techniques used to reduce computational complexity such as Rao-Blackwellisation, and various other sampling and resampling strategies need to be considered in the improvement process as well.

Bibliography

[1] J. J. Spilker Jr., "Fundamentals of signal tracking theory," in *Global Positioning System: Theory and Application, Volume 1, B.W. Parkinson and J.J. Spilker Jr., (eds.), vol. 163, Progress in Astronautics and Aeronautics*, Washington, DC, AIAA, Inc., 1996, pp. 245-328.

[2] R. E. Kalman, "A new approach to linear filtering and prediction problems," *Transactions of the ASME-Journal of Basic Engineering,* vol. 82, pp. 35-45, 1960.

[3] R. E. Kalman and R. S. Bucy, "New results in linear filtering and prediction theory," *Transactions of the ASME, Series D, Journal of Basic Engineering,* vol. 83, pp. 95-107, 1961.

[4] A. Jazwinski, Stochastic processes and filtering theory, Academic Press, 1970.

[5] B. D. O. Anderson and J. B. Moore, Optimal filtering, Prentice Hall, 1979.

[6] S. J. Julier and J. K. Uhlmann, "A general method for approximating nonlinear transformations of probability distributions," in *Technical Report, Dept. of Engineering Science, University of Oxford*, 1996.

[7] S. J. Julier and J. K. Uhlmann, "A new extension of the Kalman filter to nonlinear systems," *Proc. of Int. Symposium on Aerospace/Defense Sensing, Simul. and Controls,* pp. 182-193, 1997.

[8] J. E. Handschin, "Monte Carlo techniques for prediction and filtering of nonlinear stochastic processes," *Automatica,* pp. 555-563, 1970.

[9] N. Gordon, D. Salmond and A. F. M. Smith, "Novel approach to non-linear and non-Gaussian Bayesian state estimation," *Proc. Inst. Elect. Eng., F,* vol. 140, pp. 107-113, 1993.

[10] J. MacCormick and A. Blake, "A probabilistic exclusion principle for tracking multiple objects," *Proc. Int. Conf. Comput. Vision,* pp. 572-578, 1999.

[11] J. Carpenter, P. Clifford and P. Fearnhead, "Improved particle filter for nonlinear problems," in *Proc. Inst. Elect. Eng., Radar, Sonar, Navig.*, 1999.

[12] D. Crisan, P. Del Moral and T. J. Lyons, "Non-linear filtering using branching and interacting particle systems," *Markov Processes Related Fields,* vol. 5, no. 3, pp. 293-319, 1999.

[13] K. Kanazawa, D. Koller and S. J. Russell, "Stochastic simulation algorithms for dynamic probabilistic networks," *Proc. 11th Annu. Conf. Uncertainty AI,* pp. 346-351, 1995.

[14] P. Groves, Principles of GNSS, Inertial, and Multisensor Integrated Navigation

Systems, Boston|London: Artech House, 2008.

[15] R. Brown, "Receiver Autonomous Integrity Monitoring," in *Global Positioning System: Theory and Applications, Volume 2, B.W. Parkinson and J.J. Spilker Jr., (eds.)*, Washington, D.C., AIAA, Inc., 1996, pp. 143-165.

[16] P. Groves, "Fault Detection and Integrity Monitoring," in *Principles of GNSS, Inertial, and Multisensor Integrated Navigation Systems*, Boston|London, Artech House, 2008, pp. 451-470.

[17] B. Clark, "Fault Detection and Exclusion in Deeply Integrated GPS/INS Navigation," PhD Thesis, Auburn University, Auburn, Alabama, 2012.

[18] K. Borre, D. Akos, N. Bertelsen, P. Rinder and S. Jensen, A Software-Defined GPS and Galileo Receiver: A Single Frequency Approach, Boston: Birkhauser, 2007.

[19] J. Bao-Yen Tsui, Fundamentals of global positioning system receivers: A software approach, John Wiley & Sons, Inc., 2000.

[20] E. Kaplan and C. Hegarty, Understanding GPS: Principles and applications, Boston|London: Artech House, 2006.

[21] "Official U.S. Government information about the Global Positioning System (GPS) and related topics," January 2016. [Online]. Available: http://www.gps.gov/.

[22] N. Harper, "Server-Side GPS and Assisted-GPS in Java," in *GNSS Technologies and Applications*, Artech House, 2009.

[23] C. Wu and C. He, "Interference Analysis among Modernized GNSS," in *ICCP*, October 2011.

[24] M. Lashley, "Modeling and Performance Analysis of GPS Vector Tracking Algorithms," PhD Thesis, Auburn University, Auburn, Alabama, 2009.

[25] G. Kitagawa, "Monte Carlo filter and smoother for non-Gaussian non-linear state space models," *J. Comput. Graph. Statist.*, vol. 5, no. 1, pp. 1-25, 1996.

[26] O. Julien, "Design of Galileo L1F Receiver Tracking Loops," PhD Thesis, University of Calgary, Calgary, Alberta, 2005.

[27] A. Papoulis, Probability, Random Variables, and Stochastic Processes, London: Mc-Graw Hill, 1965.

[28] K. L. Chung, A Course in Probability Theory, Academic Press, 1968.

[29] G. Brodin, "GNSS Code and Carrier Tracking in the Presence of Multipath," *Proc. ION*

GPS-96, pp. 1389-1398, 1996.

[30] L. Liu and M. Amin, "Comparison of Average Performance of GPS Discriminators in Multipath," *Proc. IEEE ICASSP 2007,* pp. 1285-1288, 2007.

[31] J. Chen, L. Cheng and M. Gan, "Modeling of GPS Code and Carrier Tracking Error in Multipath," *Chinese Journal of Electronics,* vol. 21, no. 1, pp. 78-84, January 2012.

[32] J. Chen, L. Cheng and M. Gan, "Model and Simulation of Multipath Error in DLL for GPS Receiver," *Chinese Journal of Electronics,* vol. 23, no. 3, pp. 508-515, July 2014.

[33] Y. Luo, Y. Wang, S. Wu and P. Wang, "Multipath effects on vector tracking algorithm for GNSS signal," *Science China, Information Sciences,* vol. 57, October 2014.

[34] J.-M. Sleewaegen, " Multipath Mitigation, Benefits from using the Signal-to-Noise Ratio," in *Proceedings of the 10th International Technical Meeting of the Satellite Division of The Institute of Navigation (ION GPS 1997)*, Kansas City, MO, September 16-19, 1997.

[35] M. Lashley and D. Bevly, "Analysis of discriminator based vector tracking algorithms," in *Proceedings of the National Technical Meeting of The Institute of Navigation*, San Diego, 2007.

[36] M. Lashley and D. Bevly, "Comparison of Traditional Tracking Loops and Vector Based Tracking Loops for Weak GPS Signals," in *ION GNSS 20th International Technical Meeting of the Satellite Division*, Fort Worth, TX, 2007.

[37] J. Ray, "Mitigation of GPS Code and Carrier Phase Multipath Effects Using a Multi-Antenna System," *PhD Thesis,* March 2000.

[38] V. Heiries, "Optimisation d'une chaîne de réception pour signaux de radionavigation par satellite à porteuse à double décalage (BOC)," *PhD Thesis,* 2007.

[39] S. Kay, Fundamentals of statistical signal processing, Volume II: Detection theory, Prentice Hall, 1998.

[40] O. Mubarak and A. Dempster, "Exclusion of Multipath-Affected Satellites Using Early Late Phase," *Journal of Global Positioning Systems,* vol. 9, no. 2, pp. 145-155, 2010.

[41] O. Mubarak, "Analysis of Early Late Phase for Multipath Mitigation," *ION GNSS 21st. International Technical Meeting of the Satellite Division,* pp. 669-678, 16-19 September 2008.

[42] M. Brenneman, Y. Morton and Q. Zhou, "An ANOVA-Based GPS Multipath Detection Algorithm Using Multi-Channel Software Receivers," in *proceedings of 2008 IEEE/ION Position, Location and Navigation Symposium*, 2008.

[43] Y. Fang, Y. Hong, O. Zhou, W. Liang and L. WenXue, "A GNSS Satellite Selection Method Based on SNR Fluctuation in Multipath Environments," *International Journal of Control and Automation,* vol. 8, no. 11, pp. 313-324, 2015.

[44] A. Beitler, A. Tollkuehn, D. Giustiniano and B. Plattner, "CMCD: Multipath Detection for Mobile GNSS Receivers," in *proceedings of 2015 International Technical Meeting of The Institute of Navigation*, Dana Point, California, January 26 - 28, 2015.

[45] A. Dierendonck, P. Fenton and T. Ford, "Theory and Performance of Narrow Correlator Spacing in a GPS Receiver," *NAVIGATION, Journal of the Institute of Navigation,* vol. 39, no. 3, pp. 265-283, 1992.

[46] V. Veitsel, A. Zhdanov and M. Zhodzicshky, "The Mitigation of Multipath Errors by Strobe Correlators in GPS/GLONASS Receiver," *GPS Solutions,* vol. 2, no. 2, pp. 38-45, 1998.

[47] G. McGraw, "Practical GPS Carrier Phase Multipath Mitigation using High Resolution Correlator Techniques," *Proc. IAIN World Congress/ION Annual Meeting,* pp. 373-381, 2000.

[48] G. McGraw and M. Braasch, "GNSS Multipath Mitigation using Gated and High Resolution Correlator Concepts," *Proc. ION National Technical Meeting,* pp. 333-342, 1999.

[49] B. Townsend and P. Fenton, "A Practical Approach to the Reduction of Pseudorange Multipath Errors in a L1 GPS Receiver," *Proc. 7th International Technical Meeting of the Satellite Division of the Institute of Navigation, Part 1 (of 2), Proc. ION GPS,* vol. 1, pp. 143-148, 1994.

[50] J. Sleewaegen and F. Boon, "Mitigating short-delay multipath: a promising new technique," *Proc. ION GPS,* pp. 204-213, 11 - 14 September 2001.

[51] S. Kay, Fundamentals of statistical signal processing, Volume I: Estimation theory, Prentice Hall, 1993.

[52] R. van Nee, "The Multipath Estimating Delay Lock Loop," *IEEE 2nd International Symposium on Spread Spectrum Techniques and Applications,* pp. 39-42, 1992.

[53] C. Cahn and M. Chansarkar, "Multipath Corrections for a GPS Receiver," *Proc. 10th International Technical Meeting of the Satellite Division of the Institute of Navigation (ION-GPS),* vol. 1, pp. 551-557, 1997.

[54] L. Weil, "Multipath Mitigation using Modernized GPS Signals: How Good Can it Get?," *Proc. 17th International Technical Meeting of the Satellite Division of the Institute of Navigation (ION GPS),* pp. 493-505, 2002.

[55] P. Fenton and J. Jones, "The Theory and Performance of NovAtel Inc.'s Vision Correlator," *Proc. 19th International Technical Meeting of the Satellite Division of the Institute of Navigation (ION GNSS' 05),* p. 2178–2186, September 2005.

[56] M. Sahmoudi and R. Landry, "Multipath Mitigation Techniques Using Maximum-Likelihood Principle," *Inside GNSS,* pp. 24-29, November/December 2008.

[57] D. Kumar and K. Lau, "Deconvolution Approach to Carrier and Code Multipath Error Elimination in High Precision GPS," *Proc. 1996 National Technical Meeting of the Institute of Navigation,* pp. 729-737, January 1996.

[58] S. Lohan, D. Skournetou and A. Sayed, "A Deconvolution Algorithm for Estimating Jointly the Line-Of-Sight Code Delay and Carrier Phase of GNSS Signals," *ENC-GNSS,* 2009.

[59] C. Yang and L. Porter, "Frequency-Domain Characterization of GPS Multipath for Estimation and Mitigation," *Proc. 18th International Technical Meeting of the Satellite Division of the Institute of Navigation (ION-GNSS),* September 2005.

[60] C. Yang and L. Porter, "Multipath-Desensitized Delay Estimation with GPS Signal Channel Transfer Function Filtering," *ION 61st Annual Meeting,* June 2005.

[61] Y. Chan, Q. Yuan, H. So and R. Inkol, "Detection of stochastic signals in the frequency domain," *IEEE Transactions on Aerospace and Electronic Systems,* vol. 37, no. 3, pp. 978 - 988, Jul 2001 .

[62] M. Obst, S. Bauer and G. Wanielik, "Urban Multipath Detection and Mitigation with Dynamic 3D Maps for Reliable Land Vehicle Localization," in *Proc. of IEEE/ION PLANS*, 2012.

[63] M. Sahmoudi, A. Bourdeau and J.-Y. Tourneret, "Deep fusion of vector tracking GNSS receivers and a 3D city model for robust positioning in urban canyons with NLOS signals," in *7th ESA Workshop on Satellite Navigation Technologies and European Workshop on GNSS Signals and Signal Processing (NAVITEC 2014)*, Noordwijk, Netherlands, December 3-5, 2014.

[64] J. Moreau, S. Ambellouis and Y. Ruichek, "Fisheye-Based Method for GPS Localization Improvement in Unknown Semi-Obstructed Areas," *Sensors 2017,* vol. 17, no. 119, 2017.

[65] M. Petovello and P. D. Groves, "GNSS Solutions: Multipath vs. NLOS signals," *Inside GNSS,* pp. 40-44, November/December 2013.

[66] P. D. Groves, Z. Jiang, M. Rudi and P. Strode, "A Portfolio Approach to NLOS and Multipath Mitigation in Dense Urban Areas," in *ION GNSS+ 2013*, Nashville, TN, USA, 16-20 September 2013.

[67] E. Falletti, M. Pini and L. Lo Presti, "Low Complexity Carrier-to-Noise Ratio Estimators for GNSS Digital Receivers," *IEEE Transactions on Aerospace and Electronic Systems,* vol. 47, no. 1, pp. 420-437, January 2011.

[68] K. Muthuraman and D. Borio, "C/N0 Estimation for Modernized GNSS Signals: Theoretical Bounds and a Novel Iterative Estimator," *NAVIGATION: Journal of the Institute of Navigation,* vol. 57, no. 4, pp. 309-323, 2010.

[69] A. J. Van Dierendonck, "GPS Receivers," in *Global Positioning System: Theory and Applications, Volume I*, Washington, DC, AIAA, 1996, pp. 390-396.

[70] A. Giremus, J.-Y. Tourneret and V. Calmettes, "A Particle Filtering Approach for Joint Detection/Estimation of Multipath Effects on GPS Measurements," *IEEE Transactions on Signal Processing,* vol. 5, no. 4, pp. 1275-1285, 2007.

[71] N. Viandier, D. Nahimana, J. Marais and S. Duflos, "GNSS Performance Enhancement in Urban Environment Based on Pseudo-range Error Model," in *proc. IEEE/ION PLANS*, Monterey, 2008.

[72] M. Spangenberg, V. Calmettes, O. Julien, J.-Y. Tourneret and G. Duchateau, "Detection of Variance Changes and Mean Value Jumps in Measurement Noise for Multipath Mitigation in Urban Navigation," *Journal of the Institute of Navigation,* vol. 57, no. 1, pp. 35-52, 2010.

[73] M. Lashley and D. Bevly, "Comparison of Traditional Tracking Loops and Vector Based Tracking Loops for Weak GPS Signals," in *proc. ION GNSS 20th International Technical Meeting of the Satellite Division*, Fort Worth, TX, 2007.

[74] S. Bhattacharyya and D. Gebre-Egziabher, "Development and validation of a parametric model for vector tracking loops," in *proc. 22nd International Technical Meeting of the Satellite Division of the Institute of Navigation 2009, ION GNSS 2009*, Savannah, GA, 2009.

[75] N. Kanwal, "Vector tracking loop design for degraded signal environment (Master Thesis)," Tampere University of Technology, Tampere, Finland, 2010.

[76] S. Peng, Y. Morton and R. Di, "A multiple-frequency GPS software receiver design based on a vector tracking loop," in *proc. 2012 IEEE/ION Position, Location and Navigation Symposium (PLANS)*, 2012.

[77] X. Tang, G. Falco, E. Falletti and L. L. Presti, "Performance comparison of a KF-based and a KF+VDFLL vector tracking-loop in case of GNSS partial outage and low-dynamic conditions," in *proc. 2014 7th ESA Workshop on Satellite Navigation Technologies and European Workshop on GNSS Signals and Signal Processing (NAVITEC)*, Noordwijk, 2014.

[78] Y. Wang, R. Yang, K. V. Ling and E. K. Poh, "Robust Vector Tracking Loop Using Moving Horizon Estimation," in *proc. of the ION 2015 Pacific PNT Meeting*, Honolulu, Hawaii, April 2015.

[79] S. Zhao, X. Cui, M. Jia, Z. Yao and M. Lu, "Carrier Phase Tracking and Navigation Message Demodulation Approach for Vector Tracking Loops Using Serial PLL," in *proc. 29th International Technical Meeting of the ION Satellite Division, ION GNSS+ 2016*, Portland, Oregon, September 12-16, 2016.

[80] M. Karaim, M. Youssef, T. Karamat and A. Noureldin, "Adaptive Multi-hypothesis Vector Tracking System – Design and Implementation," in *proc. 29th International Technical Meeting of the ION Satellite Division, ION GNSS+ 2016*, Portland, Oregon, September 12-16, 2016.

[81] S. F. Syed Dardin, V. Calmettes, B. Priot and J.-Y. Tourneret, "Design of an Adaptive Vector-Tracking Loop for Reliable Positioning in Harsh Environment," in *26th International Technical Meeting of the ION Satellite Division, ION GNSS+ 2013*, Nashville, Tennessee, September 16-20, 2013.

[82] S. F. Syed Dardin, V. Calmettes, B. Priot and J.-Y. Tourneret, "Adaptive GNSS signal tracking techniques in the context of a deeply integrated GNSS/INS navigation system designed for tackling multipath in urban environment," in *proc. European Navigation Conference (ENC 2013)*, Vienna, 2013.

[83] J.-R. De Boer, S. Bidon, V. Calmettes, W. Vigneau and L. Ries, "Specification of a simulator to asses the performance of adaptive vector tracking loops in urban environment," in *Workshop GNSS*, Munich, December 2013.

[84] E.-H. Shin, X. Niu and N. El-Sheimy, "Performance Comparison of the Extended and the Unscented Kalman Filter for Integrated GPS and MEMS-Based Inertial Systems," in *proc. ION NTM 2005*, San Diego, CA, 2005.

[85] Y. Li, J. Wang and C. Rizos, "Comparison of the Extended and Sigma-point Kalman Filters on Inertial Sensor Bias Estimation Through Tight Integration of GPS and INS," in *proc. ION GNSS 2006*, Fort Worth, TX, 2006.

[86] Y. Li, C. Rizos, J. L. Wang, P. Mumford and W. D. Ding, "Sigma-Point Kalman Filtering for Tightly Coupled GPS/INS Integration," *NAVIGATION,* vol. 55, pp. 167-177, 2008.

[87] D.-J. Jwo and C.-N. Lai, "Unscented Kalman filter with nonlinear dynamic process modeling for GPS navigation," *GPS Solutions,* vol. 12, pp. 249-260, 2008.

[88] J. Zhou, Y. Yang, J. Zhang, E. Edwan, O. Loffeld and S. Knedlik, "Tightly-coupled INS/GPS using Quaternion-based Unscented Kalman filter," in *proc. AIAA Guidance, Navigation and Control 2011*, Portland, Oregon, 2011.

[89] R. Zhan and J. Wan, "Iterated Unscented Kalman Filter for Passive Target Tracking," *IEEE Transactions on Aerospace and Electronic Systems,* vol. 43, no. 3, pp. 1155-1163, July 2007.

[90] R. Zhan and J. Wan, "Neural Network-Aided Adaptive Unscented Kalman Filter for Nonlinear State Estimation," *IEEE Signal Processing Letters,* vol. 13, no. 7, pp. 445-448, July 2006.

[91] Z. Jiang, Q. Song, Y. He and J. Han, "A Novel Adaptive Unscented Kalman Filter for Nonlinear Estimation," in *46th IEEE Conference on Decision and Control*, New Orleans, LA, USA, December 12-14, 2007.

[92] L. Perea, J. How, L. Breger and P. Elosegui, "Nonlinearity in Sensor Fusion: Divergence Issues in EKF, modified truncated SOF, and UKF," in *AIAA Guidance, Navigation and Control Conference and Exhibit*, Hilton Head, South Carolina, 20 - 23 August 2007.

[93] K.-H. Kim, J.-H. Song and G.-I. Jee, "The GPS Vector Tracking Loop Based on the Iterated Unscented Unscented Kalman Filter under the Large Initial Error," in *European Control Conference* , Budapest, Hungary , August 23–26, 2009.

[94] X.-J. Guo and H.-Y. Zhou, "Improved UKF Algorithm for Divergence-Suppression and Its Application to Orbit Determination," in *2010 International Conference on Intelligent System Design and Engineering Application*, 2010.

[95] H. Wang, G. Fu, J. Li, Z. Yan and X. Bian, "An Adaptive UKF Based SLAM Method for Unmanned Underwater Vehicle," *Mathematical Problems in Engineering,* vol. 2013, pp. 1-12, 2013.

[96] J. F. G. de Freitas, M. A. Niranjan, A. H. Gee and A. Doucet, "Sequential Monte Carlo methods to train neural network models," *Neural Computing,* vol. 12, p. 955–993, 2000.

[97] R. Van Der Merwe, A. Doucet, N. de Freitas and E. Wan, "The unscented particle filter," in *Dietterich T.G., Leen T.K., Tresp V. (eds): Advances in Neural Information Processing Systems (NIPS13)*, 2000, p. 584–590.

[98] J. H. Kotecha and P. M. Djuric, "Gaussian particle filtering," *IEEE transactions on signal processing,* vol. 51, p. 2592–2601, 2003.

[99] Y.-Z. Zhao, "An Improved Unscented Particle Filter with Global Sampling Strategy," *Journal of Computational Engineering,* vol. 2014, pp. 1-6, 2014.

[100] Y. Yi and D. A. Grejner-Brzezinska, "Tightlycoupled GPS/INS Integration using Unscented Kalman filter and Particle filter," in *proc. ION GNSS 2006*, Fort Worth, TX, 2006.

[101] A. Giremus, "Apports des techniques de filtrage non linéaire pour la navigation avec les systèmes de navigation inertielle et le GPS," Thèse (PhD Thesis): Ecole Nationale Supérieure de l'Aéronautique et de l'Espace, Toulouse, 2005.

[102] X. Sun, S. Zhang and Q. Hu, "Particle Filter for Positioning Accuracy Improvement in GNSS Receiver," in *proc. 3rd International Conference on Electric and Electronics (EEIC 2013)*, Hong Kong, China, December 24-25, 2013.

[103] P. Aggarwal and N. El-Sheimy, "Hybrid Extended Particle Filter (HEPF) for INS/GPS Integrated System," in *proc. ION GNSS 2009*, Savannah, GA, 2009.

[104] J. Zhou, Y. Yang, J. Zhang and E. Edwan, "Applying Quaternion-based Unscented Particle Filter on INS/GPS with Field Experiments," in *proc. 24th International Technical Meeting of The Satellite Division of the Institute of Navigation (ION GNSS 2011)*, Portland, Oregon, September 20 - 23, 2011.

[105] G. Pau Closas, "Bayesian Signal Processing Techniques for GNSS Receivers: From multipath mitigation to positioning," PhD Thesis, Universitat Politecnica de Catalunya, Barcelona, June 2009.

[106] P. Closas, C. Fernández-Prades and J. A. Fernández-Rubio, "A Bayesian Approach to Multipath Mitigation in GNSS Receivers," *IEEE Journal of Selected Topics in Signal Processing,* vol. 3, no. 4, pp. 695-706, August 2009.

[107] G. Feng, "Research on Ultra-Tight Integration Technology for GNSS/SINS Integrated Navigation Systems," in *Sun J., Jiao W., Wu H., Lu M. (eds) China Satellite Navigation Conference (CSNC) 2014 Proceedings: Volume III. Lecture Notes in Electrical Engineering, vol 305*, Berlin, Heidelberg, Springer, 2014, pp. 533-548.

[108] G. L. Fay, "Nonlinear GPS Code Tracking Using a Particle Filter Vector Delay Lock Loop for Interference Mitigation," PhD Thesis, University of California, Los Angeles, 2010.

[109] G. G. Goad and L. Goodman, "A modified Hopfield tropospheric refraction correction model," in *proc. American Geophysical Union Annual Fall Meeting*, San Francisco, California, December 12-17, 1974.

[110] J. A. Klobuchar, "Ionospheric Time-Delay Algorithms for Single-Frequency GPS Users," *IEEE Transactions on Aerospace and Electronic Systems,* Vols. AES-23, pp. 325-331, May 1987.

[111] R. Van Der Merwe, A. Doucet, N. de Freitas and E. Wan, "The Unscented Kalman Filter," in *proc. 13th International Conference on Neural Information Processing Systems*, Denver, CO, 2000.

[112] C. Musso, N. Oudjane and F. LeGland, "Improving regularised particle filters," in *Sequential Monte Carlo Methods in Practice, A. Doucet, J. F. G. de Freitas, N. J. Gordon (Eds.)*, New York, Springer-Verlag, 2001.

[113] M. S. Arulampalam, S. Maskell, N. Gordon and T. Clapp, "A Tutorial on Particle Filters for Online Nonlinear/Non-Gaussian Bayesian Tracking," *IEEE Transactions on Signal Processing,* vol. 58, no. 2, pp. 174-188, February 2002.

[114] W. Fasheng and L. Yuejin, "Improving particle filter with a new sampling strategy," in *proc. 4th International Conference on Coputer Science and Education*, July 2009.

[115] M. P. Shutzenberg, "A generalization of the Fréchet-Cramér inequality to the case of Bayes estimation," *Bull. Amer. Math. Soc.,* vol. 63, 1957.

[116] H. L. Van Trees, Part I of Detection, Estimation and Modulation Theory, New York: Wiley Interscience, 1968.

[117] B. Z. Bobrovsky, E. Mayer-Wolf and M. Zakai, "Some classes of global Cramer-Rao bounds," *Ann. of Stat.,* vol. 15, pp. 1421-1438, 1987.

[118] B. Z. Bobrovsky and M. Zakai, "A lower bound on the estimation error for Markov processes," *IEEE Trans. Automat. Contr.,* vol. 20, no. 6, pp. 785-788, December 1975.

[119] I. Reuven and H. Messer, "A Barankin-type lower bound on the estimation error of a hybrid parameter vector," *IEEE Trans. Inform. Theory,* vol. May, no. 3, pp. 1084-1093, May 1997.

[120] A. J. Weiss and E. Weinstein, "A lower bound on the mean square error in random parameter estimation," *IEEE Trans. Inform. Theory,* vol. 31, no. 5, pp. 680-682, September 1985.

[121] P. Tichavsky, C. Muravchik and A. Nehorai, "Posterior Cramér-Rao bounds for discrete-time nonlinear filtering," *IEEE Trans. Sig. Proc.,* vol. 46, no. 5, pp. 1386-1396, 1998.

[122] A. Mohammadi, "Distributed Implementations of the Particle Filter with Performance Bounds," PhD Thesis, York University, Toronto, Ontario, November 2013.

[123] L. Zao, R. Niu and P. Varshney, "Conditional posterior Cramér-Rao lower bounds for nonlinear sequential Bayesian estimation," *IEEE Trans. Sig. Proc.,* vol. 60, no. 10, pp. 5549-5556, 2011.

[124] F. Gustafsson, "Particle filter theory and practice with positioning applications," *IEEE Aerospace and Electronic Systems Magazine,* vol. 25, no. 7, pp. 53-82, July 2010.

[125] T. Bréhard and J.-P. Le Cadre, "Initialization of Particle Filter and Posterior Cramér-Rao Bound for Bearings-Only Tracking in Modified Polar Coordinate System," RR-5074, INRIA, Rennes, France, 2004.

[126] R. Misra and S. Palod, "Code and carrier tracking loops for GPS C/A code," *International Journal of Pure and Applied Sciences and Technology,* vol. 6, no. 1, pp. 1-20, 2011.